UNIVERSITAT DE BARCELONA

GPS present-day kinematics of the eastern Betics, Spain

Ana Echeverria Moreno

GPS PRESENT-DAY KINEMATICS OF THE EASTERN BETICS, SPAIN

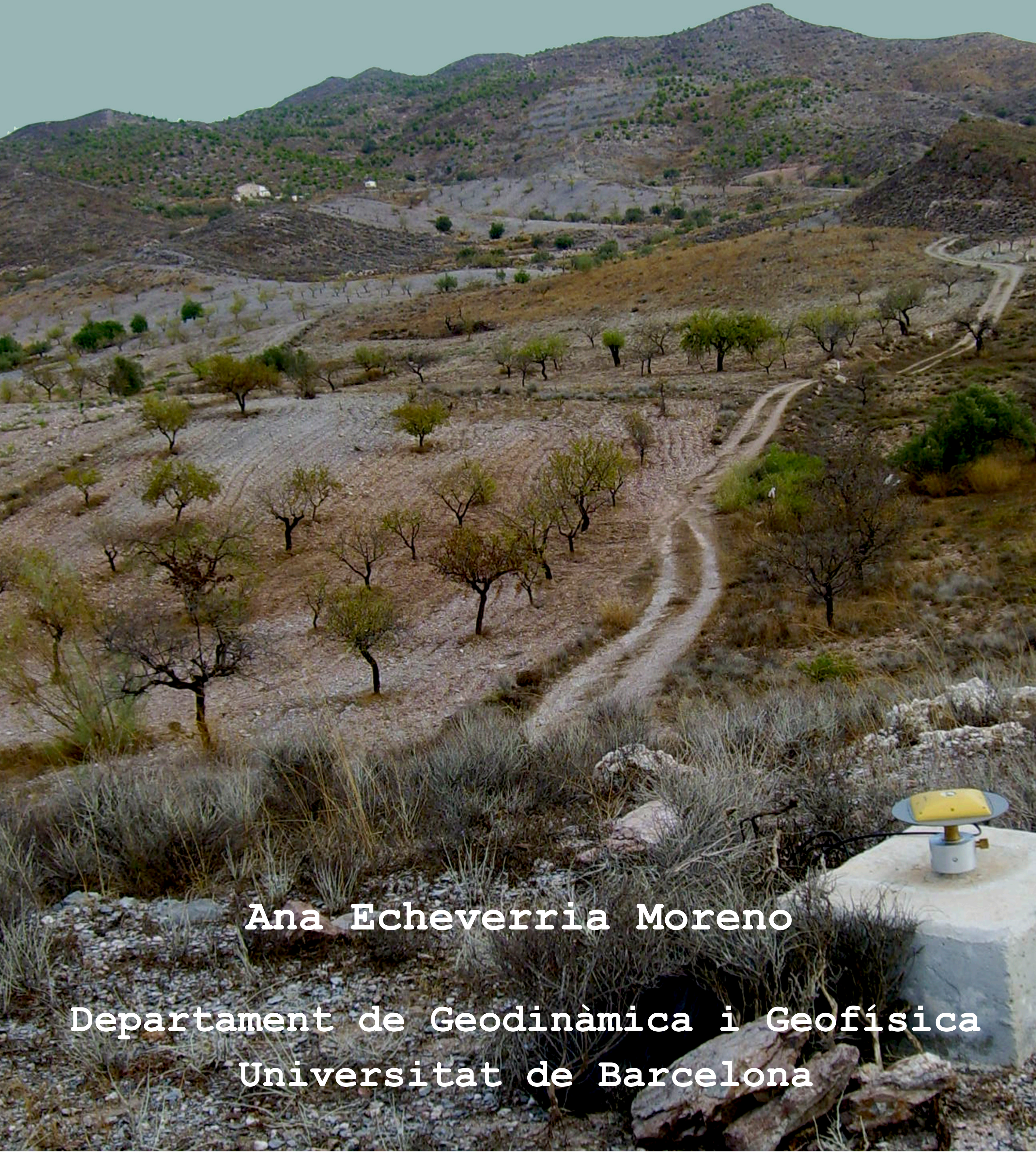

Ana Echeverria Moreno

Departament de Geodinàmica i Geofísica
Universitat de Barcelona

Universitat de Barcelona
RISKNAT – Grup de Riscos Naturals
Departament de Geodinàmica i Geofísica

GPS present-day kinematics of the eastern Betics, Spain

Memòria presentada per

Ana Echeverria Moreno

Per optar al títol de Doctora dins del programa de doctorat de Ciències de la Terra de la Universitat de Barcelona sota la direcció del Dr. **Giogi Khazaradze**.

Barcelona, Abril del 2015.

Dr. Giorgi Khazaradze
Director

Dra. Emma Suriñach
Tutora

Aquesta tesi s'ha pogut realitzar gràcies a la beca predoctoral APIF (Ajuts de Personal Investigador en Formació) de la Universitat de Barcelona, al projecte Topo-Iberia (CSD2006-00041) del Ministerio de Economía y Competitividad en el programa CONSOLIDER-INGENIO-2010 i a la prestació per desocupació del Ministerio de Empleo y Seguridad Social.

Els següents projectes i grups d'investigació han finançat part d'aquesta tesi: el Departament de Geodinàmica i Geofísica, el Grup de Recerca en Riscos Naturals RISKNAT (2014SGR/1243), la Facultat de Geologia, el Laboratori d'Estudis Geofísics Eduard Fontseré de l'Institut d'Estudis Catalans, els projectes CuaTeNeo (CGL2004-21666-E), EVENT (CGL2006-12861-C02-01) i SHAKE (CGL2011-30005-C02-02 SHAKE) i Geomodels Research Institute.

A la meva família,

Agraïments - Acknowledgments

"Es busquen estudiants". Qui m'anava a dir que aquell cartell penjat l'any 2006 al costat de l'ascensor acabaria desembocant en aquesta aventura, resultat de la qual ha estat aquesta tesi. Aquest treball és la culminació d'anys d'investigació en el quals no he estat sola. És per tot això que m'agradaria donar les gràcies a moltes persones pel seu suport, dedicació i ajuda, sense les quals això no hagués tingut cap mena de sentit.

Primer de tot, voldria donar-li les gràcies al Dr.Giorgi Khazaradze, director i incitador a que em plantegés demanar una beca per poder fer la tesi. La major part dels coneixements i habilitats adquirides durant aquests anys (ja siguin sobre GPS, construcció, informàtica, ...) han estat gràcies a ell. Gracias Gia, sobre todo por volverme a encauzar cuando, sabemos que han sido varios momentos, perdía el norte o me iba por las ramas, გმადლობთ. També vull agrair l'omnipresència de la tutora de la tesi, la Dra. Emma Suriñach, sempre al peu canó fos el que fos.

També voldria agrair la dedicació i facilitat brindada pels responsables de les meves estades de recerca a Bologna i Lisboa. Vorrei inoltre estendere i miei ringraziamenti al Dr. Enrico Serpelloni per avermi guidato nell'interpretazione delle velocità e nell'introduzione ai profili ed al block modelling. Riconosco che si è trattata di un'esperienza di appendimento esaustivo e molto gratificante. Il mio soggiorno di studio all'INGV non sarebbe stato lo stesso senza la collaborazione preziosa di Bruni, Irene, Lentizia, Roberto, Sheldoff, Adriano e Simone. Thank you Susana Custódio for explain me moment tensor and in general for having more idea about the "seismic world", muito obrigada. A tu Josep Batlló, gràcies per fer-me veure el variat mon de les magnituds i catàlegs sísmics. Tot i no haver utilitzar les relacions i recopilacions fetes, ara m'ho miro tot des d'un altre punt de vista.

Gràcies a totes les persones que han col·laborat en les campanyes de camp, des d'estudiants, a treballadors del ROA, professors i becaris. Particularment, voldria agrair l'Eva, Gia, Diego, Marta F., Marta G., Bego, Borja, Asier, Kimbo, Ferran, Ainhoa, Albert i Elena per acompanyar-me ja fos a mesurar estacions de CuaTeNeo o a arreglar les estacions GATA, ASIN o LNDA. També voldria agrair a totes les persones i institucions que s'ocupen de la gestió i manteniment de les estacions contínues així com les persones que hi ha darrera dels programes utilitzats en aquesta tesi. A totes les persones que han dissenyat i mantenen el funcionament dels programes GAMIT/GLOBK (especialment al Bob King per tenir sempre una resposta quasi immediata al correu solucionant dubtes o problemes) i Generic Mapping Tools, GMT, ja que la majoria de les figures han estat realitzades amb aquest programa. També voldria agrair, tant per la creació de Tdefnode com per la dedicació i amabilitat, a Robert McCaffrey. Ja sigui per les classes quasi particulars del programa, com també per les nocions més bàsiques sobre deformació.

Gràcies a tot el personal del Departament de Geodinàmica i Geofísica, tant a l'equip docent i investigador com administratiu (Ana, Joan Ramón i Mª José, la vecinita). Heu fet que hagi estat una etapa molt agradable i m'hagi sentit com a casa. Gràcies Eulàlia pels debats d'aquests últims mesos i fer que no deixés abandonada la geologia. Gràcies Maria, Eulàlia i Marta (i flaguitos) per portar-me al camp, veure la falla in situ no te preu! En especial, vull agrair la sort d'haver-me topat amb meravelloses persones, mis becarios por el mundo: Eva, Diego, Lena D., Rosario, Félix, Marta F., Cris, Manu, Sara, Mar, Xènia, Perla, Joan, Eloi, Fabi(án), Lena E., i Marta G. Els dinars i altres 'eventos varios' no haurien estat el mateix sense vosaltres. Doneu vida a la "carpa" i als sofàs! Sou únics.

A tots els amics/amigues i companyes de pis (ho sento, no he posat tots els noms un per un per no allargar-ho més), que heu estat sempre presents tot i no entendre gaire bé què feia. Gràcies per ajudar-me a desconnectar amb un cervesa o animant-me a acabar per tal de veure la llum. Capítulo aparte para ti Eva, no sé ni que decir. Simplemente, que no concibo esta tesis sin ti, sin tu ayuda, sin tus comentarios dentro y fuera del despacho (aún me RIOJ), sin nuestras discusiones sobre las cosas más básicas, sobre el fichero más remoto de Gamit o Tdefnode o sobre la serifa y diseños artísticos. Siempre te estaré eternamente agradecida. Ah, y no me olvido de los autógrafos del Pau...

Per últim, i no menys important, voldria agrair a la meva família el seu suport incondicional. Si fins i tot heu agafat una estima especial a Landa! Simplement, gràcies per ser com sou i per demostrar-m'ho cada dia. Elena, Albert i Bego, aquesta tesi va per vosaltres.

A tots vosaltres i els que m'heu sofert, Gràcies Per Ser-hi

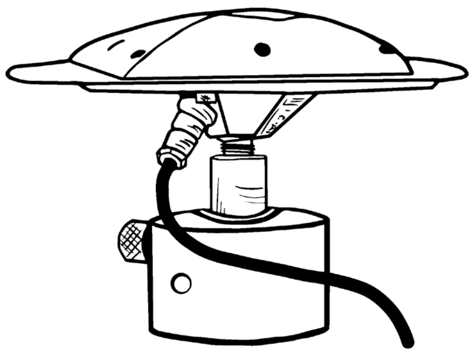

Disseny cortesia de NOU132

Table of contents

Abstract

Crustal deformation refers to the changing earth's surface caused by tectonic forces that gradually accumulate within the crust and then usually cause earthquakes. For this reason, understanding the details of deformation and its effects on faults is important. Spatial geodetic technique, and Global Positioning System (GPS) in particular, provides a fundamental tool for observing the kinematics of contemporary crustal deformation rates that can be used to identify tectonically active faults or regions. In this thesis, we contribute to understanding the ongoing crustal deformation of the eastern Betics using GPS measurements.

The eastern Betic Cordillera, south-eastern Spain, is one of the most seismically active area within the Iberian Peninsula. The Eastern Betic Shear Zone (EBSZ) in the Betic Cordillera absorbs part of the convergence between the Eurasia and African (Nubia) plates, stretching for ~250 km from Alicante to Almeria. The EBSZ is a NE-SW transpressive left-lateral trending fault-system that is composed by several individual faults. Listed from south to north: Carboneras, Palomares, Alhama de Murcia, Carrascoy and Bajo-Segura.

The CuaTeNeo GPS network was installed in 1996 in the eastern Betics with the main goal of determining the ongoing activity of the abovementioned fault systems (specifically of the Carboneras, Palomares and Alhama de Murcia faults). The network consists of 15 highly stable monuments, covering an area of 120x50 km in Murcia and Almeria. The network has been observed five times in 1997, 2002, 2006, 2009 and 2011. The results presented here are based on the analysis of the data of these five campaigns, spanning 15 year long time period and the data from continuous GPS stations of various public networks, such as REGAM, MERISTEMUM, IGN and RAP. In addition, several stations specially designed to detect tectonic crustal deformations have also been included: GATA station from Cabo de Gata and four Topo-Iberia network stations located within the study area.

The most prominent feature of the GPS velocity field is the NW oriented motion of the majority of the stations at rates ranging from 0.5 to 3 mm/yr in a western Europe reference frame. This type of deformation indicates that the main driving force responsible for the observed velocities is related to the on-going convergence between Nubia and Eurasia plates.

The calculated deformation field shows evidence for localized deformation related to active faults within the area. Most of the observed deformation is concentrated in the area delimited by the Alhama de Murcia (AMF) and Palomares (PF) faults. Here the maximum shear strain rates are observed. An estimated geodetic slip rate of the AMF-PF fault system is 1.5±0.3 mm/yr, oriented

obliquely to the strike of the fault and indicating a combination of reverse and sinistral type of motion. We attribute this maximum slip rate to AMF since PF is currently either inactive or is slipping very slowly, at rates that are undetectable by the current GPS station spatial-temporal coverage. The installation of the GATA GPS station at Cabo de Gata has enabled us to obtain continuous observations from both sides of the Carboneras fault zone (CFZ) in the southern part of the study area. For the first time, it was possible to quantify the slip rate of the CFZ: a maximum left-lateral strike slip motion of 1.3±0.2 mm/yr. The coincidence of the geologic and geodetic strike-slip rates along the CFZ, illustrate that during Quaternary the northern segment of the CFZ has been tectonically active and has been slipping at a constant rate ranging from 1.1 to 1.5 mm/yr.

GPS velocities and the derived strain rate field suggest a dominant NW-SE oriented compression, with a SW-NE extension in the south-western part of the study area, west of Almeria. In this SW sector the dominance of $\dot{\varepsilon}_{max}$ indicate a presence of a thinning or extensional kinematics, related to the block escape tectonics and possibly a slab rollback.

This work demonstrates the current continuing tectonic activity of the eastern Betics and determines that Alhama de Murcia and Carboneras left-lateral faults are the most active faults. These two faults play an important role in the regional plate convergence kinematics.

Resum

El terme deformació cortical fa referència al canvi de la superfície terrestre degut a forces tectòniques que s'acumulen gradualment en l'escorça i que per tant originen terratrèmols. Per aquesta raó, és important entendre els detalls de la deformació i els seus efectes en les falles. Les tècniques geodèsiques espacials, i el GPS (Global Positioning System) en particular, proporcionen una eina fonamental per l'observació de la deformació cortical actual i es poden utilitzar per identificar regions o falles tectònicament actives. En aquesta tesi, es contribueix a entendre millor l'actual deformació cortical de les Bètiques orientals mitjançant mesures GPS.

La serralada de les Bètiques orientals, al sud-est d'Espanya, és una de les àrees sísmicament més actives de la península ibèrica. El sistema de Cisalla de les Bètiques orientals (EBSZ) absorbeix part de la convergència entre les plaques Eurasiàtiques i Africana (Nubia). L'EBSZ és un sistema de falles transpressives senestres format per diverses falles, que de sud a nord són: Carboneras, Palomares, Alhama de Murcia, Carrascoy i Bajo-Segura.

La xarxa de GPS CuaTeNeo es va instal·lar l'any 1996 a les Bètiques orientals amb l'objectiu de determinar l'activitat tectònica de l'EBSZ (específicament de les falles de Carboneras, Palomares i Alhama de Murcia). La xarxa està formada per 15 monuments altament estables localitzats a les províncies de Murcia i Almeria. La xarxa s'ha observat cinc vegades: en el 1997, 2002, 2006, 2009 i 2011. Els resultats presentats en aquesta tesi es basen en l'anàlisi de les mesures d'aquestes cinc campanyes (per un període de 15 anys) així com mesures d'estacions GPS contínues de diverses xarxes públiques com la xarxa REGAM, MERISTEMUM, IGN i RAP. A més, s'han inclòs algunes estacions dissenyades especialment per a la detecció de deformacions corticals: l'estació GATA, emplaçada al Cabo de Gata i quatre estacions de la xarxa Topo-Iberia.

El tret més important del camp de velocitats GPS obtingut és l'orientació cap al NW de la majoria d'estacions, amb unes taxes de desplaçament de 0,5 a 3 mm/a (respecte Europa occidental). Aquest tipus de deformació indica que la principal força responsable de les velocitats obtingudes està relacionada amb l'actual convergència entre les plaques de Nubia i Euràsia.

El camp de deformació obtingut mostra evidències de deformació relacionada amb falles actives dins l'àrea d'estudi. La major part de la deformació es concentra en l'àrea delimitada per les falles d'Alhama de Murcia (AMF) i Palomares (PF), on s'han observat les màximes deformacions per cisalla. La taxa de lliscament horitzontal geodèsica estimada d'1,5±0,3 mm/a pel sistema AMF-PF i orientat oblic a la traça de la falla, indica una combinació de moviment invers i levògir. Aquesta taxa de lliscament màxima s'atribueix a AMF degut a que PF és actualment inactiva o presenta taxes de

lliscament molt lentes, imperceptibles en aquest estudi GPS. La instal·lació de l'estació GATA ens ha permès disposar d'observacions continues als dos costats de la zona de falla de Carboneras (CFZ). Per primera vegada, ha estat possible la quantificació geodèsica de la taxa de lliscament de CFZ: una taxa màxima en direcció senestra d'1,3±0,2 mm/a. La coincidència de les taxes geològiques i geodèsiques al llarg de la CFZ, posen de manifest que durant el Quaternari el segment nord de la CFZ ha estat tectònicament actiu i ha estat lliscant a una taxa constant d'1,1 a 1,5 mm/a.

Les velocitats GPS obtingudes i el camp de deformació derivat d'aquestes suggereixen una compressió dominant orientada NW-SE, amb una extensió SW-NE en la part SW de l'àrea d'estudi. En aquest sector del SW, prop d'Almeria, la predominança d'$\dot{\boldsymbol{\varepsilon}}_{\boldsymbol{max}}$ indica la presència d'una cinemàtica d'aprimament o extensional, relacionada a una tectònica d'escapament de blocs i possiblement a un *slab rollback*.

Aquest treball posa de manifest l'activitat tectònica continua en l'actualitat a les Bètiques orientals i determina que les falles senestres d'Alhama de Murcia i Carboneras són les més actives. Ambdues falles juguen un paper important en la cinemàtica de la convergència de plaques regional.

List of Figures

List of Tables

Main abbreviations

AF	Albox fault
AFZ	Alpujarras fault zone
AMF	Alhama de Murcia fault
BSF	Bajo-Segura fault
CaF	Carrascoy fault
CFZ	Carboneras fault zone
CGPS	Continuous GPS
CrF	Crevillente fault
EBSZ	Eastern Betic Shear Zone
EUREF	European Reference Frame
GNSS	Global Navigation Satellite System
GPS	Global Positioning System
IGN	Instituto Geográfico Nacional from Spain
IGS	International GNSS Service
ITRF	International Terrestrial Reference Frame
JF	Jumilla fault
NNR	No-net-rotation
NRMS	Normalized Root Mean Square
PF	Palomares fault
RTK	Real-time kinematic
SF	Socovos fault
SGPS	Survey GPS
TASZ	Trans-Alboran Shear Zone

1. Introduction

1.1. Introduction

Geodesy is the science of the shape of the Earth, including its general form and precise measurements of its surface. Active tectonic studies are dependent on geodesy for measurements of almost imperceptible changes in the surface of the Earth, changes that signal ongoing tectonic activity (Keller and Pinter, 1996).

Global Positioning System (GPS) was originally designed for military purposes by the US Air Force in the early 70s. Initially, even for the military that had an access to the P-code, the obtained positioning precision could only reach few meters. Nowadays the precision of GPS has been improved by four orders of magnitude over the original design specifications. This high-level precision, the relative ease of acquiring GPS data and the low-cost has revolutionized its use in the civilian applications. During the last decade, it has been used extensively in the geophysical research, such as plate tectonics, seismology, atmospheric sciences, postglacial rebound, etc.

GPS, the technique used in this thesis, provides a fundamental tool for observing the kinematics of contemporary crustal deformation rates that can be used to identify tectonically active faults or regions. Moreover, space geodesy can quantify potential seismic activity even on faults that are unknown or too deeply buried to study by conventional geological or seismological techniques (Ward, 1998). By re-measuring the geodetic network at different times, it becomes possible to monitor any displacements of the stations that are caused by tectonic forces acting on the crust. Geodetic observations play an important role in determining the motions and deformations of the crust by providing instantaneous picture of global and regional motions and permit a quantification of the strain accumulation.

In general, motion is studied by two main analyses or descriptions: kinematics and dynamics. An example given in Schwarz et al. (1987) points out the difference between the two types of studies:

"*Modeling the movement of a vehicle in three-dimensional space requires either the knowledge of the forces causing the motion or the measurement of the vehicle motion in a given three-dimensional coordinate system. The first type of modeling will be called dynamic, the second kinematic*". In this thesis, we provide a kinematic analysis of the observed crustal deformations in SE Spain, particularly the eastern Betics.

Eastern Betics refers to the easternmost part of the Betic Cordillera, located in the SE Spain (Figure 1.1). This range together with the Rif Mountains and Alboran Sea form the Gibraltar Arc, an arcuate Alpine orogenic belt. In more detail, the study area is defined by the extension of the CuaTeNeo GPS network. This network was specifically designed to determine the ongoing tectonic deformation of the region where Alhama de Murcia, Palomares and Carboneras faults are located. This faults form part of the Eastern Betic Shear Zone, a lithospheric shear system composed by left-lateral strike-slip faults, which accommodated a large part of the Neogene and Quaternary shortening (Bousquet, 1979; Sanz de Galdeano, 1990; Masana et al., 2004).

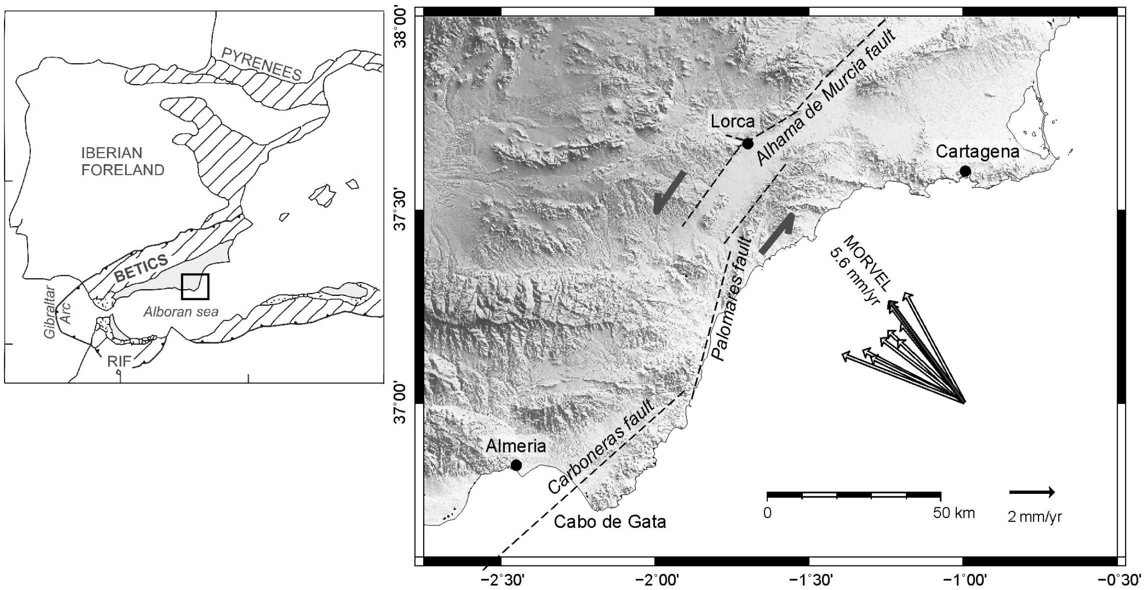

Figure 1.1: *Left)* Location of the study area in the western Mediterranean. Striped areas show Alpine orogenic belts. *Right)* Plate-convergence vectors from different models calculated at 37ºN, 1ºW and study area extension. The plate motion models are GEODVEL (Argus et al., 2010), MORVEL (DeMets et al., 2010), GSRM v1.2 (Kreemer et al., 2003), REVEL (Sella et al., 2002), APKIM2005 DFGI and IGN (Drewes, 2009), HS3-NUVEL 1A (Gripp and Gordon, 2002), APKIM2000.0 (Drewes, 1998; Drewes and Angermann, 2001), ITRF2000 (Drewes and Angermann, 2001), HS2-NUVEL 1A (Gripp and Gordon, 1990; DeMets et al., 1994), NUVEL 1A (DeMets et al., 1994), NUVEL 1 (Argus and Gordon, 1991). We have chosen throughout this thesis the MORVEL model vector (in black).

The Neotectonic period (the youngest, unfinished tectonic stage) in the eastern Betics started in the Upper Miocene (e.g. Bousquet and Montenant, 1974; Garcia-Dueñas et al., 1984) and is related to the convergence between the Nubia (Africa) and Eurasia plates. The present-day convergence between these two plates is in the order of 4 to 6 mm/yr directed approximately in the NW direction based on geodetic, geophysical and seismologic data (Sella et al., 2002; McClusky et al., 2003; Fernandes et al., 2007; Serpelloni et al., 2007; DeMets et al., 2010; Argus et al., 2011). Depending on the study, this orientation can vary up to 45 degrees (Figure 1.1). Throughout this thesis, we have opted to use the NNR-MORVEL56 (Argus et al., 2011) model, constructed from marine geophysical, seismologic and geodetic data instead of GEODVEL model (Argus et al., 2010) obtained from only geodetic observations (GPS, VLBI, SLR and DORIS) due to better agreement with velocity vectors calculated in this thesis. We attribute this discrepancy to the reference frame realization for our regional scale study, where we used the western Eurasia frame as opposed to the entire Eurasian plate, as used in GEODVEL model.

The boundary between Nubian and Eurasian plates in eastern Betics is diffuse and can be defined by a broad zone of deformation, also reflected by a broad distribution of seismicity. The Betics is one of the most seismically active zones in the Iberian Peninsula. The recent Lorca earthquake of 2011 (M_w 5.2) is a clear example of its current seismic activity. For this reason, it is important to determine how this seismic activity and associated deformation is accommodated in the area. The quantification of crustal deformation and fault-slip rates is necessary for improving seismic hazard estimations and to improve the study of seismic risk in SE Spain.

1.2. Objectives

The main goal of this thesis is to contribute to understanding the ongoing crustal deformation of the eastern Betics. In order to reach the main goal, the following specific objectives have been proposed:

- To determine the horizontal present-day GPS velocity field and provide a kinematic analysis of the area. In this part, the main contribution is to provide the unpublished velocities of CuaTeNeo network.
    - To estimate a geodetic slip-rate of Alhama de Murcia fault and determine possible GPS displacements related to Lorca 2011 earthquake.

- To derive and quantify strain-rates from the CuaTeNeo velocity field.

- To identify the most active faults in SE Betics, to determine geodetic fault slip-rates and to compare with the existent geological data. This information would be relevant to seismic hazard studies.
    - To determine whether the Carboneras fault is actively deforming fault and estimate its geodetic slip-rate.

1.3. Thesis structure

This dissertation is composed mainly of two parts. The first part concerns the methodology and state of the art of the region. This part includes Chapters 2, 3 and 4. In the second part, composed by Chapters 5, 6, 7 and 8, we present GPS analysis and interpretation of the results. A flow chart in Figure 1.2 summarizes the structure of the second part of the thesis.

Chapter 2 introduces main concepts related to crustal deformation and seismic cycle. It provides the basis of strain calculation and the relation between geodesy and deformation, seismic and aseismic detection.

Chapter 3 is dedicated to the overview of the kinematics, seismic and tectonic frame of the study area. We also provide a summary of the most relevant GPS studies conducted in the region previous to this study.

Chapter 4 introduces the basics of Global Positioning System, a theoretical review of GPS signal, errors and positioning. In this chapter is also presented the data used in this thesis. The observations from campaign and permanent networks are described, as well as the processing procedure for each set of data.

Chapter 5 presents the results obtained from GPS processing. This chapter is centered in the CuaTeNeo velocity field and their strain rate calculation. A detailed analysis and interpretation is also provided. Finally, the combination of this velocity field with the velocity field derived from continuous stations is also included.

The following two chapters further examine the main active faults detected in the area. In Chapter 6, we center on Alhama de Murcia fault. The chapter includes a velocity profile across the fault as well as an integration of geodetic data with the seismic information related to 2011 Lorca earthquake.

Chapter 7 focuses on Carboneras fault zone. Detailed combined velocity field and profile across the structure is facilitated and discussed. We performed a comparison between seismic and geodetic strain rates with the objective of determine the possible aseismic component of the Carboneras fault.

In Chapter 8, we integrate all the information included in the previous chapters in order to provide an overall picture of the broad area. We determine the geodetically active faults and suggest velocity domains with the aim of include this data in kinematic models.

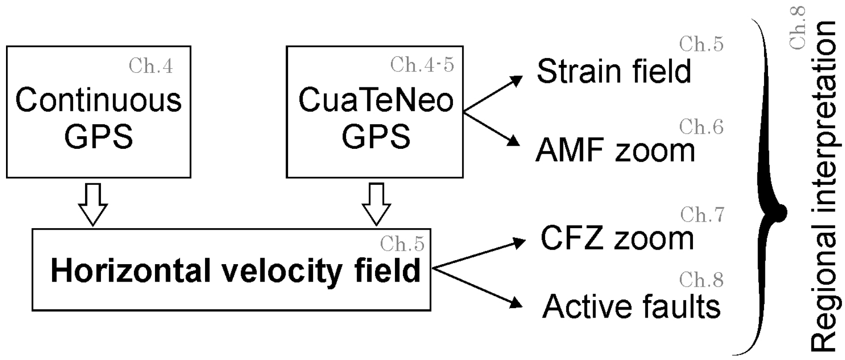

Figure 1.2: Flow chart of the structure of the second part of this thesis. Abbreviations: AMF- Alhama de Murcia fault and CFZ- Carboneras fault zone

Finally, Chapter 9 highlights the main conclusions and provides a line of future work. The recommendations intend to give a compilation of future work not be conducted during this thesis or subjects that we realized during this research are important to develop in the future.

This thesis also includes three appendixes. The first one includes a detailed geological map, where GPS stations are also shown (Appendix A). The second one shows GPS time-series of the CuaTeNeo network (Appendix B). The third annex (Appendix C) includes copies of the articles published in the following peer-reviewed scientific journals, which were based on the results presented in this thesis:

- Echeverria, A., Khazaradze, G., Gárate, J., Asensio, A., Surinach, E., **2012**. Deformación cortical de las Béticas Orientales mediante GPS y su relación con el terremoto de Lorca. Fisica de la Tierra 24, 113-127.

- Frontera, T., Concha, A., Blanco, P., Echeverria, A., Goula, X., Arbiol, R., Khazaradze, G., Pérez, F., Suriñach, E., **2012**. DInSAR coseismic deformation of the May 2011 Mw 5.1 Lorca earthquake, (Southern Spain). Solid Earth 3, 111-119.

- Echeverria, A., Khazaradze, G., Asensio, A., Gárate, J., Dávila, J.M., Suriñach, E., **2013**. Crustal deformation in eastern Betics from CuaTeNeo GPS network. Tectonophysics 608, 600-612.

- Echeverria, A., Khazaradze, G., Asensio, A., Masana, E., **Submitted**. Geodetic evidence for continuing tectonic activity of the Carboneras fault (SE Spain). Tectonophysics.

2. Deformation and geodesy

2.1. Deformation

Crustal deformation refers to the changing earth's surface caused by tectonic forces that are accumulated in the crust and then usually cause earthquakes. For this reason, understanding the details of deformation and its effects on faults is important. For example, figuring out which faults are most likely to produce the next earthquake can have important implications for the seismic hazard assessment.

Rocks change their shape and volume when they are subjected to stress. Stresses are caused by forces that are exerted on the edges or interior of a material. The forces that cause deformation of rock are referred to as stresses (Force/unit area)

Deformation refers to any change in shape, position or orientation of a body resulting from the application of a differential stress (Van der Pluijm and Marshak, 1997). The components of deformation consist of up to four components (Figure 2.1), which are divided in two groups:

i) Rigid body deformation: **translation** and **rotation**. The body undergoes changes in the position and the orientation.

ii) Non-rigid body deformation (internal deformation or **strain**): **distortion** and **dilatation**. Both components cause changes in shape and/or internal geometric relationships.

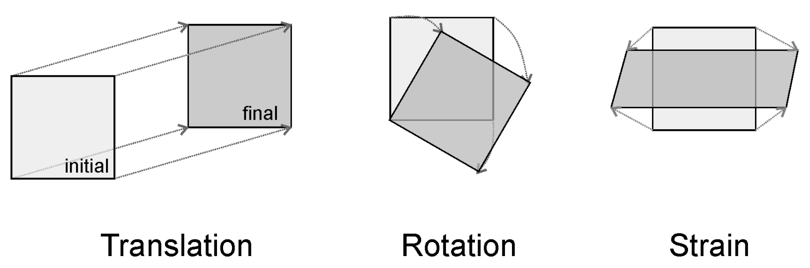

Figure 2.1: Components of deformation

In GPS deformation analysis, we usually refer to infinitesimal strain where the strain increment is of the order of 1-2% compared to the dimension of the deforming body/area. We also refer to the Lagrangian description of motion, which starts with an initial configuration and projects to a final, deformed configuration (the opposite approach is the Eulerian, which starts with the deformed configuration).

Since this thesis does not address the vertical component of the velocity, we always refer to 2-D analysis, i.e. horizontal infinitesimal strain rates. For this analysis, several assumptions have been carried out: *a)* plane-strain deformation; *b)* strain is homogeneous; *c)* neglecting vertical velocities does not affect the final interpretation. The bibliography about deformation and strain is wide and some of definitions and formulations in this work have been taken of Means (1976), Van der Pluijm (1997), Allmendinger et al. (2007, 2012) and Cardozo and Allmendinger (2009). See this works and references therein for much information.

2.1.1. Velocity gradients in 2-D

The velocity data obtained by GPS are instantaneous velocities and show the direction and rate of motion. In the limit as time shrinks to zero, the velocity vector and the displacement vector (u) converge and become identical as defined in the same reference frame. Hence, in bibliography, the displacement gradient tensor is usually used instead velocity gradient tensor.

The change in displacements with positions ($\Delta u/\Delta x$) is called displacement gradient. The displacement gradient tensor (e_{ij}) is an asymmetric tensor (formed by nine independent components in 3-D analysis), which can be decomposed into two parts: the symmetric part is the infinitesimal strain rate tensor ($\dot{\varepsilon}_{ij}$) and the antisymmetric part is the rotation rate tensor ($\dot{\omega}_{ij}$).

The rotation tensor in 2-D can be written as:

$$\dot{\omega}_{ij} = \begin{bmatrix} 0 & -\dot{\Omega} \\ \dot{\Omega} & 0 \end{bmatrix} \tag{2.1}$$

and the symmetric infinitesimal strain rate tensor as:

$$\dot{\varepsilon}_{ij} = \begin{bmatrix} \dot{\varepsilon}_{xx} & \dot{\varepsilon}_{xy} \\ \dot{\varepsilon}_{yx} & \dot{\varepsilon}_{yy} \end{bmatrix} \tag{2.2}$$

The velocity measured at a GPS site is the result of three components of deformation: translation, rotation and strain (change in shape and volume/area) of the crust. So, the E-W velocity (v_x) and N-S velocity (v_y) equations can be written as:

$$\begin{aligned} v_x &= (x_0\, \varepsilon_{xx}) + (y_0\, \varepsilon_{xy}) - (y_0\, \omega) + (t_x) \\ v_y &= (x_0\, \varepsilon_{xy}) + (x_0 \omega) + (y_0\, \varepsilon_{xy}) + (t_y) \end{aligned} \tag{2.3}$$

where x_0, y_0 are the initial positions and t_x, t_y are the translation terms. To solve the equations system, data from at least three non-aligned stations are needed, since there are six unknowns ($t_x, t_x, \omega, \varepsilon_{xx}, \varepsilon_{xy}$ and $\varepsilon_{xy} = \varepsilon_{yx}$) and for each GPS site there are two equations (v_x and v_y).

2.1.2. Strain

Strain is a dimensionless quantity and is usually expressed in *strains,* since it represents a change in length divided by the initial length. The "units" used in infinitesimal **strain rate** studies using GPS data (change in length/time) are nano-strains per year. The unit of **nstrain/yr** equals to 10^9/yr and corresponds to an elongation (positive in sign) or shortening (negative in sign) of 1 mm per 1000 km per year.

The uncertainty of strain estimate is a function of the individual uncertainties in the velocity estimates and how these uncertainties map into the model space.

When measuring strain, there are three types of properties we can measure:

- changes in the lengths of lines: elongation (extension $\dot{\varepsilon}_{max}$ or shortening $\dot{\varepsilon}_{min}$.)
- changes in angles: shear strain ($\dot{\varepsilon}_{sh-max}$)
- changes in volume: dilatation

Regarding Eq. 2.2 (strain rate tensor), the principal strain rate axes are the eigenvectors of the strain rate tensor. The eigenvalues of $\dot{\varepsilon}_{ij}$ are the principal strains in the principal directions (eigenvectors). The largest eigenvalue is the greatest principal strain rate ($\dot{\varepsilon}_{max}$), and the smaller eigenvalue is the $\dot{\varepsilon}_{min}$. Positive eigenvalue means stretching and negative compression. The shear strain is at 45º to the maximum principal strain axis and the maximum shear strain rate ($\dot{\varepsilon}_{sh-max}$) is the shear rate across the direction of its maximum value and its significance is alteration in shape (total angular change) independently of magnification or reduction:

$$\dot{\varepsilon}_{sh-max} = \dot{\varepsilon}_{max} - \dot{\varepsilon}_{min} \tag{2.4}$$

The dilatation or volume strain is independent of the axes of coordinate system, since it is the first invariant of the infinitesimal strain rate ($\dot{\varepsilon}_{max}+\dot{\varepsilon}_{min}$, the trace of $\dot{\varepsilon}_{ij}$). Assuming a constant volume (2-D), if the dilatation is negative, this indicates excess shortening in the horizontal plane and requires vertical thickening. On the contrary, a positive dilatation (($\dot{\varepsilon}_{max}+\dot{\varepsilon}_{min}$)>0) can indicate an active normal faulting and crustal thinning is required to maintain a constant volume (Allmendinger et al., 2007; Cardozo and Allmendinger, 2009).

2.1.3. Deformation computation from GPS data

2.1.3.1. Strain rate field

Fitting a strain model to velocity data is a crucial interpretation of data since allows detecting where and how much material has been deformed (Cardozo and Allmendinger, 2009). In this thesis we have calculated the strain and rotation rates with the SSPX software (Cardozo and Allmendinger, 2009). This software calculates best-fitting strain tensors (using the inverse problem) given velocity vectors. If we consider three GPS sites, the Equation 2.3 can be arranged into a single matrix equation:

$$d = G \cdot m \tag{2.4}$$

Being d the vector with known velocities, G the matrix with initial positions of the stations and m the vector of unknown model parameters. The software solves for m multiplying d by the inverse of matrix G.

The software uses several strategies for calculating strain across a region. These include: Delaunay triangulation, grid-nearest neighbor and grid-distance weighted methods. In the first two, SSPX solves the inverse problem using singular value decomposition, meanwhile in the third approach it uses the weighted least-square solution.

- **Delaunay triangulation**: with this approach deformation is calculated over triangles (the minimum number of stations necessary) constructed over each GPS station. This approach provides an irregular view of the deformation over a region since the station location geometry generally is unequally spaced.

- **Grid-nearest neighbor**: the deformation is calculated at the center of each cell of a regularly spaced grid. The velocity gradients are calculated from a fixed number of stations (*n*), defined by the user but always $n \geq 3$ that are closest to each node. The larger n, the more the smoothing of the deformation. This strategy is useful when computing strain in highly heterogeneous velocity fields (Cardozo and Allmendinger, 2009).

- **Grid-distance weighted**: this third approach also establishes a grid over the region of interest, but all of the stations are subject to weighting the contribution of each station according to its distance from the node. This approach provides a smoother strain than the previous two methods and is effective for visualizing regional patterns (Cardozo and Allmendinger, 2009).

2.1.3.2. GPS velocity profiles

A simple approach to determine the GPS strain related to a geological feature (i.e. fault) is to construct a transect perpendicular to that structure. Plotting the displacement vectors of the stations against their positions along a transect allows to determine the strain between stations. The slope of the profile plot (Figure 2.2) represents the extension in the direction of the transect (the displacement gradient in one dimension) (e.g. Allmendinger et al., 2012). For that, the GPS velocities are decomposed in two components: parallel and perpendicular to the profile direction.

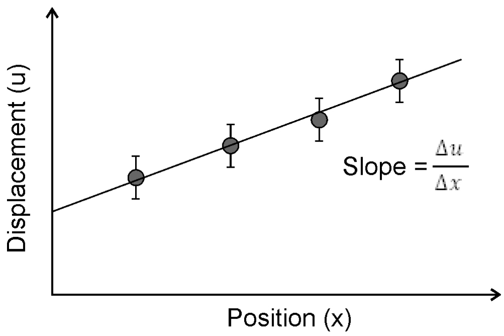

Figure 2.2: Plot of displacement versus position along the profile. The slope of the profile is the displacement gradient, i.e., strain (adapted from Allmendinger et al. (2012)).

Constructing a GPS profile across a theoretical fault, we can decompose the GPS velocity in the profile parallel component (i.e. fault perpendicular) and profile perpendicular component (i.e. fault parallel). Through the profile perpendicular velocity component, we can determine the strike-slip velocity fault related along the profile. On the opposite side, in a profile parallel velocity component we can determine the component of shortening/extension rate across the fault.

2.2. Seismic cycle

In 1910 Reid (Reid, 1910) proposed the "elastic rebound" theory following the 1906 San Francisco earthquake on the San Andreas fault. The theory assumes that the crust gradually stores elastic stress that is released suddenly during an earthquake, releasing the accumulated energy and returning to original undeformed state. According to the elastic rebound theory, in seismic cycle, the **inteseismic** phase (Figure 2.3) is generally the majority of the cycle, the steady motion occurs away from the fault and the fault itself is "locked", although some aseismic creep can also occur on it. Is the period between two main events. Immediately prior to rupture there is the **preseismic** stage in which foreshocks or other possible precursory effects can occur. The **coseismic** phase is the earthquake itself, during which sudden slip on a fault generates seismic waves. It occurs when the amount of strain accumulated during the interseismic phase exceeds the frictional forces that are preventing slip the locked portion of the fault ruptures and rocks on either side of the fault slide. The **postseismic** phase includes a period after the occurrence of the event where aftershocks and transient afterslip occur for a variable period (minutes to years). Depending on the duration and the time of the GPS measurements, geodesy gives insight into the seismic cycle before, after and between earthquakes. Due to the large duration of the cycle, it is difficult to study the entire seismic cycle.

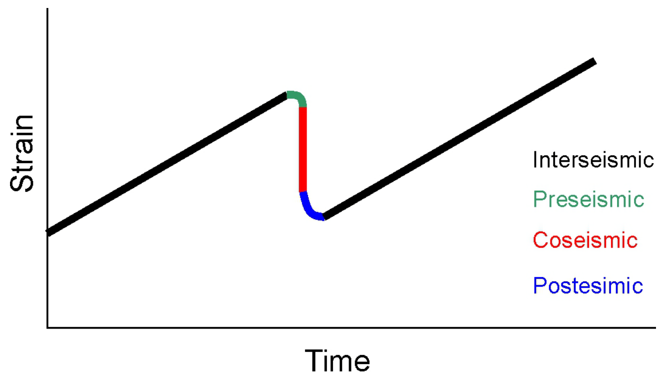

Figure 2.3: Seismic cycle phases schema. Strain accumulation and release over time along a fault.

2.2.1. Elastic fault deformation

The effect of locked faults (interseismic stage) can be modeled using the elastic dislocation theory assuming an elastic half-space (Savage, 1980; Okada, 1985). The theory is widely used to model geodetic strain due to co-seismic and/or interseismic deformation, such as surface deformation predicted for any slip distribution at depth (e.g. Vernant, 2015). Assuming an elastic rebound of an infinitely long 2-D strike-slip fault, Savage (1970) proposed an idealized model where interseismic strains accumulate uniformly throughout the deformation cycle having the same spatial pattern as coseismic strains (but opposite in sign). In this model, illustrated in Figure 2.4, the fault slips at a constant rate ($\dot{u}$) from the locking depth (D) to great depth during the interseismic phase. The surface velocity $v(y)$ follows arctangent equation:

$$v(y) = \frac{\dot{u}}{\pi}\, tan^{-1}\left[\frac{y}{D}\right] \tag{2.5}$$

where y is the distance from the fault. Note that from this equation on the fault trace $(y = 0)$ the velocity is 0 and the velocity far from the fault is equal to half the fault slip rate (Figure 2.4). The accumulation of strain near the faults can help to detect active faults.

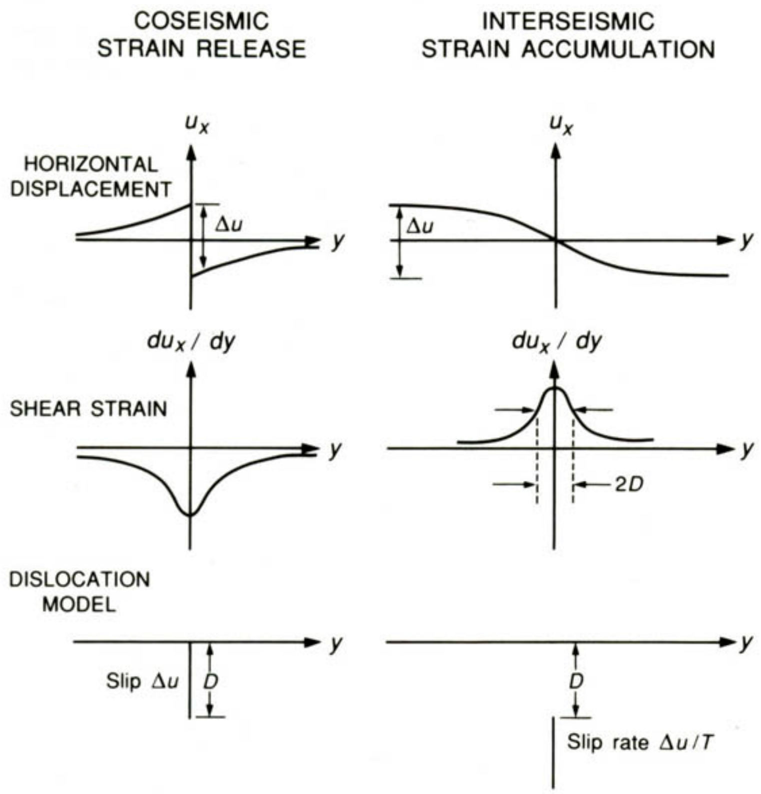

Figure 2.4: Elastic half-space model for earthquake cycle. Expected velocities and strain-rate profiles across an active locked fault. In a coseismic phase, the coseismic slip (Δu) is released along depth D. The interseismic phase consists of steady inter-earthquake aseismic slip at constant rate ($\dot{u} = \Delta u/T$ where T is the earthquake recurrence) from the locking depth D. u_x: horizontal displacements parallel to fault; du_x/d_y: shear-strain component parallel to fault; y: distance from fault (from Thatcher (1990)).

2.2.2. Inelastic deformation

Geodetic measurements can reveal various important details of neotectonic motion. Creep is defined as a motion on a fault that is not accompanied by measurable seismic activity (aseismic creep). However, recent works show that tectonic faults fail in a continuous spectrum of modes including creep events and strain transients, slow and silent earthquakes, low frequency earthquakes, tectonic fault tremor and post-earthquake afterslip (i.e. Marone and Richardson, 2012).

In dislocation models creeping is equal to D=0 (Eq. 2.5), all is free slipping, the fault is unlocked. In that way, the surface velocity across the fault will be an offset straight line (Figure 2.5), instead of an arctangent curves shown in Figure 2.4.

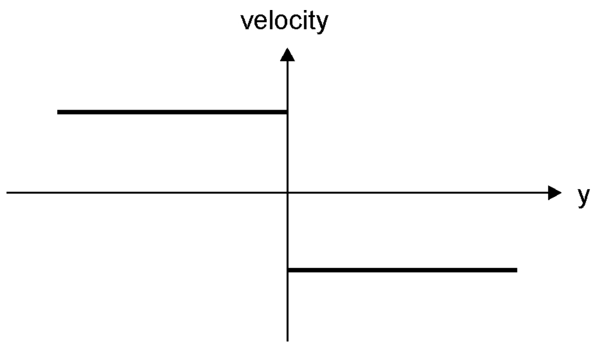

Figure 2.5: Theoretical profile with aseismic slip (unlocked fault).

3. Seismotectonic setting

The western limit of the Alpine-Mediterranean system is the Gibraltar Arc, an arcuate shaped fold-and-thrust belt formed as a result of complex tectonic processes that involves convergence between Africa and Eurasia tectonic plates (e.g. Dewey et al., 1989). The Gibraltar Arc is formed by the Betic Cordillera in southern Spain, together with the Rif Mountains in northern Africa and the Alboran Sea basin in between (Figure 3.1).

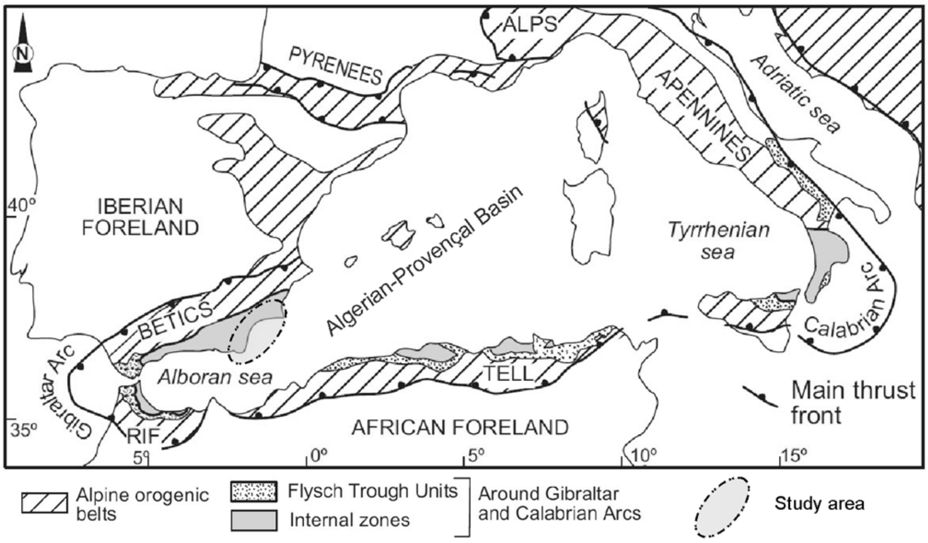

Figure 3.1: Simplified tectonic map of Western Mediterranean showing Alpine orogenic belts and localization of the study area (modified from Crespo-Blanc and Frizon de Lamotte (2006)).

Structurally the Betic Cordillera (or simply the Betics) is divided into three major domains: the Internal and External Zones and the Flysch Trough Units (Figure 3.2). The Internal Zone, also known as the Alboran Domain, is formed by three overthrusted complexes (from bottom to top): Nevado-Filabride, Alpujarride and Malaguide complexes. These complexes are composed mainly of metamorphosed Paleozoic and Mesozoic rocks separated by Neogene intermontane basins. The External Zone, consists of Mesozoic to Tertiary rocks not affected by metamorphism and are characterized by thin-skinned tectonics. The Flysch Trough units are formed by siliciclastic deposits sedimented in a deep basin. The most recent phase of the Internal Zone evolution is related to formation of Neogene to Quaternary basins (Alboran back arc basin, Guadalquivir foreland basin and intermountain basins, such as Guadalentín near the town of Lorca; Figure 3.2) that were filled after the general alpine folding and uplifted rapidly since Pliocene, driven by continuing convergence of the Africa and Eurasia plates (Rosenbaum et al., 2002).

With the subduction of the African plate in the Neo-Alpine stage, the Algerian-Provençal Basin was open (Figure 3.1) and produced the expulsion and extensive stretching of the Internal Zones to the west, which in turn deformed the External Zones (Sanz de Galdeano, 1990). The emplacement of the Internal Zones due to closing of the Western Mediterranean area mainly occurred in the Burdigalian period (Boccaletti et al., 1987). Superficially, the contact between the Internal and External Zones occurs by overthrusting of the Internal onto the External Zone, resulting in the maximum crustal thickness near this feature, which decreases rapidly towards the Alboran Sea.

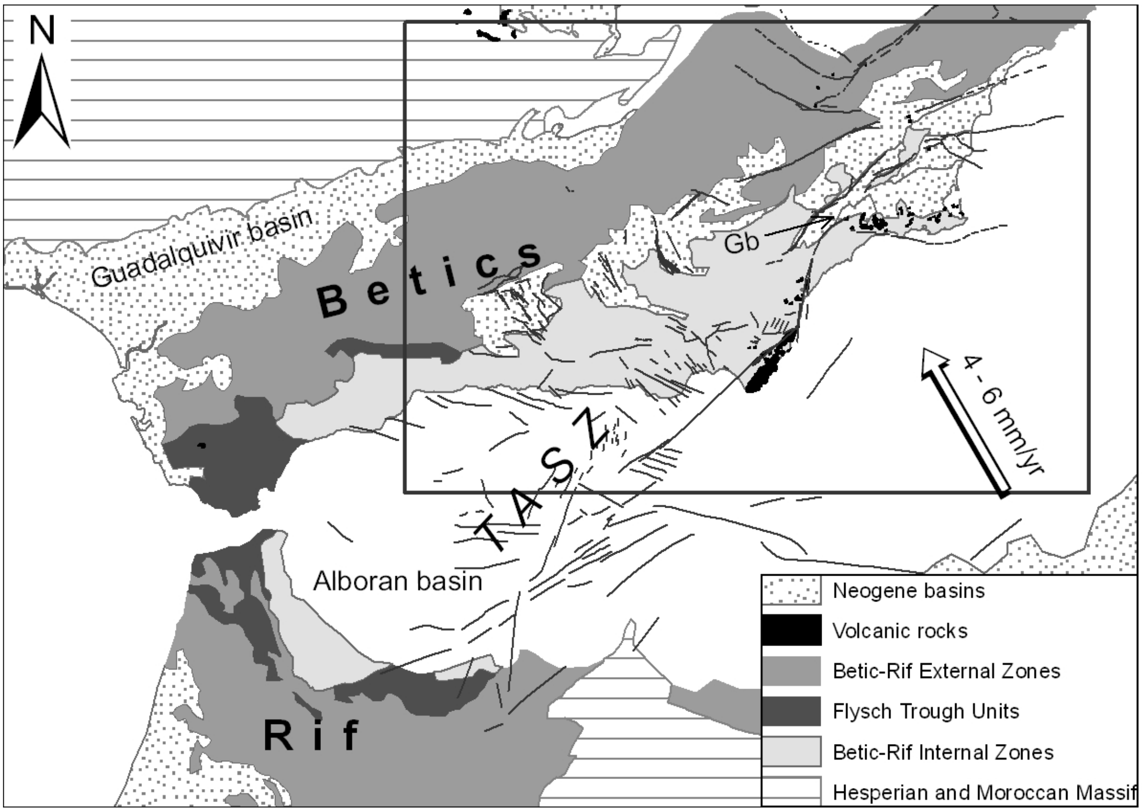

Figure 3.2: Geo-tectonic map of the Gibraltar Arc. Arrow shows convergence vector between Eurasia and Nubia plates. Box indicates the area enlarged in Figure 3.4. TASZ: Trans-Alboran Shear Zone and Gb: Guadalentin basin. Faults from QAFI database (García-Mayordomo et al., 2012) and Gràcia et al. (2012).

During the Miocene, shortening in the External Zones was coeval with the formation and opening of the Alboran Sea and adjacent areas that was under extension regime, with a ENE-WSW direction (Galindo-Zaldívar et al., 1999; Sanz de Galdeano and López-Garrido, 2000). The extension in the Alboran Domain was accompanied by calk-alkaline volcanism, especially active during late Miocene (e.g. Torres-Roldán et al., 1986). Since the late Tortonian, the horizontal compression was NW-SE, rotating to N-S to the middle Pliocene, and changing to NNW-SSE during the upper Pliocene and Pleistocene (D'Estevou and Montenat, 1985; Montenat et al., 1987; De Larouzière et al., 1988). This compressional regime produced reverse faults, folds (generally oriented E-W) and structural inversion of previous normal and strike-slipe faults (e.g. Weijermars et al., 1985; Morel, 1989; Galindo-Zaldívar et al., 1993; Meghraoui et al., 1996; Martínez-Martínez and Azañón, 1997), producing notable vertical movements in the Betics (Sanz de Galdeano and Alfaro, 2004). This last geodynamic stage is related to the Nubia/Eurasia convergence and establishes the actual stress conditions (e.g. Palano et al., 2013).

Different geodynamic models (Figure 3.3) have been proposed to explain the evolution of the Betic-Rif area, with continental extension in the Alboran Sea within a general compressional context, as well as the detection of a high velocity body under the Gibraltar region at ~100-700 km depth (e.g. Blanco and Spakman, 1993; Calvert et al., 2000; Bonnin et al., 2014).

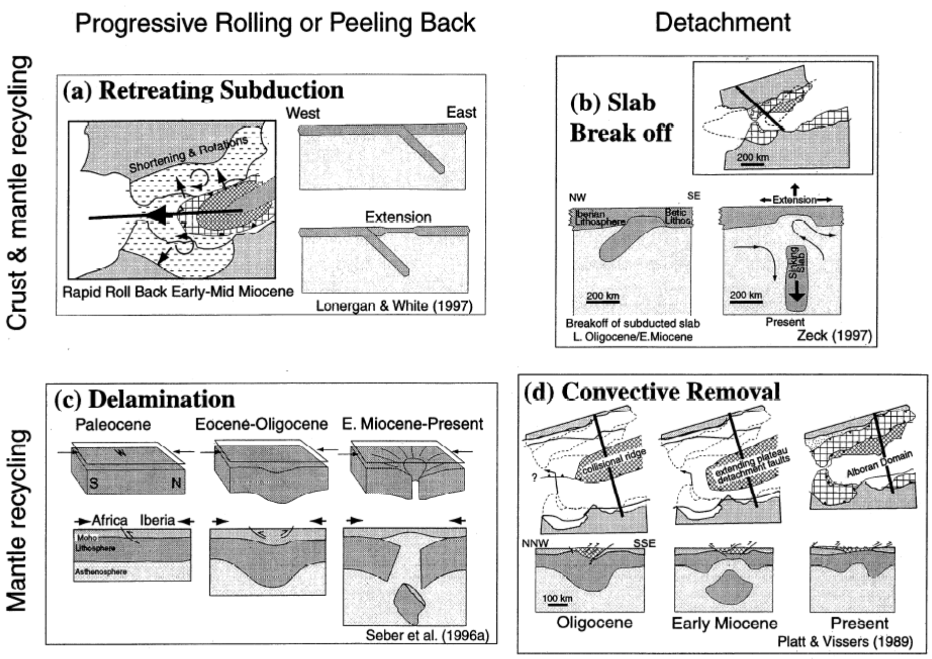

Figure 3.3: Some of different models proposed to explain the geodynamic evolution of the Gibraltar region (from Calvert et al. (2000)). See text for more explanation.

Among the numerous existing geodynamic models, the most popular are:

a) westward rollback of an east-ward subducting slab that generated backarc extension (e.g. Blanco and Spakman, 1993; Royden, 1993; Lonergan and White, 1997; Gutscher et al., 2002; Faccenna et al., 2004);

b) break-off of subducted lithospheric slab (Blanco and Spakman, 1993; Zeck, 1996); subduction without convergence (Jolivet et al., 2008);

c) convective removal of mantle lithosphere thickened that caused uplift and extension (Houseman et al., 1981; Platt and Vissers, 1989);

d) delamination of overthickened continental lithosphere (García-Dueñas et al., 1992; Seber et al., 1996; Mezcua and Rueda, 1997; Calvert et al., 2000; Valera et al., 2008);

e) rapid westward motion of Alboran microplate between Africa and Iberia (including the Internal Zone), causing the radial thrusting around the Gibraltar region (Andrieux et al., 1971; Leblanc and Olivier, 1984);

f) other hybrid models proposing for example, a combination of slab roll-back and lithosphere removing (e.g. Duggen et al., 2004; Vergés and Fernàndez, 2012; Palomeras et al., 2014).

Recent studies based on different type of geophysical data tend to favour the sinking of a lithospheric slab with an associated roll-back (e.g. Diaz et al., 2010; Vernant et al., 2010; Gutscher et al., 2012; Palano et al., 2012; Bezada et al., 2013; Miller et al., 2013; Bonnin et al., 2014; Palomeras et al., 2014). Nevertheless, the debate about these models and wether the subduction is active or not is still under debate (e.g. Gutscher et al., 2002; Bezada et al., 2013; Bonnin et al., 2014).

3.1. Active tectonics

Active tectonics is widely defined as the ongoing deformation of the surface of the earth (Wallace, 1986). In this Section, we provide a brief description of the main faults of the study area (Figure 3.4), most of them active. The eastern Betics, has a variety of known faults, where two types dominate:

i) major strike-slip shear zones like the Alhama de Murcia and Carboneras fault zones (e.g. Bousquet, 1979; Keller et al., 1995), most of them the constituents of the Eastern Betic Shear Zone.

ii) normal faults of variable scale, oriented NNW-SSE to NW-SE near Almeria (i.e. the Adra fault (Gràcia et al., 2012) and the Balanegra fault (e.g. Galindo-Zaldivar et al., 2003)).

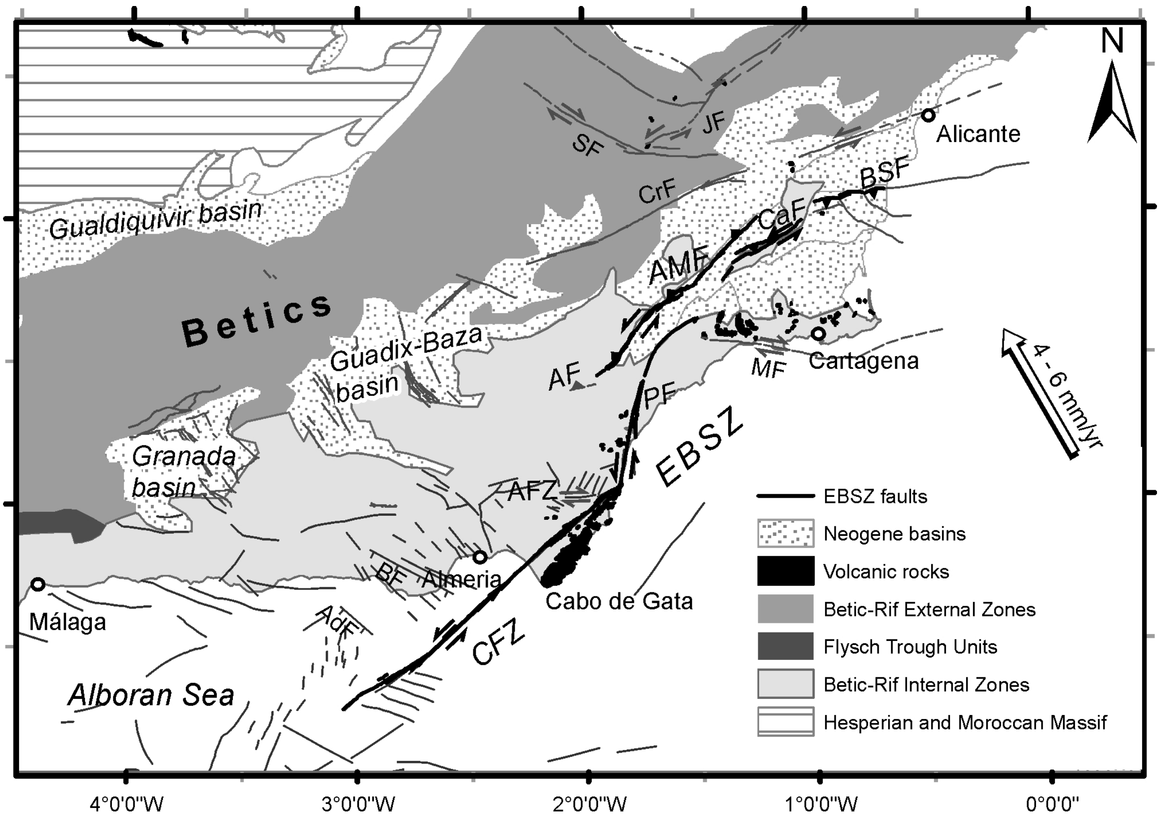

Figure 3.4: Geo-tectonic map of eastern and central Betics. Arrow shows convergence vector between Eurasia and Nubia plates. Faults from QAFI database (García-Mayordomo et al., 2012) and Gràcia et al. (2012). EBSZ forming faults in black. Abbreviations are: SF - Socovos fault; JF - Jumilla fault; CrF - Crevillente fault; BSF - Bajo-Segura fault; CaF - Carrascoy fault; AMF - Alhama de Murcia fault; AF - Albox fault; PF - Palomares fault; CFZ - Carboneras fault zone; MF - Moreras fault; AFZ - Alpujarras fault zone; BF - Balanegra fault and AdF - Adra fault. For a detailed geological map of this area, see Appendix A.

3.1.1. The Eastern Betic Shear Zone (EBSZ)

The NE-SW trending Trans-Alboran Shear Zone (TASZ) is a main crustal structural feature in Gibraltar Arc region (Frizon de Lamotte et al., 1980; De Larouzière et al., 1988) (Figure 3.2). The Eastern Betic Shear Zone (EBSZ), a lithospheric shear system, can be considered as the Betic part of the TASZ (Bousquet, 1979; Weijermars, 1987; De Larouzière et al., 1988; Silva et al., 1993) and consists of several left-lateral strike-slip faults, spanning over 250 km from Alicante to Almeria: the **Bajo-Segura**, **Carrascoy**, **Alhama de Murcia**, **Palomares** and **Carboneras** faults (Figure 3.4). According stress field variations during upper Neogene and Quaternary (from NW-SE to N-S), these structures acted as reverse and/or sinistral strike-slip faults (e.g. Bousquet, 1979; Sanz de Galdeano, 1983; Montenat et al., 1987; De Larouzière et al., 1988).

The EBSZ faults accommodated a large part of Neogene and Quaternary shortening (Bousquet, 1979; Sanz de Galdeano, 1990). Paleoseismic and geologic studies suggest several paleo-earthquakes, indicating a seismogenic potential of theses faults (e.g. Masana et al., 2004). Neogene volcanism, plutonism and metallogeny are related in the EBSZ. The better expression of the volcanism is the calc-alkaline Cabo de Gata volcanic region (also extending into Alboran Sea) and the alkali basaltic volcanism in the Cartagena area. Magmatic activity is spatially linked to the strike-slip faults and is related to a strong thermal anomaly (De Larouzière et al., 1988; Soto et al., 2008).

In the Iberian Peninsula, the EBSZ absorbs part of the convergence between the Eurasian and Nubian plates (Masana et al., 2004), which is on the order of 4 to 6 mm/yr in the NNW direction (e.g. Lonergan and White, 1997; McClusky et al., 2003; Serpelloni et al., 2007; Argus et al., 2011; Figure 3.4). Although no direct GPS observations have been published for the EBSZ, Vernant et al. (2010) do determine 0.9-1.2 mm/yr of left-lateral and 0.2-0.8 mm/yr of fault normal slip rates for the EBSZ from kinematic block modeling.

3.1.1.1. EBSZ faults

The **Bajo-Segura fault** (BSF) is a ~60 km long blind reverse fault with an ENE-WSW orientation characterized by net slip of 0.2-0.4 mm/yr (García-Mayordomo, 2005; García-Mayordomo and Martínez-Díaz, 2006; Alfaro et al., 2012). The **Carrascoy fault** (CaF) is ~30 km long and is the western continuation of the BSF (e.g. Silva et al., 1993). The CaF has a sinistral and reverse sense of movement, with an estimated horizontal rate of 0.5 mm/yr based on channel offset studies (Silva, 1994; García-Mayordomo, 2005). New paleoseismologic studies confirm the Quaternary activity of this fault and calculate a maximum magnitude of Mw 6.7 for the SW segment (Martín-Banda et al., 2014). The **Alhama de Murcia fault** (AMF) is the longest onshore fault in the EBSZ and is divided into segments based on seismicity, tectonics and geomorphology. This fault is considered one of the most active faults in the eastern Betics and was studied extensively during the last three decades (e.g. Martínez-Díaz and Hernandez Enrile, 1992; Masana et al., 2004; Martínez del Olmo et al., 2006; Meijninger and Vissers, 2006; Ortuño et al., 2012). The AMF is a left-lateral strike-slip fault with a reverse component of motion (e.g. Martínez-Díaz, 2002). To the south, the **Palomares fault** (PF) runs NNE-SSW and changes its orientation to NE-SW in the northern part, oriented approximately parallel to the southern termination of the AMF (Figure 3.4). The PF kinematic evolution included changing in its behavior from mainly left-lateral strike-slip before the Messinian to normal type extension afterwards (García-Mayordomo, 2005). The southernmost fault of the EBSZ is the **Carboneras fault** (CFZ), a left-lateral transpressive structure that extends ~50 km onshore and runs south offshore under the Alboran Sea for ~100 km (Gràcia et al., 2006; Moreno, 2011). The CFZ has a clear morphologic expression revealing its relatively young activity. Paleoseismologic studies reveal a minimum offset of 1.1-1.3 mm/yr for the NE part of the CF (Moreno, 2011).

The AMF and the CFZ are the most important faults in the study area: they are large faults, present higher slip rates and probably, are the most well studied faults of the EBSZ. Because of all these in the Chapters 6 and 7 we will focus on both faults, below we provide more detailed information, focusing on their recent activity.

3.1.1.2. Alhama de Murcia fault

The Alhama de Murcia has been described as one of the most active Quaternary active faults in the eastern Betics (e.g. Silva et al., 1993; Martínez-Díaz, 1998; Masana et al., 2004). In fact, the destructive M_w 5.2 Lorca earthquake (described in Section 3.2.1) that occurred on May 11th of 2011 is attributed to this fault (e.g. Martínez-Díaz et al., 2012a). The fault has a strong morphologic expression, forming three ranges in the hangingwall block (Sierra de Las Estancias, Sierra La Tercia and Sierra Espuña, Figure 3.5) and bounds the Neogene Guadalentín (the footwall block) depression to the west.

Based on the geometry, morphology, seismicity and the relief of the hangingwall block of the fault trace, Martínez-Díaz et al. (2012b) have subdivided the AMF into four segments, which from south to north are: Goñar-Lorca, Lorca-Totana, Totana-Alhama, Alhama-Alcantarilla (Figure 3.5). A horsetail reverse splay, the Goñar fault system (Ortuño et al., 2012), defines the southern end of the AMF. Paleoseismologic study carried out by Ortuño et al. (2012) identified a minimum of six paleoearthquakes in the Goñar fault system, where the deformation has been partitioned into the different strands. The neotectonic activity of the AMF is transferred to the adjacent structures; to the north is to the Carrascoy fault (Martínez-Díaz, 2002; Insua-Arévalo et al., 2012) and to the south to the Albox fault (Masana et al., 2005).

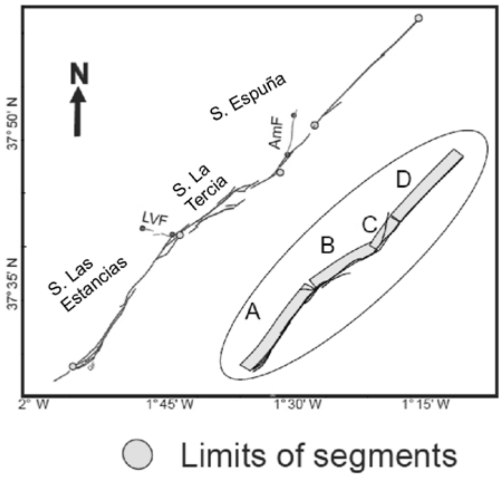

Segments	A) Goñar-Lorca	B) Lorca-Totana	C)Totana-Alhama	D) Alhama-Alcantarilla
Geometry and Kinematics				
Average Strike(º):	215	238	221	225
Dip (º):	70	70	70	70
Rake (º):	20	18-75	-	-
Sense of Movement:	SR	R to SR	RS	RS
Length (km):	28.0.	20.0.	12.0.	25.0
Min Depth (km):	0	0	0	0
Max Depth (km):	12.0	12.0	12.0	12.0
Width (km):	12.8	12.8	12.8	12.8
Area (km²):	357	276	132	300
Quaternary Activity				
Age of the Youngest Deposits Affected by the fault:	Holocene	Holocene	Middle Pleistocene	Middle Pleistocene
Vertical Slip Rate (m/ka or mm/yr) :	0.200	0.16	-	0.07
Horizontal Slip Rate (m/ka or mm/yr) :	0.5	0.21	-	-
Net Slip Rate (m/ka or mm/yr) :	0.5	0.3	-	0.07
Maximum earthquake mag.	7.0	6.5	5.8	6.5

Figure 3.5: Synthesis of the segmentation of the Alhama de Murcia fault and summary of the main parameters of fault activity for each segment (modified from Martínez-Díaz et al. (2012b); data of the table collected from Martínez-Díaz (1998), Masana et al. (2004), García-Mayordomo (2005), Ortuño et al. (2012)). LVF: Las Viñas fault; AmF: Amarguillo fault

The AMF has been studied by paleoseismological studies (Silva et al., 1997; Martinez-Diaz et al., 2001; Martínez-Díaz et al., 2003; Masana et al., 2004; Masana et al., 2005; Ortuño et al., 2012), in particular the Lorca-Totana and Goñar-Lorca segments. The horizontal slip rates determined by these studies range between 0.06 to 0.53 mm/yr (Masana et al., 2004; Martínez-Díaz et al., 2012b; Ortuño et al., 2012). New study integrating 3D-trenches and morphotectonic analyses of offsets in the Lorca-Totana segment, suggests a higher minimum strike-slip rate, with a preliminarily estimate of 0.6±0.1 mm/yr (Ferrater et al., 2015).

In terms of seismicity, several historical damaging earthquakes have been attributed to the AMF (e.g. events with EMS I>VII: Lorca 1579, 1674 and 1818, Lorquí 1911) and scattered instrumental seismicity is present (see Section 3.2 for details). Nevertheless, there is a significant seismic gap in the southern part of the AMF, in the Goñar-Lorca segment, characterized by the presence of fault gouge (e.g. Martínez-Díaz, 1998; Rodriguez-Escudero et al., 2012). This fault gouge and pseudo-ductile textures in these brittle clay-rich rocks are typical of ductile fault rocks, i.e. aseismic creep. However, Rodriguez-Escudero et al. (2014) found pulverized quartz in the fault rock and propose an occurrence of earthquake as a mechanism for the pulverization, caused by a normal stress drop associated with passing of seismic waves though the rocks.

3.1.1.3. Carboneras fault zone

The Carboneras fault zone (also known as Serrata fault or Almeria fault) is a major crustal-scale fault located just east of the city of Almeria (Figure 3.6), which is thought to reach up to the Moho (Pedrera et al., 2010). Soto et al. (2008) suggest that the fault runs through a domain with partial melting in the deepest crust. On surface, the fault has a clear morphologic expression that changes its width along the fault length from a single trace to a 2 km wide fault zone (Moreno et al., 2008). The fault separates the Cabo de Gata volcanic massif from the Nijar Neogene basin. To the north the fault ends in Sierra Cabrera, joining with the PF and to the south it ends in a structural high in the Alboran Sea (Gràcia et al., 2006). Two first order segments are defined mainly based on changes in the fault trace orientation: the North Carboneras fault (NCF) and the South Carboneras fault (SCF) (Moreno, 2011) (Figure 3.6).

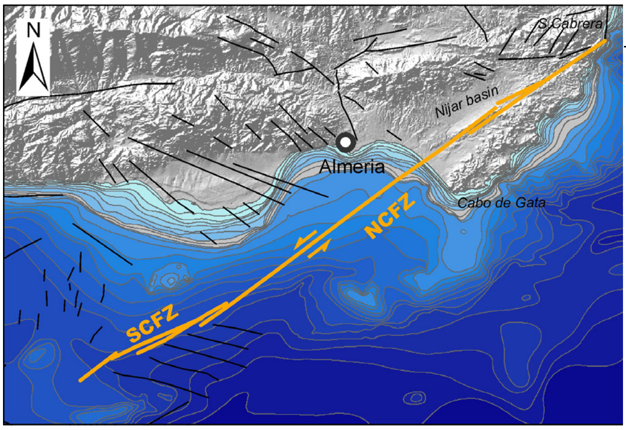

	NCF	SCF
Average strike (º)	N048	N057
Dip (º)	90	90
Rake (º)	10	0
Depth (km)	0-11	0-11
Width (km)	11	11
Vertical slip rate (mm/yr)	>0.04	0.04
Horizontal sip rate (mm/yr)	>1.1-1.3	(?) 0
Net slip rate (mm/yr)	>1.1-1.3	0.04
Max. earthquake mag.	7.4±0.3	6.9±0.3

Figure 3.6: Synthesis of the segmentation of the Carboneras fault and summary of the main parameters of fault activity for each segment. Segmentation and parameters from Moreno (2011), Moreno et al. (2010a; 2010b); bathymetry from Open Geospatial Consortium (OGC) from the Junta de Andalucia (www.juntadeandalucia.es/medioambiente/site/rediam/).

The CFZ is characterized by the highest geologic fault slip rates (according to the QAFI database, García-Mayordomo et al. (2012)) constrained to date in the Iberian Peninsula. The estimated geologic slip rates at the CFZ range between 0.05-2 mm/yr depending on the utilized method and the covered time-period (Hall, 1983; Montenat et al., 1990; Bell et al., 1997; Moreno, 2011). The most recent paleoseismological studies constrained the minimum strike-slip rate of the NCF to 1.1-1.3 mm/yr for the Quaternary period (Moreno, 2011).

The instrumental and historical seismicity related to the CFZ is scarce apart from the 1522 Almeria (MSK I=VIII-IX) earthquake that was probably generated by an offshore segment of the Carboneras fault (Reicherter and Hübscher, 2007, Moreno, 2011). The presence of fault gouges in the northern part of the fault were attributed to the aseismic creeping of the fault (e.g. Keller et al., 1995), thus questioning the capability of the CFZ to produce large earthquakes. On the other hand, Faulkner et al. (2003) suggest the possibility of a 'mixed mode' seismicity, where creep occurs along the strands of velocity strengthening and is interrupted by seismic events within the more competent dolomite blocks. Soto et al. (2008) relate the partial melting in the deep crust with the eventually creep due to a reduction of the strength. However, recent paleoseismological studies (Moreno, 2011) provided evidence for the seismogenic nature of the CFZ by finding the record of the occurrence of moderate earthquakes in the past.

3.1.2. Other faults

There are several other important faults that fall within the wide study area, but do not form part of the EBSZ (Figure 3.4). In the northern sector these faults are the Jumilla, Socovos and Crevillente faults. The **Jumilla fault** zone (JF) is a NE-SW topographic lineament consisting of sinistral strike-slip faults arranged en-echelon (Van Balen et al., 2013). The **Socovos fault** (SF) is a dextral strike-slip fault with an orientation NW-SE and then change to roughly E-W. It is an 80 km long fault with associated structures, active during Quaternary (Sánchez-Gómez et al., 2011; Pérez-Valera et al., 2014). The JF and SF are located in the Extenal Zones and can be kinematically connected (Van Balen et al., 2013). The ENE-WSW **Crevillente fault** (CrF), or Cadiz-Alicante fault, is a strike-slip discontinuous fault that constitutes an important crustal discontinuity (Sanz de Galdeano, 2008). It is formed by a several parallel faults that behaved as reverse right-lateral faults until late Tortonian, but presently each segment is suspected to be moving independently, in accordance with the local conditions (Sanz de Galdeano, 2008). Left-lateral geodetic slip rate of 0.44-0.75 mm/yr (Sánchez-Alzola et al., 2014 5833) defines the easternmost segment.

In the south-central sector, other important faults are the Moreras fault, the Albox fault and the Alpujarras fault zone (Figure 3.4). The **Moreras fault** (MF) is a WNW-ESE trending right-lateral and normal fault (Rodríguez-Estrella et al., 2011) and is the onshore continuation of Escarpe de Mazarrón (García-Mayordomo, 2005). The **Albox fault** (AF) is a ENE-WSW reverse fault located south to AMF. Most of the N-S shortening during recent times was accommodated by the AF (Masana et al., 2005). The **Alpujarras fault zone** (AFZ) is composed of several faults (e.g. Polopos and Lucainena or Gafarillos faults) with an E-W orientation that acted as right-lateral strike-slip faults in the Lower Miocene, but are dominantly reverse since Upper Miocene (Sanz de Galdeano, 1996). The AFZ has been interpreted as an ensemble of various transfer faults (Sanz de Galdeano, 1996; Sanz de Galdeano et al., 2010). The dextral-reverse Polopos fault is one of the AFZ constituent faults (Figure 3.7) with recent activity (up to late Pleistocene) (Giaconia et al., 2012).

Other families of minor faults were also active during the Quaternary within the study area. Some of these structures are NW-SE to WNW-ESE trending **normal faults** related to active extension in the upper crust near Almería (Martínez-Díaz and Hernández-Enrile, 2004; Marín-Lechado et al., 2005; Sanz de Galdeano et al., 2010; Giaconia et al., 2013), extended across the central and eastern Betics (Galindo-Zaldivar et al., 2003; Marín-Lechado et al., 2005; Pedrera et al., 2006) (Figure 3.4). Similar to WNW-ESE normal faults, Gràcia et al. (2006) describe N-S normal faults on the northwestern block of CFZ. All these normal faults are abundant within the area located between the dextral AFZ and the sinistral CFZ (Figure 3.4). For this reason, several authors (e.g Martínez-Díaz and Hernández-Enrile, 2004; Martínez-Martínez et al., 2006; Sanz de Galdeano et al., 2010; Giaconia et al., 2014) have suggested that the CFZ and the AFZ strike-slip faults act in conjuntion with the normal faults. The CFZ and/or the AFZ have been interpreted as a transfer faults accommodating heterogeneous extension (Martínez-Martínez et al., 2006; Giaconia et al., 2014). Martínez-Díaz and Hernández-Enrile (2004) proposed a conceptual model, where a tectonic block bounded by both strike-slip faults escapes to the west, driven by the Eurasia/Africa convergence. This way, the authors have related the existence of the extensional structures to a local extension linked with the compressive tectonics.

3.2. Seismicity

The most seismically active region in the Iberian Peninsula includes the Alboran Sea, the Betic Cordillera, containing the study area and the Pyrenees. As can be seeing from the inset of Figure 3.7, earthquakes are mainly concentrated along the Pyrenees, Betic-Rif chain and northern Algeria. However, no obvious linear distribution along the plate boundaries can be observed. This may be due to the existence of wide zone of deformation, resulting in a diffuse plate boundary between the Africa and Eurasia plates (e.g. Stich et al., 2003). The study area is characterized by low to moderate seismicity (M<5.5) with the majority of the hypocenters located in the crust (0-40 km) (e.g. Buforn et al., 1995; Stich et al., 2003; Buforn et al., 2004). Outside the study area, further west, exists also intermediate (40-150 km) and deep (>600 km; e.g. the 2010 Granada event with M_w 6.2 (Buforn et al., 2011)) seismicity, generally linked with the subducted slab (e.g. Ruiz-Constán et al., 2011).

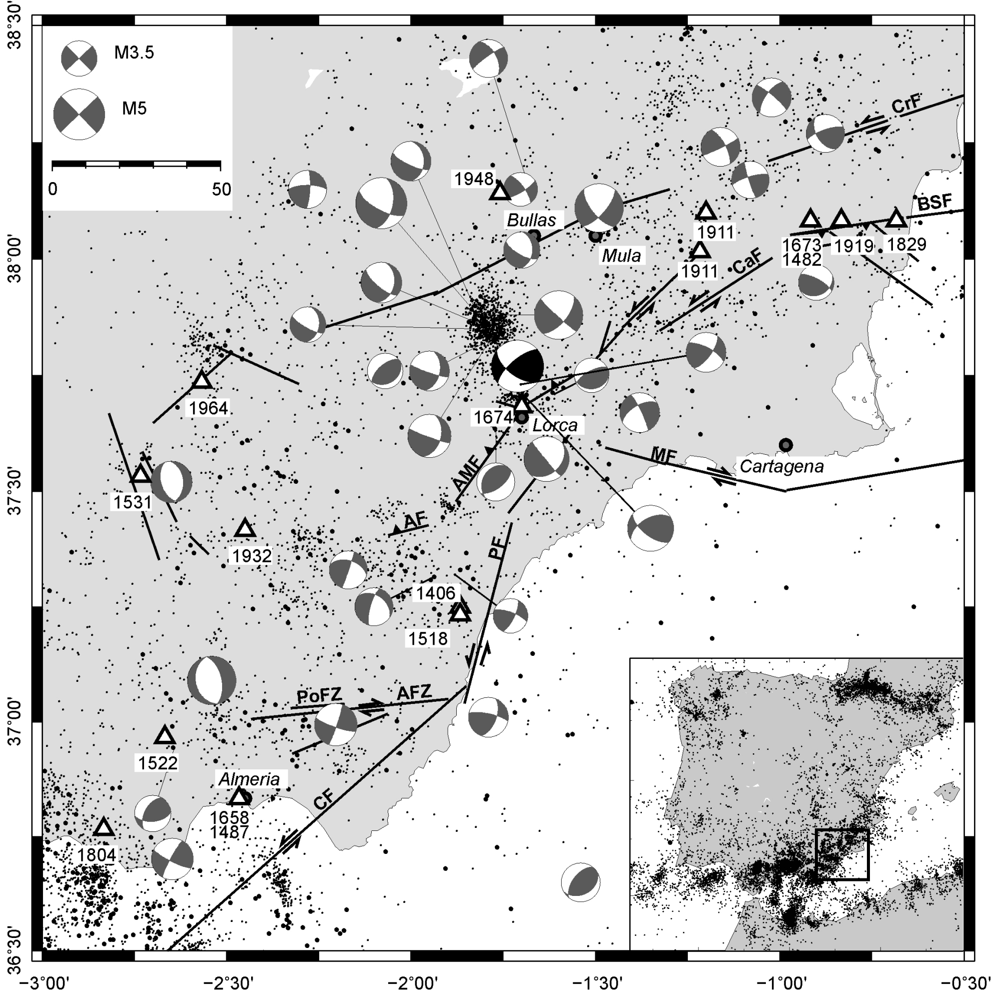

Figure 3.7: Seismotectonic map of the eastern Betics. Instrumental seismicity from IGN catalog (1973-2011) (www.ign.es) with depths ranging 0-50 km. Thicker black points indicate earthquakes with M>3. Historical seismicity (white triangles) is from the IGN catalogue and are labeled by date (Table 3.1). Grey focal

mechanisms are from Stich et al. (2003; 2006; 2010) (1984-2008) and IGN catalog (2009-2011) (www.ign.es). The black focal mechanism corresponds to the main May11th, 2011 Lorca event (López-Comino et al., 2012). The inset shows seismicity for the entire Iberian Peninsula. Abbreviations are: CrF - Crevillente fault; BSF - Bajo-Segura fault; CaF - Carrascoy fault; AMF - Alhama de Murcia fault; AF - Albox fault; PF - Palomares fault; CF - Carboneras fault; MF - Moreras fault: AFZ - Alpujarras fault zone; PoFZ - Polopos fault zone.

Within the study area the instrumental seismicity (Figure 3.7) is characterized by low magnitude earthquakes, reaching maximum values of M_w5.0 (covering from 1937 to 2011 with hypocenters 0-50 km in depth, IGN catalog (www.ign.es)). These earthquakes are usually related to minor faults (e.g. Martínez-Díaz and Hernández-Enrile, 2004) located within the crustal blocks bounded by the major faults, such as AMF, AFZ and CFZ. Rodríguez-Escudero et al. (2013) interpret the events with M_w<5 as part of the background seismicity, which can occur at any point within the crustal blocks bounded by the large E-W to NE-SW strike-slip faults. Precisely along these major faults (i.e. CFZ or AMF) is where earthquakes of M_w>5.5 are expected by these authors.

A cluster of seismicity is located between the Crevillente (CrF) and the Alhama de Murcia (AMF) faults (~37º45'N, -1º45'E, Figure 3.7) that corresponds to four notable seismic series that occurred since 1999: the 1999 Mula series (M_w 5.1) (Buforn and Sanz de Galdeano, 2001), related to the Crevillente fault (e.g. Buforn et al., 2005), the 2002 Bullas series (M_w 5.0) (Buforn et al., 2005), the 2005 Bullas-La Paca series (M_w 4.8) (Benito et al., 2007) and the 2011 Lorca series (M_w 5.2) (e.g. López-Comino et al., 2012) attributed to the Alhama de Murcia fault (Martínez-Díaz et al., 2012a). The remainder of the study area is characterized by a diffuse seismicity not obviously associated with a fault.

We compiled focal mechanisms from published results in order to identify the predominant style of faulting and the spatial distribution. Specifically, we used 35 focal mechanisms (Figure 3.7) from Stich et al. (2003; 2006; 2010), who estimated moment tensors for regional earthquakes of M_w>3.2 from 1984-2008, and the Instituto Geográfico Nacional (IGN) (www.ign.es) for focal mechanism acquired between 2009-2011 with M_w>3.5. The majority of focal mechanisms indicate strike-slip motion with minor normal or thrust component. No obvious groups or clusters of similar mechanisms are clearly identified. Nevertheless, in the NE-SW striking bend roughly following the EBSZ, left-lateral strike-slip events are common. However, note the presence of two focal mechanisms with purely thrust type motion near the AMF.

Table 3.1: Historical seismicity of the eastern Betics, plotted in Figure 3.7 (from IGN catalog, www.ign.es). Abbreviations are the provinces: A - Alicante; AL - Almeria; GR - Granada, MU -Murcia

Lon	**Lat**	**MSK Int.**	**Date**	**Location**
-1.87	37.25	VII-VIII	1-jan-1406	Vera.AL
-0.92	38.09	VIII	10-oct-1482	Orihuela.A
-2.47	36.83	VIII	1-nov-1487	Almería.AL
-1.87	37.23	VIII-IX	9-nov-1518	Vera.AL
-2.67	36.97	VIII-IX	22-sep-1522	W.Alhama de Almería.AL
-2.73	37.53	VIII-IX	30-sep-1531	Baza.GR
-2.47	36.83	VIII	31-dec-1658	Almería.AL
-0.92	38.08	VIII	15-jan-1673	Orihuela.A
-1.7	37.68	VIII	28-aug-1674	Lorca.MU
-2.83	36.77	VIII-IX	25-oct-1804	Dalías.AL
-0.68	38.08	IX-X	21-mar-1829	Torrevieja.A
-1.22	38.02	VIII	21-mar-1911	Las Torres de Cotillas.MU
-1.2	38.1	VIII	3-Apr-1911	Lorquí.MU
-0.83	38.08	VIII	10-sep-1919	Jacarilla.A
-2.45	37.42	VIII	5-mar-1932	Lucar.AL
-1.76	38.14	VIII	23-jun-1948	Cehegin.MU
-2.57	37.74	VIII	9-jun-1964	SW Galera.GR

In terms of the historical seismicity, since the 15th century the study area has experienced at least 10 MSK intensity>X earthquakes (Martínez Solares and Mezcua, 2002). Most of them are linked to the EBSZ faults, such as AMF or PF. The most important events include the Torrevieja (1829, I=IX-X), Almería (1522, I= IX), Dalías (1804, I=VIII-IX), Baza (1531, I=VIII-IX), Vera (1406, I=VII-VIII and 1518, I=VIII-XI), and Lorca (1674, I=VIII) earthquakes (Lopez Casado et al., 1995) (Figure 3.7, Table 3.1). Interestingly, no earthquakes with MSK intensity>VIII have been recorded within the study area since modern instruments have been installed.

Several studies have estimated the stress field in the area, based on the inversion of earthquake focal mechanisms. From a regional point of view, the Betic Cordillera and Alboran Sea are under a horizontal compression in NW-SE to N-S direction with some localized horizontal tension in E-W to WSW-ENE direction (e.g. Buforn et al., 1995; Herraiz et al., 2000; Henares et al., 2003; Buforn et al., 2004; Stich et al., 2006; Sánchez-Alzola et al., 2014). The coexistence of tension and compression is perhaps due to local changes in the positions of σ_1 and σ_2 (horizontal and vertical stress, respectively) (De Vicente et al., 2008; Sanz de Galdeano et al., 2010). Rodríguez-Pascua and De Vicente (2001) determine two simultaneous orientations of maximum horizontal stress from the inversion of 28 focal mechanisms for the eastern Betics: the NW-SE, defined by reverse faults and coincident with the plate convergence, and the NE-SW, defined by normal faults. Palano et al.

(2013), through stress indicators (borehole breakouts, inversion of focal mechanisms and geological indicators) suggested that plate-driving forces (Eurasia/Nubia convergence) provide the main component of the total stress field in the Gibraltar Arc area. The authors also detect a secondary stress-pattern that can be linked to the gravitational potential energy field (related to variations of the crustal thickness) which can produce local rotations of the stress field and consequently, cause changes in the "faulting style" (e.g. normal faulting in central Betics).

3.2.1. The 2011 Lorca earthquake

On May 11th, 2011 a M_w=5.2 earthquake took place near the city of Lorca (Figure 3.8) (e.g. López-Comino et al., 2012). The event caused nine casualties, considerable damage to numerous buildings and had a major impact on media and society in Spain. This earthquake was preceded by another significant magnitude 4.5 event and was followed by numerous aftershocks of magnitudes lower than 3.9.

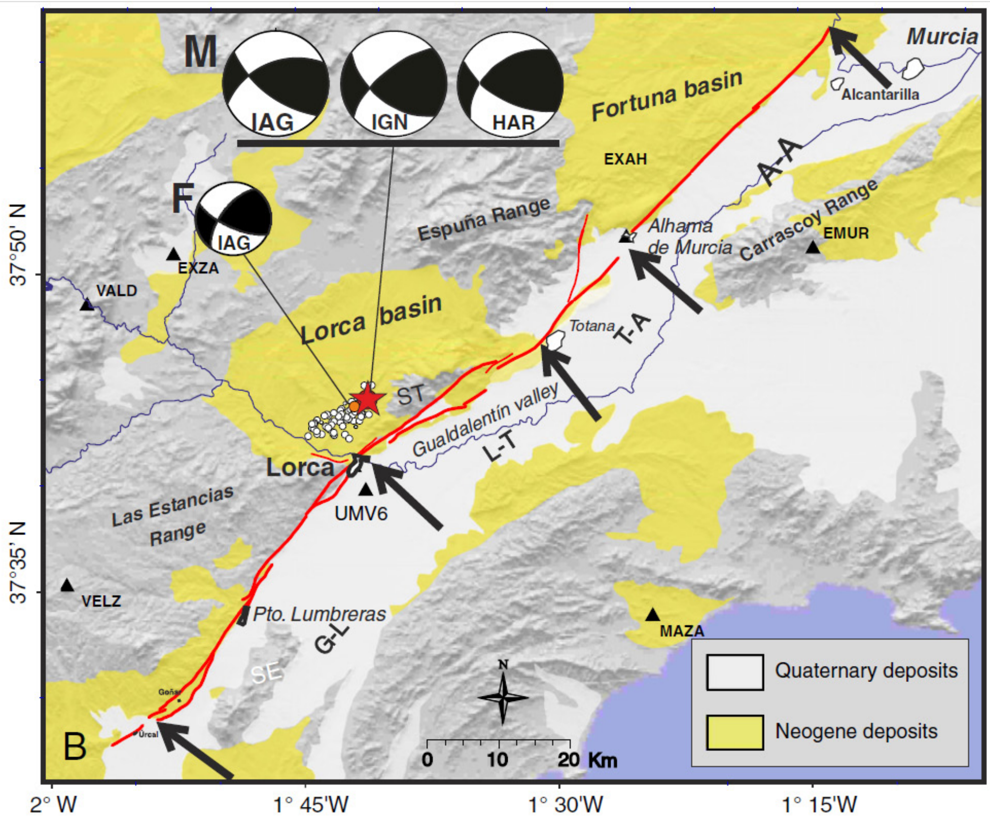

Figure 3.8: Location of the 2011 Lorca earthquake series and the AMF trace. Mainshock (M; red star) and aftershocks location are from López-Comino et al. (2012). The focal mechanisms of the foreshock (F) and mainshock are from several agencies (Instituto Andaluz de Geofisica, Insisuto Geografico Nacional and

Harvard University). Arrows indicates the limits of the four main segments of the AMF (from Martínez-Díaz et al. (2012a)).

The 2011 Lorca earthquake series has been attributed to the AMF, specifically to the intersegment zone between Goñar-Lorca and Lorca-Totana segments (Vissers and Meijninger, 2011; Martínez-Díaz et al., 2012a), and with SW propagating rupture along the fault (López-Comino et al., 2012). The propagation direction was exerted by the geometry of the fault zone and the frictional properties of the fault rocks involved (Niemeijer and Vissers, 2014). The focal mechanism of the main event shows oblique reverse faulting (IGN, 2011; López-Comino et al., 2012), compatible with the kinematics determined by geologic studies for the AMF (e.g. Masana et al., 2004; Martínez-Díaz et al., 2012b).

3.3. Previous geodetic studies

Currently, very few GPS-derived studies of the eastern Betics are published. Nonetheless, several more regional studies partially included the area (e.g. Fernandes et al., 2003; McClusky et al., 2003; Nocquet and Calais, 2004; Stich et al., 2006; Fernandes et al., 2007; Serpelloni et al., 2007; Tahayt et al., 2008; Vernant et al., 2010; Koulali et al., 2011; Palano et al., 2013; Asensio, 2014; Garate et al., 2015). These works concentrate on studying a wider region of Betic-Rif plate boundary and therefore, are only partially relevant to this study. Especially, since in most of these studies, the derived GPS velocities within our study area were statistically insignificant at 95% confidence level.

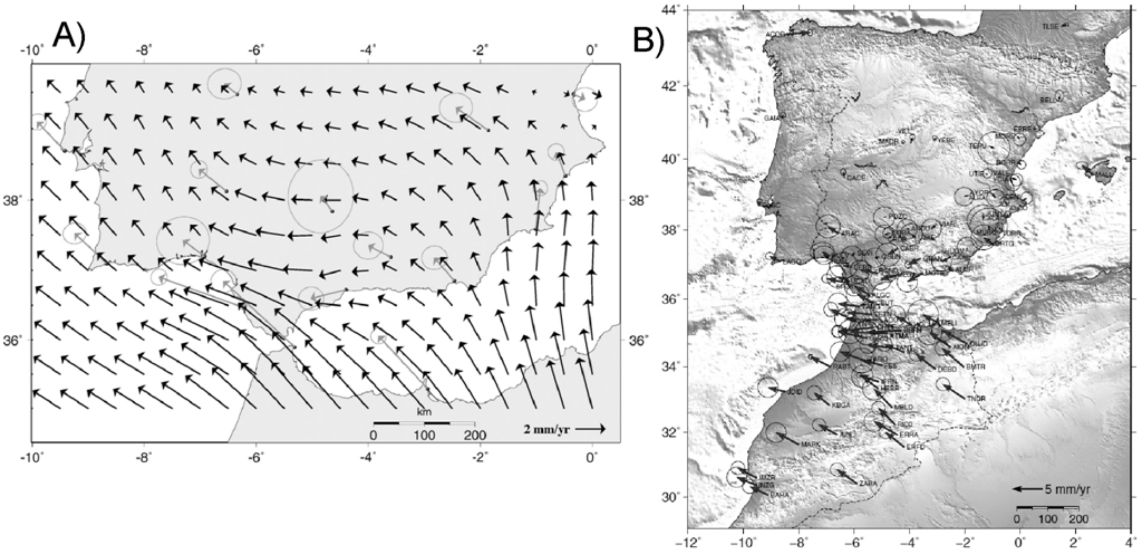

Figure 3.9: Velocity fields around Betics and Rif area. *A)* GPS site velocities (grey arrows in the background) and grid interpolation velocities, with respect to the stable part of Europe (from Pérez-Peña et al. (2010)). *B)* GPS velocities with respect to Eurasia and 95% confidence ellipses (from Koulali et al. (2011)).

In summary, the main results and observations of previous geodetic works include:

i) A general NW-SE oriented trend of motion in the Rif and western Betics (e.g. Palano et al., 2013) parallel to the Nubia/Eurasia convergence with rates of 1 to 4 mm/yr.

ii) An anomalous westerly motion of up to ~4 mm/yr in the central part of the Rif (Fadil et al., 2006; Vernant et al., 2010; Koulali et al., 2011) (Figure 3.9).

iii) Dominantly W-SW motion along the southern margin of the Betics, from Almeria to Cádiz, on the order of 1 to 3 mm/yr (Koulali et al., 2011; Palano et al., 2013), which was linked by Stich et al. (2006) to an on-going SW-NE extension.

iv) More northerly motion, reaching ~2 mm/yr, were suggested by Pérez-Peña et al., (2010) farther to the east, close to the city of Cartagena

These variations in the observed velocity orientations in the Betics and north Africa have been explained in the context of Eurasia-Nubia plate boundary geometry with two recent kinematic block models: Vernant et al. (2010) characterize a 1-2 mm/yr W-NW motion on the Betic Cordillera and define two additional blocks in the boundary zone: the Alboran-Rif block and the Betic block. Alternatively, Koulali et al. (2011) prefer a plate boundary geometry that combines the SW Betics, Alborán Sea and central Rif in one block. The recent work of Asensio (2014), delimits more accurately the previous models in the eastern Betics (the boundary follows the EBSZ), due to the inclusion of the results presented in this thesis and published in Echeverria et al., (2013).

3.3.1. Strain rate calculations

Strain rate parameters were calculated from velocities obtained in the Betic-Rif region by some of the authors (e.g. Pérez-Peña et al., 2010; Palano et al., 2013; Alfaro et al., 2014; Garate et al., 2015). We provide bellow a description of the work of Palano et al. (2013), which is the most recent and complete work, that included the highest number of GPS velocities (Figure 3.10).

Palano et al. (2013) calculated the 2-D strain rate tensor from a grid of interpolated GPS velocities. They obtained the higher strain rate values (~90 nstrain/yr) in the Rif, in the Nekor/Al-Hoceima area, characterized by a counterclockwise rotation. The Alboran domain is characterized by WSW-ENE extension and shortening reaching the same magnitude. Concerning the EBSZ, they characterized it by a NNW-SSE shortening of ~25 nstrain/yr, accompanied by a counterclockwise rotation (Figure 3.10).

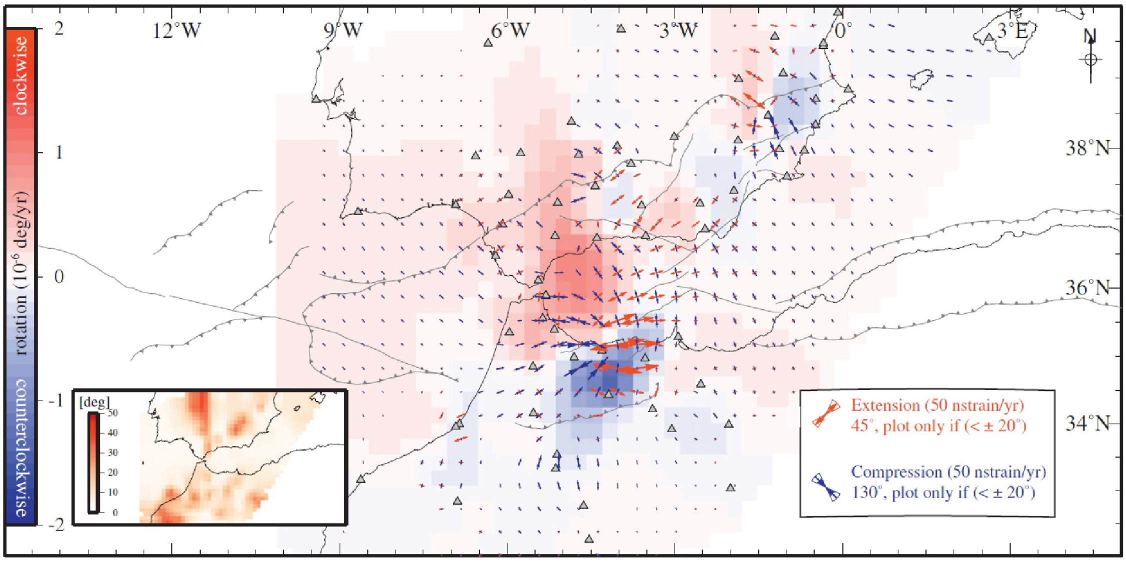

Figure 3.10: GPS strain rate parameters, where arrows represent the greatest extensional (red) and contractional (blue) horizontal strain-rates. Grid coloring indicates the rotational strain-rate where red is clockwise and blue counterclockwise rotation (from Palano et al. (2013)).

The recent work of Alfaro et al. (2014) calculated a gridded strain rate tensor in the Bajo-Segura basin from a local survey-mode GPS network (Figure 3.11). They obtained a predominance of the shortening axis, varying from 35 nstrain/yr oriented NNW-SSE in the south (near BSF) to 10 nstrain/yr oriented N-S in the north, near CrF. The extensional axis, $\dot{\varepsilon}_{max}$, are less than 30 nstrain/yr.

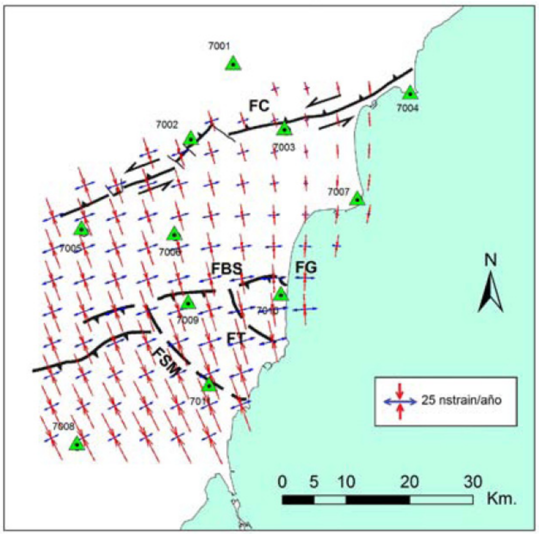

Figure 3.11: Main strain axes estimated over a superposed grid of the Bajo-Segura basin network. Blue arrows indicate extension while red ones indicate shortening (from Alfaro et al. (2014)).

4. GPS data and processing

A system called NAVSTAR GPS (NAVigation System with Timing And Ranging Global Positioning System) was developed by the US Department of Defense in 1973. This system, also known as GPS, is the most widely used Global Navigation Satellite System (GNSS) in the world. The term GNSS refers to a constellation of satellites providing signals from space transmitting positioning and timing data. Other common GNSS systems are the Russian GLONASS (GLObalnaya NAvigatsionnaya Sputnikova Sistema), the Chinese BeiDou Navigation Satellite System and the European GALILEO.

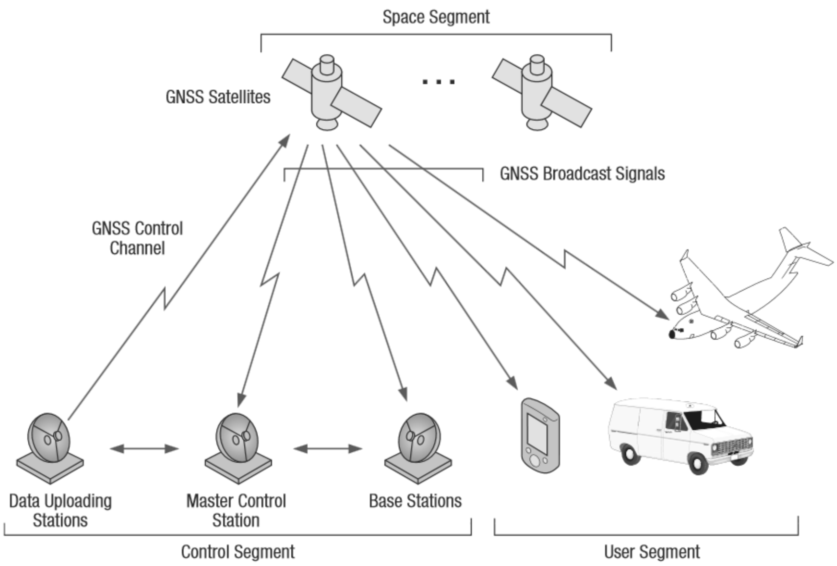

Figure 4.1: GNSS segments (from Jeffrey (2010)).

GNSS satellite systems consist of three major components or segments: Space Segment, Control Segment and User Segment (Figure 3.1). The Space Segment includes the constellation of GPS satellites, which transmit the signals to the user. The Control Segment is responsible for the monitoring and operation of the space segment and finally, the User Segment includes user hardware and processing software to derive and apply location and time information. From here on, we will focus on GPS system, since this the GNSS system was used in this thesis.

4.1. The Global Positioning System (GPS)

The GPS is a worldwide radio-navigation system formed from a constellation of satellites and their ground stations. This system is based on the principle of trilateration, the method of determining position by measuring distances to points of known positions (e.g. Blewitt, 2009).

The three GPS segments are:

- The Space Segment includes the constellation of GPS satellites (24-31). The GPS was designed originally based on 24 satellites distributed in 6 orbital planes, with an inclination of 55º (Figure 4.2). There are extra satellites (one satellite in each orbital plane) to maintain the coverage whenever the baseline satellites are serviced or decommissioned. In this way, it ensures the visibility of at least four satellites anywhere. The orbit of the satellites has an altitude of ~20.200 km, circling each satellite the Earth twice a day (www.gps.gov/systems/gps/space/#generations). The GPS satellites (Figure 4.2) provide a platform for radio transceivers, atomic clocks, computers, and various ancillary equipment (e.g. solar panels) to operate the system (Hofmann-Wellenhof et al., 2001).

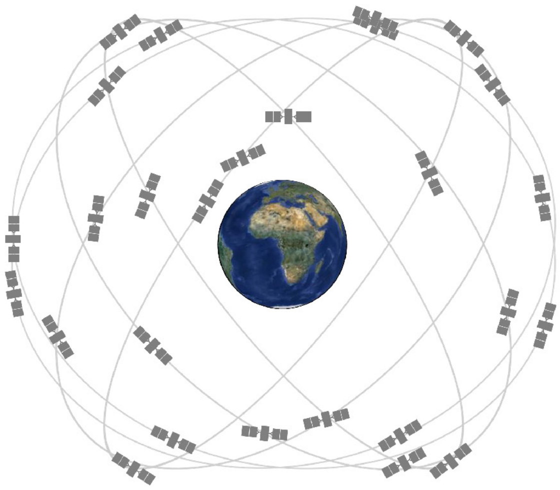

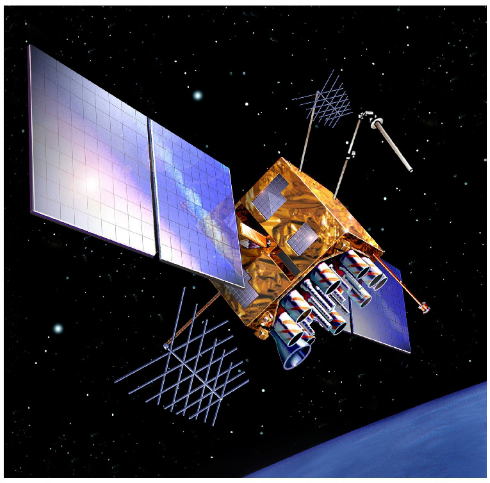

Figure 4.2: Space Segment: satellite constellation (left) and GPS satellite, model BLOCK IIR (right). (From www.gps.gov/systems/gps/space/).

- The Control Segment comprises a ground-based network of master control stations, ground control stations and monitor stations. The 16 monitor sites control the signals of the satellites and status, and relay this information to the master control station. The master control station, located at Colorado Springs, analyses the signals then transmits orbit and time corrections to the satellites through ground control stations (or data uploading stations Figure 4.1) (Jeffrey, 2010).

- The User Segment is the equipment (antenna, receiver and processing software), which processes the received signal from the satellites for positioning, navigation and timing applications.

4.1.1. GPS signal

GPS satellites transmit signals in a frequency band referred to as L-band, a portion of the radio spectrum between 1 and 2 GHz. The fundamental frequency is 10.23 MHz, which is used to create two carrier signals, L1 and L2. The frequency of L1 is 1575.42 MHz (wavelength of 19.0 cm) and the frequency of L2 is 1227.60 MHz (wavelength of 24.4 cm). These dual frequencies are essential for eliminating the ionospheric refraction (see section 3.1.2), the major source of noise (Hofmann-Wellenhof et al., 2001). Within the GPS modernization programs, the U.S government is launching new GPS satellites that are capable of transmitting three new signals designed for civilian use: L2C, L5 and L1C (gps.gov/systems/gps/modernization/civilsignals/).

The carriers L1 and L2 are modulated by code to provide satellite clock readings to the receiver and to transmit this information. The code consist of apparent random sequences of binary values, which repeat after some chosen interval time, and known as pseudorandom noise (PRN) sequence. There are three types of code on the carrier signals: the **C/A-code** (available for civilian use), the **P-code** (only for military use and authorized users) and the **Navigation Message**.

The **C/A** code or Coarse Acquisition Code is modulated on the L1 and is repeated every millisecond. It is a pseudo-random code, which appears to be random, but is in fact generated by a known algorithm. The C/A code contains information about the satellite clock time when the signal was transmitted (with an ambiguity of 1 ms) A different code is assigned to each satellite, so the satellites can be uniquely identified.

The **P-code** or Precise Code is transmitted on L1 and L2 and is identical on both and is repeated every 267 days. The P-code has a shorter wavelength, which enables a higher precision of the range measurement. Unlike the C/A-code, the P-code can be encrypted by the U.S. military services by a process known as Anti-Spoofing (A/S). The P-code is encrypted to the Y-code, the sum of the P-code and the encrypting W-code. Hence, access to the P-code is only possible when the secret conversion algorithm is known (generally for military use).

The **Navigation Message** is a low bit rate message and can be found on the L1. The Navigation Message essentially contains information about the satellite health status, the satellite clock corrections, ionosphere information, almanac data (a crude ephemeris for all satellites) and broadcast ephemeris (satellite orbital parameters), from which the receiver can compute the satellite coordinates.

4.1.2. GPS observables

The GPS observables are ranges which are deducted from measured time or phase differences between received signals and receiver generated signals. The ranges are biased by satellite and receiver clock errors, so they are denoted as pseudoranges. As mentioned before, GPS is based on trilateration, a method of determining position by measuring distances to points of known positions (the positions of the satellites in view) (Blewitt, 2009). At a minimum, trilateration requires three ranges but GPS point positioning requires 4 pseudoranges to 4 satellites.

4.1.2.1. The pseudorange observable

GPS receivers cannot measure ranges (distance between the satellite antenna and the antenna of the GPS receiver) directly, but rather pseudoranges. A pseudorange P_r^s is a measurement of the difference in time between the receiver's local clock and an atomic clock on board a satellite (Blewitt, 2009). The time difference is multiplied by the speed of light (c) to convert it into units of range (meters):

$$P_r^s = c\,(T_r - T^s) \tag{4.1}$$

where T_r is the known reading of the receiver clock when the signal is received and T^s is the reading of the satellite clock when the signal was transmitted (Figure 4.3). However, the time measurements on the satellite and receiver are biased, due to the lack of time synchronization between both clocks. So, if we include the clock bias (τ), the pseudorange expression as a function of the true time the signal was received ($t;\ t_r = T_r - \tau_r$) becomes:

$$P_r^s(t) = \rho_r^s + c\tau_r - c\tau^s \tag{4.2}$$

Where ρ_r^s is the range from receiver to the satellite. Adding the propagation medium effects (the ionospheric delay, ΔI and the tropospheric delay, ΔT), and the rest of error sources ϵ, the pseudoranges can be modeled as:

$$P_r^s(t) = \rho_r^s + c(\tau_r - \tau^s) + \Delta I + \Delta T + \epsilon \tag{4.3}$$

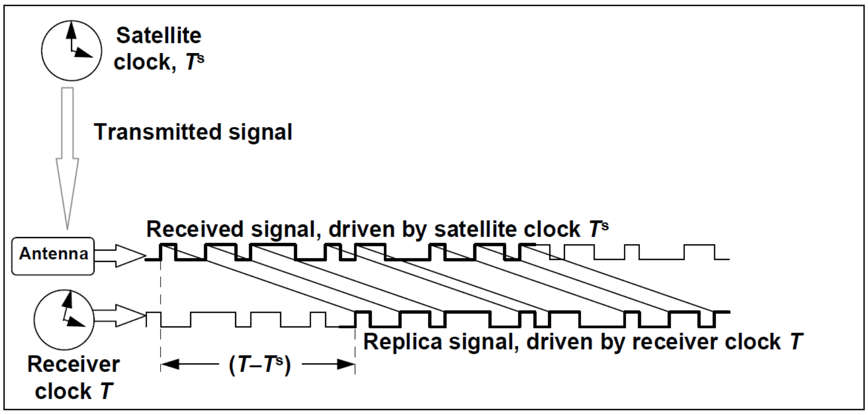

Figure 4.3: Schema of how the GPS pseudorange observation is related to the satellite and receiver clocks (from Blewitt (1997)).

The clock bias is the same for all observed satellites, so it can be estimated as one extra parameter. Therefore, point positioning with GPS requires pseudorange measurements to at least four satellites, to estimate three coordinates of the receiver and the clock bias.

4.1.2.2. The phase observable

The carrier phase observable is used for high precision applications (Blewitt, 1997), such as this study, because the precision of the carrier phase is much higher than the precision of the pseudorange code as its wavelength is much shorter. The carrier phase ϕ_r^s observable (L1 and L2) is defined as the difference between the phase of the incoming carrier wave ϕ^s and the phase of the reference signal generated by the receiver ϕ_r . Only the fractional carrier phase can be measured when a satellite signal is acquired, i.e. an integer number N of full cycles is unknown, N is called integer ambiguity.

The measured carrier phase in cycles can be transformed to equivalent distance units multiplying by the wavelength (λ) of the carrier. So, the phase observable, in units of distance, can be written as:

$$\phi_r^s(t) = \rho_r^s + c(\tau_r - \tau^s) + \lambda \cdot N - \Delta I + \Delta T + MP + \epsilon \tag{4.4}$$

Equations 4.3 and 4.4 are very similar, the major difference being the presence of the ambiguity term. The minus sign of the ionospheric delay indicates the increase of the phase velocity (Blewitt, 1997).

4.1.3. Error sources

The code and phase pseudorange are affected by systematic errors or biases and random noise. Errors affecting GPS solutions can be classified into four main groups:

i) Satellite related errors: clock bias and orbital errors.

The data concerning ephemerides (provided in the navigation message) may not exactly model true satellite motion or the exact rate of the clock drift, causing an error.

ii) Signal propagation related errors: ionospheric refraction and tropospheric refraction.

The GPS signal cross the ionosphere and troposphere, causing a change in the speed and direction of signal propagation. The ionosphere is an ionized medium and affect the electromagnetic signals propagation. The tropospheric delay or tropospheric refraction is due to the effect of the neutral atmosphere (i.e., the non-ionized part), a non-dispersive medium.

To mitigate the effect of the ionospheric error, the two carriers L1 and L2 can be linearly combined to obtain another frequency, the so-called LC or L3 'ionosphere-free' combination of carrier phase, defined as:

$$\phi_{LC} = 2.546\phi_{L1} - 1.984\phi_{L2} \tag{4.5}$$

iii) Receiver related errors: antenna phase center variation, clock bias and multipath.

The GPS measurements are referred to the electrical phase of the antenna, the apparent source of radiation. The exact position of the phase center is modeled and tabulated for each type of antenna, including a phase center offset a phase center variation. Multipath is when a signal emitted by a satellite arrives at receiver via more than one path, caused by reflecting surfaces near the receiver.

iv) Non-GPS related errors: solid Earth tide, atmosphere and hydrological loading and ocean and pole tide.

The Earth's crust responses elastically to the gravitational attraction of the Sun and Moon (solid Earth tide), to the ocean tides, to a time-varying atmospheric pressure distribution, to shifts in the pole rotation and to the influence of variation in water masses accumulating on the Earth. The majority of these Earth related deformation cause a significant effect on the vertical component and a small component in the horizontal components (e.g. Watson et al., 2006).

In the software GAMIT/GLOBK used in this thesis for process, we used the IERS03 model (McCarthy and Petit, 2004) for correct the solid Earth tide, the FES2004 model (Lyard et al., 2006) for the ocean tide, the IERS conventions (McCarthy, 1996) for the pole tide and the non-tidal atmospheric loading corrections, implemented using the code developed by Paul Tregoning (Tregoning and van Dam, 2005) of the Australian National University. The hydrological loading were not implemented in the software and due to the difficulty to quantify the load signal, was not applied in the processing.

4.1.4. GPS positioning

Various strategies can be employed when processing the GNSS (and GPS) data. The coordinate of a single point can be determined using a single receiver (point positioning) or using two receivers and combining the measurements to the same satellites (relative positioning). Both positioning can be done in static (fixed antenna) or kinematic mode (mobile antenna). The observation technique followed in this thesis is the static relative positioning, the most accurate positioning technique, which will be summarized in this section. Originally, relative positioning was only possible by post-processing data. Today, real-time data transfer over short baselines is possible, enabling real-time computation of baseline vectors, and has led to the real-time kinematic (RTK) technique. However, the precision of the RTK (generally of centimeters) is less than the post-processed positioning, which can reach sub-milimetric levels.

There are three ultrahigh-precision software packages which are widely used around the world by researchers. The first one uses Precise Point Positioning (PPP) whereas the last two use relative positioning.

- GIPSY-OASIS II software, by JPL, California Institute of Technology, USA (www.gipsy-oasis.jpl.nasa.gov/).
- BERNESE software, by Astronomical Institute, university of Bern, Switzerland (www.bernese.unibe.ch/).
- GAMIT-GLOBK software, by MIT, USA (www-gpsg.mit.edu/~simon/gtgk/). The software adopted in this study. This package uses double differences.

4.1.4.1. Relative positioning

In relative or differential positioning, the coordinates of an unknown point are determined with respect to a known point. This technique aims the determination of the vector between the two points, which is often called the baseline vector or simply baseline. Assuming simultaneous observations at both the reference (A) and the unknown point (B) to satellites j and k (Figure 4.4), linear combinations can be formed leading to single-differences, double-differences and triple-differences. Differences can be accomplished across receivers, satellites or time.

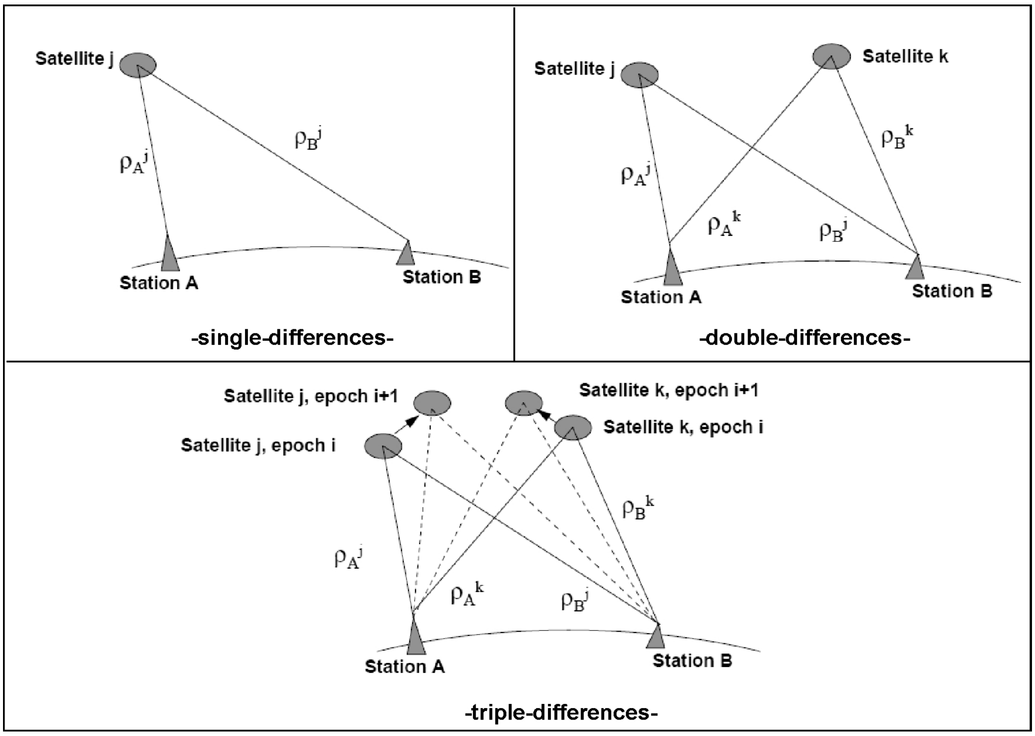

Figure 4.4: Differential positioning geometry, modified from Blewitt (1997).

In relative positioning many effects and errors can be cancelled out since these errors affect the absolute positions of the simultaneously observing GPS system to the same extent. Single-differences observables (the carrier phase or the pseudorange) eliminate the satellite clock error, since two receivers observe the same satellite. In double-differences, where two receivers observe two satellites, the receiver clock bias is eliminated. Triple-differences, based on differencing two double differences between two epochs, eliminate the time dependent ambiguity. The GAMIT-GLOBK uses double-differences and uses triple-differences in editing data (Herring et al., 2010b).

Simplifying the carrier phase observable equation and adapting to Hofmann-Wellenhof (2001) nomenclature, the carrier phase expressed in cycles is given by:

$$\phi_r^s(t) = \frac{1}{\lambda}\rho_r^s(t) + N + f^s \Delta\delta_r^s(t) \tag{4.6}$$

where λ is the wavelength, $\rho_r^s(t)$ the range from the receiver to the satellite, N is the ambiguity, f^s is the frequency of the satellite signal and $\Delta\delta_r^s(t)$ is the combined receiver and satellite clock bias. Splitting this term into two parts: $\Delta\delta_r^s(t) = \delta_r(t) - \delta^s(t)$, where the former is the receiver related term and the later the satellite related term,

$$\phi_r^s(t) + f^s\delta^s(t) = \frac{1}{\lambda}\rho_r^s(t) + N + f^s\Delta\delta_r\ (t) \tag{4.7}$$

If two receivers A and B observe the same satellite j and using the Eq. 4.7, the phase equations for the two points are:

$$\begin{aligned} \phi_A^j(t) + f^j\delta^j(t) &= \frac{1}{\lambda}\rho_A^j(t) + N_A^j + f^j\Delta\delta_A(t) \\ \phi_B^j(t) + f^j\delta^j(t) &= \frac{1}{\lambda}\rho_B^j(t) + N_B^j + f^j\Delta\delta_B(t) \end{aligned} \tag{4.8}$$

The single-difference phase or the difference of the two equations ($\phi_B^j(t) - \phi_A^j(t)$) is:

$$\phi_{AB}^j(t) = \frac{1}{\lambda}\rho_{AB}^j(t) + N_{AB}^j + f^j\Delta\delta_{AB}(t) \tag{4.9}$$

Note the cancellation of the satellite clock bias compared with Eq. 4.7. If the baseline length between receivers is small compared to the satellite orbit altitude, the effect of orbital errors may also largely mitigated.

In double-differencing, where the two receivers observe two satellites (j and k), two single-differences may be formed according the previous equation:

$$\begin{aligned} \phi_{AB}^j(t) &= \frac{1}{\lambda}\rho_{AB}^j(t) + N_{AB}^j + f^j\Delta\delta_{AB}(t) \\ \phi_{AB}^k(t) &= \frac{1}{\lambda}\rho_{AB}^k(t) + N_{AB}^k + f^k\Delta\delta_{AB}(t) \end{aligned} \tag{4.10}$$

Subtracting these single-differences and assuming equal frequencies for the satellite signal ($f^j = f^k$), the obtained equation can be written as:

$$\phi_{AB}^{jk}(t) = \frac{1}{\lambda}\rho_{AB}^{jk}(t) + N_{AB}^{jk} \tag{4.11}$$

The cancellation of the receiver clock biases result from the assumption of simultaneous observations and equal frequencies of the satellite signals. This is the reason why double-differences are preferably used (e.g. GAMIT/GLOBK package), although this approach causes an increase in random and multipath errors.

Triple-differencing is based in double-differences between two epochs (t_1 and t_2) and therefore the time independent ambiguities are eliminated. Being the two double-differences

$$\phi_{AB}^{jk}(t_1) = \frac{1}{\lambda}\rho_{AB}^{jk}(t_1) + N_{AB}^{jk}$$
$$\phi_{AB}^{jk}(t_2) = \frac{1}{\lambda}\rho_{AB}^{jk}(t_2) + N_{AB}^{jk} \tag{4.12}$$

the triple-difference equation can be written as:

$$\phi_{AB}^{jk}(t_{1,2}) = \frac{1}{\lambda}\rho_{AB}^{jk}(t_{12}) \tag{4.13}$$

4.2. SGPS data

In this thesis, we have used two different types of GPS data recording procedures: the survey or campaign mode (SGPS) and the continuous mode (CGPS). Each data set was processed independently, in order to conserve the same window of data span for each processing. In this section, we provide a description of these two types of data sets and the processing procedure that was followed.

The difference between SGPS and CGPS lies in the method of data acquisition. The survey-mode consists on antennas set up over monuments for short periods (campaigns), while in the continuous mode GPS stations are recording permanently (generally every 1 or 30 seconds). The duration of campaigns is usually hours, days, or weeks. The SGPS stations are usually used in particular area for special science research, covering small areas.

In this thesis we have observed and processed the geodetic network CuaTeNeo, installed by the Universitat de Barcelona in the study area in 1996. This network forms part of the main results presented in this work and have never been published previously (these results ensued in Echeverria et al. (2013)). Of the five campaigns that have been realized in total, I have participated in two of them.

4.2.1. Survey GPS networks

4.2.1.1. CuaTeNeo network

The CuaTeNeo geodetic network (Figure 4.5) was built in 1996 to quantify current crustal deformation rates in the eastern Betic mountains (specifically of the Alhama de Murcia, Palomares and Carboneras faults). The network was installed in the frame of the project '*Cuantificación de la Tectónica Actual y Neotectónica en la parte oriental de la Peninsula Ibérica*' (PB93-0743-C02-01) and was initiated by the University of Barcelona (UB) and the Institut Cartogràfic de Catalunya (ICC) (Castellote et al., 1997), and later joined by the San Fernando Royal Naval Observatory (ROA). The network is placed in the Almeria and Murcia provinces (eastern Iberian Peninsula).

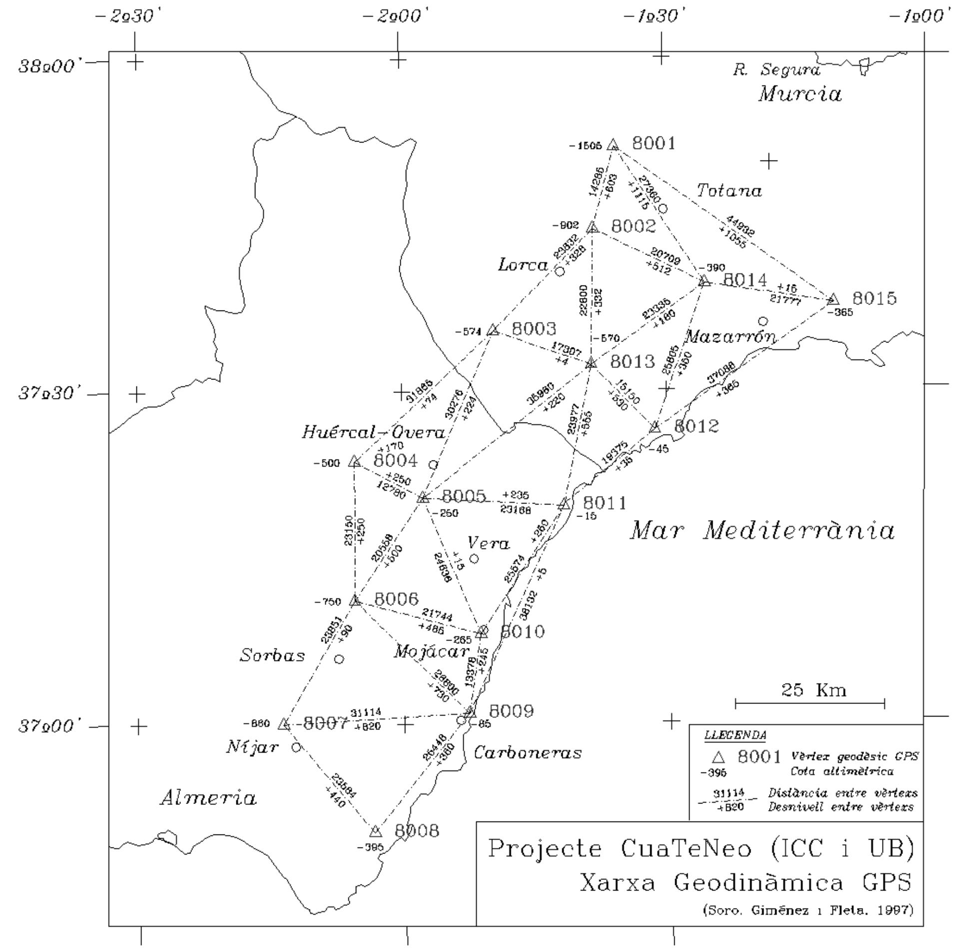

Figure 4.5: CuaTeNeo network design with the monument number identification (ID) and the distance between sites. Maximum distance: 44.9 km and minimum distance: 12.8 km (from Soro et al.(1997)).

The network consists of 15 GPS monuments placed on bedrock, from which 11 were built using concrete monuments with steel rebar perforating the bedrock up to 1 meter depth (to ensure good coupling) with embedded 5/8" threads (to guarantee correct centering of GPS antennas during observational campaigns) (Figure 4.6). The remaining four monuments, due to difficult access, consist of simple 5/8" threads cemented into bedrock and referred to as nail type monuments.

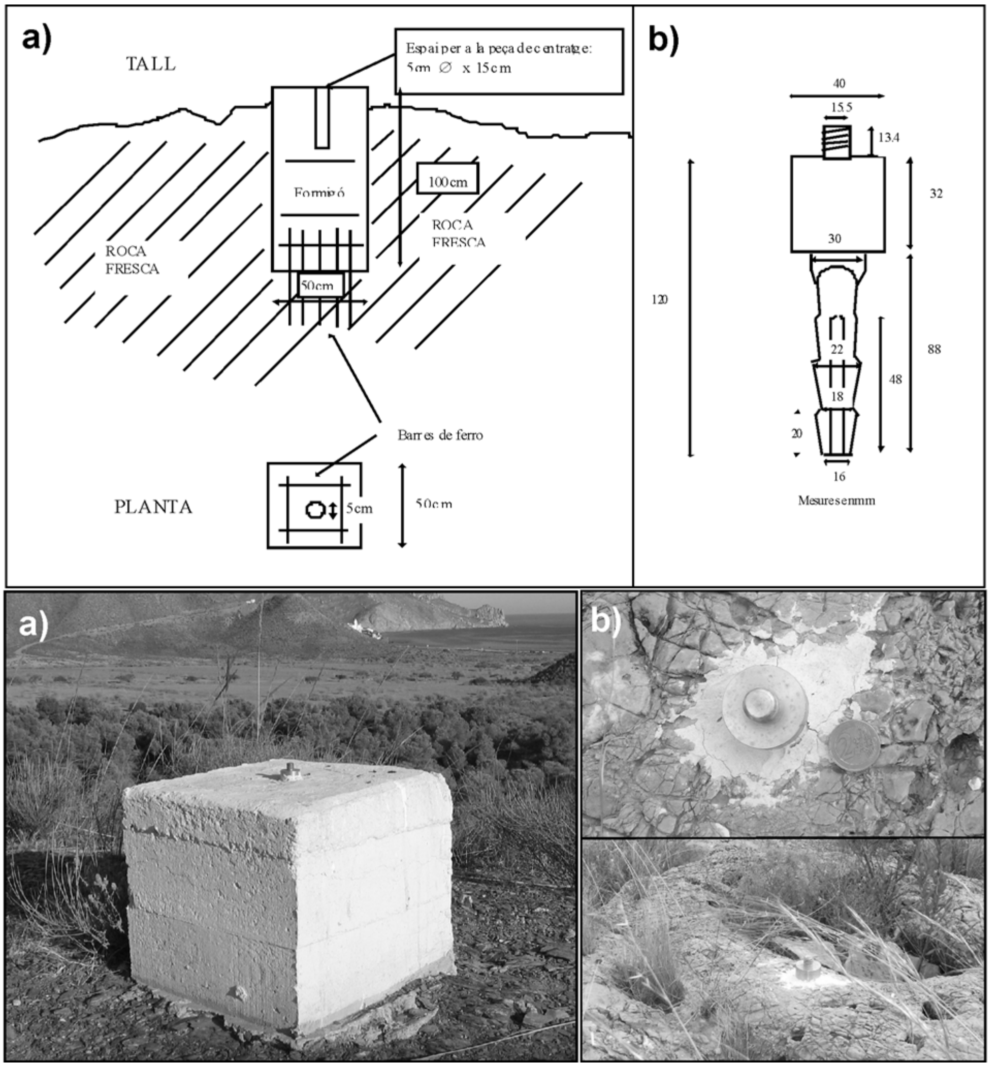

Figure 4.6: Sketch and photos of the two types of monuments of CuaTeNeo network. *a)* Concrete monument. *b)* Nail type monument with the approximately dimension (in mm).

Table 4.1: ID and site name, location, type of monument and bedrock and years of campaigns observed.

ID	CODE	Location	Monument	Rock	Survey Measurements				
					1997	2002	2006	2009	2011
8001	ESPU	Sierra Espuña	Pillar	Limestone	x	x	x	x	x
8002	TERC	Sierra de la Tercia	Pillar	Dolostone	x	x	x	x	x
8003	MELL	Cuesta del Mellado	Pillar	Sandstone and quartz	x	x	x	x	x
8004	PUAS	Cerro Púas	Pillar	Phyllite	x	x	x	x	
8005	HUER	Huercal-Overa	Thread	Dolostone	x	x	x	x	
8006	CUCO	Cerro Cuco	Pillar	Schist	x	x	x	x	
8007	HUEB	Huebro	Pillar	Limestone	x	x	x	x	
8008	RELL	La Rellana	Pillar	Dacite	x	x	x	x	
8009	CARB	Carboneras	Thread	Andesite	x	x	x	x	

8010	MOJA	Mojácar	Thread	Limestone	x	x	x	x	
8011	PANI	Pozo del Espartos	Thread	Rhyodacite	x	x	x	x	
8012	MONT	Montalbán	Pillar	Phyllite	x	x	x	x	x
8013	PURI	Casa Reverté	Pillar	Gneiss	x	x	x	x	x
8014	GANU	Sierra de Almenara	Pillar	Serpentine	x	x	x	x	x
8015	MAJA	Collado de Majasarte	Pillar	Schist	x	x	x		x

The network has been observed in five campaigns conducted in 1997, 2002, 2006, 2009 and 2011. In general, intermittent campaigns should be conducted in the same months to minimize seasonal effects. The campaigns were conducted in the months of September and October, except for the first 1997 and the last 2011 campaigns. The 1997 campaign was conducted in April. The 2011 campaign was organized in spring instead of the autumn, since it was specifically aimed to measure possible co-seismic deformation caused by the May 11, 2011 Lorca earthquake. For this reason, the 2011 campaign only the seven nearest points to the earthquake were observed: ESPU, TERC, MELL, MONT, PURI, GANU and MAJA (Figure 4.7 and Table 4.1). All sites occupied during each campaign were observed for three or more consecutive days in at least 8 hour long sessions. The first two campaigns (1997 and 2002) used Trimble 4000SSE receivers with Trimble 22020.00 GP antennas. Topcon GB1000 receivers with PG-A1_6 w/GP antennas were used since 2006. We employed special antenna adapters (Figure 4.8) to ensure correct antenna orientation to North and to avoid errors in antenna height.

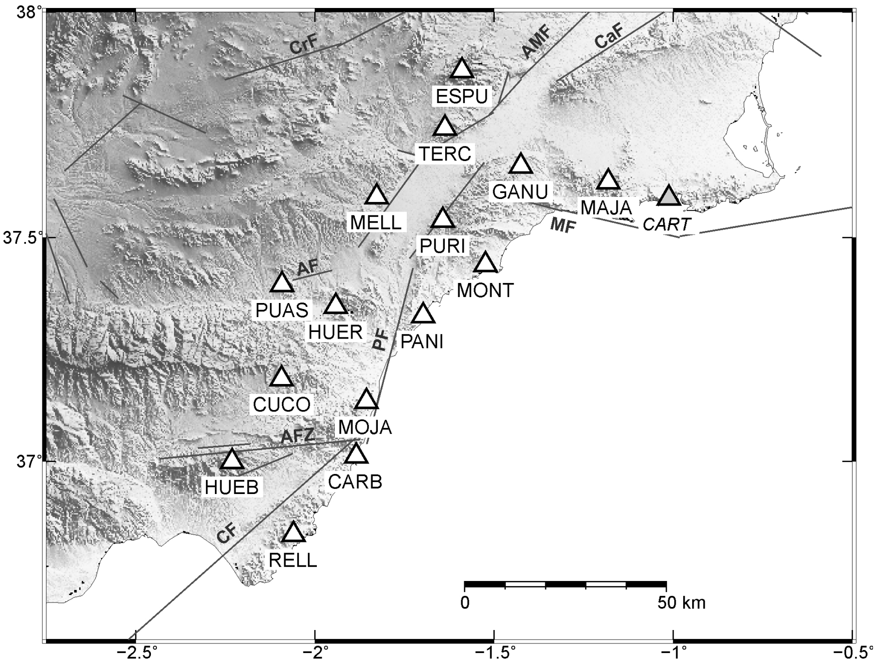

Figure 4.7: Location of CuaTeNeo network stations and main Quaternary active faults (García-Mayordomo et al., 2012). CART station, drawn in gray, has been also included in SGPS database (see section

4.3.2). abbreviations are: CrF - Crevillente fault; BSF - Bajo-Segura fault; CaF - Carrascoy fault; AMF - Alhama de Murcia fault; AF - Albox fault; PF - Palomares fault; CF - Carboneras fault; MF - Moreras fault: AFZ - Alpujarras fault zone.

Figure 4.8: Photo of the PURI concrete monument with the adapter and PG-A1_6 w/GP antenna in 2009.

4.2.1.2. Others survey networks

In 1999 the Universities of Alicante and Jaén installed a GPS network in the Bajo Segura basin (Alfaro et al., 2000). This network, together with CuaTeNeo network provides coverage over all EBSZ. The network consists of 11 geodetic vertexes and has been observed in four campaigns between 1999 and 2013. Results can be found in Alfaro et al. (2014) and Sánchez-Alzola et al. (2014), see Section 3.3.1.

In Granada Basin, in the central sector of the Betic Cordillera, has been installed a non-permanent network (Gil et al., 2002). This network consists of 15 reinforced concrete pillars anchored to rock. The first campaign was conducted in 1999.

4.2.2. Processing methodology

In order to calculate the velocity vectors of CuaTeNeo stations, we processed data from 44 GPS stations. Among these, 16 stations were SGPS: the 15 points of the CuaTeNeo network and one station placed in Cartagena (CART, Figure 4.7), belonging to the San Fernando Royal Naval Observatory (ROA). Station CART is a continuously recording site installed in 1998. Since the data availability was intermittent, we treated it as a SGPS station, analyzing data from the same days as the 2002, 2006, 2009 and 2011 CuaTeNeo surveys. In addition, we analyzed 28 CGPS stations, the majority belonging to EUREF (http://epncb.oma.be/; Bruyninx, 2004) and/or International GNSS Service (IGS) (http://igscb.jpl.nasa.gov/; Dow et al., 2008) networks and are distributed throughout Iberia, Eurasia and Africa (Figure 4.9). CGPS sites were selected using a criterion of having at least 10 years of data availability to ensure similar time span as of the CuaTeNeo data. To ensure robust velocity estimation and consequently, a better reference frame for the SGPS sites, we analyzed these CGPS stations for an entire time-span of the campaign data from 1997 to the end of 2011. To accelerate the processing procedure, especially at the post-processing step of the data analysis, CGPS data were processed for every 10 days instead of daily observations.

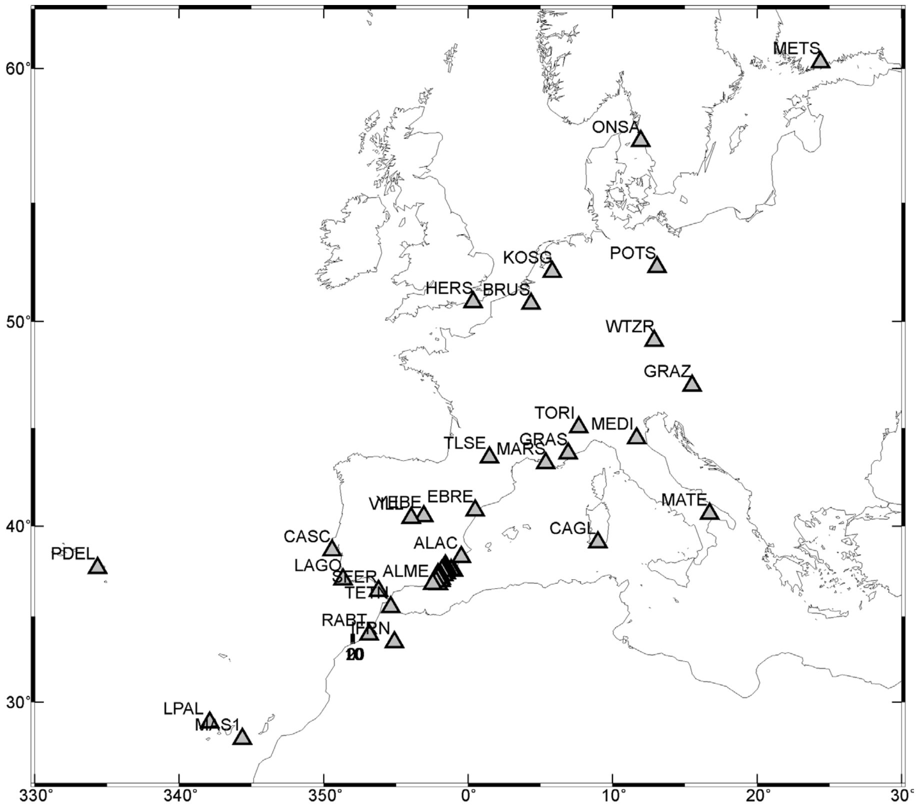

Figure 4.9: Location of the 44 GPS stations processed for 1997-2011 period in this thesis.

GPS data were processed using GAMIT/GLOBK 10.4 (Herring et al., 2010b) software developed at Massachusetts Institute of Technology (MIT) (http://gpsg.mit.edu/simon/gtgk). This package uses double differences of phase and code data to compute a network solution. GAMIT/GLOBK analysis strategy has been well documented in literature (e.g. Dong et al., 1998; McClusky et al., 2000; Reilinger et al., 2006; Herring et al., 2010b), because of that only a guideline followed and the relevant parameters are presented here.

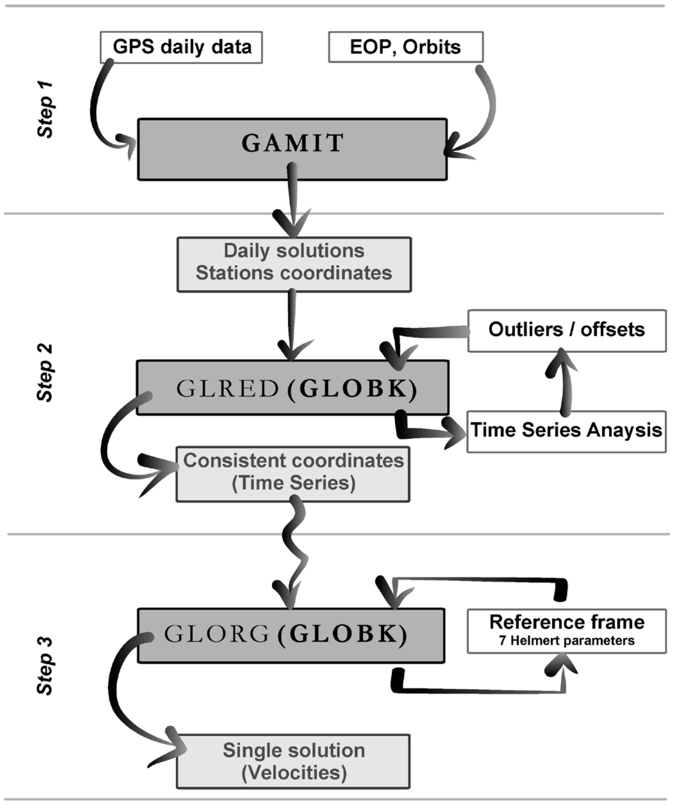

Figure 4.10: Summary of analysis strategy used with GAMIT/GLOBK software

Table 4.2: Detailed description of the parameters used in the processing.

GAMIT	
Experiment	Baseline (orbits are fixed)
Station Error	Elevation
Elevation cutoff	10º
Satellite orbits	IGS final orbits
Choice of observable	LC_AUTCLN (ambiguities fixed using pseudo-ranges constraints)
Mapping function for atmospheric delay	GMF (Boehm et al., 2006)
Zenith delay	Estimated every 2 hour-intervals
Solid-Earth tide model	IERS03 (McCarthy and Petit, 2004)
Ocean loading model	FES2004 (Lyard et al., 2006)
Hydrological loading effects	Not applied
Antenna model	IGS08
GLOBK	
Reference frame	ITRF2008 (Altamini et al., 2011)
Periodic signal	Annual
Stations for stabilization	ALAC, ALME, BRUS, CAGL, CASC, EBRE, GRAS, HERS, IFRN, KOSG, LAGO, AMRS, MEDI, METS, ONSA, PDEL, POTS, RABT, SFER, TETN, TLSE, TORI, VILL, YEBE.

To obtain GPS station velocities we followed a three-step approach described by McClusky et al. (2000; 2003) (Figure 4.10 and Table 4.2). First, daily GPS phase observations were processed using GAMIT by applying loose a priori constraints (in order to estimate station coordinates), the zenith delay of the atmosphere at each station and orbital and Earth orientation parameters (EOP). It is called loose because all the estimated parameters at this step are estimated simultaneously without applying tights constrains. Second, consistent station coordinates were obtained from the loosely constrained solutions using the *glred* module from GLOBK. The daily time series of each site were visually inspected and obvious outliers removed. We corrected offsets due to earthquakes, antenna or hardware changes (Figure 4.11). The CuaTeNeo cleaned time series are included in Appendix B.

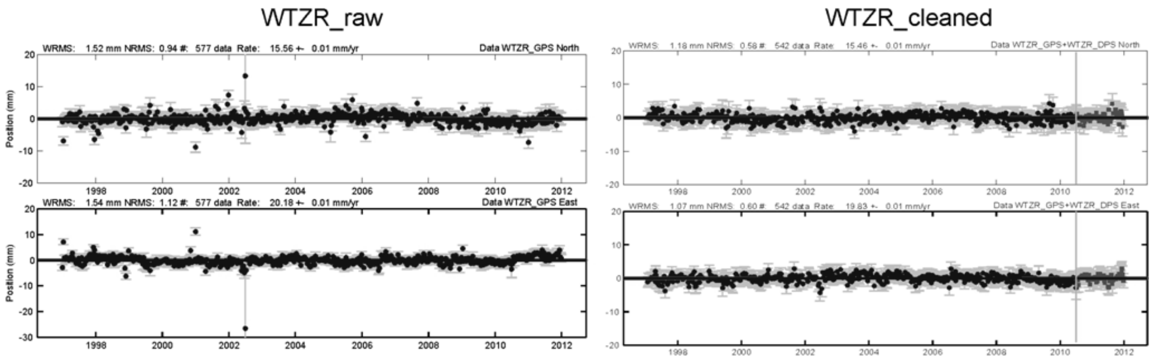

Figure 4.11: Time-series of WTZR station components (Germany): N-S component up and E-W component down. *Left)* Raw time-series. *Right)* Cleaned time-series: the outliers have been removed and offset due to antenna change corrected (vertical bar in 2010). Outliers can be done for being a large error bar or differing from the linear trend.

In the final step, all data were combined into a single solution, estimating positions, velocities and uncertainties for each station in a given reference frame. This final step is divided into two parts following Steblov et al. (2003) and Kotzev et al. (2006). First, the GPS solution is realized in the no-net-rotation (NNR) ITRF2008 global reference frame (Altamini et al., 2011) by minimizing the differences using Helmert transformation between our estimated horizontal velocities for the reference stations and their corresponding velocities in ITRF2008 (Figure 4.12). NNR reference frame assumes no net rotation of the lithosphere as a whole, i.e. sum of the absolute motion of all plates weighted by their area is zero. A NNR is sometimes referred to as “absolute” plate motion. For this reason, to ease the interpretation of the obtained results in the second step we choose a set of CGPS stations that can be attributed to be belonging to a non-deforming part of Eurasia and we transform the ITRF2008 solution into a western Europe reference frame by minimizing the residual velocities for these stations. The result of this transformation is an Euler vector that defines the motion of the western Europe or Eurasia. This reference frame realization allows calculating a "relative" motions with respect to the stable part of the Eurasia plate and thus, makes it easier to detect actively deforming regions.

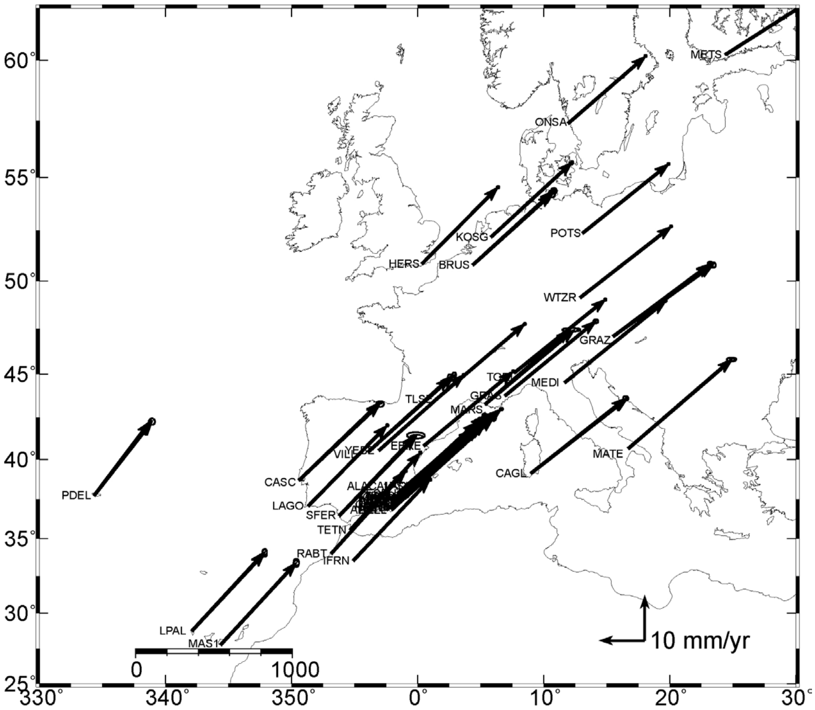

Figure 4.12: Velocities of GPS sites in ITRF2008 reference frame with 95% confidence error ellipse.

4.2.2.1. Characterization of errors

A rigorous estimation of uncertainties for the GPS velocities is especially important due to the low deformation rates (<2 mm/yr in this study area). Assuming only pure white noise (random noise) and ignoring correlated ('red') noise in GPS time-series leads to underestimation of the calculated velocity uncertainties (e.g. Mao et al., 1999). For our 28 CGPS sites, random noise may be reduced to a negligible level and the character of the correlated noise can be evaluated (e.g. Williams et al., 2004; Bos et al., 2013). In general, a correlated noise can be estimated from time series using spectral analysis, but cannot be easily implemented in a GLOBK velocity solution, which is performed with a Kalman Filter that accepts only first-order Gauss-Markov processes. Instead, we use the realistic sigma (RS) method developed by Herring (2003) and described later by Reilinger et al. (2006) for the CGPS sites. This method is computationally efficient and handles time series with varying lengths and data gaps. The RS method assumes a first-order Gauss-Markov process to take into account the fact that in the presence of correlated noise, χ^2/dof of the time series as a function of averaging time, does not remain constant (as with white noise) but increases asymptotically. By estimating amplitude and the time constant of the exponential function, and afterwards evaluating the function for infinite averaging time, we determine the random-walk value that will produce a realistic uncertainty for the velocity estimate (see Shen et al., 2011 for details). We applied the RS algorithm to our continuous station time series after removing the best-fit annual signal, and then included the estimated random walk for each component of each station in our velocity solution.

No attempt to apply the RS algorithm was made on the campaign sites (SGPS), where random (white) noise is dominant. Instead we added 0.4 mm/√yr and 0.6 mm/√yr (for the nail type monuments) of random walk noise for SGPS stations to account for possible random walk due to monument instability (see Langbein and Johnson, 1997 for details). Additionally, several SGPS observations for the 2002 campaign are downweighted (Figure 4.13 and Appendix B). Human error likely accounts for these outliers since the same team and equipment measured these problematic stations.

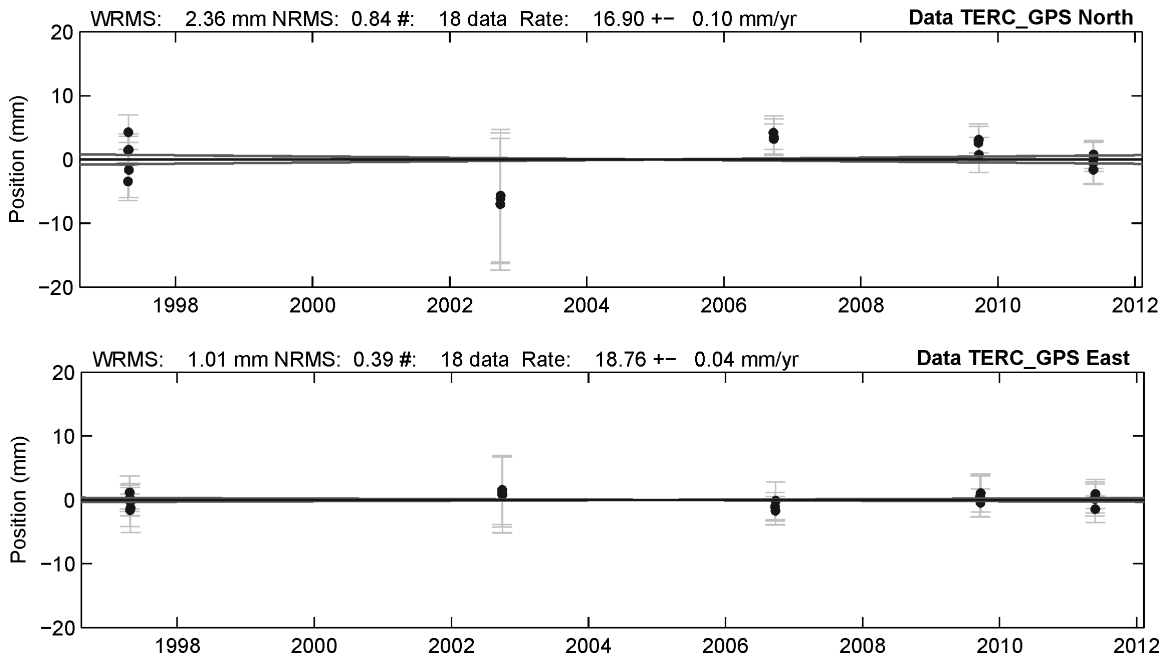

Figure 4.13: Time series of the SGPS TERC (Sierra la Tercia, Murcia). Up, the N-S component and down the E-W component. Note the larger error bar for the 2002 campaign (see text for more explanation).

The Figure 4.14 shows histograms of the normalized rms (nrms) for the CuaTeNeo stations. If the data from all sites are properly weighted for their short-term scatter, the distribution of scatters among the sites should be approximately Gaussian with the median nrms ~1 (Herring et al., 2010b). In spite of small sample the histograms are approximately normal but with a tendency to small values (the mean for both components is 0.8). This could be related to the down-weighted data.

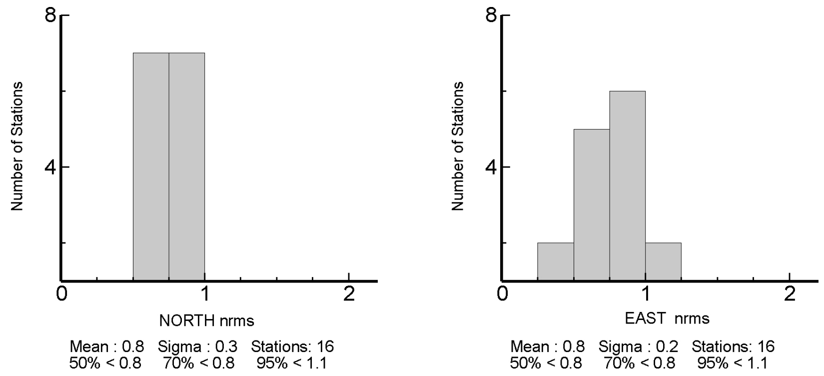

Figure 4.14: Histogram of the normalized rms for the SGPS CuaTeNeo stations.

4.3. CGPS stations

The continuously recording GPS stations (CGPS) have several obvious benefits over the SGPS stations such as an increase of the precision (due to the reduction in RMS scatter of daily position estimates, 24 hour long daily observations, elimination of setup and antenna related errors), real-time measurements and a possible detection of short-term geodetic signals from pre and post-seismic effects. Today, numerous arrays of CGPS receivers operate worldwide. These arrays are implemented by various organizations (public and private), covering varying size geographic areas, such as continents or small regions.

4.3.1. Continuous GPS networks

In Spain, several regional networks have developed in the last decade. Some of them were implemented for a real-time high accuracy positioning (e.g. RTK or DGPS corrections). The eastern Betics area includes 25 stations from different networks. Here we provide a description of these networks and the characteristics of the stations located in the study area for which we calculated the velocity vector (Section 5.2). With the exception of Topo-Iberia network and GATA CGPS station, all continuous GPS observations analyzed were retrieved from public networks, which are described below.

ERGNSS Permanent network from IGN (Instituto Geográfico Nacional from Spain) (http://www.ign.es/ign/layoutIn/actividadesGeodesiaGnss.do; Cano Villaverde et al., 2011). The network consists 41 continuously operating stations of which 20 are integrated in the European network EUREF and two in the international network IGS. It was the first network installed in Spain that launched the first station in 1996. Data at 30 seconds rate have been downloaded at ftp://ftp.geodesia.ign.es/.

R.A.P. 'Red Andaluza de Posicionamiento' (http://www.ideandalucia.es/portal/web/portal-posicionamiento/rap; Berrocoso et al., 2006). The RAP network is located in the Andalucía region. Is formed by 22 permanent stations and has the main goal of provide data for post-processing operations and broadcasting differential corrections. The Laboratorio de Astronomía, Geodesia y Cartografía (LAGC, http://lagc.uca.es/) from the Universidad de Cádiz does the maintenance and the geodetic control of the whole network. The first two stations were installed in 2005 although until 2010 the network was not complete. Data at 30 seconds rate have been downloaded at ftp://rap.uca.es/.

REGAM 'Red Geodésica Activa de la Región de Murcia' (http://iderm.imida.es/iderm/geodesia/index.htm). This network belongs to the region of Murcia (Consejería de Obras Públicas y Ordenación del Territorio). Although initially was formed by seven stations in 2008, it consists actually of 12 stations CGPS. The REGAM network provides RTK positioning services by the VRS (Virtual Reference Stations) approach. RINEX files (1s, 5s or 30s sampling) are available for download at ftp://62.14.244.61/.

Meristemum (http://gps.medioambiente.carm.es/). This network belongs also to the region of Murcia (Consejería de Agricultura y Agua). The MERISTEMUM network was installed in 2006 and provides RTK positioning services by the MAC (Master Auxiliary Concept) approach by seven permanent stations. Data at 30 seconds can be downloaded at ftp://meristemum.carm.es/GPS/.

ERVA 'Red de Estaciones de Referencia de Valencia' (http://icverva.icv.gva.es:8080/). The ERVA network is located in the Valencia region and provides RTK positioning possibilities and data for post-processing. It was installed in 2005 and consists of eight permanent stations. Data at 30 seconds rate have been downloaded at ftp://icvficheros.icv.gva.es/. Since Valencia region is located in the northern limit of the studied area, only one station was included in the analysis.

4.3.1.1. Proprietary networks

The following stations (the constituents of Topo-Iberia network and GATA station) were built specifically with the specific aim of studying tectonic crustal deformations. During and before this thesis I have participated on the whole process of the installation of one of the stations of Topo-Iberia network and the maintenance of some stations of Topo-Iberia and GATA station.

Topo-Iberia

The Topo-Iberia network (Garate et al., 2015) was installed in 2008 as part of the '*Geosciences in Iberia: Integrated studies on topography and 4-D evolution ("Topo-Iberia")'* project (CSD2006-00041). Topo-Iberia is a multidisciplinary research program funded by the Spanish Ministry of Science and Education under the 'CONSOLIDER-IMAGENIO 2010' program of excellence. The objective of

Topo-Iberia is to understand the interaction between deep, superficial and atmospheric processes, by integrating research on geology, geophysics, geodesy and geotechnology (www.ija.csic.es/gt/rc/LSD/PRJ/indexTOPOIBERIA.html). This thesis is part of the Topo-Iberia project and was partially funded by the subprogram of GPS.

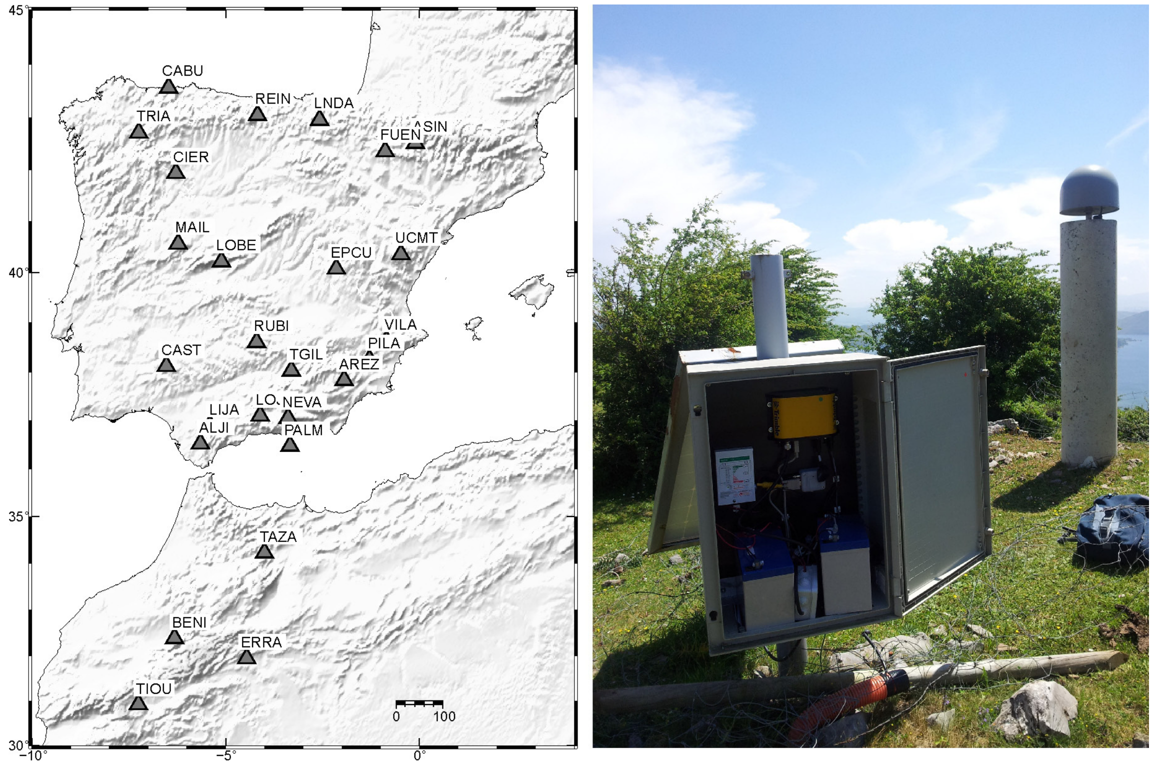

Figure 4.15: *Left)* Map with the location of the 26 CGPS of Topo-Iberia network. *Right)* Photo of the monumentation of LNDA station, located near Vitoria. It consists of a concrete pillar with the antenna and dome and the box containing the receiver, modem and batteries. Behind the box, there is a solar panel.

Topo-Iberia network consists of 26 permanent recording stations and covers the Iberian Peninsula and part of Morocco. The network has been designed as two X-shaped transects crossing the peninsula from NE to SW and NW to SE. Universitat de Barcelona, particularly Dr. Khazaradze, is the responsible of three stations in the north-east of the peninsula: ASIN, FUEN and LNDA (Figure 4.15). Although these stations are not in the area of study, has been participating in the maintenance and reparation of these stations. Most of the stations have a monument type of concrete pillar on bedrock. The hardware of the stations includes the Trimble NetRS receiver and TRM29659.00 choke-ring antenna. In some cases, a SCIGN dome protected the antenna. For detailed information as the requirements for the emplacements or the transmission and storage data see Asensio (2014).

GATA

The GATA continuous GPS station was installed by the Universitat de Barcelona in December 2008 as part of the *EVENT* (*'Integración de nuevas tecnologías en paleosismologia: Caracterización de fallas generadoras de Terremotos y tsunamis en el Sur de Iberia'*) project (CGL2006-12861-C02-01/BTE) with the specific objective of quantifying the present-day slip rates of the Carboneras fault zone (CFZ) (Khazaradze et al., 2010). The station was installed 2 km SW from the village of Rodalquilar in the Sierra de Cabo de Gata, close to (~ 200 m) CuaTeNeo monument RELL (Figure 4.16).

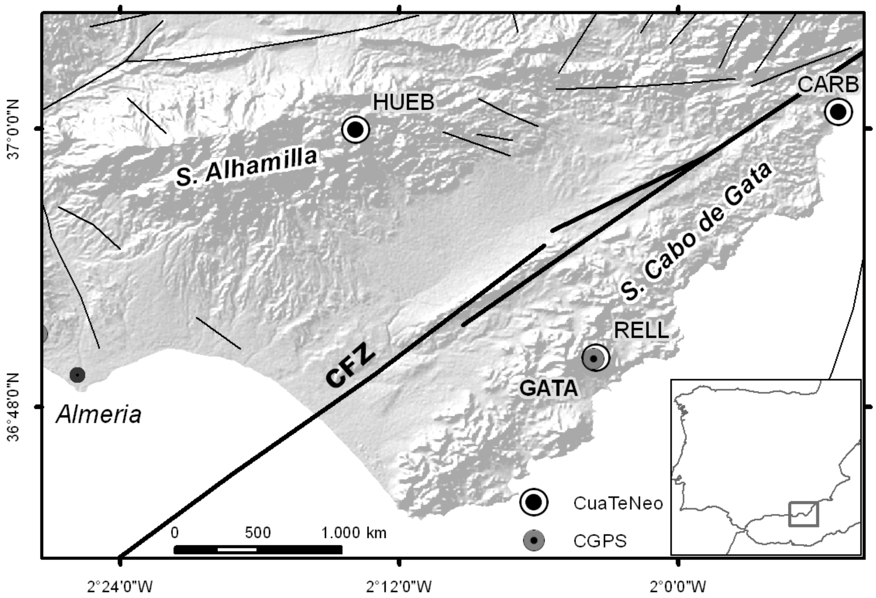

Figure 4.16: Location of GATA CGPS and CuaTeNeo points near the station. CFZ: Carboneras fault zone. Fault traces from Gràcia et al.(2012).

The monumentation consists of the short drill brace type monument designed by UNAVCO (Figure 4.17), consisting of 4 solid stainless steel rods, anchored at least half a meter into the bedrock (Miocene volcanic rocks). This type of monumentation ensures a good long-term stability of the station. The monument is also equipped with the SCIGN type antenna adapter and the PVC SCIT type dome to protect the antenna. The hardware includes the Leica GRX1200+GNSS receiver and the AT504GG choke-ring antenna, powered by an 80-watt solar panel. The data is stored in two data buffers with respective sampling frequencies of 30 seconds and 1 Hz. The communication with the station is provided by the Movistar GPRS/UMTS protocol using NetBox Wireless Router NB2210. Since 2011, the station has experienced hardware problems, related to the malfunction of the solar power system and a GPRS modem (see gaps in the time series in Figure 4.17).

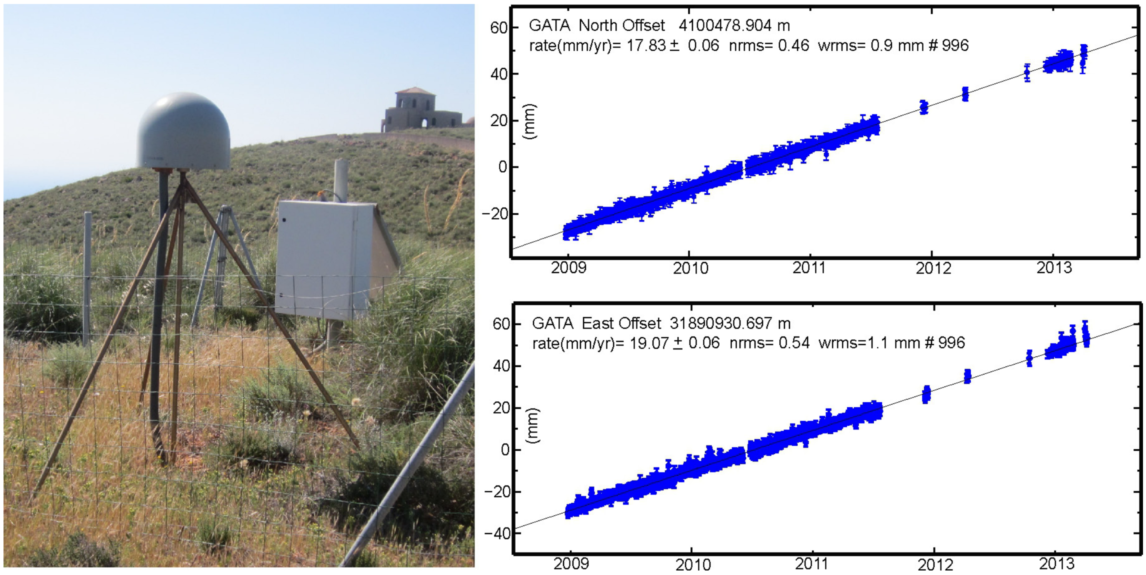

Figure 4.17: *Left)* Short drill braced type monument and time-series of GATA CGPS station, installed in December of 2008. *Right)* North-south (top) and east-west (bottom) components with 1σ errors are given in global ITRF2008 reference frame. Note gaps related to hardware problems.

4.3.2. Processing methodology

In this second set of data, we processed 4.5 yr data from 75 continuously recording GPS (CGPS) stations located both in eastern Betics and throughout Eurasia and Africa (Figure 4.9). Twenty-five of the 75 CGPS are located in the eastern Betic zone (Figure 4.18). GPS data were processed with GAMIT/GLOBK software 10.4 (Herring et al., 2010b) (www-gpsg.mit.edu/~simon/gtgk/), following the methodology described in Section 4.2.2.

The time-span of the analyzed data was the same: from 2008.8 to 2013.3, which equals to 4.5 yr of observations. This type of time-span is sufficient to appropriately model the annual oscillations in the resulting time-series and achieve optimal resolution of the velocity estimates (Blewitt and Lavallée, 2002) (Figure 4.19). The choice of the time-span is dictated by the data availability from the GATA station, which was installed in December of 2008.

The realization of the reference frame step ("stabilization") is performed by the *glorg* module. *Glorg* minimizes, in an iterative scheme, the departure from a priori values of the coordinates of a selected set of stations while estimating a rotation and translation of the frame (Herring et al., 2010a). The stations (distributed along the whole area) used for the stabilization in this case were: ABAN, ALAC, ALBA, ALCA, ALCO, ALME, ALMR, AREZ, AYOR, BOR1, BRUS, CAAL, CAGL, CARA, CASC, CEU1, DENI, EBRE, GAIA, GARR, GATA, GRAS, GRAZ, HERS,

HUOV, JOZE, JUMI, LAGO, LLIVA, LPAL, MALL, MARS, MAS1, MATE, MAZA, MLGA, MORA, MOTR, MRCI, MURC, ONSA, PALM, PDEL, PILA, POTS, RABT, ROND, SFER, TERU, TETN, TGIL, TLSE, TORR, UJAE, UTIE, VIAR, VILL, WTZR, YEBE, ZARA and ZIMM.

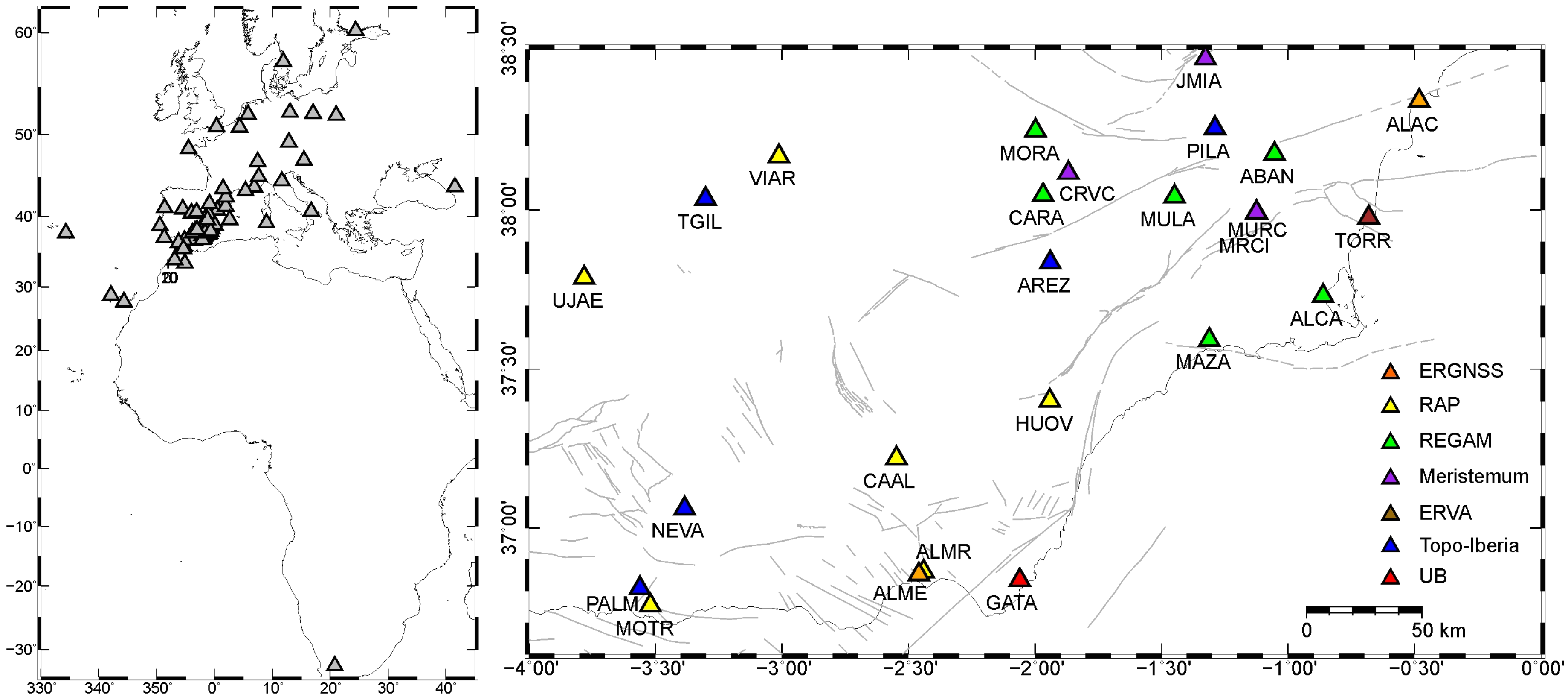

Figure 4.18: *Left)* Location of 75 CGPS stations processed for 2008.8-2013.3 period. *Right)* Detail of the location of 25 CGPS stations differentiated by networks in eastern Betics area. Active fault traces from García-Mayordomo et al. (2012) and Gràcia et al. (2012)

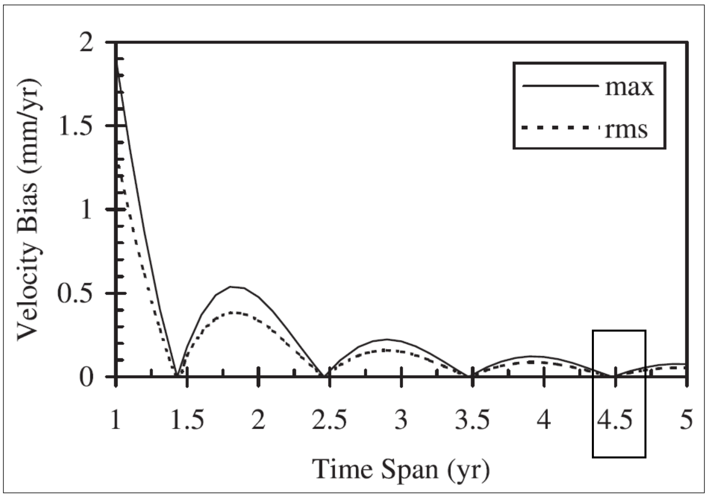

Figure 4.19: Velocity bias from an annual signal versus data span. Max shows the maximum possible bias (modified from Blewitt and Lavallé(2002)). The bias becomes small after 3.5 years of observation (4.5 yr time-span in one of the minimum bias).

The formal errors were obtained firstly removing the annual signal and then applying the Real Sigma (RS) algorithm implemented in the GLOBK module (Herring, 2003). As a result, to obtain the final velocity solution and an error estimate, the estimated random walk through the RS algorithm was included for each component of the individual station (Reilinger et al., 2006; Shen et al., 2011).

In order to validate the formal errors we compared the resulting uncertainties (from GLOBK) with the uncertainties calculated using the CATS software (Williams, 2008), which uses a Maximum Likelihood Estimation (MLE) method to fit a multi-parameter model to CGPS time series. During this procedure, first we have calculated the spectral index for each station and component and fit it to a power law function:

$$P_x(f) = P_0 \left(\frac{f}{f_0}\right)^k \tag{4.14}$$

where f is the temporal frequency, P_0 and f_0 are normalizing constants and k is the spectral index (Williams et al., 2004 and references therein). White noise is characterized by $k = 0$, random walk by $k = -2$ and flicker noise by $k = -1$. We verified that time-series are affected by white and flicker noise, since the calculated spectral indexes always lie between 0 and -1 (see the example of ALMR station in Figure 4.20). In addition, the power spectrum showed the annual component present in the time series. As a result, we estimate velocity uncertainties using CATS and compare them with the uncertainties obtained by the RS algorithm. The mean difference between the two approaches is 0.05 mm/yr for 25 CGPS stations. The CATS analysis is only applicable for stations with continuous data, i.e. without renames or gaps. The maximum difference is in the North component of CAAL station and because of that, we added random-walk noise in order to equalize.

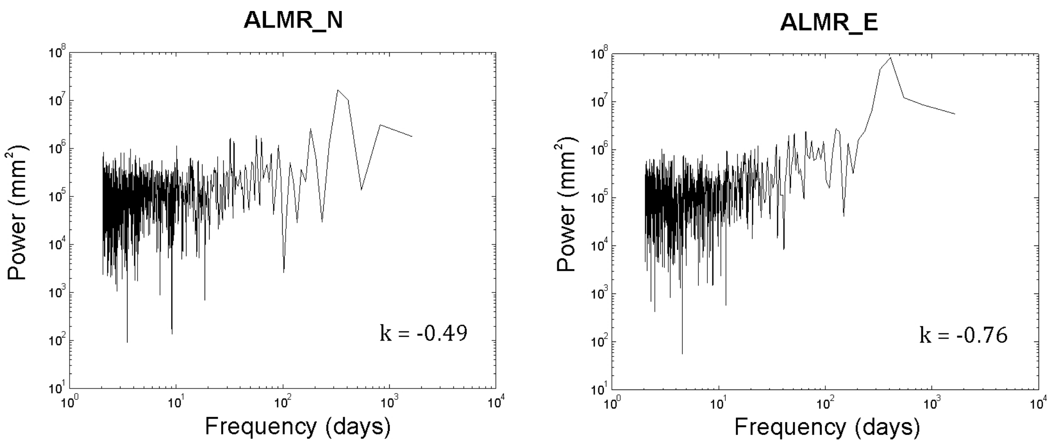

Figure 4.20: Power spectra of N (north) and E (east) components of ALMR CGPS (located in Almeria). k indexes are also indicated (random walk: $k = 0$ and flicker noise: $k = -1$). Note the peak frequency around a year (annual signal).

4.4. Combining velocities

Finally, as an alternative to carrying out a completely new processing of the entire GPS data, we combine the SGPS velocity solutions with CGPS velocities. The combination was done with the program *Velrot,* included in the GAMIT/GLOBK package. This program adjusts two velocity fields into desired frame based on common stations. In this case, we rotate the ITRF2008 CGPS velocity field (System 1) into the western Europe reference frame of the SGPS velocity field (System 2, Figure 4.21). The 23 common sites used in the combination were: ALAC, YEBE, VILL, TETN, SFER, RABT, LAGO, CASC, MAS1, LPAL, PDEL, MATE, GRAZ, POTS, WTZR, ONSA, MEDI, CAGL, TORI, GRAS, TLSE, EBRE and HERS. Common stations are used to transform Sys1 to best match Sys2.

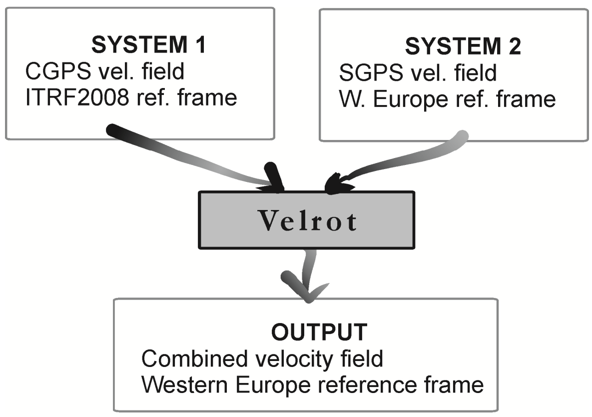

Figure 4.21: Velocities combination schema using Velrot program.

5. Velocity field

This chapter contains a recapitulation of the results and discussion concerning the velocity field in eastern Betics. It has been divided into two main parts corresponding to the different kind of processed data (SGPS and CGPS). The main emphasis is given to the first part, since the CuaTeNeo network velocities are the main results of the thesis. For this reason, during the analysis of the CuaTeNeo results we provide an accurate analysis of the velocities, as well as, strain rate calculation. In the second part, we present the CGPS velocity field, as well as its combination with the SGPS data presented in the first part of this chapter.

5.1. CuaTeNeo velocity field

To derive the velocity field of the CuaTeNeo SGPS stations (see Section 4.2.2 for the detailed processing methodology), we selected a group of CGPS stations used to define the reference frame after considering various sets of stations forming part of the western Eurasia plate. A selection criteria were: horizontal residual velocity less than 0.5 mm/yr and errors less than 0.3 mm/yr. As a result, we derived a set of six GPS stations (identified with stars in Table 5.1 and Figure 5.1) that define our reference frame with a weighted root mean square of 0.17 mm/yr (Figure 5.2). The Euler pole of rotation was calculated at Longitude 97.75±0.52°W and Latitude 54.94±0.75°N with a rotation rate of 0.2603±0.001°/Myr.

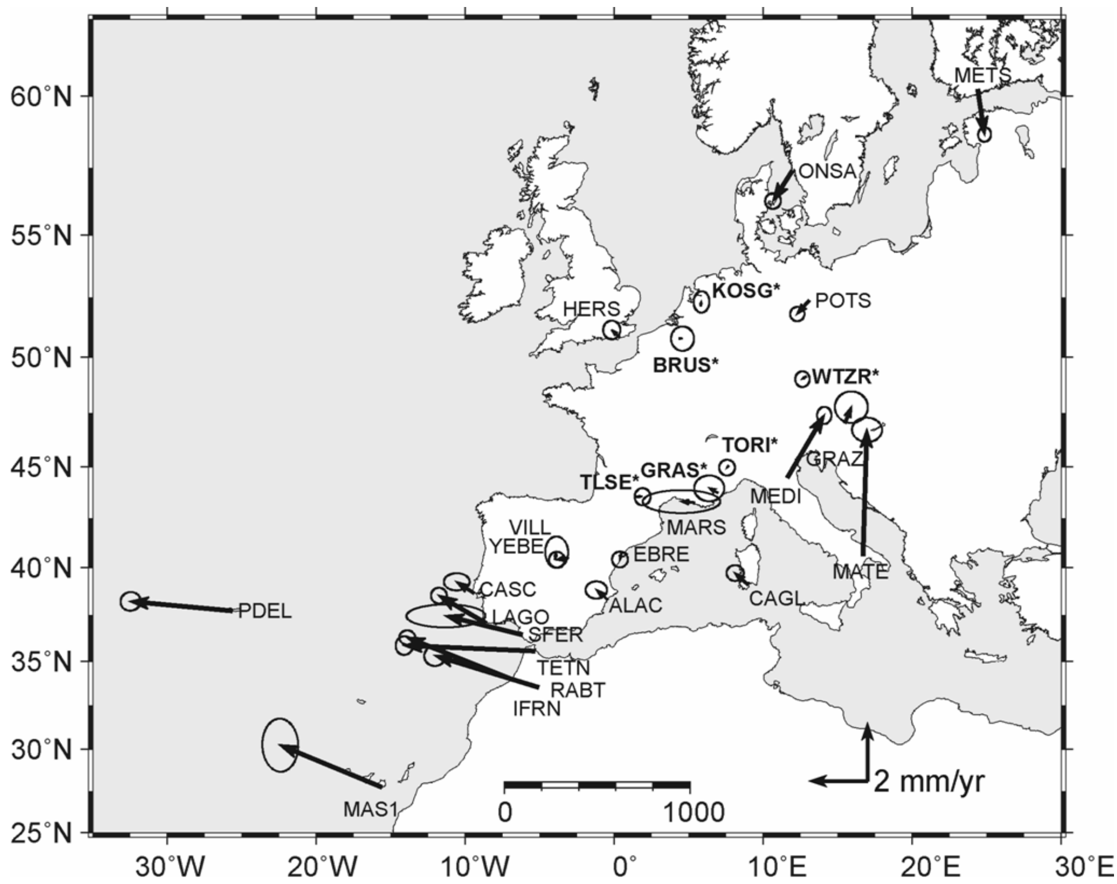

Figure 5.1: Regional map including CGPS stations from Europe and north Africa. Velocities are in the western Europe reference frame, defined by the six stations labeled with asterisks (Table 5.1).

The present-day velocity vectors are shown in Figure 5.3 and Table 5.1. To derive these results, we used an assumption of constant velocities between the five surveys (1997-2011 campaigns). Although this assumption is used commonly when treating the survey style GPS data, one should still be careful when dealing with possible disturbances due to nearby earthquakes or local site instabilities. The velocity field includes the 16 survey style GPS stations (15 CuaTeNeo and CART) and the CGPS station ALME, located in Almeria and belonging to the ERGNSS network of the IGN (www.ign.es). This is the only CGPS station within the study area that had observations comparable to the duration of the CuaTeNeo data (i.e. more than 15 years).

Table 5.1: Horizontal GPS velocities in western Europe reference frame with 1σ uncertainties and correlations (ϱ) between the east (V_e) and north (V_n) components of velocity. V_{Hor} and Az are the horizontal velocity magnitudes and azimuths. Stars (*) indicate CGPS stations used to define the western Europe reference frame (Figure 5.1). Station codes in italics refer to CuaTeNeo stations with a nail type monument (Figure 4.6b). Sites presented in Figure 5.3 are in bold.

CODE	Long. (ºE)	Lat. (ºN)	Ve (mm/yr)	1σ (mm/yr)	Vn (mm/yr)	1σ (mm/yr)	ϱ	V_{Hor} (mm/yr)	1σ (mm/yr)	Az (ºN)
ALAC	359.519	38.339	-0.4	0.2	0.3	0.1	0.009	0.50	0.14	312
CART	358.988	37.587	-0.8	0.3	0.9	0.3	0.015	1.20	0.25	321
MAJA	358.819	37.623	-0.6	0.2	1.3	0.2	0.002	1.40	0.20	335
GANU	358.575	37.658	0.0	0.2	1.3	0.2	0.001	1.27	0.20	1
MONT	358.476	37.439	-0.4	0.2	1.7	0.2	-0.002	1.78	0.19	347
ESPU	358.411	37.870	-0.7	0.2	0.3	0.2	-0.001	0.71	0.20	294
TERC	358.363	37.742	-0.8	0.2	0.0	0.2	0.001	0.82	0.20	269
PURI	358.357	37.538	-0.8	0.2	1.7	0.2	0.000	1.86	0.19	334
PANI	358.302	37.325	-0.4	0.3	0.8	0.3	0.005	0.92	0.26	336
MELL	358.173	37.590	-0.7	0.2	0.2	0.2	0.004	0.73	0.20	287
MOJA	358.144	37.134	-1.3	0.3	1.6	0.3	0.015	2.06	0.27	321
CARB	358.115	37.012	-0.8	0.2	1.4	0.2	0.003	1.57	0.22	329
HUER	358.058	37.346	-0.9	0.3	1.2	0.3	0.008	1.49	0.28	324
RELL	357.941	36.836	-1.0	0.2	1.3	0.2	0.003	1.66	0.19	323
PUAS	357.908	37.395	-1.2	0.2	0.7	0.3	0.018	1.39	0.24	301
CUCO	357.907	37.184	-0.8	0.2	1.0	0.2	0.005	1.33	0.23	321
HUEB	357.769	36.999	-1.8	0.3	0.6	0.3	0.008	1.93	0.25	288
ALME	357.541	36.853	-1.7	0.1	-0.2	0.1	0.003	1.69	0.11	263
YEBE	356.911	40.525	-0.4	0.1	-0.1	0.1	0.002	0.40	0.11	260
VILL	356.048	40.444	0.0	0.2	0.2	0.2	-0.017	0.24	0.22	9
IFRN	354.892	33.540	-3.5	0.2	1.1	0.1	0.015	3.68	0.15	287
TETN	354.637	35.562	-4.4	0.1	0.2	0.1	0.009	4.44	0.12	272
SFER	353.794	36.464	-2.6	0.6	0.6	0.2	0.017	2.67	0.53	284
RABT	353.146	33.998	-3.6	0.1	1.4	0.1	0.003	3.86	0.11	292
LAGO	351.332	37.099	-1.6	0.1	0.9	0.1	0.002	1.83	0.11	300
CASC	350.581	38.693	-0.6	0.3	0.1	0.3	0.000	0.56	0.34	278
MAS1	344.367	27.764	-3.5	0.3	1.4	0.4	-0.023	3.73	0.27	293
PDEL	334.337	37.748	-3.5	0.1	0.3	0.1	0.036	3.47	0.14	275
METS	24.395	60.217	0.2	0.1	-1.5	0.1	0.054	1.54	0.10	171
MATE	16.704	40.649	0.1	0.2	4.3	0.2	-0.016	4.28	0.17	2
GRAZ	15.493	47.067	0.2	0.2	0.5	0.2	-0.003	0.58	0.22	21
POTS	13.066	52.379	-0.4	0.1	-0.5	0.1	0.020	0.60	0.10	222
WTZR*	12.879	49.144	-0.1	0.1	-0.1	0.1	-0.003	0.15	0.10	238
ONSA	11.926	57.395	-0.7	0.1	-1.0	0.1	0.023	1.21	0.11	213
MEDI	11.647	44.520	1.2	0.1	2.1	0.1	0.010	2.45	0.12	30
CAGL	8.973	39.136	-0.4	0.1	0.4	0.1	0.004	0.59	0.12	312
TORI*	7.661	45.063	-0.1	0.1	-0.1	0.1	0.007	0.08	0.11	220
GRAS*	6.921	43.755	-0.3	0.2	0.2	0.2	0.001	0.32	0.20	300
KOSG*	5.810	52.178	0.0	0.1	0.1	0.2	0.021	0.13	0.15	9
MARS	5.354	43.279	-0.4	0.5	0.0	0.2	0.001	0.43	0.54	275
BRUS*	4.359	50.798	0.1	0.2	0.0	0.2	0.004	0.11	0.16	90

TLSE*	1.481	43.561	0.2	0.1	0.0	0.1	0.002	0.21	0.11	87
EBRE	0.492	40.821	-0.1	0.1	-0.3	0.1	-0.006	0.27	0.11	193
HERS	0.336	50.867	-0.3	0.1	0.2	0.1	0.000	0.35	0.12	313

Eastern Betics GPS-derived velocities in a western Europe reference frame are shown in Figure 5.2 and Figure 5.3. The most prominent features are the dominant direction of motion roughly parallel to Nubia/Eurasia convergence and the reduction of motion inland. Coastal stations in the middle of the network have 1-2 mm/yr velocities oriented 329±15º (i.e. NW-NNW), which align well with the convergence direction between Nubia and Eurasia plates (323º±1.8, Figure 5.3) and is predicted by NNR-MORVEL56 (Argus et al., 2011) plate kinematic model. Within this group (Figure 5.2), some stations exhibit small anomalous behavior, such as GANU (northward motion) and PANI (slower motion than the other coastal stations). Three GPS sites located west of Alhama de Murcia fault (ESPU, TERC and MELL) show the lowest velocities (<1 mm/yr) with a more westerly orientation (Figure 5.3). The same sense of motion is present for two stations in the southern part (ALME and HUEB), but with twice as much velocity.

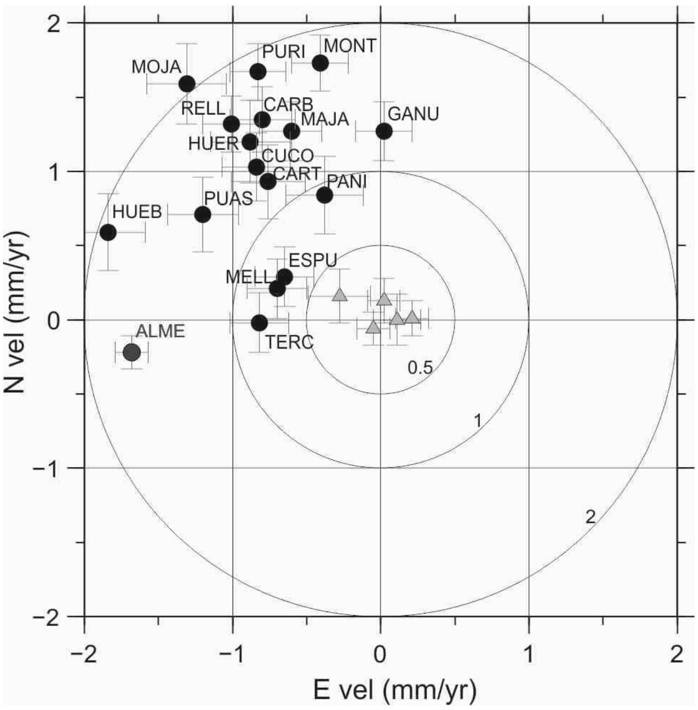

Figure 5.2: East and North component velocities in western Europe reference frame. CuaTeNeo sites and ALME are shown as black circles. CGPS sites used to define the reference frame (sites with asterisk in Table 5.1) are shown as grey triangles. Error bars represent 1σ uncertainties.

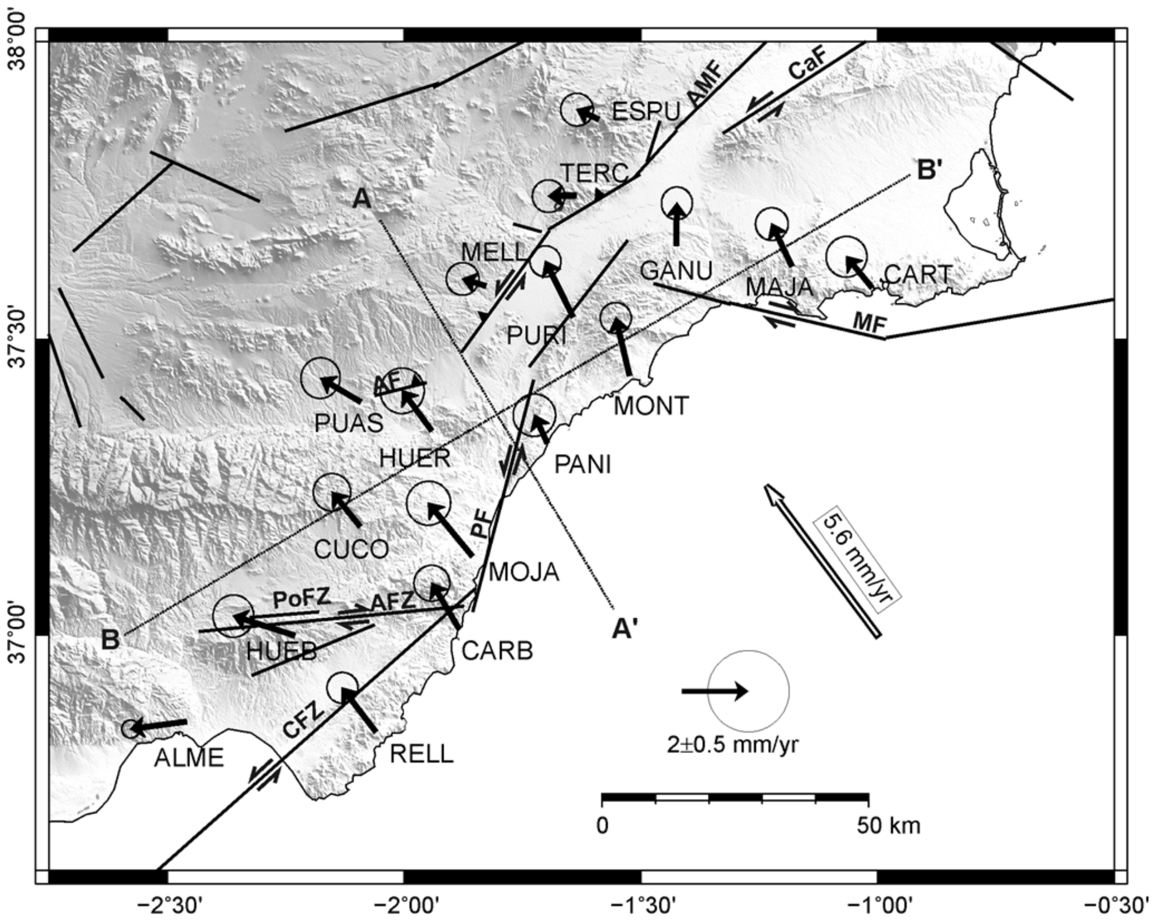

Figure 5.3: CuaTeNeo GPS velocities in western Europe reference frame with 95 % confidence error ellipses. Plate convergence velocity from NNR-MORVEL56 model (Argus et al., 2010). Transects A-A' and B-B' are velocity profiles shown in Figure 5.4. Abbreviations are: CaF - Carrascoy fault; AMF - Alhama de Murcia fault; AF - Albox fault; PF - Palomares fault; CFZ - Carboneras fault zone; MF - Moreras fault: AFZ - Alpujarras fault zone; PoFZ - Polopos fault zone.

5.1.1. Discussion

Judging by the fact that the majority of the stations move roughly parallel to the direction of convergence of Nubia and Eurasia plates (Figure 5.3), we conclude that the interaction of these tectonic plates provides the main driving force responsible for the ongoing crustal deformation in the region. As expected, the observed velocities reach their highest values along the coast, with a maximum rate at MOJA of ~2 mm/yr. This value represents approximately 1/3 of the overall convergence rate (5.6 mm/yr) between the two plates calculated from NNR-MORVEL56 (Argus et al., 2011). The remainder of this convergence occurs within the wide deformation zone that includes the Alboran Sea and the Rif mountains. Judging by elevated rates of seismicity (Figure 3.7) and geodetic studies in the Rif (e.g. Tahayt et al., 2008), we consider the bulk of the missing 3 to 4 mm/yr of deformation is most likely concentrated in northern Africa.

Directly comparing our velocity field with other published velocities is difficult because no work has been published with detailed results of GPS crustal deformation within the study area. Also, although there have been some publications with a more regional emphasis that included some continuous GPS velocities within the study area (Pérez-Peña et al., 2010; Koulali et al., 2011; Palano et al., 2013), as a rule, these velocities where characterized by large uncertainties, often exceeding the presented velocity values. Hence, a statistically meaningful comparison of these results is not useful. Nevertheless, in general terms, our results are consistent with previous studies, where the velocities within the EBSZ range between 1-3 mm/yr with respect to Eurasia.

Comparing the orientation of the 17 velocity vectors and the plate convergence azimuth predicted by the NNR-MORVEL56 model at 1ºW, 37ºN, three main groups of stations with approximately homogenous sense of motion can be identified (Figure 5.3):

i) The first group of 12 stations that move parallel to the Nubia/Eurasia convergence direction, with the rates ranging from 1 to 2 mm/yr. In this group, there are several stations that exhibit small anomalous behavior. For example, station PUAS is moving in a more westward direction than the dominant motion of the group, especially compared to the nearest station HUER located close to Huércal-Overa. This motion could be caused by the proximity to the Albox fault (AF) or the horse-tail termination of the AMF. Station PANI, located at the beach of Cala Panizo, moves considerably slower than the neighboring coastal stations (<1 mm/yr). This behavior can be real, although we suspect that the instability of the monument and/or observational errors is the cause of this anomalously slow movement. PANI station marker is a nail type monument (Table 4.1), located in highly fractured rock that can easily suffer local disturbance. Finally, stations GANU and MONT move more northward, deviating from the dominant convergence direction. This motion could be related to Palomares fault (PF) or other minor faults in the area.

ii) The second group is formed by three stations: ESPU, TERC and MELL, which are located on the west side of the AMF. This group is characterized by the smallest velocities and suggests that they belong to a stable part of Iberia. However, the observed minor westerly component of motion at these three stations, indicate they still contain some residual motion that can be attributed to the continuing tectonic activity of the AMF or other faults to the north (e.g. Crevillente). See Chapter 6 for more details.

iii) The third group contains 2 stations: ALME and HUEB, which are located in the SW corner of the network and exhibit a clearly more westerly motion than the rest of the stations. Similar direction of motion has also been detected for stations located farther to the west, that fall outside the study area (Vernant et al., 2010; Palano et al., 2013). This change in the observed velocity orientations will be discussed in details in Chapter 7.

5.1.2. Velocity profiles

The obtained horizontal velocities are plotted parallel and perpendicular to the dominant velocity direction (N329º), which roughly coincides with plate convergence direction (Figure 5.4). Profile A-A' shows -0.015±0.005 (mm/yr)/km of shortening, equivalent to -15±5 nstrain/yr (Figure 5.4). This strain rate indicates a faster movement of the coastal stations relative to the inland stations, resulting in a compression. The highest variation in velocities is observed near Alhama de Murcia fault (AMF). We will concentrate on this region in Chapter 6. The strain rate along the coastal profile B-B' is statistically insignificant at 1σ level: 2±3 nstrain/yr, indicating that no differential motion along the coast can be detected for the observed time period (Figure 5.4). In the calculation of the linear trends for the above profiles, we have excluded stations belonging to the third group (ALME and HUEB), since they clearly exhibit a different sense of motion (especially in B-B' profile).

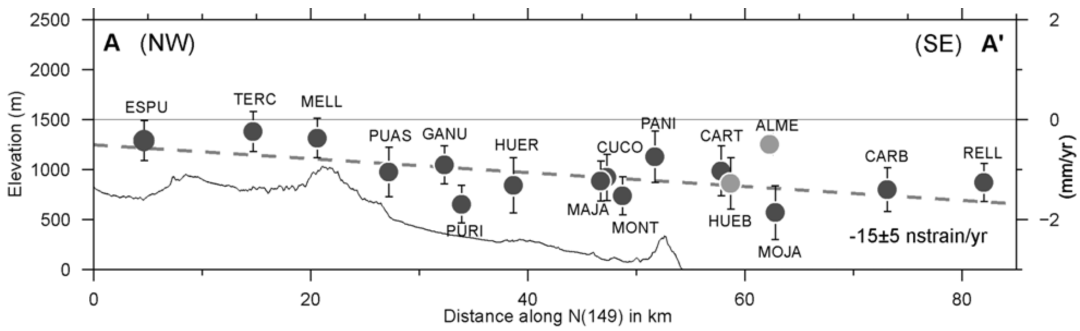

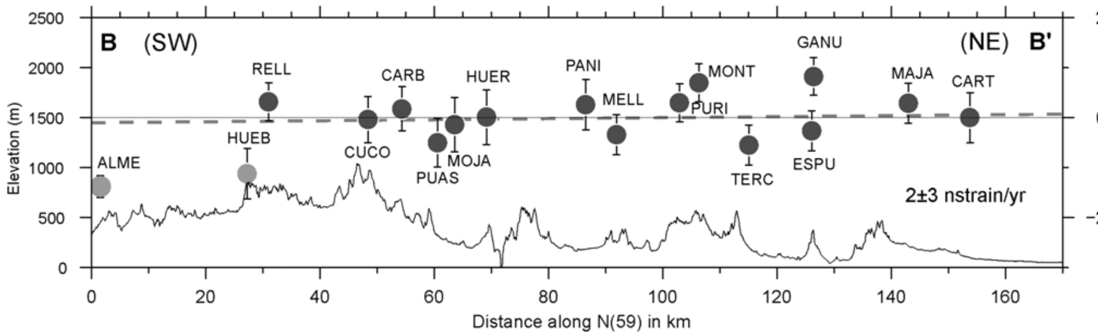

Figure 5.4: Projected parallel (A-A') and perpendicular (B-B') velocities to plate motion direction (Figure 5.3) with 1σ uncertainties (vertical error bars). The irregular line on the bottom shows the topography along the corresponding profile, with a vertical exaggeration of 1:9 and 1:17 for A-A' and B-B', respectively. *Top)*

Profile A-A' along the direction of plate motion and predominant velocity (N149º). *Bottom)* Profile B-B' along the coast, N59º, perpendicular to the A-A' profile. ALME and HUEB, plotted in light grey, have been excluded in slope estimate.

5.1.3. Strain rate calculation

We calculated strain rate parameters using the estimated velocities for the 15 CuaTeNeo stations plus CART and ALME using the SSPX software package (Cardozo and Allmendinger, 2009). We used the grid-nearest neighbor approach that computes strain rate at the center of each square (see Section 2.1.2 for more details). The following optimal parameters were chosen for the strain calculation: a grid spacing of 10 km and the six nearest stations located within a distance of 50 km. These parameters ensure small local variations and avoid smoothed regional patterns, since the strain field is not homogeneous throughout the area. The horizontal principal strain rate axes ($\dot{\varepsilon}_{max}$ and $\dot{\varepsilon}_{min}$) and dilatation are shown in Figure 5.5a. Figure 5.5b shows maximum shear strain rates ($\dot{\varepsilon}_{sh-max}$) and their directions. Only significant values at 1σ level are presented. A convention of positive strain rates indicating extension is used.

The absolute values of the calculated strain rates show the $\dot{\varepsilon}_{min}$ are usually greater than $\dot{\varepsilon}_{max}$. The maximum shortening rate equals $\dot{\varepsilon}_{min} = -49\pm5$ nstrain/yr while the maximum extension rate ($\dot{\varepsilon}_{max}$) is 29±8 nstrain/yr at 1σ level (Figure 5.5a). The orientation of shortening and extension axes is mostly NNW-SSE and ENE-WSW, respectively, as expected from Nubia/Eurasia plate convergence. The highest shortening rates are located in the northern sector (around AMF-PF and Cartagena), which decrease significantly towards the south, where an extensional tectonics becomes dominant. The maximum shear strain rate ($\dot{\varepsilon}_{sh-max}$) is a measure of a maximum change in the angle between two line segments that were orthogonal in the undeformed state (Turcotte and Schubert, 1982). Maximum values of $\dot{\varepsilon}_{sh-max}$ are obtained around the AMF zone (65±9 nstrain/yr at 1σ level) indicating tectonic activity (Figure 5.5b and 2.4). Furthermore, the orientation of the left-lateral shear planes of $\dot{\varepsilon}_{sh-max}$ in this region (~210°N) is in good agreement with the strike of the AMF (~225°N).

Summing the shortening and extensional rates and assuming a constant volume we can compute a 2D dilatation rate. A negative value of dilatation indicates an excess of shortening in the horizontal plane and requires vertical thickening to maintain constant volume. On the contrary, when the dilatation is positive, we get an excess of extension and vertical thinning is required to maintain constant volume (Allmendinger et al., 2007). The calculated 2D dilatation rates show only two areas where statistically significant results at 1σ level are present (Figure 5.5a). On the one hand, the area in the NE part shows negative dilatation rates, which remain significant at 2σ level. On the other hand, in the SW part, the dilatation rates are positive but less robust since they are statistically insignificant at 2σ level. In terms of calculated rates, the maximum thickening in the NE area is -44±12 nstrain/yr, and the maximum thinning in SW is 16±15 nstrain/yr.

In terms of the rotation rates, a clear dominance of the counterclockwise rotation (CCW) is observed in most of the study area (Figure 5.5c). The highest rotation rates are seen near the AMF-PF left-lateral faults in the north and CFZ in the south-west. The CCW rotation rates range between 1.25±0.04°/Myr to 0.07±0.05°/Myr at 1σ level, assuming a constant rate through time.

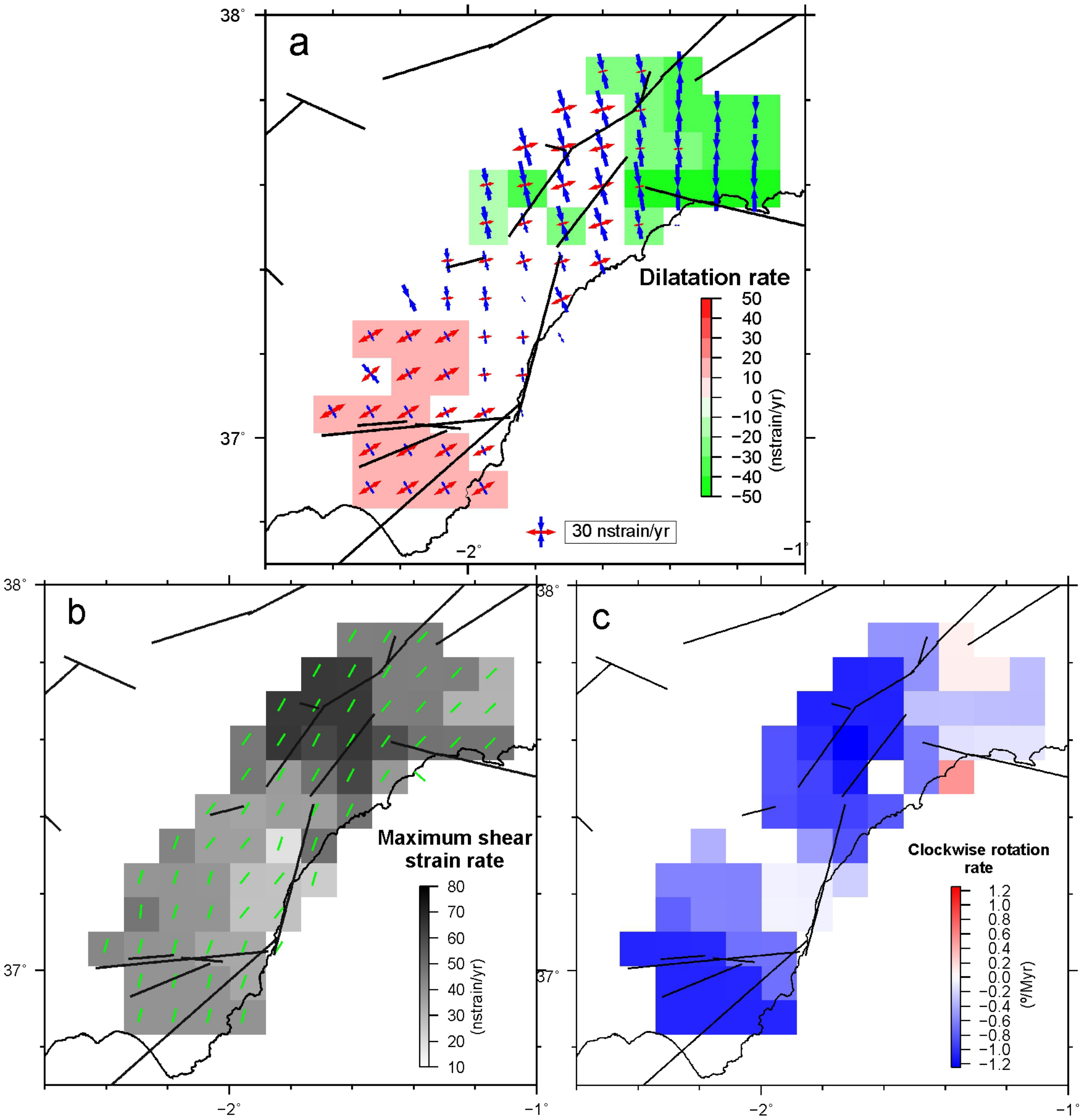

Figure 5.5: GPS strain-rate field computed over 10 km grid spacing with the 6 nearest neighbor method using SSPX software (Cardozo and Allmendinger, 2009). Only statistically significant values at 1σ level are shown. a) Principal infinitesimal horizontal strain rate axes: $\dot{\varepsilon}_{min}$ in dark convergent arrows; $\dot{\varepsilon}_{max}$ in lighter divergent arrows. Grid coloring indicates 2D dilatation rates, where red extension and green compression. b) Maximum shear strain rates ($\dot{\varepsilon}_{sh-max}$) represented by grey shaded square grids. Left-lateral planes orientations

are shown in green. c) Rotation rate values in red indicate clockwise rotation (CW) and blue indicate counterclockwise rotation (CCW).

The orientation and magnitude of the principal strain rate axes obtained by the inversion of the GPS data are in agreement with the previous studies (Palano et al., 2013) that calculate the strain tensor for the Gibraltar Arc area. Principal strain rates and dilatations (Figure 5.5a) indicate two distinct zones of significant deformation but opposite behavior. The NE sector, with $|\dot{\varepsilon}_{min}|>|\dot{\varepsilon}_{max}|$ and negative 2-D dilatation, is coherent with a convergent regime. Maximum shear strain values are also observed in this region (Figure 5.5b), indicating the presence of a transpressive regime, expressed by reverse and left-lateral faults (e.g. AMF). The SW sector around Almeria, presents the opposite situation, with a $|\dot{\varepsilon}_{max}|>|\dot{\varepsilon}_{min}|$ and, to a lesser extent, positive 2-D dilatation, consistent with active normal faulting. On a larger scale, this behavior is also consistent with the geodynamic scenarios proposed for the Betic evolution in this area, which includes a SW motion due to a rollback subduction (e.g. Gutscher et al., 2012) and/or delamination process (e.g. Calvert et al., 2000; Mancilla et al., 2013). We observe the sector between these two zones with significantly less internal deformation (i.e. dilatation), although individual points move with significant velocities. This zone can be interpreted as a rigid block that translates to the N-NW, where the majority of strain is accommodated on the AMF.

The $\dot{\varepsilon}_{min}$ axes in the northern area rotate from NNW-SSE in the AMF zone to N-S in the Cartagena area where extension axes are insignificant, indicating uni-axial N-S convergence. This type of convergence would suggest reverse fault kinematics for the Moreras fault (MF) (Figure 5.3) located in this region, contradicting the description provided by the QAFI geological database (García-Mayordomo, 2005; García-Mayordomo and Jiménez-Díaz, 2010) where the MF is characterized by a normal/dextral motion. More regional studies of the earthquake focal mechanisms, however, suggest a N-S compression for this region (Henares et al., 2003). It should be mentioned that our strain rate calculation for the region is based over an irregular distribution of GPS stations. In the NE part of the network the stations are arranged linearly, forming an E-W trend, and no data are available to the south (Alboran Sea) or to the north. Hence, further investigation of the Moreras fault is necessary.

The counter-clockwise (CCW) rotation calculated from the GPS velocities is in agreement with the general trends of paleomagnetic rotation rates computed in the eastern Betics Internal Zone (e.g. Calvo et al., 1997; Mattei et al., 2006). This CCW motion has been attributed to the presence of left-lateral faults (e.g. Calvo et al., 1997). Indeed, the maximum rotation rates, calculated from our GPS field, coincide with the left-lateral strike slip faults AMF and PF in the north and CFZ in the south-west.

5.2. Combined velocity field

5.2.1. CGPS velocity field

We obtained a CGPS velocity field by analyzing daily records of the continuously recording GPS stations spanning a time period from 2008.8-2013.3 (conditioned by the GATA data availability). As we mentioned in Section 4.3, 25 CGPS stations are located in eastern Betics area and the correspondent velocities are provided in Table 5.2 and Figure 5.6. For the subsequent combination with the CuaTeNeo velocity field (Section 4.4), the CGPS velocity vectors were obtained in the ITRF2008 global reference frame (note the difference in magnitude of the velocity vectors with Table 5.1, in a western Europe reference frame).

Table 5.2: Horizontal GPS velocities in ITRF2008 frame with 1σ uncertainties and correlations (ϱ) between the east (V_e) and north (V_n) components of velocity. V_{Hor} and Az are the horizontal velocity magnitudes and azimuths. Velocities for the 25 CGPS located in Figure 5.6

CODE	**Long. (ºE)**	**Lat. (ºN)**	**Ve (mm/yr)**	**1σ**	**Vn (mm/yr)**	**1σ**	**ϱ**	**V_{Hor} (mm/yr)**	**1σ**	**Az (ºN)**
ALAC	-0.481	38.339	19.5	0.2	16.6	0.2	0.009	25.61	0.18	50
TORR	-0.681	37.975	19.6	0.1	17.1	0.1	0.004	26.04	0.14	49
ALCA	-0.861	37.731	19.9	0.1	17.4	0.1	0.003	26.47	0.12	49
ABAN	-1.054	38.175	19.2	0.2	17.9	0.2	0.005	26.24	0.17	47
MURC	-1.123	37.99	19.7	0.1	17.0	0.1	0.003	25.99	0.11	49
MRCI	-1.125	37.992	19.7	0.1	17.2	0.2	0.003	26.09	0.14	49
PILA	-1.289	38.254	19.0	0.1	17.7	0.1	0.003	25.96	0.13	47
MAZA	-1.31	37.593	19.2	0.1	18.3	0.1	0.006	26.5	0.14	46
JMIA	-1.327	38.471	19.2	0.3	16.2	0.2	0.004	25.12	0.25	50
MULA	-1.449	38.041	18.9	0.1	16.7	0.1	0.003	25.2	0.13	48
CRVC	-1.869	38.115	18.7	0.2	16.6	0.4	0.002	25.02	0.3	48
AREZ	-1.94	37.835	18.6	0.1	16.8	0.1	0.005	25.03	0.13	48
HUOV	-1.942	37.402	19.2	0.1	17.1	0.1	0.005	25.72	0.13	48
CARA	-1.968	38.046	18.8	0.2	16.0	0.2	0.011	24.64	0.16	50
MORA	-1.999	38.248	19.2	0.2	16.5	0.2	0.003	25.29	0.18	49
GATA	-2.061	36.835	19.1	0.1	17.9	0.1	0.007	26.14	0.14	47
ALMR	-2.441	36.863	18.2	0.1	16.9	0.1	0.005	24.79	0.14	47
ALME	-2.459	36.852	18.5	0.1	16.4	0.1	0.004	24.72	0.13	48
CAAL	-2.548	37.221	18.8	0.2	16.6	0.3	0.002	25.08	0.23	48
VIAR	-3.013	38.168	18.4	0.1	16.0	0.2	0.006	24.35	0.13	49
TGIL	-3.303	38.034	18.7	0.1	16.3	0.1	0.005	24.8	0.12	49
NEVA	-3.386	37.063	18.2	0.2	16.0	0.1	0.002	24.25	0.15	49
MOTR	-3.521	36.755	16.9	0.1	15.2	0.1	0.006	22.76	0.13	48
PALM	-3.562	36.809	17.3	0.1	15.4	0.1	0.005	23.1	0.12	48
UJAE	-3.782	37.788	18.1	0.1	16.7	0.3	0.004	24.62	0.19	47

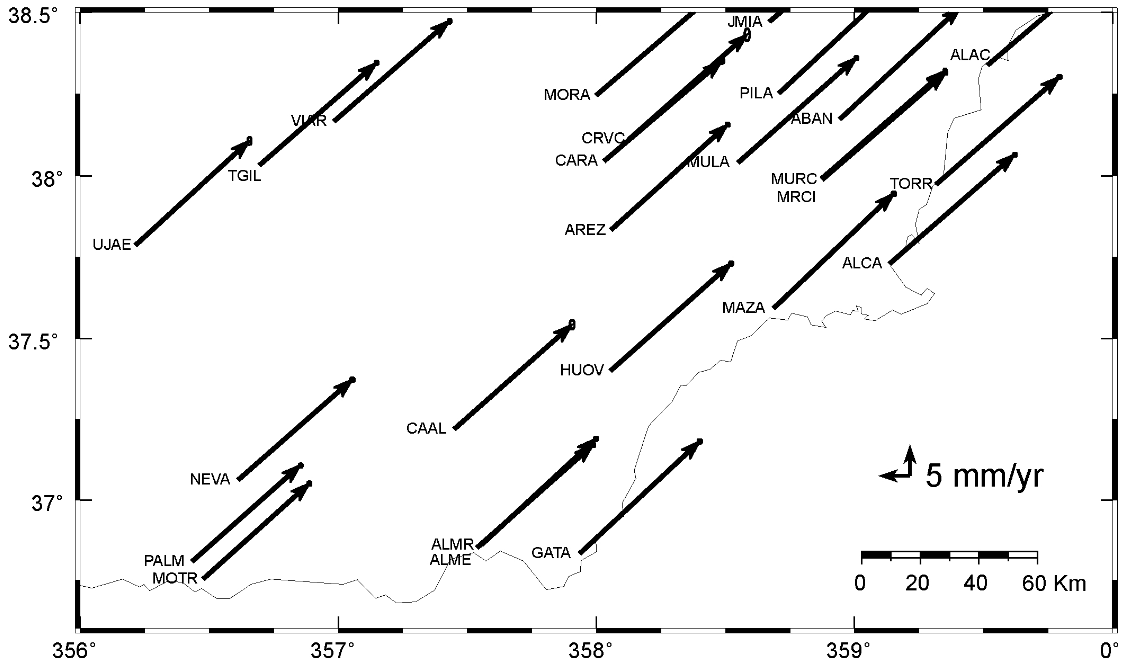

Figure 5.6: Velocities of CGPS sites in ITRF2008 reference frame with 95% confidence error ellipses.

5.2.2. Combination of SGPS and CGPS velocities

The previously CuaTeNeo velocity field obtained from 1997-2011 data observations was combined with the CGPS velocity field obtained from data processed during 2008-2013. The combination was done with *Velrot* from the GAMIT/GLOBK package (see Section 4.4). The final reference system was the western Europe used in Section 5.1. Thus, the CGPS velocities were rotated into the SGPS reference frame. The resulting average rms of the combination is 0.28 mm/yr, indicating a good adjustment. For the common stations that were present in both velocity fields, we choose the CGPS velocities, processed daily for a 4.5 yr time period and with a major errors than the SGPS velocities (conservative option). The difference between the velocities of the common sites is insignificant (Figure 5.7).

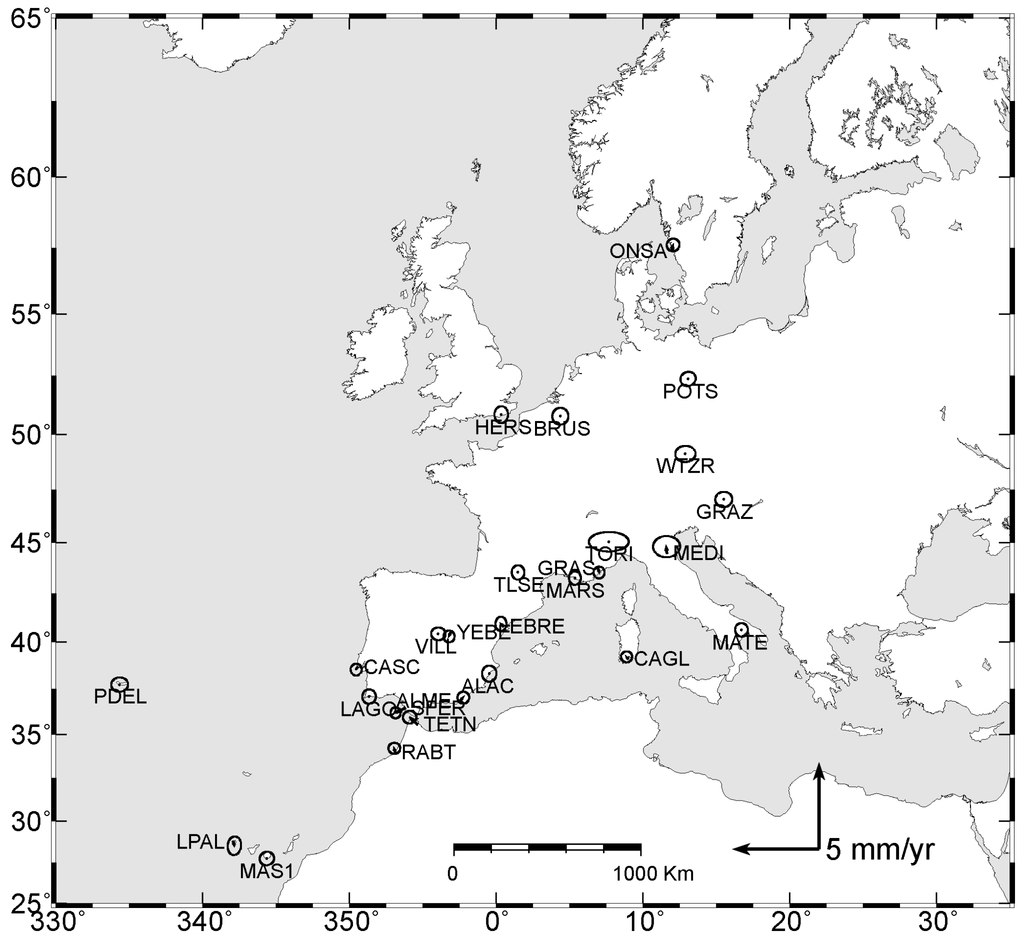

Figure 5.7*:* Differences between the velocities of the common sites used in the combination step (CGPS and SGPS velocity fields) with 95% confidence error ellipses.

The velocity combination of the SGPS and CGPS velocity fields provides a higher spatial coverage, especially to the north of the CuaTeNeo network and to the west of the CFZ area. As can be seen in Figure 5.8 the CGPS data available in the CuaTeNeo area is scarce, so the analysis and discussion presented in the previous section is not affected.

The velocity combination has been done with two main purposes: *i)* to include the GATA CGPS station and to expand the area near the Carboneras fault zone, as we have seen a significant velocity variation; *ii)* to have a complete coverage of the EBSZ and the main faults described in Section 3.1 with the aim of determining the geodetically active faults and to have a broader overview of the eastern Betics. Because of that, an extended description and interpretation of this velocity field can be found in Chapters 7 and 8.

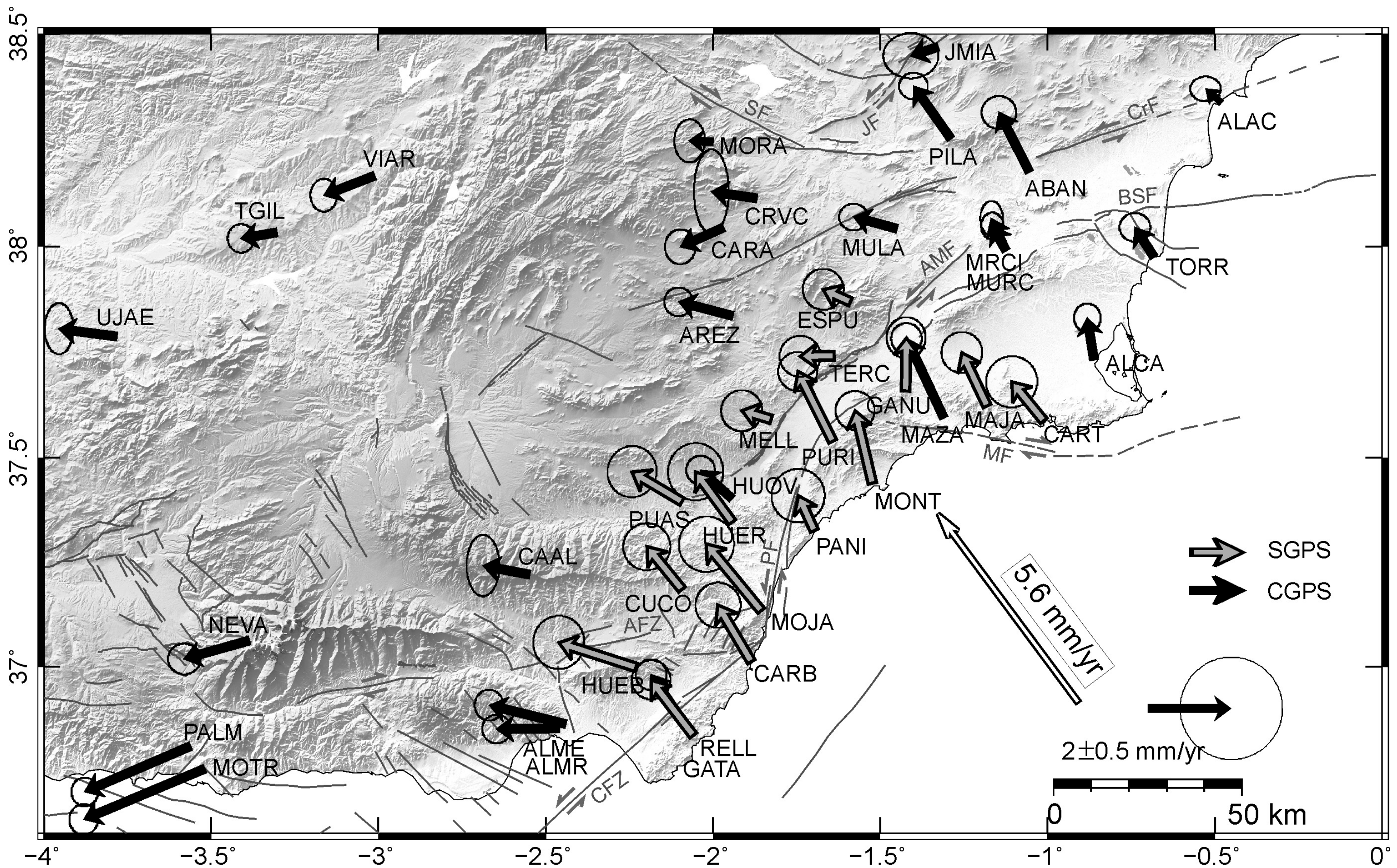

Figure 5.8: Combined SGPS and CGPS velocity field in western Europe reference frame with 95% confidence ellipses. Plate convergence velocity from NNR-MORVEL56 (Argus et al., 2011). In gray velocities from CuaTeNeo network, in black CGPS stations. Abbreviations are: SF - Socovos fault; JF - Jumilla fault; CrF - Crevillente fault; BSF - Bajo-Segura fault; CaF - Carrascoy fault; AMF - Alhama de Murcia fault; AF - Albox fault; PF - Palomares fault; CFZ - Carboneras fault zone; MF - Moreras fault; AFZ - Alpujarras fault zone.

6. Alhama de Murcia fault

In this chapter, we focus our studies on the Alhama de Murcia and Palomares fault system (AMF-PF). The local geology, tectonics, seismicity (e.g. 2011 Lorca earthquake) and our strain rate field (see Section 5.1.3) suggest that the bulk of the observed crustal deformation is concentrated here. As we detected in the previous chapter, the maximum values of $\dot{\varepsilon}_{sh-max}$ and $\dot{\varepsilon}_{min}$ are observed in this area.

6.1. Velocity field

Horizontal velocities of the 6 nearest CuaTeNeo sites to AMF-PF system are shown in Figure 6.1 and Table 6.1. These velocities represent an inter-seismic phase of deformation averaged over the 15 years of SGPS observations. As we noted in the previous chapter, the area around Alhama de Murcia and Palomares faults is characterized by the highest shortening and shear strain rates within the study area, as well as, by a significant change in magnitude and orientation of the velocities in the NW block of AMF versus the SE block of PF (Figure 6.1).

Table 6.1: Horizontal GPS velocities (Figure 6.1) in western Europe reference frame with 1σ uncertainties and correlations (ϱ) between the east (V_e) and north (V_n) components of velocity. V_{Hor} and Az are the horizontal velocity magnitudes and azimuths.

CODE	Long. (ºE)	Lat. (ºN)	Ve (mm/yr)	1σ	Vn (mm/yr)	1σ	ϱ	V_{Hor} (mm/yr)	1σ	Az (ºN)
GANU	358.575	37.658	0.0	0.2	1.3	0.2	0.001	1.27	0.20	1
MONT	358.476	37.439	-0.4	0.2	1.7	0.2	-0.002	1.78	0.19	347
ESPU	358.411	37.870	-0.7	0.2	0.3	0.2	-0.001	0.71	0.20	294
TERC	358.363	37.742	-0.8	0.2	0.0	0.2	0.001	0.82	0.20	269
PURI	358.357	37.538	-0.8	0.2	1.7	0.2	0.000	1.86	0.19	334
MELL	358.173	37.590	-0.7	0.2	0.2	0.2	0.004	0.73	0.20	287

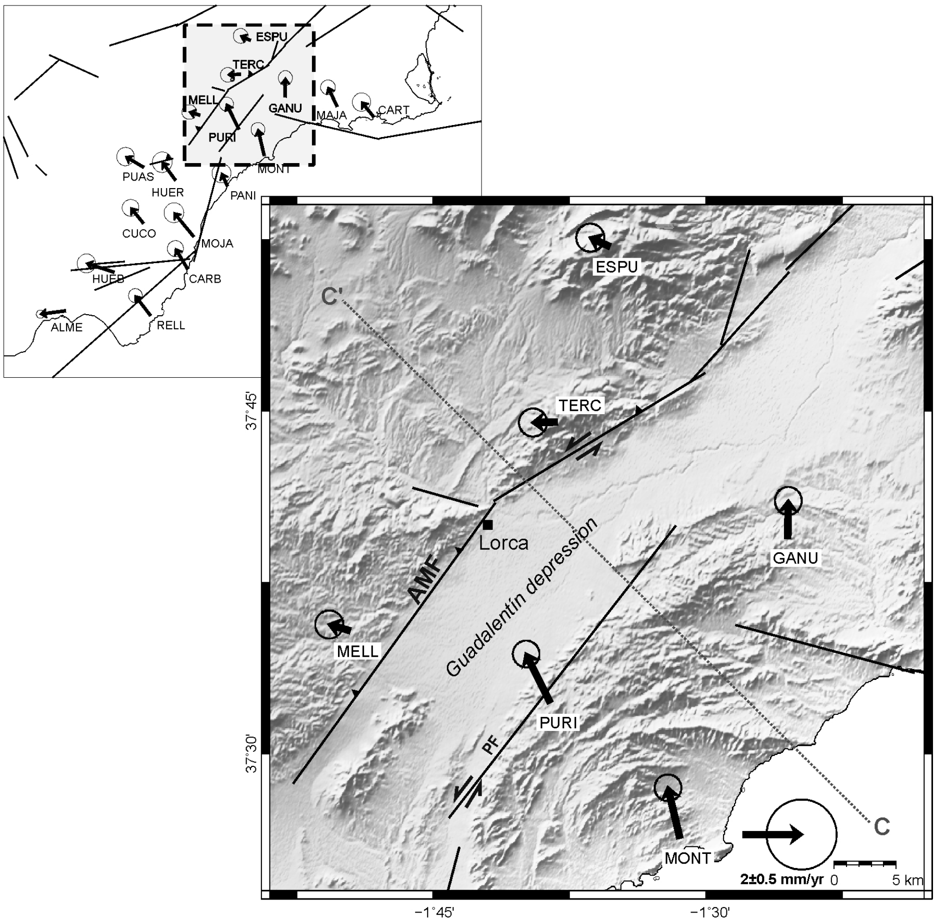

Figure 6.1: Detailed inter-seismic GPS velocities of the AMF–PF zone. See Figure 6.2 for the projected velocities along the C-C' profile. The inset indicates the area enlarged over the CuaTeNeo velocities with 95% confidence ellipses.

6.1.1. Velocity profile

In order to determine a fault slip-rate we chose an AMF normal profile (C-C') with a strike of N315°E (Figure 6.1). Our goal is to quantitatively measure differential motion between the two groups of stations. We estimated a slope by linear regression for each group separately (NW and SE block stations), instead of performing linear fit for all six stations. This way we calculated offsets between the two groups (Figure 6.2), which we interpret as geodetically estimated slip rate for the AMF (and PF). It is important to keep in mind that this analysis does not include the NE segment of the AMF.

In the C-C' profile, we decomposed and projected the profile parallel and perpendicular velocities. We detect statistically significant (at 1σ level) differential motion between the two groups in both components as a velocity offset (ΔV_c and ΔV_{ss}). The calculated slopes for each group of stations are essentially flat, indicating that each group of stations is on a rigid block, without any significant strain rate accumulation. The profile parallel velocity component (i.e. AMF perpendicular) indicates a compression rate of **ΔV_c = 0.8±0.4 mm/yr** in N315°E direction between the SE and NW blocks (Figure 6.2). The offset calculated for the profile perpendicular velocity component ("strike-slip") is **ΔV_{ss} = 1.3±0.2 mm/yr** (Figure 6.2). The comparison of these two offsets indicates the dominance of the left-lateral strike-slip kinematics with an approximate ratio of 60% vs. 40%. Summing both components by trigonometry, the total horizontal slip rate is **1.5±0.3 mm/yr** with an azimuth of N12°E with respect to the northwestern block.

These offsets are calculated for a swath of ~12 km width that encompasses the two important faults: AMF and PF. Currently, the relative partitioning of deformation between these two faults cannot be determined, since no measurements are available within the area separating the two faults. Nevertheless, we think that the bulk of the measured offset comes from the AMF, which presents considerably higher seismicity (instrumental and historical) than the PF and has more geologic evidence of quaternary activity (Martínez-Díaz et al., 2012b).

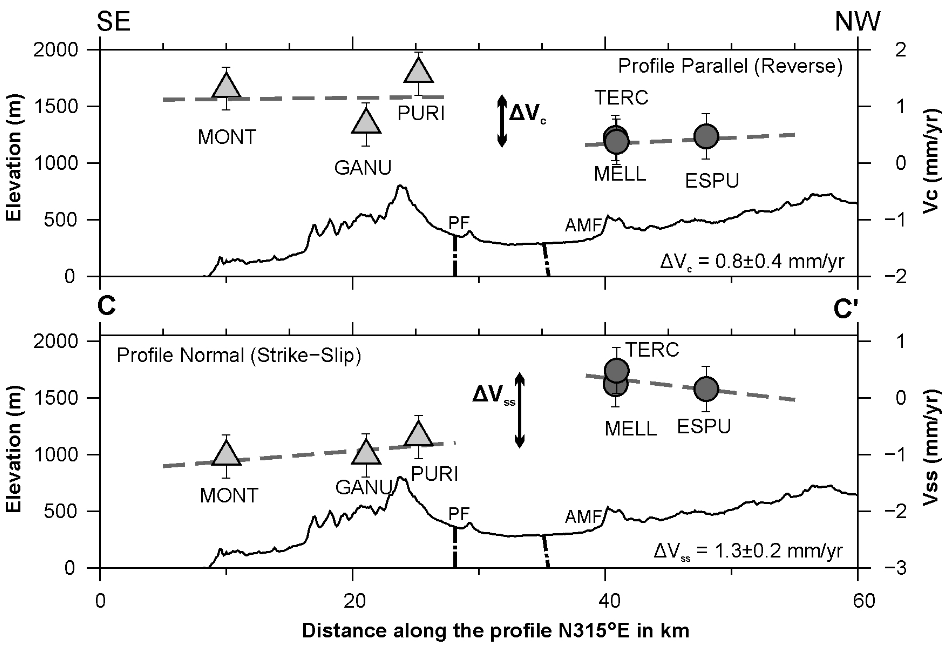

Figure 6.2: C-C' profile (azimuth N315°E) parallel and normal velocities with 1σ uncertainties (vertical bars). Location of the profile is shown in Figure 6.1. Dashed straight lines show linear regression fit for the individual group of stations, used to estimate the offsets. Topography is represented with an irregular line with a vertical exaggeration of 1:9. Stations on the NW side of the AMF are plotted as triangles and as circles on the SE side. The intersection with the AMF and PF are shown as short vertical lines on the bottom. *Top)* Profile parallel (AMF normal) velocities. ΔV_c is the compressive differential motion (velocity offset) between the two blocks. *Bottom)* Profile normal (AMF parallel) velocities. ΔV_{ss} is the strike-slip differential motion between the two blocks.

6.2. The Lorca 2011 earthquake

Two weeks after the occurrence of the Lorca earthquake, the UB group organized a special post-event campaign of the CuaTeNeo sites located near the epicenter of the earthquake (see Section 4.2.1.1). The main objective of the campaign was to detect possible co-seismic and/or post-seismic deformation related to the event.

The nearest stations to epicenter are the SGPS TERC, in Sierra la Tercia, and two CGPS stations located in the city of Lorca, identically named. For distinctions, we renamed LORC station of the Meristemum network as LRCA (Figure 6.3). Both stations, and specially LRCA, are located in the Guadalentín basin.

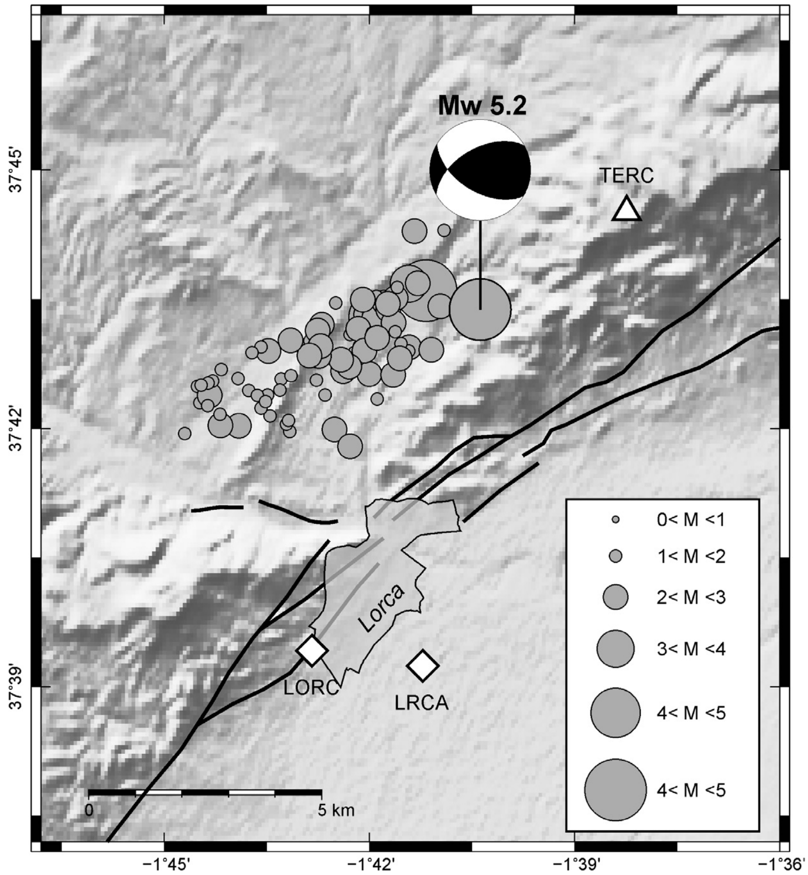

Figure 6.3*:* Detailed zoom of the Lorca area. The focal mechanism of the main 2011 Lorca earthquake and its aftershock seismic sequence are taken from López-Comino et al. (2012). The location of LORC, LRCA and TERC GPS stations are shown. Fault trace from QAFI database(Martínez-Díaz et al., 2010).

6.2.1. GPS co-seismic signal

The continuous station LORC (belonging to REGAM network, see Section 4.3.1), located closer to the AMF, is installed on the roof of a fire station building. The antenna is screwed to a steel mast, with a base of a concrete cube of 0.5 m side, integral with the structure (Figure 6.4). Structural damage due to earthquake were significant, affecting the antenna (pers. comm. Ramon Pablo Garcia of the Region de Murcia). During the occurrence of the earthquake, the station was not operational, so no data was recorded.

Figure 6.4: Pictures of LORC and LRCA CGPS stations. *Left)* LORC antenna (from www.cartomur.imida.es/regam/lorca.htm). *Right)* Building where LRCA station is located and zoom of the antenna (www.gps.medioambiente.carm.es/).

The continuous LRCA station (Meristemum network) is located on the roof of a one-story house (Figure 6.4). The station was installed in 2006 but until 2008 there are no data since the location was changed. This station was recording during the earthquake. It must be pointed out, that already before the occurrence of the Lorca earthquake, the analysis of the LRCA data from 2008 has indicated a highly anomalous behavior at this site, most likely due to the instability of the building caused by a local subsidence.

Specifically, we have estimated that the LRCA CGPS station was subsiding with a rate of ~95 mm/yr and moving horizontally (an order of magnitude faster and in the opposite directions that the surrounding stations) in a velocity that shows a clearly non-tectonic origin (Figure 6.5). In fact, González and Fernández (2011) reported before the earthquake, based on InSAR analysis, an important subsidence rate at the sedimentary basin of about 100 mm/yr due to intensive groundwater extraction. This rate of subsidence is two orders of magnitude higher than the expected tectonic signal and is more than sufficient to be detected by the campaign observations. Nevertheless, the CuaTeNeo GPS stations have not shown any appreciable subsidence at any of its stations. This is not surprising, since all of the network monuments were installed in bedrock and the observed subsidence takes place within the sedimentary basin.

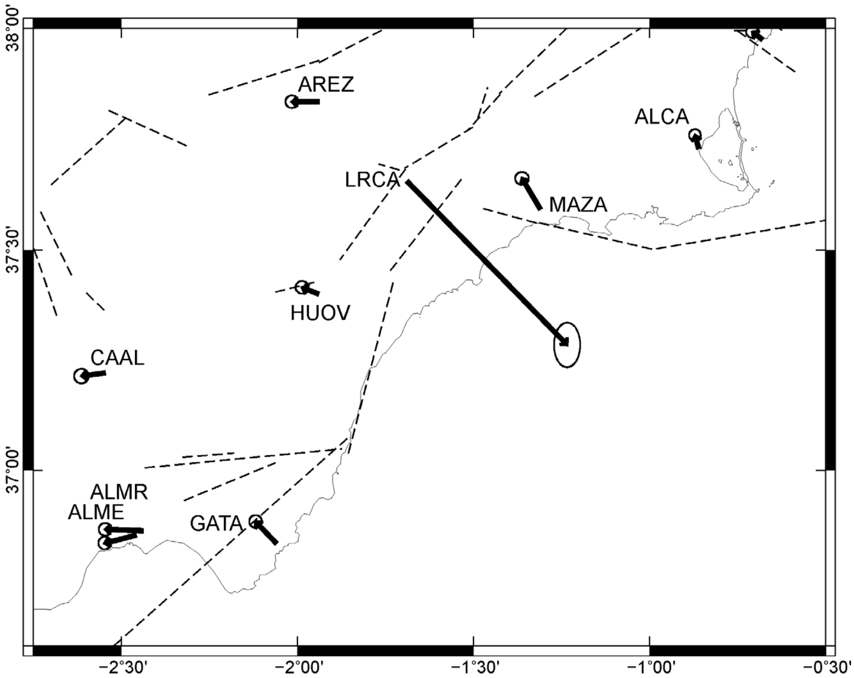

Figure 6.5: Preliminary velocity vectors of CGPS stations showing an anomalous, non-tectonic motion of the LRCA station.

Our detailed analysis of the 2011 post-event CuaTeNeo data has not identified any co-seismic deformation related to the earthquake, including at a closest station TERC, which was located just 4 km NE from the epicenter of the earthquake (Figure 6.3 and Figure 6.6). Nevertheless, both CGPS stations located in Lorca show a jump in the time-series related to the earthquake occurrence time (Figure 6.7). We estimated a co-seismic jump for the LRCA station to be equal to 6±0.6 mm towards the north and -0.7±0.5 mm to the west. In the vertical direction, the jump was statistically insignificant. In the case of LORC station, although it was inoperative, we calculated a jump between February and November of 2011: -0.8±0.7 mm to the south and 9.9±1.1 mm to the east. The apparent contradiction between the co-seismic displacements of LORC and LRCA are explained by the important damage of the building where the LORC antenna is located. For this reason, data from this station and perhaps partially LRCA station should be treated with caution, since the observed movements can be not only related to the slip on the fault, but also to the structural damage and deformation of the building where the antennas are mounted. This fact underlies the importance of specifically designed and built monuments, similar to the Topo-Iberia CGPS stations (see Chapter 4.3.1.1).

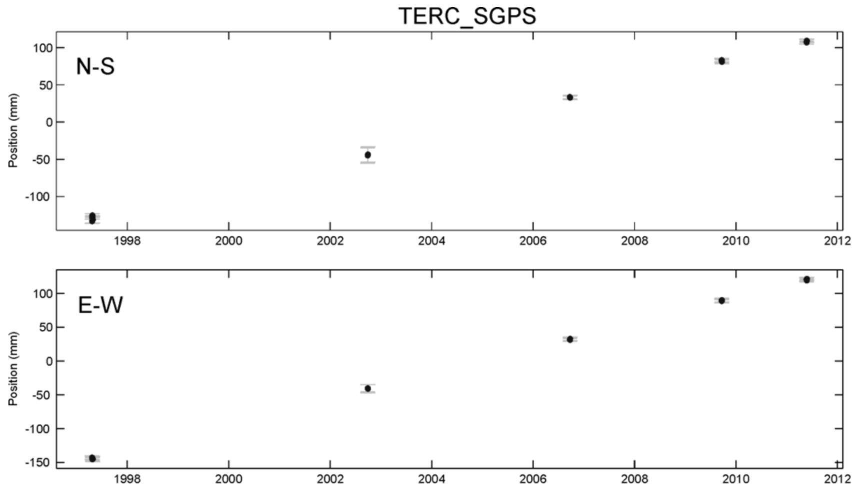

Figure 6.6: Time-series of TERC CuaTeNeo station in ITRF2008 reference system with 1σ uncertainties.

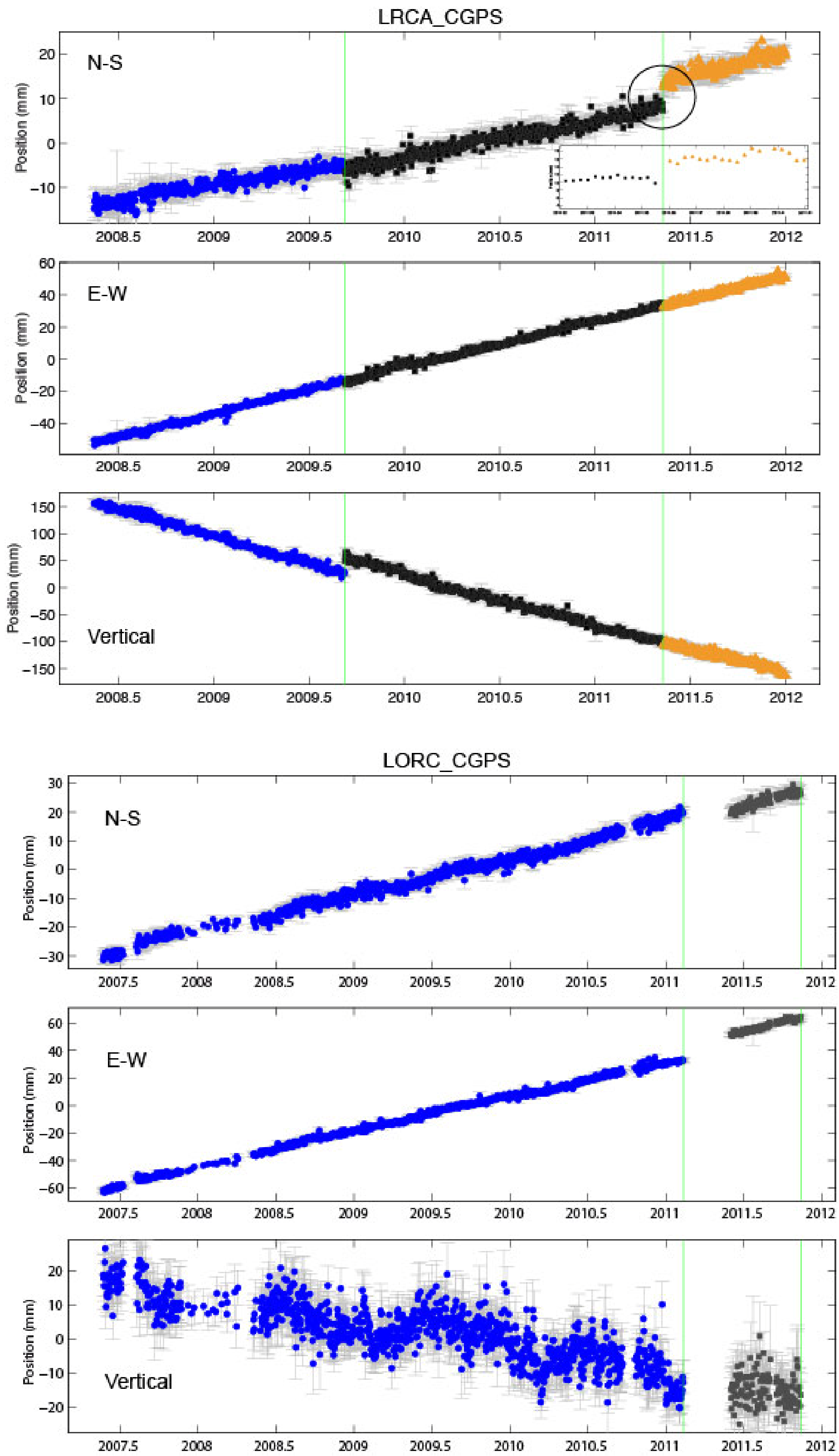

Figure 6.7: Time-series of LORC (up) and LRCA CGPS (down) stations in the ITRF2008 reference system. Vertical lines (and color changes) depict dates of hardware changes and/or earthquake occurrence (in 2011). The N-S component, where the co-seismic offset (LRCA) and lack of data (LORC) can be seen, includes a zoom of the time-series.

6.3. Discussion

Since the co-seismic signal of the Lorca earthquake was not detected by the CuaTeNeo network, the GPS velocities presented in this study represent the inter-seismic phase of earthquake deformation cycle. The oblique (reverse-sinistral) slip rate of 1.5±0.3 mm/yr calculated for the AMF is consistent with the behavior of the fault suggested by geologic observations (Masana et al., 2004; Vissers and Meijninger, 2011; Martínez-Díaz et al., 2012b; Ortuño et al., 2012) and also is in agreement with the 2011 Lorca earthquake focal mechanism (Figure 6.8). The P and T axes orientations for the focal mechanism of the main earthquake (López-Comino et al., 2012) are N167-190°E and N270°E, respectively. GPS principal strain axes orientations calculated at the center of AMF-PF region using the six stations (Figure 6.8) are $\dot{\varepsilon}_{min}$=N164°E°±7°E and $\dot{\varepsilon}_{max}$=N254°±7°E (at 1σ level), in good agreement with the above P-T axes orientations.

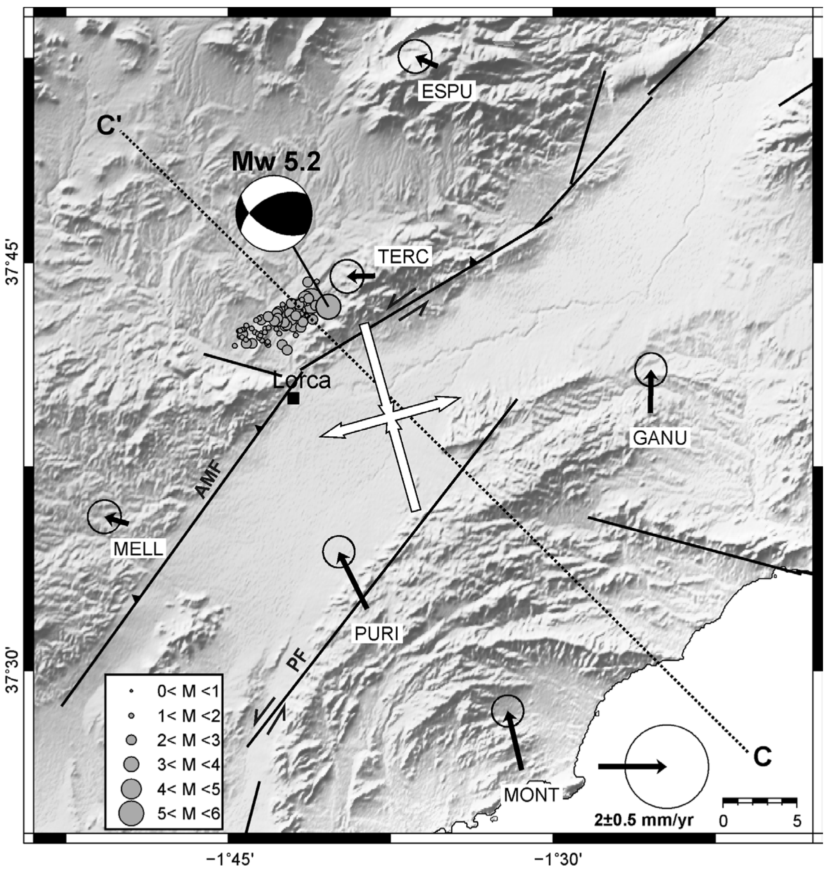

Figure 6.8: Detailed zoom of the AMF–PF zone. The focal mechanism of the main 2011 Lorca earthquake and its aftershock distribution are shown. Calculated strain rates determined at the center of the 6 stations are shown as a white cross with: $\dot{\boldsymbol{\varepsilon}}_{\boldsymbol{max}}$= 26±22 nstrain/yr and $\dot{\boldsymbol{\varepsilon}}_{\boldsymbol{min}}$= -39±3 nstrain/yr. See Figure 6.9 for the projected velocities along the profile (C-C').

In the previous section, we calculated the horizontal offset from ΔV_c and ΔV_{ss} from the GPS velocity profiles of the AMF-PF zone (Figure 6.8). The total horizontal slip rate is 1.5±0.3 mm/yr with an azimuth of N12°E with respect to the northwestern block. The slip rate for the AMF segments based on paleoseismological studies suggests lower values of geologic slip rates, that range between 0.06 and 0.53 mm/yr (Masana et al., 2004; Martínez-Díaz et al., 2012b; Ortuño et al., 2012). Nevertheless, recent paleoseimological studies (Ferrater et al., 2015) propose a preliminary minimum left-lateral slip-rate of 0.6±0.1 mm/yr based on channel offsets caused by the fault (see Section 3.1.1.2 for more details). The underestimation of the paleoseismological slip rates is expected, since these values do not correspond to the entire fault, but rather to a specific segment of the fault. On the other hand, the GPS slip rates represent an upper bound of the overall slip rate (e.g. Reilinger et al., 2006), since it has been assumed that all the measured deformation occurs on the AMF and no slip is accumulated on secondary faults and/or no internal strain accumulation has been considered. Taking the above arguments into account, the estimated geodetic slip rate can be considered to be in agreement with paleoseismological slip rate estimates.

6.4. Elastic dislocation modeling

6.4.1. Inter-seismic velocities

As we mentioned in Section 3.1.1.2, the SW segment of the AMF may be aseismic (e.g. Rodríguez-Escudero et al., 2012) while other sections are obviously seismic since they produce significant earthquakes, such as the 1964 and 2011 Lorca earthquakes. Several studies, based on comparison of the seismic moment release with geodetic deformation, have suggested a dominance of aseismic deformation in the Betics, Alboran Sea and north of Morocco (Stich et al., 2007; Pérez-Peña et al., 2010). In order to distinguish whether the measured geodetic deformation is indicative of aseismic or locked type behavior of the AMF, we used a 2D elastic dislocation model following Okada's (1992) formulation. As can be seen from Figure 6.9, our modeling results cannot differentiate between the shallow locked fault and the aseismic (i.e. stepwise) motion across the fault. However, the preference for a shallower locked fault is clear, since the 12 km deep fault produces significantly worse fit with the data. This observation is also in agreement with a shallow hypocenter (4.6 km) of the 2011 Lorca earthquake (López-Comino et al., 2012).

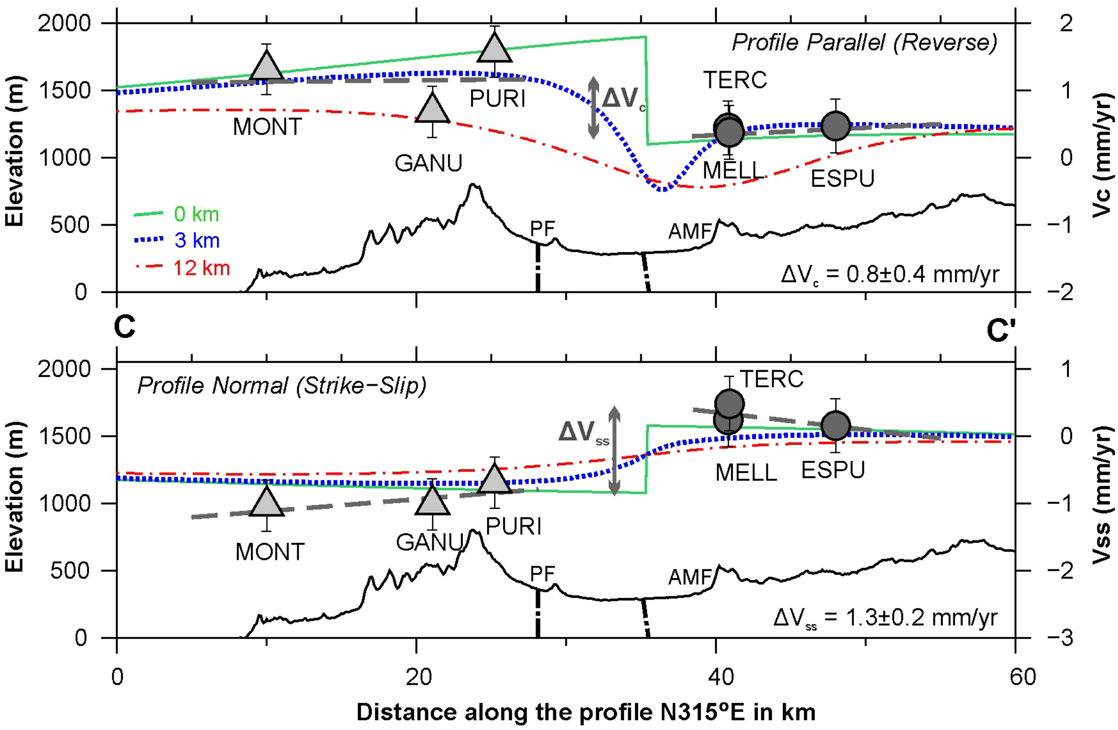

Figure 6.9: C-C' profile (azimuth N315°E) parallel and normal velocities with 1σ uncertainties (vertical bars). Location of the profile is shown in Figure 6.8. Dashed straight lines show linear regression fit for the individual group of stations, used to estimate the offsets. Three other curves represent the prediction of the 2D Elastic dislocation model according to Okada (1992) formulation: 1) continuous green straight line represents an aseismic motion; 2) blue thick-dotted line corresponds to a fault locked to 3 km depth; 3) red

dashed-dotted line is a model prediction for the fault locked to 12 km depth. In all 3 models we used the far field displacement corresponding to the MORVEL model velocities projected along the AMF. Topography is represented with an irregular line with a vertical exaggeration of 1:9. Stations on the NW side of the AMF are plotted as triangles and as circles on the SE side. The intersection with the AMF and PF are shown as short vertical lines on the bottom. *Top*) Profile parallel (AMF normal) velocities. ΔV_c is the compressive differential motion (velocity offset) between the two blocks. *Bottom*) Profile normal (AMF parallel) velocities. ΔV_{ss} is the strike-slip differential motion between the two blocks.

In conclusion, based on this simple modeling effort, we can say that our results preclude the distinction of the aseismic or seismic nature of deformation across the SW part of the AMF and/or PF. It would be essential to establish new geodetic points in the region separating the two faults.

6.4.2. Co-seismic displacements

Several models have been published in order to calculate the co-seismic displacements along and around the AMF (Frontera et al., 2012; González et al., 2012; Martínez-Díaz et al., 2012a; De Michele et al., 2013). Most of these works performed an inversion of the InSAR data. We provide a summary of the parameters used by these authors in Table 6.2.

Table 6.2: Compilation of parameters used in the elastic dislocation models in different studies. Htop and Hbottom are the depth of the fault top and bottom edge. R means reverse slip and LL left-lateral slip. Method refers to the model abbreviations used, W: Wang et al.(2003) and O: Okada (1985). Parameters marked with an asterisk were fixed in the model.

	Strike º	**Dip** º	**Rake** º	**Htop** km	**Hbottom** km	**Length** km	**Slip** cm	**Method**
Frontera et al. (2012)	245*	65*	58*	1*	3*	4*	15*	W
Martínez-Díaz et al.(2012a)	235*	55*	39*	1.5	4.9	3	15	O
González et al.(2012)	230	70	21	0	3.2	4	5 R 13 LL	O
De Michele et al.(2013)	245	45	77*	3.2*	5.4*	2.9*	21 R* 6.5 LL*	O
This model	235*	55*	39*	1.5*	4.9*	4*	12.5*	O

In order to calculate the co-seismic displacements, especially in the LRCA and TERC emplacements, we applied an elastic dislocation model of Okada (1985) in the area. Since only one co-seismic measurement was available, it was impossible to do a formal inversion of the GPS data and thus, we performed a simple forward modeling. For this purpose we have adapted the parameters of Martínez-Díaz et al. (2012a) for the fault orientation and the earthquake slip. The resulting modeled co-seismic displacement field on a regularly spaced grid is shown in Figure 6.10.

As can see in Figure 6.10 and Table 6.3, the horizontal deformation predicted by the numerical model agrees well with the co-seismic jump observed at the LRCA CGPS station from the analysis of the N-S, E-W and vertical time-series. The examination of the modeled horizontal motion makes easier to appreciate why we were not able to detect any co-seismic motion even at the closest CuaTeNeo station TERC after performing a post-earthquake campaign.

Table 6.3: Comparison of numerical model and observed displacements for the LRCA CGPS.

Component	**Observed**	**Modeled**
S-N	6 ± 0.6 mm	6.4 mm
W-E	-0.7 ± 0.5 mm	-0.2 mm

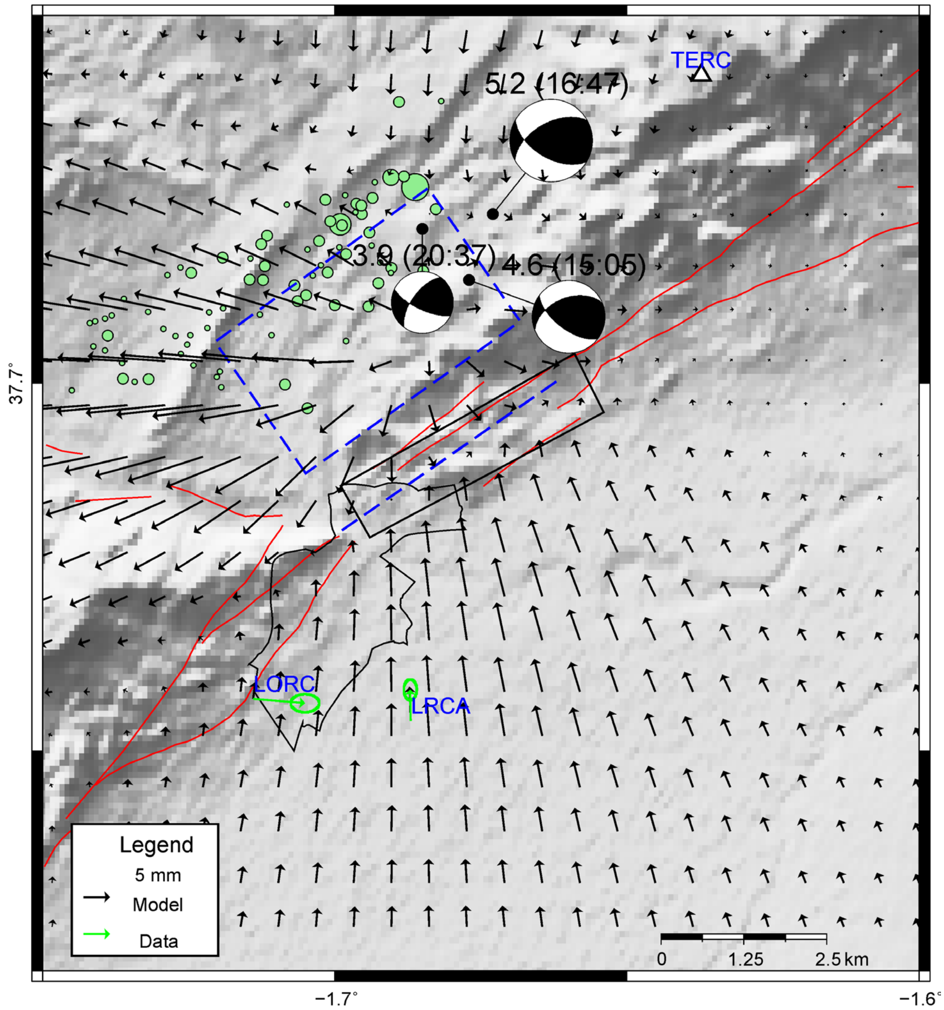

Figure 6.10: Horizontal co-seismic displacement field obtained by numerical model. The fault plane is represented by discontinuous blue rectangle and its projection to the surface by a blue line. Focal mechanisms for the Mw5.2 Lorca earthquake, Mw 4.6 foreshock and Mw aftershock from López-Comino et al. (2012). Observed displacement vectors for the LORC and LRCA stations are in green. TERC CuaTeNeo station location is shown to illustrate the insignificant co-seismic deformation.

González et al. (2012) also calculated the displacements in the LRCA station. They estimated the average position 3 days before and after the event and computed the displacements: 4.2±0.8 mm to the north, -0.9±0.8 mm towards the west and -2.3±3.3mm of subsidence. These values are of the same order as our observed and modeled displacements. In addition, the authors processed high-rate GPS data (1 Hz sampling) and did not find any relevant transient deformation that could be related to the Lorca earthquake. That is, the earthquake had no evidence of post-seismic deformation.

7. Carboneras fault zone

This chapter is dedicated to the other region of interest described in Chapter 5: the Carboneras fault zone (CFZ). The CFZ is characterized by the highest geologic fault slip rates (according to the QAFI database, García-Mayordomo et al. (2012)) constrained to date in the Iberian Peninsula. The estimated geologic slip rates at the CFZ range between 0.05-2 mm/yr depending on the utilized method and the covered time-period (Hall, 1983; Montenat et al., 1990; Bell et al., 1997; Moreno, 2011). The most recent paleoseismologic studies constrained the net-slip rate to 1.1-1.3 mm/yr for the Quaternary period (Moreno, 2011).

7.1. Velocity field

The present-day horizontal velocity field around CFZ is shown in Figure 7.1 and Table 7.1. We used the combined velocity field, which contains CuaTeNeo stations and CGPS as the new stations GATA (UB), NEVA and PALM (Topo-Iberia network). The estimated velocities range between 1.1 and 3.1 mm/yr. As it would be expected, the stations located closer to the Nubia/Eurasia plate boundary, along the coast, move faster than the stations located farther inland (CUCO, CAAL and NEVA). As mentioned earlier, the overall convergence rate between Nubia/Eurasia plates is of the order of 4 to 6 mm/yr (e.g. McClusky et al., 2003; Serpelloni et al., 2007; Argus et al., 2011), which means that a significant portion of this overall budget is accommodating within the study area.

The most important feature of the obtained velocity field is a significant change in the orientation of the calculated velocities from east to west (Figure 7.1). In the western Europe reference frame, the easternmost stations move at rates of 1.3-2.0 mm/yr in the direction of the Nubia/Eurasia convergence. Stations located to the west, starting from HUEB SGPS, show a more westerly-south-westerly motion, exhibiting a counter-clockwise rotation. The westernmost PALM and MOTR CGPS stations show the highest velocities (2.8±0.1 and 3.1±0.1 mm/yr, respectively) that are oriented south-west.

In order to ease the interpretation of the CFZ kinematics we fix GATA SPGS station in Figure 7.1, instead of using a western Europe fixed reference frame. The transformed GPS velocities show a clearly left-lateral motion of the CFZ (compare GATA-RELL to HUE-ALMR-ALME stations).

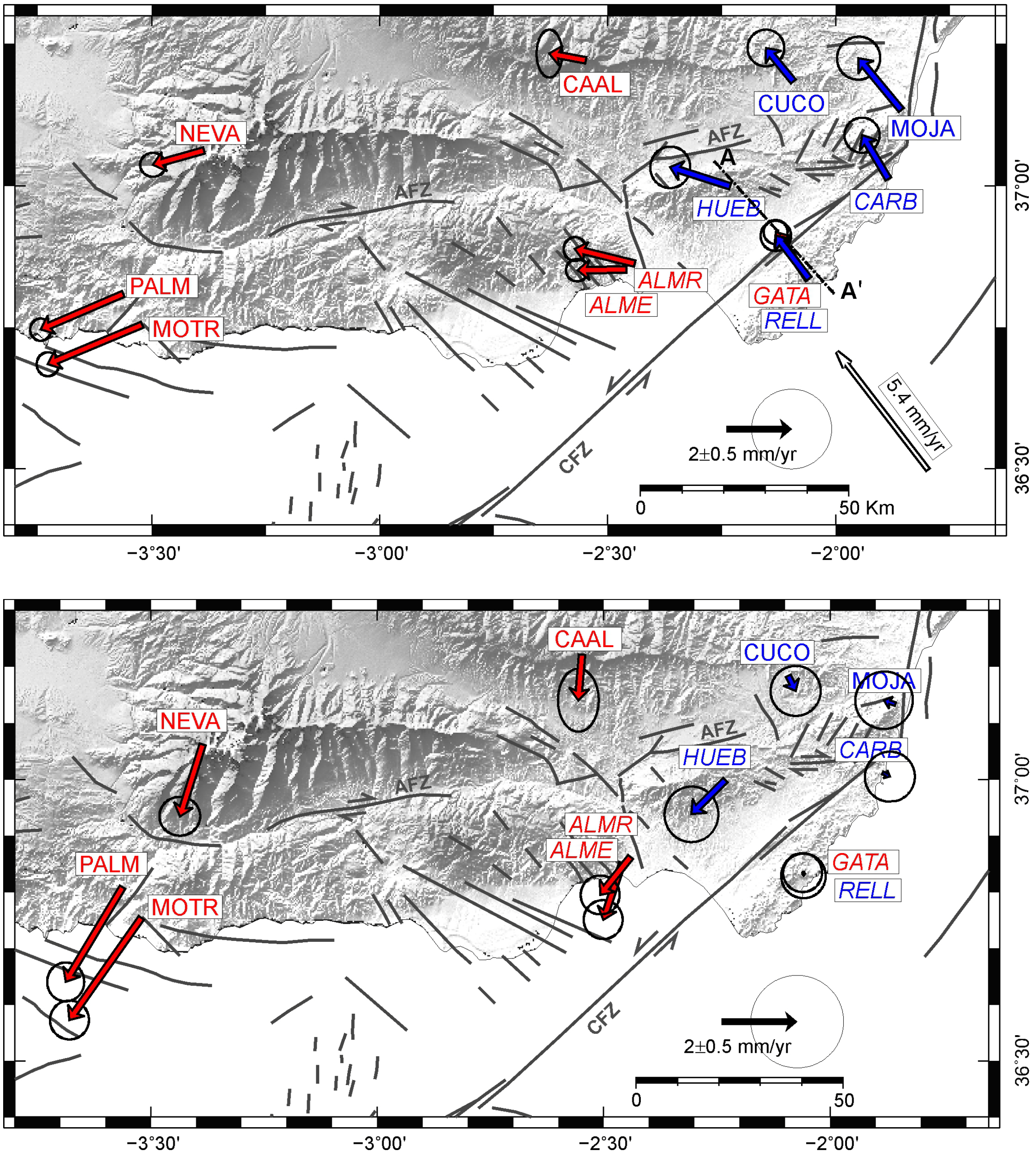

Figure 7.1: GPS velocities with 95% confidence error ellipses. CGPS and SGPS stations shown in red and dark blue, respectively. Stations included in A-A' profile (Figure 7.2 and Figure 7.3) are labeled in italic. Plate

convergence velocity from NNR-MORVEL56 model (Argus et al., 2011). Active faults from Gràcia (2012). *Top)* GPS velocities in western Europe reference frame. *Bottom)* GPS velocities in GATA reference frame.

Table 7.1*:* Horizontal GPS velocities and 1σ uncertainties of the stations included in the study area and the global stations used in the rotation to western Europe reference frame used by Echeverria et al. (2013). Ve is the east component, Vn the north component and HorV the horizontal magnitude with the corresponding azimuth (Az). Rho is the correlation between Ve and Vn and 1sig are the 1σ uncertainties. Station codes in italic refer to sites presented in A-A' profile.

CODE	**Lat. (ºN)**	**Long. (ºE)**	**Ve (mm/yr)**	**1sig**	**Vn**	**1sig**	**Rho**	**HorV (mm/yr)**	**1sig**	**Az (ºN)**
ALME	-2.459	36.852	-1.5	0.1	0.0	0.1	0.000	1.50	0.14	269
ALMR	-2.441	36.863	-1.8	0.1	0.5	0.2	0.001	1.88	0.14	284
CAAL	-2.548	37.221	-1.1	0.2	0.2	0.3	0.000	1.14	0.17	281
CARB	-1.885	37.012	-0.8	0.2	1.4	0.2	0.003	1.57	0.22	329
CUCO	-2.093	37.184	-0.8	0.2	1.0	0.2	0.005	1.33	0.23	321
GATA	-2.061	36.835	-1.0	0.2	1.5	0.2	0.003	1.76	0.15	326
HUEB	-2.231	36.999	-1.8	0.3	0.6	0.3	0.008	1.93	0.25	288
MOJA	-1.856	37.134	-1.3	0.3	1.6	0.3	0.015	2.06	0.27	321
MOTR	-3.521	36.755	-2.9	0.1	-1.2	0.2	0.002	3.13	0.14	247
NEVA	-3.386	37.063	-1.6	0.2	-0.4	0.2	-0.001	1.62	0.16	254
PALM	-3.562	36.809	-2.5	0.1	-1.1	0.1	0.000	2.75	0.13	247
RELL	-2.059	36.836	-1.0	0.2	1.3	0.2	0.003	1.66	0.19	323

7.1.1. Velocity profile

To assess the present-day slip-rates related to CFZ we constructed a velocity profile with a strike of 138º, perpendicular to the CFZ trace (Figure 7.1). Although there are only a few stations on each side of the fault, the differential motion between each group is evident and can be estimated. Specifically, the stations of the eastern block of CFZ move at 1.6-1.8 mm/yr with an azimuth of 325º (with respect to the western Europe reference frame). The nearest stations to the fault on the western block move at a rate of 1.5-1.9 mm/yr in an average direction of 280º.

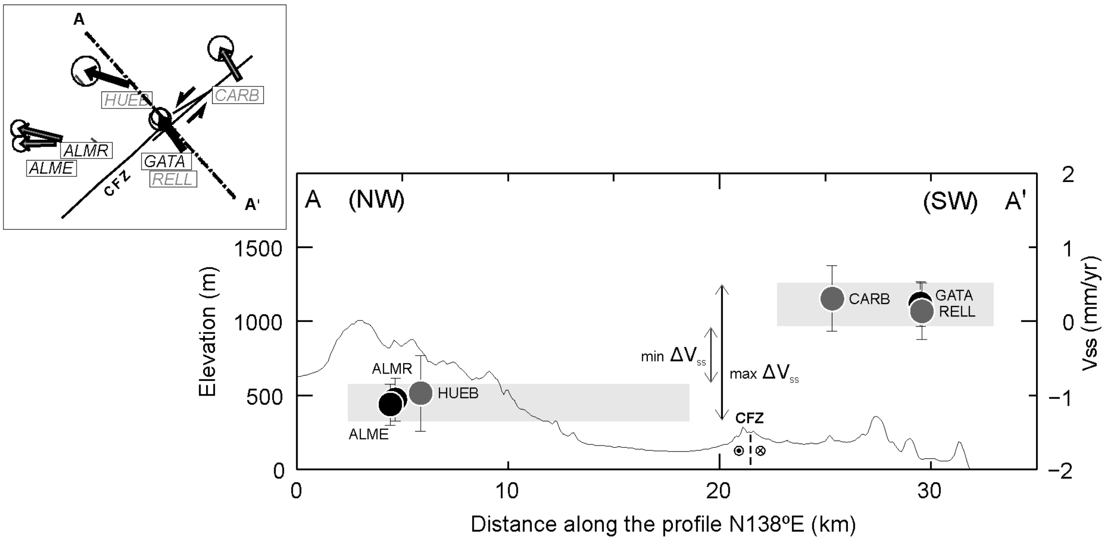

Figure 7.2: A-A' profile perpendicular velocities with 1σ error bars. Location of the profile is shown in Fig. 5.14. Topography is represented with an irregular line on the bottom. ΔV_{ss} is the fault parallel strike-slip differential motion (velocity offset) between the two blocks. The intersection of the CFZ trace with the profile is shown as short dashed vertical line on the topographic profile.

To derive the geodetically estimated slip rate we assume that the differential motion between the two groups of stations, located on each side of the CFZ, is related solely to this fault. By projecting the velocities to the profile parallel and perpendicular direction, we obtain the compressive (ΔV_c) and strike-slip (ΔV_{ss}) fault slip-rate components, respectively. Only the strike-slip component shows a significant differential motion across the CFZ (Figure 7.2). To calculate the slip rate, we assume that each area behaves as a rigid block, without an internal strain. This assumption is supported by the fact that the velocities on each side of the fault are almost identical. Taking into account the velocity errors, we obtain a minimum and maximum values for ΔV_{ss}: 1.1 to 1.5 mm/yr, which are equivalent to a strike-slip rate of 1.3±0.2 mm/yr. The fault normal (i.e. profile parallel) compression (ΔV_c) across the CFZ is less statistically insignificant (Figure 7.3). On the other hand, if we exclude a northerly motion of the station ALMR from the calculations and only consider ALME and HUEB stations, we can obtain a statistically significant compressive slip rate of 0.4±0.2 mm/yr. As a result, taking into account the sparse spatial coverage of the stations and disregarding ALMR (discussion in the next subsection), we can only conclude that the compressive motion (ΔV_c) across the CFZ is considerably less than the strike-slip motion and it should not exceed 0.6 mm/yr.

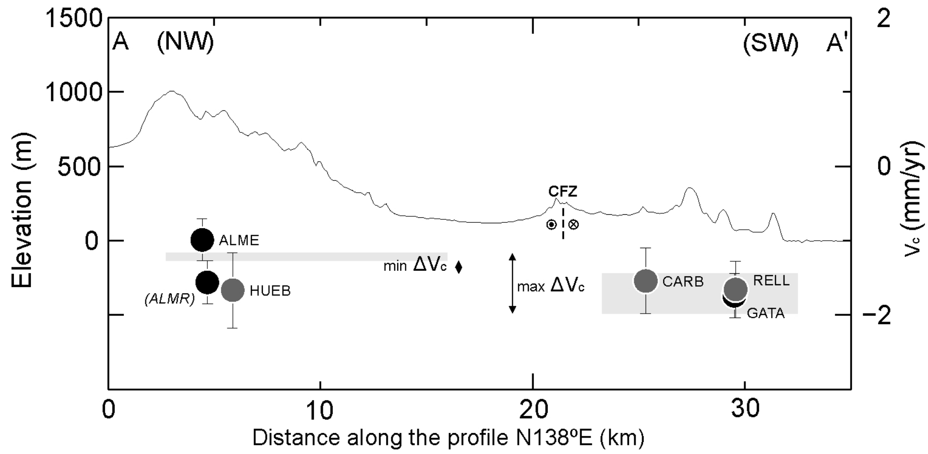

Figure 7.3: A-A' profile parallel velocities with 1σ error bars. Location of the profile is shown in Figure 7.1 and 7.2. Topography is represented with an irregular line on the bottom. ΔV_c is the fault shortening differential motion (velocity offset) between the two blocks excluding ALMR station. The intersection of the CFZ trace with the profile is shown as short dashed vertical line on the topographic profile.

7.1.2. Discussion

In this thesis, for the first time, we have been able to quantify the present-day horizontal crustal deformation rates of the Carboneras fault zone, using continuous and campaign GPS observations conducted during the last decade. The almost identical velocity vectors observed at two closely located stations (GATA (CGPS, 4.5 yr processed) and RELL (SGPS, 15 yr processed)) are an evidence of the high accuracy of the presented results. This good agreement between the two independent observations also reaffirms the usefulness of the campaign-style GPS observations, even when the deformations are slow, like in eastern Betics. By contrast, two other stations located on the opposite side of the CFZ in Almeria: ALME and ALMR, exhibit significant differential motion, which is likely due to the instability of the monuments or the buildings (including the surrounding ground) where these stations are emplaced.

In addition, since these stations are somewhat farther from the CFZ, the calculated velocities could be affected by other minor faults (e.g. NW-SE normal faults), thus causing the observed variation in the GPS velocities. We assumed, however, that the vectors calculated for these two stations are due to the CFZ since the movement observed at ALMR and ALME is similar to the velocity of the HUEB station, located on the same side of the CFZ but farther to the east (Figure 7.1). It should be mentioned that ALME and ALMR stations, unlike the Topo-Iberia and CuaTeNeo networks and GATA station, were build for the purpose of satisfying surveying needs of the local community, but not for measuring sub-millimetre level tectonic deformations.

The obtained horizontal velocity field for the SE Betics confirms the continuing tectonic activity, at least, of the on-shore section of the northern segment of the Carboneras fault (see NCF in Figure 3.6). We find that the left-lateral motion dominates the kinematics of the CFZ, with a strike-slip rate of 1.3±0.2 mm/yr along N48º direction. The shortening component is significantly lower and poorly constrained (ΔV_c=0.4±0.2 mm/yr without ALMR). Thus, the GPS measurements suggest a dominance of the strike-slip motion in the transpressional kinematics of the CFZ, coherent with a positive flower structure in La Serrata (e.g.Reicherter and Reiss, 2001; Moreno, 2011).

The GPS derived geodetic fault slip rates presented here can be considered as maximum values, since we assumed that all the observed differential motion is elastic, solely due to the CFZ and no possibility of the distributed deformation due to secondary faults was considered. The most recent study, integrating both onshore and offshore paleoseismic and geomorphologic results, using the youngest faulted features, obtain the minimum Quaternary strike-slip rates between 1.1 and 1.3 mm/yr (Moreno, 2011). These results are in good agreement with the geodetic slip rates presented in this work, suggesting that most of the deformation registered by GPS can be attributed solely to the activity of the CFZ. Combining the geologic (minimum values) and geodetic (maximum values) slip rates, we can conclude that the strike-slip rate of the CFZ must be enclosed between the minimum geologic slip rate of 1.1 mm/yr and the maximum geodetic slip rate of 1.5 mm/yr. The slip rates obtained by Moreno (2011) are mainly based on deflected geomorphological and young buried gullies onshore and offshore along the northern segment of the Carboneras fault (NCF) and cover different Quaternary geologic periods. Considering the similarity of paleoseismic and geodetic slip rates measured at different points along the NCF segment, the slip rate of the entire NCF must be approximately constant during the Quaternary.

7.2. Geodetic strain rate

For the selected 6 stations in the velocity profile, we calculated the strain rate field (Figure 7.4) by the inversion of the GPS data for the CFZ using SSPX software (Cardozo and Allmendinger, 2009). Horizontal principal strain rate axes calculated at the center of these six stations show a predominance of a compressive strain rate $\dot{\varepsilon}_{min}$= -26.2±8 nstrain/yr oriented N354º. The extensional component is less: $\dot{\varepsilon}_{max}$ of 18.1±7 nstrain/yr with an azimuth of N84º. The resulting left-lateral shear plane of $\dot{\varepsilon}_{sh-max}$ has an orientation of N39º, sub-parallel to CFZ trace (N48º).

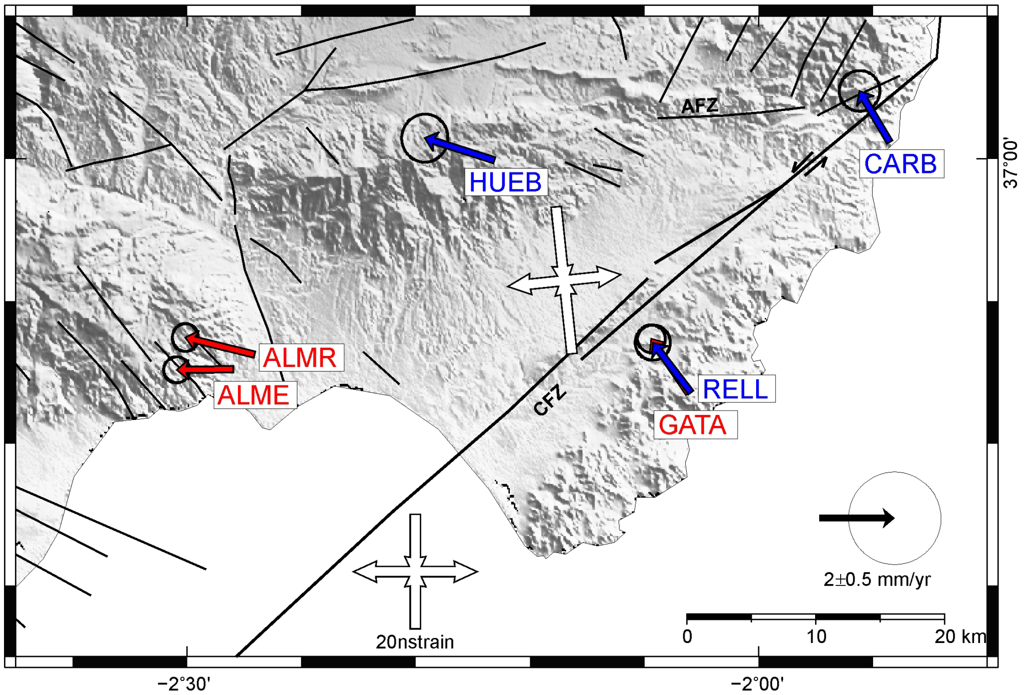

Figure 7.4: Detailed zoom of the GPS horizontal velocities of the CFZ. GPS velocities with 95% confidence error ellipses in western Europe reference frame. CGPS and SGPS stations shown in red and dark blue, respectively. Calculated strain rates determined at the center of the 6 stations are shown as a white cross. Active faults from Gràcia (2012).

We calculated also the strain rate field for the whole area, including not only the CFZ, from the stations included in Figure 7.1. Horizontal principal strain rate axes calculated at the center of these 12 stations show a predominance of an extensive strain rate $\dot{\varepsilon}_{max}$= 22±4 nstrain/yr oriented N52º. The shortening component is less: $\dot{\varepsilon}_{min}$ of -8.3±1 nstrain/yr with an azimuth of N322º

Unfortunately, due to the poor spatial distribution of the GPS stations, we cannot discern with certainty whether the accumulated strain is released aseismically (e.g. as a creep) or the fault is locked and is being loaded for the occurrence of the earthquake. However, taking into account the paleoseismological results that show evidence of repetitive large paleoearthquakes along the CFZ (e.g. Gràcia et al., 2006; Moreno, 2011), a locked fault scenario seems more plausible. In contrast, Faulkner et al. (2003) suggest a mixed mode fault slip behaviour (when fault creep is interspersed with seismic locking) for the CFZ, drawing an analogy with the Parkfield section of the San Andreas fault. The clarification of the issue of seismic or aseismic behaviour of the CFZ is crucial for the seismic hazard calculations and thus, the future studies should include the densification of the measurements along the fault-perpendicular profile.

With the aim of go in depth about this issue, we developed a comparison between geodetic and seismic rates to know what amount of geodetic strain is released by seismicity (see next Section). Because the small area and the limited GPS data, we applied this methodology to a broad area, the same area as we presented the velocity field (Figure 7.1).

7.3. Seismic strain rate

Seismic strain rate computes the strain rate seismically released. Geodetic strains take into account the total value of the active deformation, but cannot discern between the seismic components from the asesimic ones. Because of that, the comparison of seismic and geodetic strain rates becomes essential for determining the seismic hazard of an active region. In this way, in case of presence of aseismic component in a region, the geodetic strain rate would be bigger than seismic strain rates if the entire seismic cycle is represented in the catalog. Several studies have been conducted in different places comparing seismic and geodetic strain rates (e.g. Kreemer et al., 2000; Masson et al., 2005; Pancha et al., 2006; Rontogianni, 2010). The advantage of the seismological approach is that it represents an intermediate approach between the geodetic (~10 yr) and geologic (~10^4 yr) time-scales.

7.3.1. Methodolgy

The relation between the average strain rate tensor of a seismogenic volume and the earthquake activity, which is calculated as a sum of the moment tensors, was first described by **Kostrov** (1974):

$$\dot{\varepsilon}_{ij} = \frac{1}{2\mu V t} \sum_{n=1}^{N} M_{ij}^{n} \tag{7.1}$$

where V is the seismically straining volume, μ is the shear modulus and M_{ij} are the moment tensor elements of the nth earthquake out of N earthquakes over a t time interval. This simple relationship is true assuming that all the deformation in a volume is seismic.

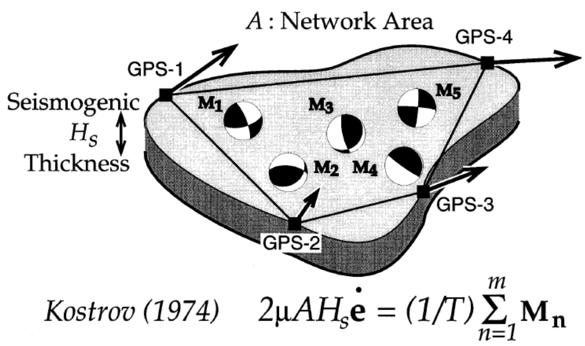

Figure 7.5: Conceptual cartoon showing the relation between the potential rate of seismic moment release and the observed geodetic strain rate within a GPS network. Area A and seismogenic thickness Hs define the seismically straining volume (from Ward (1998)).

To obtain a reasonable strain rate estimate from earthquakes requires an observation period of earthquakes to be much longer than the recurrence interval of the largest events. In the case of the Betics, due to the long recurrence periods in this slowly deforming zone, we have used also a modified formula of Kostrov, suggested by **Papazachos and Kiratzi** (1992). The latter method is mainly based on formulations of Kostrov (1974), Molnar (1979) and Jackson and McKenzie (1988). The authors estimate the "magnitude" of the deformation $(\dot{M}_0)$ from the seismicity record, instead of relying solely on the shorter and less complete moment tensor catalog. Nevertheless, the "shape or style" of the deformation $(\bar{F}_{ij})$ is still estimated from the available moment tensor solutions. According to Papazachos and Kiratzi (1992) the Kostrov's formula can be decomposed as:

$$\dot{\varepsilon}_{ij} = \frac{1}{2\mu V} \bar{F}_{ij} \cdot \dot{M}_0 \tag{7.2}$$

Where $\bar{F}_{ij} = \frac{\sum_{n=1}^{N} M_{ij}^{n}}{\sum_{n=1}^{N} M_0^{n}}$ is a unit-scaled tensor, proportional to the "average" sum of Kostrov formula and describes the style of deformation. M_{ij}^{n} and M_0^{n} are the moment tensor elements and the corresponding scalar moment, respectively, of the *n*th focal mechanism.

The annual scalar moment rate, $\dot{M}_0$, is calculated, according to Molnar (1979), based on the seismic moment released by the maximum earthquake in the seismogenic zone ($M_{0,max}$):

$$\dot{M}_0 = \frac{\alpha}{1-\beta} \cdot M_{0,max}^{1-\beta} \tag{7.3}$$

where $\alpha = 10^{\left[a+\left(\frac{bd}{c}\right)\right]}$ and $\beta = b/c$ are related to a and b constants of the Gutenberg-Richter relationship: $\log N = a - bM$; and c and d constants of the moment-magnitude relationship: $\log M_0 = cM + d$.

The Papazachos-Kiratzi formulation has also the advantage of including the deformation due to small earthquakes ($M_w < 3.5$), which do not have focal mechanisms estimated. Stich et al. (2007) demonstrate that small events ($M_w < 3.5$) contribute up to 20% of the seismic deformation in the Betic-Rif area. However, this approach has the disadvantage that the "shape factor" ($\bar{F}_{ij}$) is an averaged sum of normalized seismic moment tensor, i.e. gives the same weight to small and big events. Therefore, in an ideal scenario, this approach has to be applied in areas with homogeneous deformation.

Note that μ and the V parameters are common for both approaches and only influence the obtained strain rate magnitude, and not the style of deformation. The area (A) and the thickness of the seismogenic layer (H), are used to calculate the volume V and define the dimensions of the deforming body.

The resulting eigenvectors of the seismic strain rate tensor correspond to $\dot{\varepsilon}_1$ (contraction), $\dot{\varepsilon}_2$, and $\dot{\varepsilon}_3$ (extension). $\dot{\varepsilon}_1$ and $\dot{\varepsilon}_3$, projected to the horizontal plane can be compared with the geodetic strain rates $\dot{\varepsilon}_{min}$ and $\dot{\varepsilon}_{max}$, respectively, obtained from the GPS velocities.

7.3.2. Input data

In order to estimate the seismic strain rate it is necessary to have a reliable and complete seismicity catalog. For this purpose, we have compiled two catalogs with the main objective of having an homogeneous magnitude (i.e. M_w): the seismic catalog, containing the historical and instrumental events and the focal mechanisms catalog.

For the **seismic catalog**, we used the compilation done for a re-examination of the seismic hazard in Spain (IGN, 2013). Hereafter we will refer to this catalog as IGN_2013 catalog in order to abbreviate and avoid confusion with the online catalog (containing different kind of magnitudes). This catalog covers a time period from year 1048 to 30/06/2011 with depths ranging from 0 to 65 km. The final catalog, declustered, revised and homogenized using M_w type magnitudes, is available for earthquakes with M_w>3, although the magnitude of completeness is M_w 3.5 (IGN, 2013). In the study area, there are a total of 356 earthquakes with M_w from 3 to 6.5 (Figure 7.6), covering the 1487.8-2010.8 time period and depths ranging from 0 to 60 km (Table 7.3).

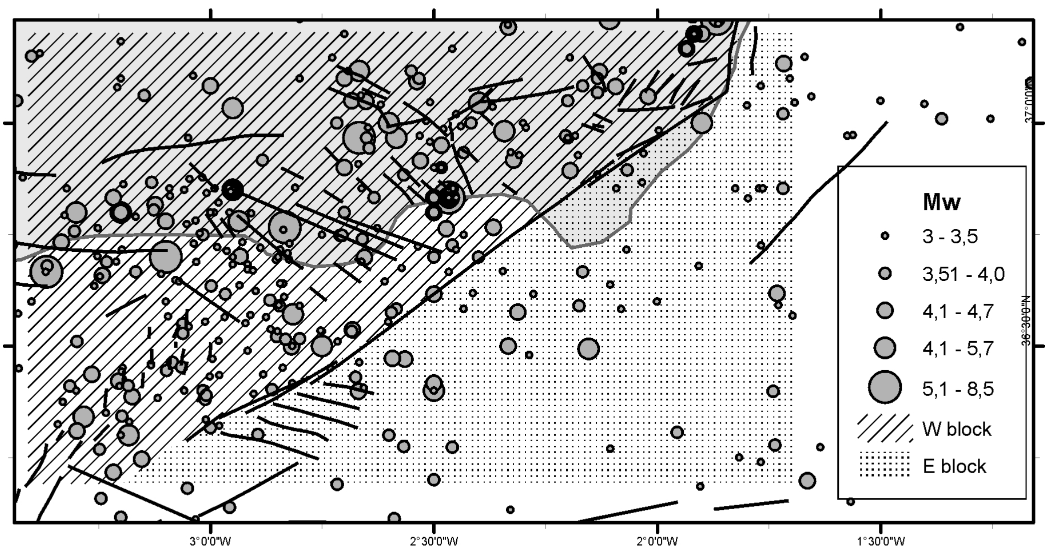

Figure 7.6: Seismicity of the IGN_2013 catalog in the study area, subdivided by two regions, corresponding to both blocks of the CFZ, drawn by different pattern. Active faults from Gràcia (2012).

The second catalog includes the compilation of **moment tensors** including the maximum time span possible from available literature and public catalogues. The master catalog used was the Instituto Andaluz de Geofisica (IAG) moment tensor project (Stich et al., 2003; 2006; 2010), since it was specifically created to perform time-domain moment tensor inversion of small to moderate events (m_b>3.5) in the Ibero-Maghreb area. In the cases where only the fault plane solutions were available (i.e. inverted from P-wave first-motion arrivals), we used the MoPaD software (Krieger and Heimann, 2012) to obtain the moment tensor. We decompose the moment tensor into an isotropic part, a double couple and a compensated linear vector dipole, following the convention given by Jost and Hermann (1989). The coordinate system chosen was the *USE* (Up, South, East), which equals to *r, theta, phi*, in the Harvard CMT convention (Dziewonski et al., 1981). The M_o was obtained by the relationship with M_w of Hanks and Kanamori (1979), in dyn·cm units. For the events listed in Martínez-Martínez et al. (2006), we chose the correspondent M_w of the instrumental catalog of IGN (2013), since the original source was in m_b.

The final catalog has 37 focal mechanisms in the study area, from 1910 to 2013, with magnitudes ranging from M_w3.3 to 6.1 (Figure 7.7 and Table 7.3). The orientation of P and T axes, which was obtained with ObsPy software (Beyreuther et al., 2010), is similar for all the events. The average P axis is oriented NNW-SSE (N340±15º), analogous to the plate convergence and T axis has an average orientation of ENE-WSW (N069±14º), compatible with the NW-SE normal faults (Figure 7.8).

Figure 7.7: Map of the study area with focal mechanisms compilation (see Table 7.2 for correspondence with ID number). The 1910 Adra focal mechanism is marked in black. P and T axes of the focal mechanisms are shown as gray and white dots, respectively.

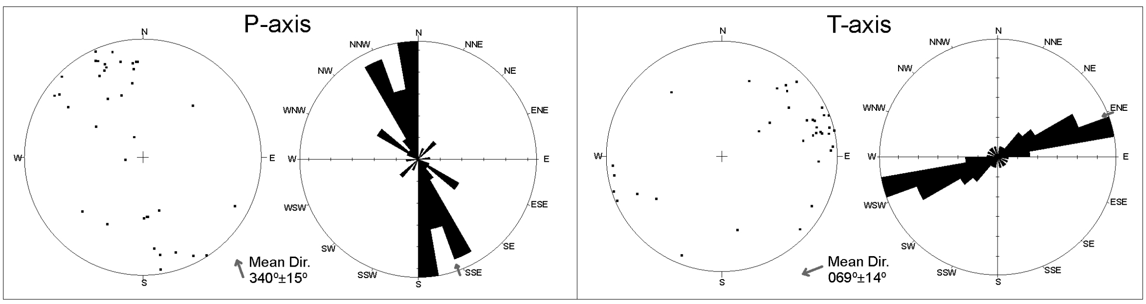

Figure 7.8: Stereographic projection (equal area plot) and rose diagrams of the P and T axes orientations for the displayed focal mechanisms in Figure 7.7. Mean resultant direction (gray arrow) and 95% confidence interval obtained by GEOrient software, following Fisher (1995).

Table 7.2: Compilation of focal mechanisms in the study area. Moment-tensor elements in the standard spherical coordinate system. In Cartesian coordinates, $m_{rr}=m_{zz}$, $m_{tt}=m_{xx}$, $m_{pp}=m_{yy}$, $m_{rt}=m_{xz}$, $m_{rp}=-m_{yz}$, and $m_{tp}=-m_{xy}$.

ID	Long. (º)	Lat. (º)	Depth (km)	Date	m_{rr} (dyn·cm)	m_{tt} (dyn·cm)	m_{pp} (dyn·cm)	m_{rt} (dyn·cm)	m_{rp} (dyn·cm)	m_{tp} (dyn·cm)	M_w	Ref.[a]
1	-3.08	36.58	16	16/06/1910	-3.50E+24	-7.20E+24	1.07E+25	-9.20E+24	3.50E+24	-6.30E+24	6.1	7
2	-2.15	36.49	12	06/01/1983	3.07E+22	6.23E+22	-9.29E+22	7.37E+22	6.90E+21	-8.76E+22	4.7	2
3	-2.20	36.55	6	20/03/1983	-1.28E+22	6.90E+21	5.90E+21	1.02E+22	-2.17E+22	4.26E+22	4.4	2
4	-2.30	37.00	9	13/09/1984	1.28E+23	-5.27E+23	4.00E+23	8.50E+22	-2.26E+23	-1.74E+23	5.1	1
5	-2.97	36.82	17	05/11/1986	-2.80E+20	1.48E+21	-1.20E+21	-3.62E+21	1.10E+21	1.95E+21	3.7	4
6	-3.02	36.87	-	23/12/1993	-5.90E+22	-4.10E+22	1.00E+23	1.50E+23	-6.60E+22	-7.50E+22	4.8	5
7	-2.85	36.63	-	04/01/1994	-1.11E+23	-7.10E+22	1.83E+23	1.36E+23	-4.80E+22	-8.00E+22	4.9	5
8	-3.00	36.82	10	18/05/1995	-2.30E+20	-1.00E+20	3.30E+20	1.70E+21	1.00E+20	1.42E+21	3.5	4
9	-2.95	36.90	4	13/12/1995	-2.79E+21	5.20E+20	2.27E+21	-1.07E+21	-8.90E+20	1.20E+21	3.6	4
10	-3.24	36.37	6	02/07/1997	-6.07E+21	-4.96E+22	5.57E+22	-2.82E+22	-7.57E+21	-8.28E+21	4.5	6
11	-3.26	36.36	10	02/07/1997	-3.63E+21	-3.96E+22	4.32E+22	-1.62E+22	-4.48E+21	-8.13E+21	4.4	6
12	-3.24	36.35	8	02/07/1997	-2.89E+20	-8.63E+21	8.92E+21	-3.42E+21	-2.99E+21	-4.66E+19	4	6
13	-3.23	36.36	10	03/07/1997	-4.72E+20	-8.57E+21	9.04E+21	-3.49E+21	6.54E+20	-1.31E+21	4	6
14	-3.24	36.45	16	07/08/1997	4.57E+20	-2.50E+21	2.04E+21	-2.38E+20	-8.68E+20	-1.32E+21	3.6	6
15	-1.79	37.01	8	06/04/1998	2.43E+21	-5.26E+21	2.83E+21	-3.71E+21	2.54E+21	-6.20E+21	3.9	6
16	-2.64	36.94	20	16/10/1998	1.94E+21	-1.67E+21	-2.67E+20	6.97E+20	-9.54E+20	-1.62E+21	3.6	6
17	-2.74	36.21	6	29/05/1999	-4.29E+21	5.53E+21	-1.24E+21	-2.74E+21	-2.13E+21	-3.93E+21	3.9	6
18	-3.13	36.36	16	27/05/2000	-4.62E+19	-2.59E+21	2.64E+21	-9.79E+20	-2.41E+20	-1.29E+21	3.6	6
19	-2.55	37.09	10	04/02/2002	-1.37E+23	1.13E+22	1.26E+23	1.07E+22	-5.91E+22	-2.78E+22	4.7	6
20	-2.20	36.99	12	06/02/2008	-1.75E+21	-1.15E+22	1.33E+22	-2.18E+21	-2.91E+21	-1.59E+22	4.2	8
21	-2.55	36.47	6	20/10/2008	-1.83E+21	-1.68E+21	3.50E+21	-1.07E+21	-2.18E+21	-2.27E+21	3.7	8
22	-2.55	36.47	14	21/10/2008	-1.38E+21	-1.67E+22	1.81E+22	-7.94E+21	-1.22E+22	-2.03E+22	4.3	8
23	-2.55	36.47	14	21/10/2008	-5.14E+21	-1.88E+22	2.39E+22	-8.61E+21	-6.84E+21	-2.21E+22	4.3	8

24	-2.55	36.47	14	21/10/2008	-6.31E+20	-3.87E+21	4.50E+21	-1.86E+21	-4.81E+20	-4.24E+21	3.8	8
25	-2.55	36.47	14	26/10/2008	-1.44E+21	-8.41E+21	9.85E+21	-2.98E+21	-1.51E+21	-8.50E+21	4	8
26	-2.55	36.47	6	07/11/2008	-1.85E+22	-1.53E+22	3.38E+22	-1.81E+22	-9.28E+21	-1.61E+22	4.4	8
27	-2.31	36.57	8	05/07/2010	-3.59E+19	-4.46E+21	-4.50E+21	1.00E+21	-3.96E+21	-2.49E+22	4.2	3
28	-2.38	36.69	10	06/07/2010	2.16E+21	2.47E+21	-4.63E+21	2.35E+21	-4.73E+21	-1.09E+22	4	3
29	-2.37	36.69	12	06/07/2010	-2.40E+20	7.74E+20	-5.35E+20	1.52E+20	-2.35E+21	-3.50E+21	3.7	3
30	-2.34	36.55	8	10/07/2010	1.11E+20	3.00E+20	-4.11E+20	1.66E+20	-7.29E+20	-1.81E+21	3.5	3
31	-2.37	36.70	20	10/07/2010	1.97E+21	-2.69E+21	7.25E+19	1.65E+21	-1.60E+21	-2.42E+21	3.7	3
32	-2.58	36.71	26	12/10/2010	6.43E+20	-2.51E+21	1.87E+21	2.87E+20	-9.83E+20	-2.34E+21	3.7	3
33	-2.58	36.72	12	04/11/2010	-4.60E+20	-2.40E+21	2.86E+21	1.21E+21	-9.07E+20	-1.12E+21	3.6	3
34	-2.58	36.72	12	04/11/2010	-2.16E+20	-1.13E+22	1.15E+22	4.57E+21	-2.04E+21	-4.94E+21	4.1	3
35	-2.64	36.48	6	18/04/2012	-1.54E+22	-8.96E+21	2.44E+22	1.16E+22	6.46E+21	-7.18E+21	4.2	3
36	-2.63	36.50	6	18/04/2012	-1.72E+21	-1.28E+21	3.00E+21	1.63E+21	-2.07E+20	-7.47E+20	3.6	3
37	-2.86	36.34	9	14/08/2013	-3.10E+20	-5.35E+20	8.45E+20	1.07E+20	7.95E+19	-5.20E+20	3.3	9

[a]**References**

1 Buforn, E., Sanz de Galdeano, C. and Udías, A., **1995**. Seismotectonics of the Ibero-Maghrebian region Tectonophysics, 248, 247-261.

2 Coca, P. and Buforn, E., **1994**. Mecanismos focales en el sur de España: periodo 1965-1985 Estudios Geológicos, 50, 33-45.

3 Martín, R., Stich, D., Morales, J. and Mancilla, F., **Submitted**. Iberia-Maghreb moment tensor solutions during Iberarray (2009-2013) Tectonophysics.

4 Martínez-Martínez, J.M., Booth-Rea, G., Azañón, J.M. and Torcal, F., **2006**. Active transfer fault zone linking a segmented extensional system (Betics, southern Spain): Insight into heterogeneous extension driven by edge delamination Tectonophysics, 422, 159-173.

5 Stich, D., Alguacil, G. and Morales, J., **2001**. The relative locations of multiplets in the vicinity of the Western Almería (southern Spain) earthquake series of 1993-1994 Geophysical Journal International, 146, 801-812.

6 Stich, D., Ammon, C.J. and Morales, J., **2003**. Moment tensor solutions for small and moderate earthquakes in the Ibero-Maghreb region Journal of Geophysical Research, 108.

7 Stich, D., Batlló, J., Morales, J., et al., **2003**. Source parameters of the MW= 6.1 1910 Adra earthquake (southern Spain) Geophysical Journal International, 155, 539-546.

8 Stich, D., Martín, R. and Morales, J., **2010**. Moment tensor inversion for Iberia-Maghreb earthquakes 2005-2008 Tectonophysics, 483, 390-398.

9 www.ign.es/ign/layoutIn/sismoFormularioTensor.do

Table 7.3: Seismic catalogs attribute table used in the computation.

CATALOG	Source	Number events	M_w range	Time span	Total M_o	Largest event	Contribution largest event
Seismic catalog (IGN_2013)	IGN (2013)	356	3-6.5	1487-2011	1.83E26 dyn·cm	1522 Almería (M_w 6.5)	40%
Focal mechanisms	Compilation from literature	37	3.3-6.1	1910-2013	1.67E25 dyn·cm	1910 Adra (M_w 6.1)	90%

From the compilation of the focal mechanisms, we have tested whether the style of deformation is homogenous in the area. We calculated the average focal mechanism ($\sum_{n=1}^{N} M_{ij}^{n}$), from which we can deduct the P and T axes orientation for the whole area and for each block of the CFZ (Figure 7.6 and Table 7.4). In addition, we have tested the influence of the 1910 Adra M_w6.1 earthquake (Stich et al., 2003; Figure 7.7), the largest event in the catalog, since it accounts for most (90%) of the total seismic moment release.

Table 7.4: Table of the resulting average focal mechanisms and strike and dip of the P- (shown as a point in the dilatational quadrant) and T- axis for different cases.

Average	**Whole area**	**Whole area (no Adra)**	**W block**	**E block**
Focal mechanism	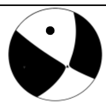		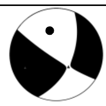	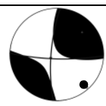
P axis (Strike /Dip)	350º/34º	169º(349º)/19º	350º/35º	138º(318º)/02º
T axis (Strike/Dip)	247º/19º	071º(251º)/20º	247º/18º	048º(228º)/18º

Although the contribution of the 1910 Adra event to the total seismic deformation is important, the resulting orientation of the P and T average axes remains similar. Note that the direction of the axes is the nearly parallel; the change is in the dip sense, which can be given since are sub-horizontal. The orientation of the P and T axes for the two blocks, independently, also has some variations, but the mean orientation remains constant. The western block, influenced by the Adra event, has the same axes orientation as the whole area. So, we can infer that both blocks present the same style of deformation and are not influenced by the Adra event. In all cases, the focal mechanisms are characterized by strike-slip and normal faulting with P- axes oriented NNW-SSE.

7.3.3. Computation

7.3.3.1. b-value

In order to calculate the strain rate with the Papazachos and Kiratzi (1992) approach, it is necessary to calculate the Gutenberg-Richter (G-R) relation and obtain the *a* and *b* values. Figure 7.9 shows the G-R relation determined for the study area using the entire catalog (IGN_2013), calculated with the ZMAP software (Wiemer, 2001), which uses the maximum likelihood solution. The b-value is widely accepted to be related to tectonics and earthquake physics, measuring the relative abundance of large and small earthquakes (Bath, 1981), ranging from $0.8<b<1.2$, with the majority ≤ 1 (e.g. Wyss, 1973).

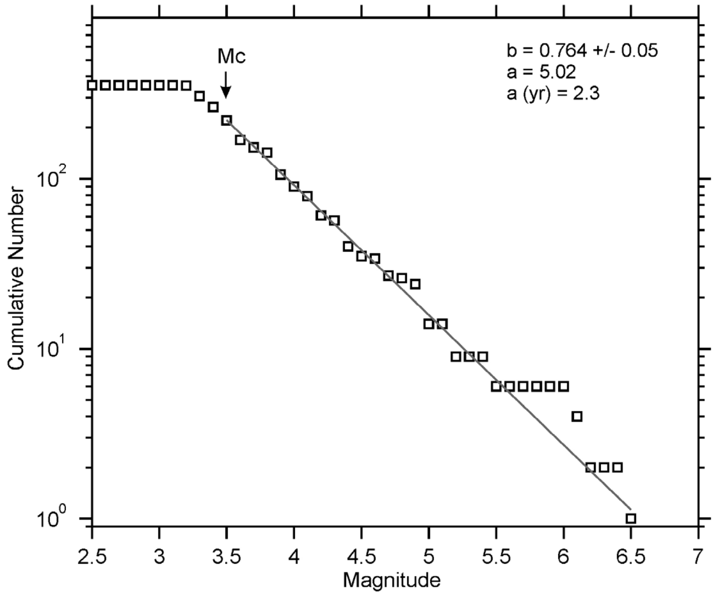

Figure 7.9: Gutenberg-Richter relation deducted for the entire IGN_2013 catalog. The magnitude of completeness (M_c) is 3.5.

To test the confidence in the results, as well as, any possible deviation in the results due to the catalog or geographic area, we have performed additional tests and calculated the G-R relation for the instrumental period (from 1975) and for the eastern and western blocks independently (Table 7.5). The results show that b-value differs significantly depending on the time span of the catalog. This variation reflects the fact that for the actual catalog, the seismic network is capable of detecting small events with more confidence, but misses some big events, due to their longer time of recurrence. For this reason, the calculated b-values tend to be higher.

Table 7.5*:* *a* and *b* values and maximum M_w observed ($M_{w,max}$) in different areas and different time span of the seismic catalog.

	Whole area			*W Block*			*E Block*		
Time span	**a (yr)**	**b**	**$M_{w,max}$**	**a (yr)**	**b**	**$M_{w,max}$**	**a (yr)**	**b**	**$M_{w,max}$**
1487-2011	2.3	0.77±0.05	6.5	2.15	0.75±0.06	6.5	2.57	0.87±0.1	5.1
1975-2011	4.2	1.09±0.08	5.1	4.33	1.16±0.1	5.1	3.5	1.06±0.2	4.8

7.3.3.2. Seismic strain rates

As we have seen before, we can consider that the whole area presents the same style of deformation and that is homogeneous. Because of that and due to the scarcity of geodetic (see Section 7.2) and seismic data, we have calculated the seismic strain rates for the whole area.

Firstly, we have computed the strain rate with the **Kostrov approach** (Eq. 7.2). We take μ=3E-11 dyn cm and H=12 km. This limit is in agreement with the depth of the Carboneras fault (Moreno, 2011) and the base of the seismogenic layer (e.g. García-Mayordomo, 2005 and Fernández-Ibáñez and Soto, 2008). The obtained principal strain rates are $\boldsymbol{\dot{\varepsilon}_1}$**= -1.21 nstrain/yr** with an azimuth of 350º and $\boldsymbol{\dot{\varepsilon}_2}$**= 1.24 nstrain/yr** oriented 247º.

Secondly, we computed the seismic strain rate with the **Papazachos and Kiratzi approach** (Eq. 7.3). As the method strongly depends on the b-value and the maximum magnitude, we have computed the principal strain rates for the all the catalog and for the instrumental period. For each time span, we calculated the stain rate for a $M_{w,max}$of 6.5 (Table 7.6) according to the maximum earthquake recorded by the catalog (i.e. 1522 Almeria M_w 6.5). In both cases, the azimuths of $\dot{\varepsilon}_1$ and $\dot{\varepsilon}_2$ are the same, 350º and 247º, respectively.

Table 7.6*:* Principal seismic strain rate axes (nstrain/yr) for the IGN_2013 catalog, covering all the period and only the instrumental period (from 1975) obtained by the Papazachos-Kiratzi approach, for a $M_{w,max}$of 6.5.

	a	**b**	$\boldsymbol{\dot{\varepsilon}_1}$	$\boldsymbol{\dot{\varepsilon}_2}$
All catalog	2.3	0.77	-2.15	2.17
Instrumental	4.2	1.09	-2.53	2.57

For both methodologies, the azimuths of principal seismic strain axes directions are the same, since the $\overline{F}_{ij}$ factor of Papazachos-Kiratzi and the summation of the moment tensor elements of

Kostrov are similar. That is, both approaches would give the same style of deformation, since both depend on the summation of focal mechanisms, but the magnitude can be different (depending on the seismic catalog).

In terms of magnitude, principal seismic strain rate axes calculated according to the methodology of Papazachos-Kiratzi are larger (Table 7.7). This fact can be expected, since the seismic catalog includes more events (but also these events are released in a longer time-period).

Table 7.7: Summary of principal strain rate axes computed by seismic and geodetic approaches for the entire area. For the Papazachos-Kiratzi we choose the entire catalog values.

	$\dot{\varepsilon}_1$ (nstrain/yr)	Az.	$\dot{\varepsilon}_2$ (nstrain/yr)	Az
GPS	-8.3±1	322º	22±4	52º
Kostrov	-1.2	350º	1.24	67º
Papazachos-Kiratzi	-2.2	350º	2.2	67º

Comparing the seismic and geodetic strain rates, one can easily see that the geodetic strain rates are significantly larger, especially in the case of $\dot{\varepsilon}_2$ (Table 7.7). This would indicate that some of the deformation measured using GPS takes place aseismically. Alternatively, it can also be due to the seismotectonic characteristics of the area, where big earthquakes are infrequent, resulting in long seismic cycles that are not covered by the seismic catalog. Although, using the Kostrov approach it is not possible to minimize the effects of having a shorter catalog than the seismic cycle duration, using the approach of Papazachos-Kiratzi it is possible to do so by varying the magnitude of the maximum earthquake in the seismogenic zone ($M_{w,max}$).

a) Influence of $M_{w,max}$ in Papazachos-Kiratzi approach

As we have seen before, from the seismic catalog, the Almeria 1522 M_w 6.5 is the biggest observed event, which has an associated uncertainty of 6.5±1.5 (IGN, 2013). Moreno (2011) from an integrated offshore and onshore of the Carboneras fault, estimated a maximum magnitude of M_w7.4±0.3 for the complete rupture of the northern segment of CFZ (NCF). Although the seismic catalog only covers a time period starting from 1048, we may be underestimating the maximum magnitude if the recurrence time is longer than the period covered by the catalog. Because of that, we calculated seismic strain rates using Papazachos-Kiratzi approach for an expected $M_{w,max}$ of 7.4. The results are ~11 nstrain/yr (for all catalog) and ~6 nstrain/yr (for the instrumental period).

Due to the strong dependence between calculated magnitude of the strain rate and the $M_{w,max}$ and *a*, *b* parameters, we have analyzed the variation of the seismic strain rate varying the range of these parameters. We have considered different $M_{w,max}$ for both pairs of *a* and *b* values, and the error associated to *b* value. This is, for the entire catalog, *a*=2.3 and *b*=0.77±0.05 while for the instrumental period (from 1975), *a*=4.2 and *b*=1.09±0.08. Plotting $\dot{\varepsilon}_1$ and $\dot{\varepsilon}_2$ against $M_{w,max}$ (Figure 7.10) we have found that there is an exponential relation. As Figure 7.10 shows, for maximum observed magnitudes smaller than 7.5, the calculated seismic strain rates are similar for both catalog periods (i.e., different *a* and *b* values). This would mean that Papazachos-Kiratzi approach does not have a good resolution with the given seismic catalog for $M_{w,max}$>7.5 in this area. We can also infer that having an adequate seismic catalog (and therefore a maximum magnitude observed in the area) is necessary to calculate meaningful seismic strain rates.

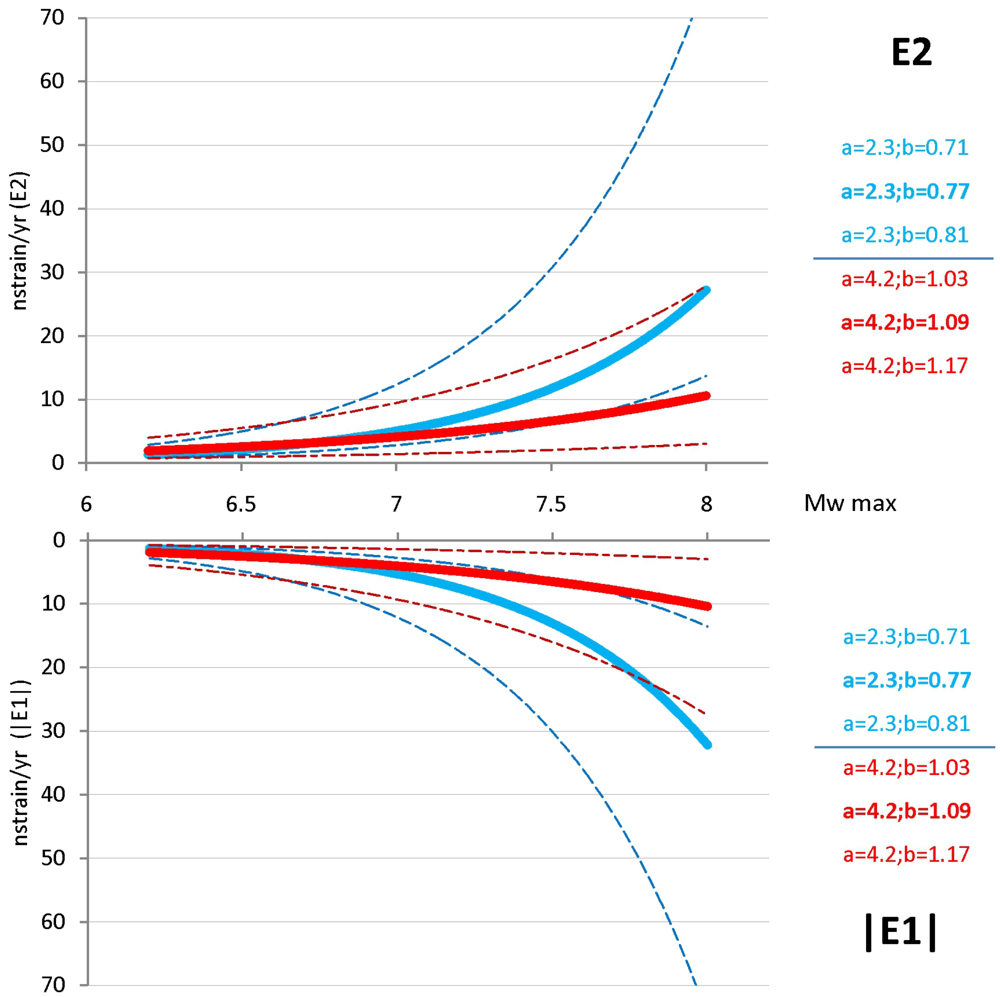

Figure 7.10: Graphic representing the relation between the seismic strain rates ($|\dot{\varepsilon}_1|$ *and* $\dot{\varepsilon}_2$) and the $M_{w,max}$ applying the Papazachos-Kiratzi approach. $\dot{\varepsilon}_1$ is shown as absolute value. Blue lines correspond to *a*

and *b* values of the entire catalog (and the pertinent errors) and red lines for the instrumental period. This graphic show the seismic strain rates calculated according to all possible variables variation.

b) Seismic vs. geodetic strain rates

Finally, in Figure 7.11 we summarized seismic and strain geodetic rates. In general, both principal strain rates are similar in magnitude except for the geodetic ones. As we saw in Section 7.2, the extensional strain rate ($\dot{\varepsilon}_{max} = \dot{\varepsilon}_2$) prevails in the strain rates obtained by GPS. For the sake of a simpler discussion, we estimated the maximum horizontal shear strain rate ($\dot{\varepsilon}_{sh-max} = \dot{\varepsilon}_2 - \dot{\varepsilon}_1$). In Figure 7.11 we can see in all cases, geodetic strain rates are larger than seismic strain rates. Even for a $M_{w,max}$ = 7.4, the maximum predicted earthquake in case of rupture of the entire NCF. This fact would suggest the presence of aseismic processes in the area. Similar results where geodetic strain rates prevail over seismic strain rates has been found in other areas like Hellenic Trench (Jenny et al., 2004), Alps (Sue et al., 2007) or Central Pannonian (Bus et al., 2009). Nevertheless, our calculations can be under-estimating seismic rates due to the incompleteness of the catalog (i.e. a big earthquake that is due is missing from the catalog), which would indicate a continuing strain accumulation, resulting in an increased level of the seismic hazard. While the magnitude of the geodetic and seismic strain rates differ considerable, their directions are very similar (Table 7.7).

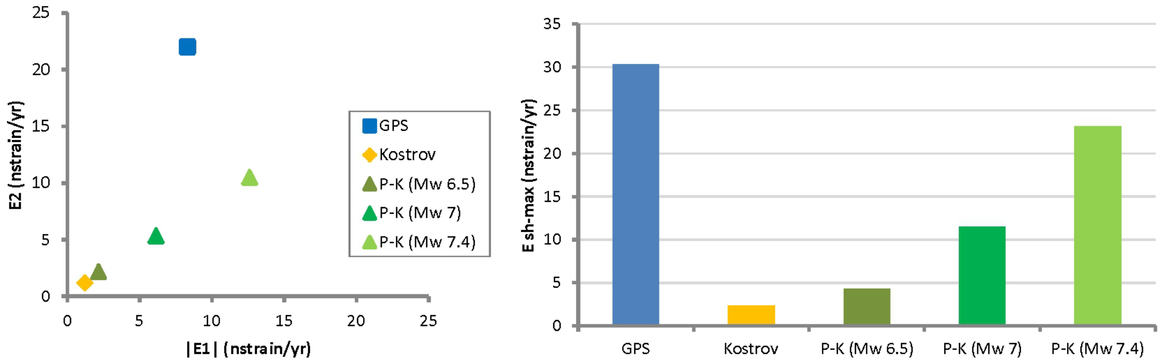

Figure 7.11: Seismic and geodetic strain rates obtained for the study area. P-K refers to Papazachos-Kiratzi approach, considering the entire catalog and different $M_{w,max}$ = 6.5, 7 and 7.4 *Left).* Principal strain rates, where $\dot{\varepsilon}_1$ is in absolute value. *Right)* Maximum shear strain rates ($\dot{\varepsilon}_{sh-max} = \dot{\varepsilon}_2 - \dot{\varepsilon}_1$) obtained by seismology or geodesy for the study area.

We note that the application of the most commonly used method of Kostrov (1974) to the study area does not provide reliable seismic strain rate estimates. This fact could be extrapolated to areas with long seismic cycle, since the moment tensor catalog in which is based this approach will be for sure shorter. However Papazachos and Kiratzi (1992) method seems more realistic than Kostrov method at least for slow deforming areas since it overcome the shortcomings of the seismological databases. This method applies to the magnitude part $(\dot{M}_0)$ the same style of deformation $(\bar{F}_{ij})$ obtained by the available focal mechanisms. It allows to incorporate the expected maximum magnitude instead of the observed maximum magnitude in the magnitude part and to be more realistic.

8. Eastern Betics kinematics

In this chapter, we include an overview and interpretation of the obtained results in this thesis. We have added a synthesis of the bigger area, with the aim of including the EBSZ zone and not only the area covered by the CuaTeNeo network.

8.1. Geodetically active faults

The crustal deformation velocity field and strain rate calculations presented in previous chapters provide clear evidence of on-going tectonic activity of the eastern Betics, implying continuing strain accumulation on regional faults. According to our investigations, the Alhama de Murcia fault (AMF) is the most evident active fault in the area (see Chapter 6 for the details).

Here, we provide a kinematic overview of other possible active faults, less evident than AMF. In order to determine fault kinematics we show in Figure 8.1 the combined velocity field (CGPS+SGPS) in different reference frames (with respect TERC and GATA stations) to facilitate a proper interpretation of the results.

We cannot explicitly quantify slip rates due to scarcity of the available data but we can attribute the type of faulting according to GPS velocities. From Figure 8.1 we can mainly infer the following key-points:

- Alhama de Murcia and Palomares faults: reverse and left-lateral movement (see Chapter 6 and Figure 8.1).
- Carboneras fault zone: left-lateral motion (see Chapter 7 and Figure 8.1b).
- Crevillente fault: left-lateral movement of the easternmost segment (compare JMIA with ALAC in Figure 8.1b); right-lateral and reverse motion for the western segment.

Anomalous behaviour in the central section (PILA and ABAN stations) of this fault (see discussion below).

- Alpujarras fault zone: right-lateral motion in the eastern (Figure 8.1b) and western (Figure 8.1a) sections.
- Bajo-Segura fault area: the observed velocity decrease from ALCA to TORR to ALAC (Figure 8.1a) suggests a shortening type kinematics.
- Carrascoy fault: shortening related to the motion of MURC or MRCI towards GANU-MAZA-MAJA (Figure 8.1a).
- Extension around PALM and MOTR stations (see discussion below).

The faulting style deducted from GPS for the mentioned active faults is consistent with most of the previously published results (see also Section 3.1). Hence, the evidence for the continuing tectonic activity of the EBSZ provided by geodesy for the past decade is consistent with geological (including paleoseismological) and geomorphological observations, spanning a considerably longer time period.

The **Crevillente fault** (CrF) shows contradictory sense of motion at its extremes, although the GPS results are not conclusive. In the western part, GPS vectors indicate dextral movement and compression meanwhile in the eastern part, closer to the city of Alicante, indicate sinistral motion. The easternmost segment is blind and even has been classified as fault normal offshore (e.g. García-Mayordomo, 2005). This complex behaviour reaffirms the concept of a Crevillente fault composed of several segments moving independently, as proposed by Sanz de Galdeano (2008). Note the discrepancy in the movement of PILA and ABAN stations in Figure 8.1, which show clearly a distinct type of motion compared to the surrounding stations. At first, one can think that these two stations are outliers. Indeed, the stability of the ABAN station can be questioned, since it belongs to REGAM network and is located on the roof of a fire station. However, station PILA belongs to Topo-Iberia network, which was specifically designed to detect crustal movements. The fact that both stations have similar velocities (direction and magnitude) and belong to different networks, suggests that both of them describe a realistic movements, probably related to tectonic deformation and are not outliers. Both stations (separated by 23 km) are located in a discontinuous, blind, part of the Crevillente fault and are positioned on the opposite sides. PILA station could be related to the prolongation of Socovos fault (SF in Figure 8.1). To clarify this anomalous behaviour of the ABAN and PILA stations, more detailed investigations would be required in the future.

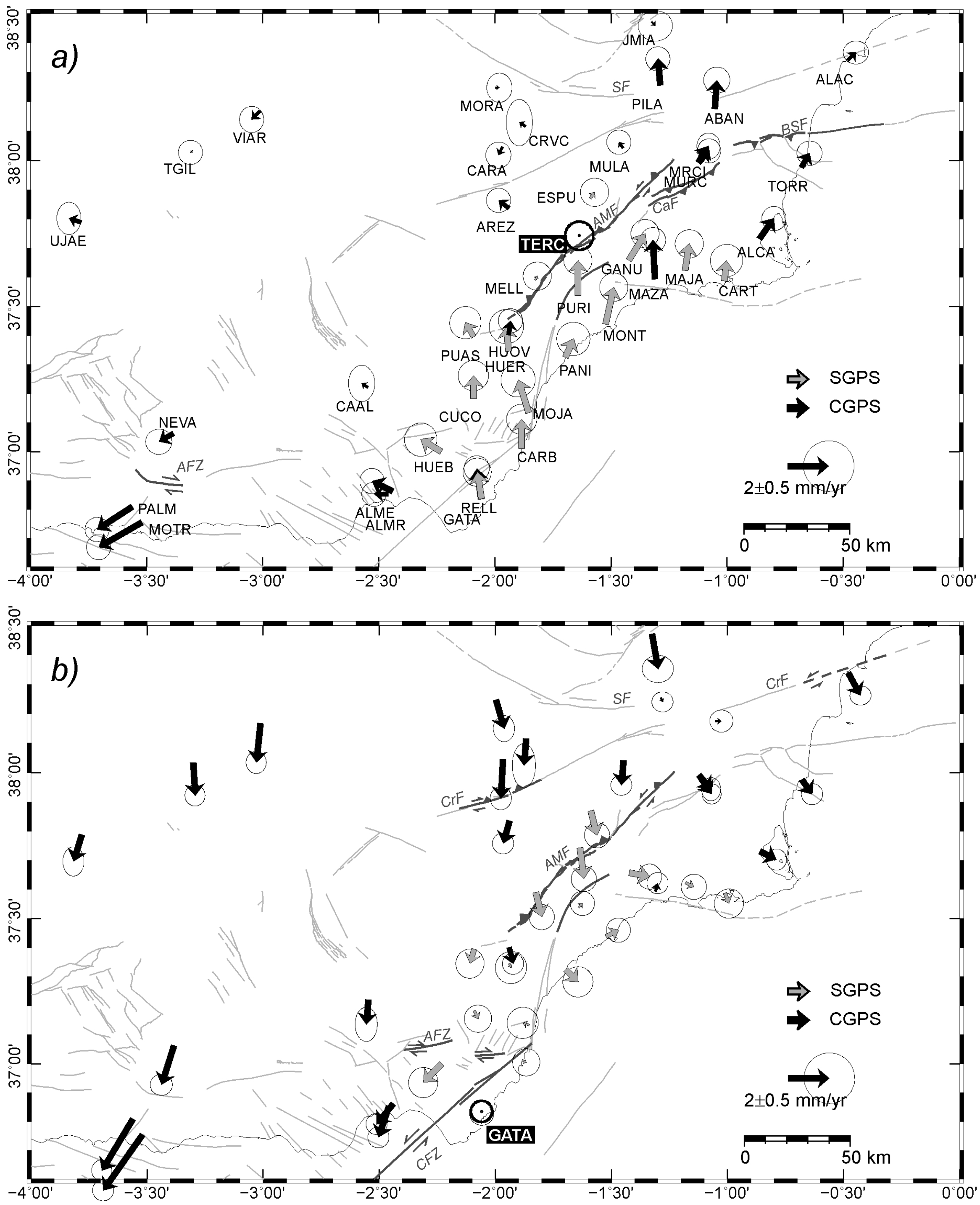

Figure 8.1: Combined horizontal velocity field with 95% confidence ellipses (from Figure 5.8). CGPS and CuaTeNeo stations shown in black and grey, respectively. In dark grey are highlight active faults referred in text. Abbreviations are: SF - Socovos fault; CrF - Crevillente fault; BSF - Bajo-Segura fault; CaF - Carrascoy fault; AMF - Alhama de Murcia fault; CFZ - Carboneras fault zone; AFZ - Alpujarras fault zone *a)* Velocities in TERC-fixed reference frame. *b)* Velocities in GATA-fixed reference frame.

8.2. Southern Betics kinematic model

The estimated velocities in eastern Betics range between 0.5 and 3.1 mm/yr in a western Europe reference frame (ALAC and MOTR stations, respectively; see Figure 8.2). As it would be expected, the stations located closer to the Nubia/Eurasia plate boundary, along the coast, move faster than the stations located farther inland. As mentioned earlier, the overall convergence rate between Nubia/Eurasia plates is of the order of 4 to 6 mm/yr (Figure 1.1), which means that a significant portion of this overall budget is accommodating within the study area.

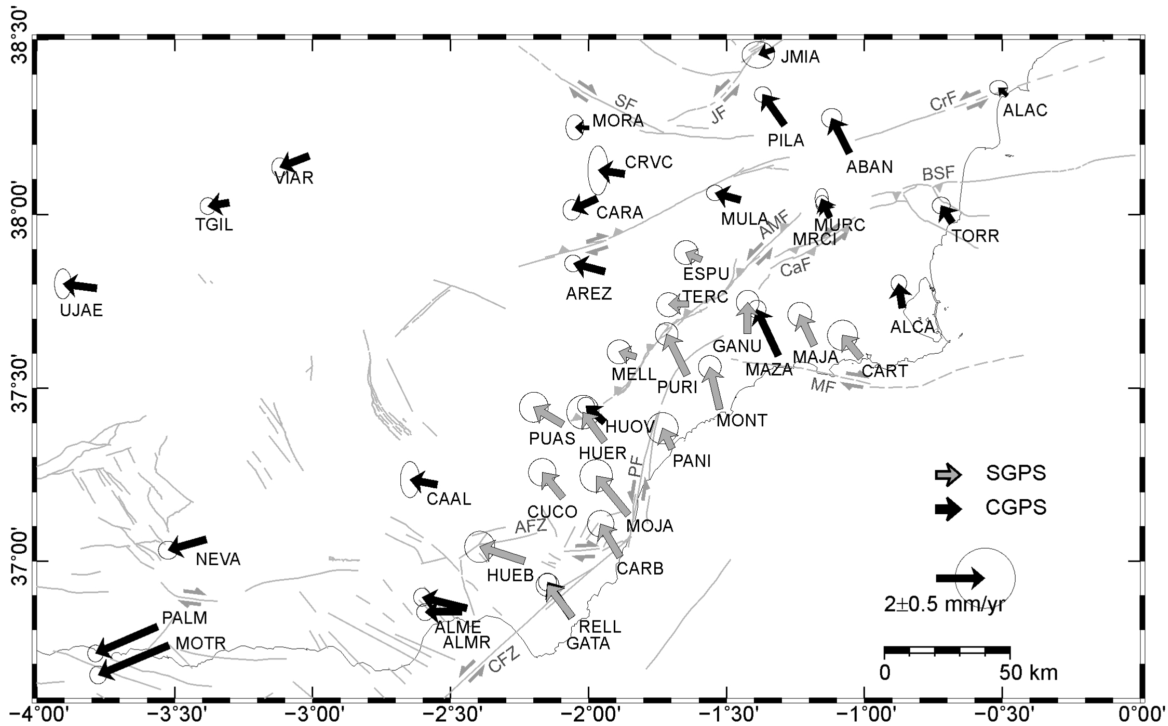

Figure 8.2: Combined SGPS and CGPS velocity field in western Europe reference frame with 95 % confidence ellipses. Fault kinematics, shown as small arrows next the faults, is deduced from GPS and literature.

As it has been noted previously, the most prominent changes in the observed velocities happen near the AMF and the Carboneras fault zone (CFZ). In Chapter 7 we focused on the kinematics of the Carboneras fault zone and dedicated very little discussion to the surrounding area. Specifically, we have not discussed the western part of the fault, where the observed GPS velocities increase in magnitude and change the direction. Because of that, here we provide a more detailed discussion about the relation of CFZ and Palomares fault and as well as the western part of CFZ.

The north-eastern termination of the CFZ continues into the Palomares fault (PF), a sinistral strike-slip fault oriented N-S (Figure 8.2). The velocities of the stations at the south-eastern block of the CFZ (GATA, RELL and CARB) and the south-western block of PF (CUCO and MOJA) show no appreciable differential motion (Figure 8.1b). This fact suggests that the on-going horizontal tectonic activity of the PF is either undetectable by the current GPS measurements or is simply inexistent. This conclusion is based on the assumption that the eastern part of the CFZ (with stations GATA, RELL and CARB) and the eastern part of the PF, where there are no nearby GPS stations, belong to the same block. Excluding station PANI, which we assumed is an outlier (see Section 5.1.1), the only stations located in the eastern block of PF are PURI and MONT. However both of these stations are located in the northern section of the Palomares fault, which precludes the determination of the activity of the southern section of the PF. Nevertheless, the overall motion of these two stations is similar to CARB, RELL and GATA that are located farther to the west.

The lack of differential motion across the PF is especially clear when examining the relative motion between the CARB and CUCO-MOJA stations (Figure 8.1b). In the northern segment of PF, which runs parallel to AMF, there are no stations on each block of the fault, so we cannot deduce whether there is a differential motion across the fault or not. But, as we discussed in Chapter 6, we attribute the bulk of the measured deformation to AMF. However, it should be mentioned that some authors do attribute a minor tectonic activity to the PF, where the suggested slip-rates are of the order of sub-millimetre per year (e.g. Booth-Rea et al., 2004; García-Mayordomo and Jiménez-Díaz, 2010) and thus, are not detectable using the current GPS station spatial and temporal coverage.

The obtained GPS velocities show a clearly opposite sense of kinematics across the Alpujarras and the Carboneras fault zones. The former shows right-lateral motion while the latter shows left-lateral motion. Martínez-Díaz and Hernández-Enrile (2004) proposed that this type of movement of the AFZ and CFZ facilitates a westward tectonic escape of the wedge bounded by these two strike-slip faults (Figure 8.3). The existence of a gradient of deformation in the escaping block favours the formation or reactivation of NNW-SSW normal faults perpendicular to the east-west extensional motion of the block. The observed W-SW gradually increasing motion of the GPS stations located in this escaping block fits well with this kinematic model (Figure 8.1b and Figure 8.2).

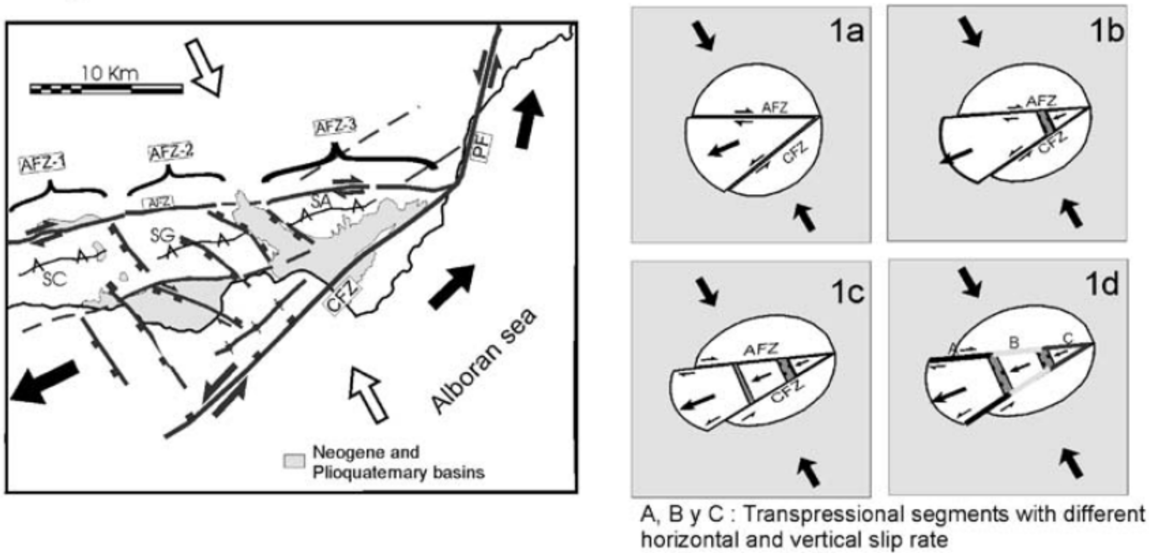

Figure 8.3: Kinematic model proposed by Martínez-Díaz and Hernández-Enrile (2004). Block escape of a wedge shaped bounded by Carboneras fault zone (CFZ) and Alpujarras fault zone (AFZ) producing local extension (from Martínez-Díaz and Hernández-Enrile, 2004).

However, the picture on a large scale is more complex. In addition to tectonic escape of CFZ-AFZ wedge, there is an east-to-west increase in the south-westward motion of the stations located north of the AFZ (compare NEVA with CAAL or CUCO in Figure 8.2). We hypothesize that in order to satisfactorily explain this complex kinematics of the crustal deformation, the existence of an additional *pulling* force is necessary. This would favour rotation and extension in the southern-central Betics, including area outside the wedge, located on the northern side of AFZ. Considering the proximity of the oceanic slab in depth (Figure 8.4), which is located further west and possibly attached to the continental crust in central Betics and eastern Rif (e.g. Bonnin et al., 2014), sub-lithospheric processes such as a rollback of the subducting slab, can be responsible for such a pull. In this context, Rutter et al. (2012) consider CFZ as part of a stretching fault system which acted as a lateral boundary of a slab rollback region (see Figure 8.4c). In this model, the area bounded by Crevillente fault to the north, and AMF-PF-CFZ to the southeast would accommodate by stretching the slab rollback. In this sense, the observed SW motion agree with this model. An observed change in the motion of the GPS velocities, starting from the location of station HUEB (2.5°W, Figure 8.2), approximately coincides with the area where a significant east-to-west increase of the lithospheric thickness is deduced from seismic studies (Levander et al., 2014). However, if these fault systems are stretching in the present, also CrF must be active. With the available GPS data, we cannot affirm that. Also, geological and geomophological data (although this type of studies are scarce) indicate low Quaternary activity of this fault, suggesting a net slip rate of ~0.1 mm/yr (e.g. García-Mayordomo et al., 2012 and references therein). We suggest that the sub-lithospheric processes affect this area in a diffuse way, being more important to the south. Thus, a GPS densification in the region west to CuaTeNeo network and between 37º-38ºN would help to clarify the kinematics and geodynamics of the southern Betics. It is noteworthy, that in this spatial gap, does exist a CGPS station of RAP network, PALC, which can help to clarify the above-mentioned interpretations. However, in this study we have not included PALC due to the limited time-span of the available data.

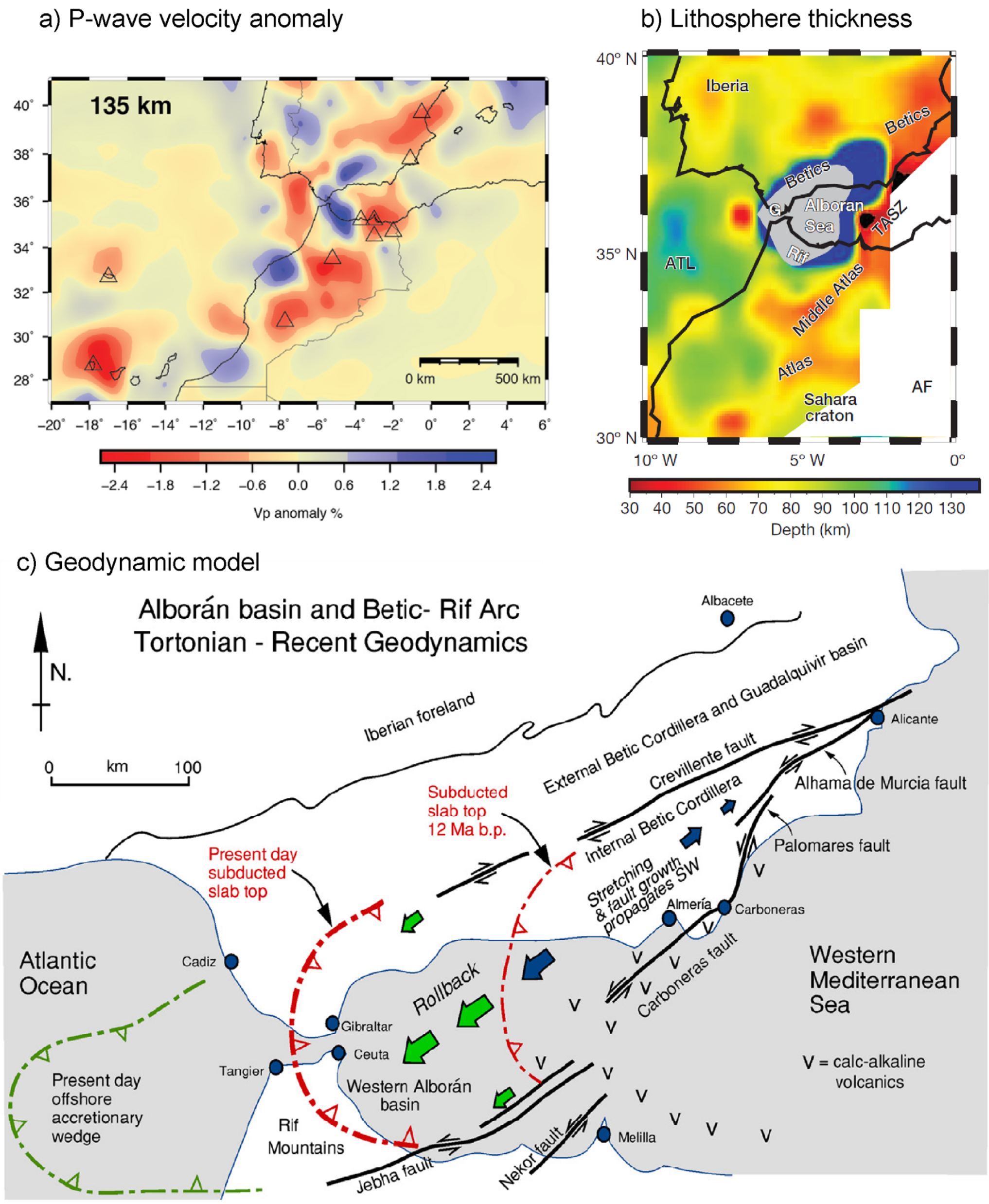

Figure 8.4: *a)* Tomographic P-wave velocity model at 135 km depth. High velocity anomaly (blue) beneath Alboran Sea is interpreted by the authors as a lithospheric slab (from Bonnin et al., 2014). *b)* Lithospheric thickness from Levander et al. (2014). *c)* Geodynamic scheme based on Lonergan and white (1997) and Gutscher (2012) (from Rutter et al. (2012)).

To summarize, we propose that the Carboneras fault zone acts as a boundary between the eastern fault-block that moves parallel to the plate convergence and the western block that moves westward due to the block escape and also influenced by deeper sub-lithospheric processes. This assumption is also supported by the description of the CFZ as a major crustal-scale fault that reaches the Moho (e.g. Pedrera et al., 2010).

On a more regional scale, Pérouse et al. (2010), combined GPS data with numerical modelling, and suggested a similar causes for the observed kinematics, caused by a combined effect of plate convergence, low rigidity of the Alboran Sea region and a S-SW directed traction related to sub-lithospheric processes.

8.3. Regional velocity domains

To study general characteristics of the observed GPS velocities, we have divided the combined velocity field into three main domains, according to the magnitude and orientation of the velocity vectors (Figure 8.5), as well as, taking into account our geodetic interpretations, as discussed throughout this thesis. In a map view, these three domains can be differentiated geographically as shown in Figure 8.6.

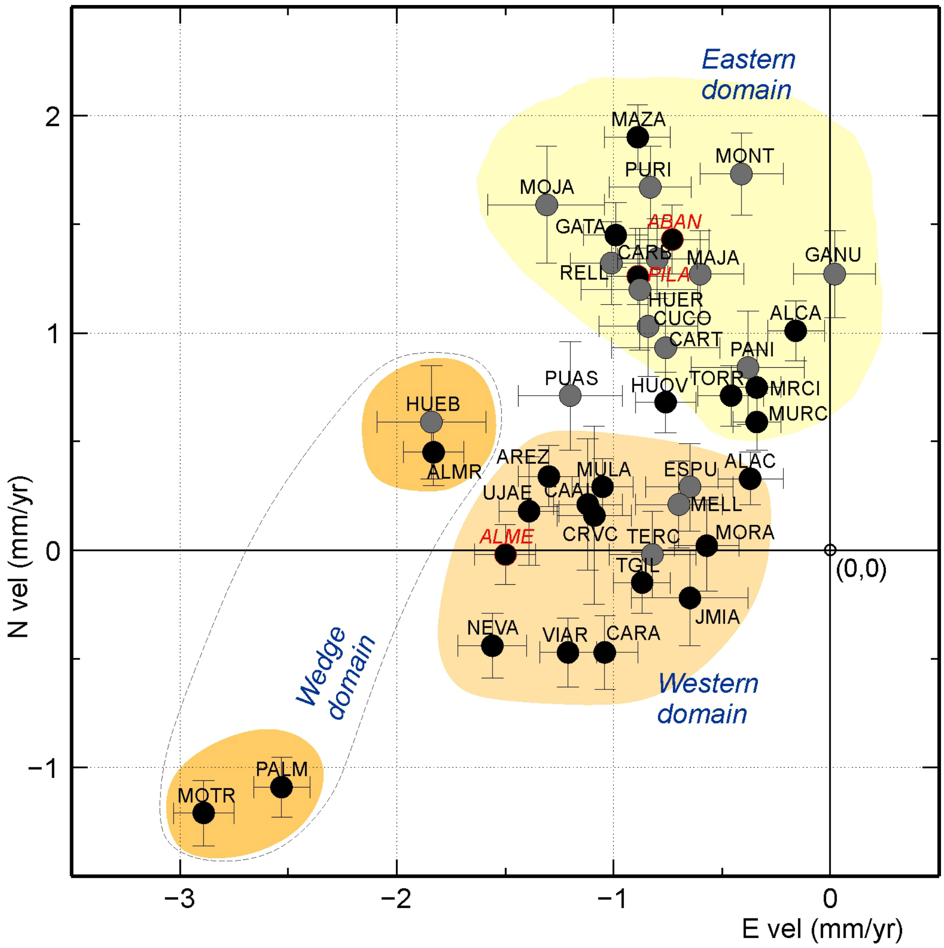

Figure 8.5: East and North component velocities in western Europe reference frame, increasing in magnitude from zero (0,0) to the left and upward, respectively. CuaTeNeo sites are in gray and CGPS in black. Error bars represent 1σ uncertainties. Color groups represent velocity domains. Station IDs in red depict "outliers" discussed in details in this section.

The 'eastern domain' includes 17 stations located in eastern sectors of AMF and CFZ as well as the southern part of AMF. This domain moves generally in a N-NW direction (w.r.t. western Europe), parallel to plate convergence. A trend of reducing velocities in the northern part of this domain is also observed (Figure 8.6). The 'western domain', on the other hand, is characterized by lower velocities, with more westerly orientations. In this domain, the reduction in the observed velocities is especially prominent in the N-S component of motion (Figure 8.5). In addition, we define a third domain, called 'wedge domain', bounded by CFZ and AFZ, which includes five stations. Inside this domain, we observe a southwesterly acceleration of the points, which is most likely driven by the block escape tectonics, as explained previously. In general, the distinction between the wedge and the western domain is not as clear, since the direction of motion on both domain is similar. However, we opted for the separation because the internal acceleration and rotation inside the wedge domain.

In Figure 8.5 and 8.6, we highlight in red the stations that in our opinion are outliers and do not belong to the domain in which they are located geographically. These stations are ABAN, PILA and ALME. ABAN and PILA stations clearly move in the same fashion as the "eastern domain", while geographically they form part of the "western domain". As discussed in the previous section, we cannot explain this anomalous behavior with the available data. Similarly, station ALME, although is located inside the wedge, shows a velocity more coherent with the "western domain" (Figure 8.5). As discussed in Section 7.1.2 we attribute this motion to the local instability of the monument or the bulding.

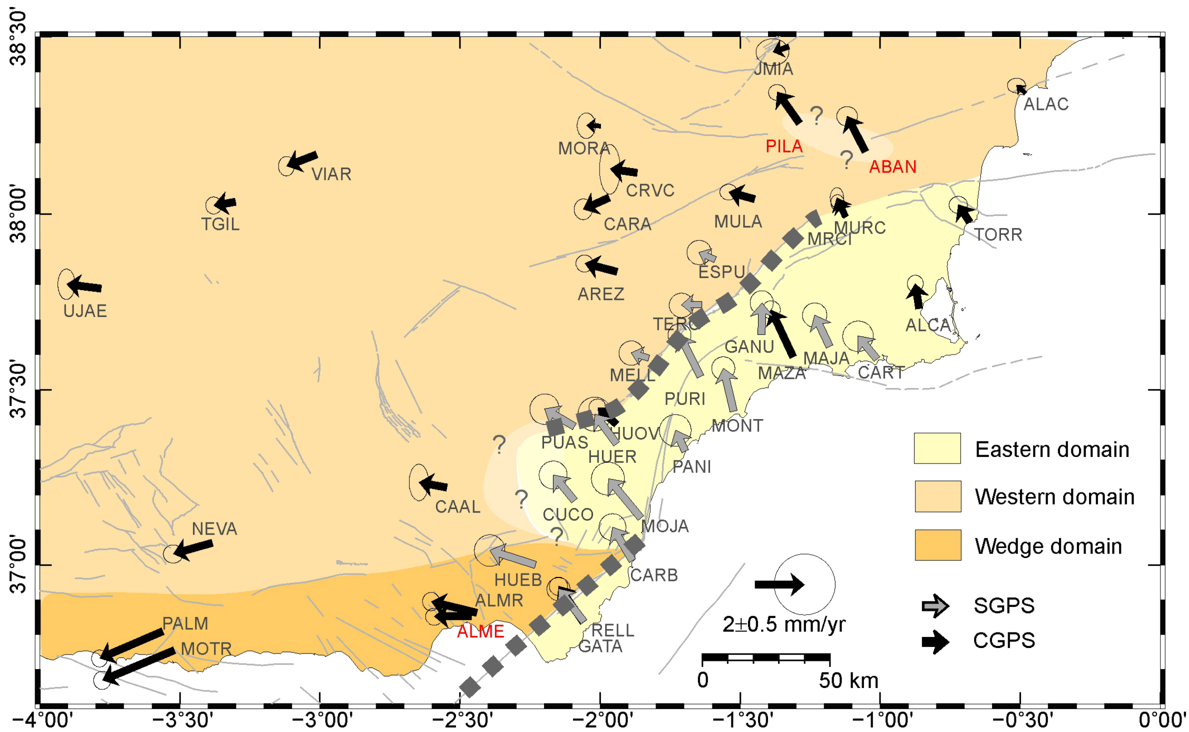

Figure 8.6: Velocity domains over combined velocity field (see Figure 8.2) with respect western Europe and 95% confidence error ellipses. Dashed thick line indicates the domains boundary, where part of the convergence is accommodated.

In general, the boundaries between these three domains, should coincide with the areas where the deformation due to plate convergence is absorbed. The principal structure where the biggest decrease in the observed velocities (shortening slip rate of ~0.8 mm/yr) is accommodated is the AMF (Figure 8.1a and 8.6). As a result, as we explained in Chapter 6, the highest strain rates are observed across this fault. To the north of the AMF, the Carrascoy and the blind reverse Bajo Segura (BSF) faults may be the continuation of this boundary. We have chosen BSF instead of Crevillente fault based on the recent GPS results (see Figure 3.11) of Alfaro et al. (2014) and the suggested deformation migration from CrF to BSF since Pliocene (Martin-Rojas et al., 2014).

To the south, the boundary may be traced through the Albox reverse fault and further west trough Corredor de Almanzora. This corridor is an E-W elongated depression deformed by widespread small-scale contractional tectonic structures located west of Albox fault (e.g. Pedrera et al., 2007; Pedrera et al., 2009). Taking into account the velocity vectors of PUAS, HUOV and HUER stations, this limit would lie in between (see Figure 8.5 where PUAS and HUOV are in a "transition zone", while HUER belongs to eastern domain). Farther south, CFZ relays AMF. In this proposed model, Palomares fault does not form part of this boundary and the step between AMF and CFZ seems to be located west of CUCO station. It is possible that some buried unknown small transfer fault facilitate this jump between the AMF and CFZ faults.

The suggested velocity domains are in good agreement with crustal blocks established by Rodríguez-Escudero et al. (2013), who used independent data based on earthquake seismicity and tectonic interpretation (Figure 8.7). Although some minor differences are observed between this model and the boundaries suggested in this thesis, the idea of blocks bounded by large E-W to NE-SW strike-slip faults prevails. Moreover, the recent work of El Moudnib et al. (2015) finds a strong change in P-wave velocity, from 8 to 24 km depth, across the TASZ (see Section 3.1.1), with slow velocities in the west and fast ones in the east. This change in seismic velocities would coincide with the offshore part of CFZ. Thus, the EBSZ, and in turn TASZ, are clearly important crustal structures, which separate different crustal blocks.

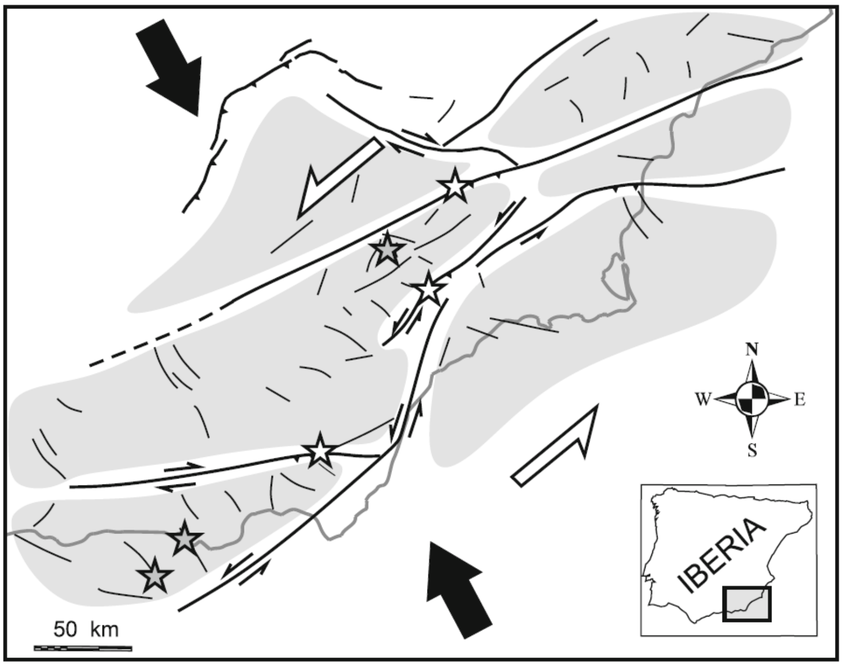

Figure 8.7: Crustal seismogenic block model from Rodríguez-Escudero et al. (2013). Crustal blocks, marked in gray, bounded by E-W to NE-SW large strike-slip faults. In these boundaries is where earthquakes M_w > 5.5 take place (white stars).

The proposed velocity domains and, especially the accommodation of deformation along AMF and CFZ, have to be considered in kinematic and geodynamic models. For example, Asensio (2014) and Asensio et al. (2014) used the CuaTeNeo velocity field and the derived implications to improve the boundary of the block model in this area. The GPS velocity domains can be treated as higher order crustal blocks, which can be further subdivided into smaller rigid blocks.

Summing up, part of the convergence between Eurasia and Nubia tectonic plates is accommodated in the eastern Betics by the Eastern Betic Shear Zone. AMF and CFZ, explored in detail in this thesis, are the main active faults in the area and present similarities but also differences. While both faults are similar in orientation and longitude, their seismic record and behavior are different. The AMF has been clearly associated with both instrumental and historical seismicity. Moreover, AMF exhibits a major reverse component, resulting in a transpressional faulting. Meanwhile, for the CFZ, while the geodetic slip-rates obtained in this thesis are of the same order of magnitude, presently very little seismicity is associated with this fault. The possibility of seismic and aseismic (mixed-mode, Section 3.1.1.3) behavior of CFZ and the active role of each of these two faults in deformation absorption and geodynamic context will require further detailed studies, especially for improving a seismic hazard evaluation.

9. Conclusions

The research presented in this thesis focuses on the use of the space-geodetic observations, such as GPS, to study present-day kinematics of the eastern Betics. Here we provide the major findings presented in this research and perspectives of future work.

9.1. Main conclusions

This work is an important contribution for the seismic hazard estimation of eastern Betics because it is the first time crustal deformation rates at this scale and detail are presented. The presented GPS-derived horizontal velocity field of the present-day crustal deformation rates in the eastern Betics is based on the analysis of 16 survey style GPS stations of the CuaTeNeo network measured over a 15 yr period from 1997 to 2011 and 25 continuous GPS stations for the time period of 2008.8-2013.3. The reported work reaffirms the usefulness of the campaign-style GPS observations even in areas with slow deformation.

The velocity field and subsequent strain rate analysis clearly illustrate that the SE part of the Betics is currently tectonically active. This is especially true near the Alhama de Murcia fault (AMF). The most prominent feature of the presented velocity field is the NW oriented dominant motion of the majority of the stations at rates ranging 0.5 to 3 mm/yr in a western Europe reference frame. This deformation indicates that the main driving force behind the observed velocities is related to the on-going convergence between the Nubia and the Eurasia plates.

GPS velocities and the derived strain rate field suggest a dominant NW-SE oriented compression, with a SW-NE extension in the south-western part of the study area. On a more detailed scale, we find two distinct zones with significant deformation but opposite behavior: the NE sector is undergoing compression, where $|\dot{\varepsilon}_{min}| > |\dot{\varepsilon}_{max}|$ and 2-D dilatation is negative, which is consistent with a convergent plate boundary. Also in this zone shear strain rate values are at its maximum, indicating a presence of a transpressive regime, expressed by reverse and left-lateral faults, such as the AMF. In the SW sector near Almeria the dominance of $\dot{\varepsilon}_{max}$ indicates a presence of a thinning or extensional kinematics, related to the block escape tectonics and possibly slab rollback.

Most of the observed deformation is concentrated within the Alhama de Murcia-Palomares faults region. The geodetic horizontal slip rate (reverse-sinistral) of 1.5±0.3 mm/yr calculated for the AMF and PF fault system corresponds to a maximum and is in good agreement with geologic observations as well as the focal mechanism of the 2011 Lorca earthquake. With the present-day GPS data, due to an absence of GPS data between the AMF and PF, it is impossible to determine the relative partitioning of deformation between the AMF and PF faults. Based on the predictions of the 2-D elastic dislocation model for the AMF, we could say that the geodetic measurements indicate that locked portion of the fault is shallow. However, our results preclude the distinction between the aseismic and/or shallow locked fault behavior at the SW part of the AMF.

The CuaTeNeo nearest stations have not identified co-seismic deformation related to 2011 Lorca earthquake (M_w 5.2). Nevertheless, detailed analysis of the time-series of the continuous GPS station (LRCA) from the city of Lorca allows the detection of co-seismic offset of ~6 mm to the North. The adopted elastic dislocation model is in agreement with the co-seismic displacements observed at LRCA station.

The analysis of the GPS data in the southern Betics, confirm and quantify the on-going tectonic activity of the onshore Carboneras fault zone (CFZ) as a left-lateral strike slip fault. For the first time, we were able to provide a quantitative measure of the present-day horizontal geodetic slip-rate of the CFZ, suggesting a maximum left-lateral strike slip motion of 1.3±0.2 mm/yr. The coincidence of the geologic and geodetic fault slip rates for the CFZ, illustrates that during Quaternary the northern segment of the CFZ has been tectonically active and has been slipping at a constant rate of 1.1 to 1.5 mm/yr.

Since we cannot discern the nature of the strain accumulation along the CFZ (e.g. creep vs. locking) by GPS data, we have attempted to compare seismic and geodetic strain rates. Geodetic strain rates are larger than seismic strain rates, suggesting the presence of aseismic processes in the area. Nevertheless, due to the large earthquake recurrence intervals, we may be underestimating the seismic strain rates. The direction of the P and T average axes are in agreement with geodetic principal strain axes.

We have also found that the Palomares fault (PF), is currently inactive or is slipping very slowly (< 0.5 mm/yr), at rates that are undetectable by the current GPS station spatial-temporal coverage.

Regarding the eastern part of the Alpujarras fault zone corridor (AFZ), our GPS measurements corroborate that this zone is active and accumulates a right-lateral motion to compensate for the observed left-lateral motion of the CFZ. These opposite type strike-slip motion across the AFZ and CFZ is a result of Nubia and Eurasia plate convergence, which results in the westward escape of the block bounded by these faults.

As a compendium, we propose in broad strokes three different domains separated by Alhama de Murcia and Carboneras faults. The eastern domain, moves parallel to Nubia-Eurasia convergence and the western domain is characterized by more westerly sense of motion. The boundary zones between these domains absorb part of the convergence, and, in case of the CFZ facilitate the block escape of the wedge domain (bounded by CFZ and Alpujarras fault zone). The wedge domain, and partially the western domain is also influenced by slab rollback

To summarize, in eastern Betics, Alhama de Murcia and Carboneras left-lateral faults are the most active faults and they play an important role in the regional plate convergence kinematics.

9.2. Future research

Here we summarize future research in order to better understand the kinematics of the area and help to answer open questions not solved in this work.

The work line most directly related with this study is the establishment of new geodetic points in the region. An alternative to built new monuments is to observe the REGENTE network (Red Geodésica Nacional por Técnicas Espaciales) from IGN (Quirós Donate and Barandillo Fernández, 1996). This network has a good and uniform spatial coverage, although the location and the design of the geodetic monuments is not optimal for detecting millimetric level tectonic deformations. Moreover, the determination of the vertical component of deformation would be very helpful for validating the suggested kinematic models, as well as to discern between the seismic and aseismic type slip at reverse faults. Long continuous time-series would be necessary in order to obtain significant results for the vertical velocities. The use of the vertical component of the survey stations is somewhat more problematic, since usually during the various campaigns variable antennas and instruments are used. Below we propose a more detailed proposal for the two priority zones:

- We propose to establish new GPS points in-between the Alhama de Murcia and Palomares faults to determine relative strain partitioning and the locking depth of AMF. In 2013, we took an advantage of a fieldwork in the area and we visited some candidate places to install these points. In order to facilitate the future work, here we provide the coordinates of two possible emplacements based on location and stability considerations (Figure 9.1). Since the subsiding Guadalentín basin is in between the both faults, it is difficult to find a stable emplacement with a bedrock. Because of that, AMF-1 is located in the unique bedrock outcrop: the Enmedio range (mesozoic rocks). As a suggestion, other station can be located near Purias (AMF-2), although it is necessary to better delimit the fault trace of the PF, in order to remain in between the two faults. The proposed locations of these points are:

  AMF-1: Sierra de Enmedio: 37°32'17.72"N, 1°46'53.21"O (RM-D19 road)
  AMF-2: Purias: 37°35'15.68"N, 1°38'6.26"O

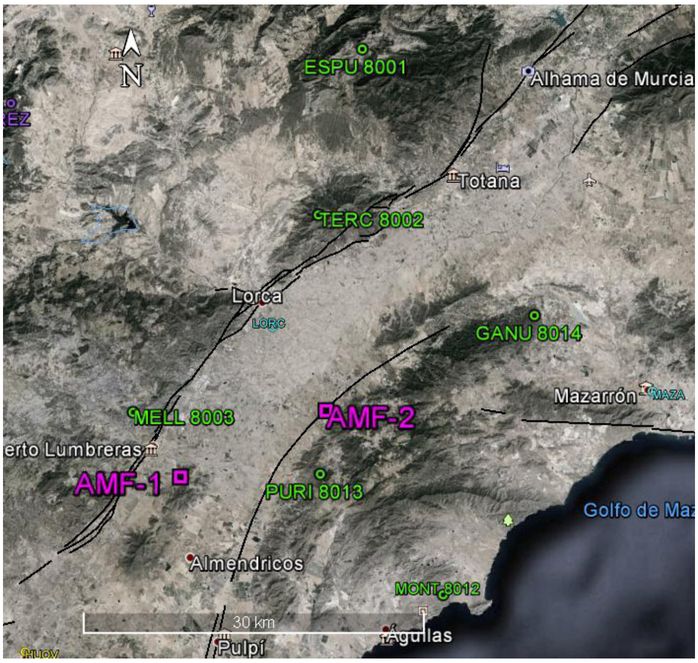

Figure 9.1: Location map of GPS stations proposed (AMF-1 and AMF-2). In green, CuaTeNeo SGPS stations and fault traces from QAFI database.

- We propose a detailed study of the Carboneras fault with the aim of determining the seismic or mixed-mode (aseismic and seismic) behaviour of the fault. This question is crucial for the improved seismic hazard calculation in the area. To this proposal, GPS stations near the fault are necessary although other approaches as rheological studies or the installation of creep meters would also be useful. Concerning this, we have modelled several locking depths for CFZ with Tdefnode (McCaffrey, 2009) and compared the model predictions with the existent data (Figure 9.2). This profile may help to better choose a localization of the future GPS stations, especially regarding their separation from the fault trace.

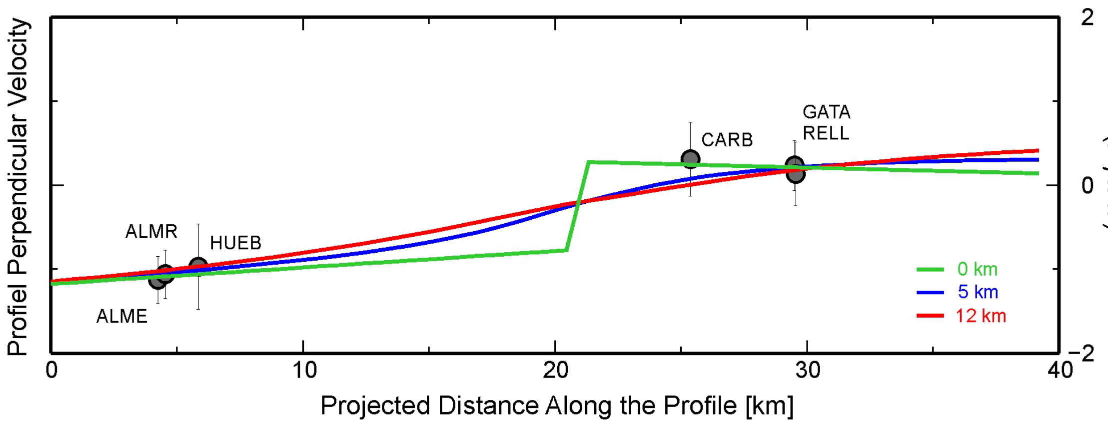

Figure 9.2: Velocity profile across the CFZ with 1σ error bars (see Figure 7.1 for profile location). The fault parallel velocity components (i.e., profile normal velocity components) are represented. The model

predictions were obtained with Tdefnode elastic block modeling program (McCaffrey, 2009) for 0 (green), 5 (blue) and 12 km (red) locking depths, assuming two rigid blocks divided by NCFZ dipping 88º.

Regarding the comparison between geodetic and seismic strain rates, the inclusion of the historical seismicity (e.g. Papazachos and Kiratzi, 1992) shall be necessary in regions of slow deformation. To obtain the associated errors of seismic strain rates would also be useful.

In order to better discern and clarify the unexpected motion of PILA and ABAN stations located near Crevillente fault, a detailed geological study of this area or the inclusion of more control points will be necessary.

In terms of regional interpretation, although we have enlarged the study area to give a general framework, detailed studies west of Motril (3.5ºW) and north of Alpujarras zone (including PALC station of the RAP network) would be necessary. Moreover, the relay between AMF and CFZ shows a step-zone where the nature of the deformation accommodation is not known. There is no known geological structure in this location that can transfer this discontinuous sinistral deformation. The combination of geomorphological, geological, seismic and geodetic studies, as well as, numerical modeling should help to clarify this region.

References

Alfaro, P., Bartolomé, R., Borque, M.J., Estévez, A., García-Mayordomo, J., García-Tortosa, F.J., Gil, A.J., Gràcia, E., Iacono, C.L., Perea, H., **2012**. The Bajo Segura Fault Zone: Active blind thrusting in the Eastern Betic Cordillera (SE Spain). J. Iberian Geol. 38 (1), 271-284. http://dx.doi.org/10.5209/rev_JIGE.2012.v38.n1.39217.

Alfaro, P., Borque, M.J., Estévez, A., Gil, A.J., Molina, S., **2000**. Red de control GPS de la Cuenca del Bajo Segura (Cordillera Betic Oriental). Geotemas 1 (4), 245-248.

Alfaro, P., Martín-Rojas, I., Estévez, A., García-Tortosa, F.J., Sánchez-Alzola, A., Borque, M.J., Rodríguez Caderot, G., De Lacy, M.C., García-Armenteros, J.A., Avilés, M., Herrera-Olmo, A., Molina, S., Rosa-cintas, S., Gil, A., **2014**. Bajo Segura basin GPS Network (Eastern Betic Cordillera). Significance on the Bajo Segura and Crevillente fault slip rates., in: Álvarez gómez, J.A., Martín González, F. (Eds.), Segunda Reunión Ibérica sobre Fallas Activas y Paleosismología (IberFault), Lorca, Murcia, Spain, pp. 205-208

Altamini, Z., Collilieux, X., Métivier, L., **2011**. ITRF2008: An improved solution of the international terrestrial reference frame, J. Geodesy, pp. 457-473. http://dx.doi.org/10.1007/s00190-011-0444-4

Allmendinger, R., W., Reilinger, R., Loveless, J., **2007**. Strain and rotation rate from GPS in Tibet, Anatolia, and the Altiplano. Tectonics 26 (3), TC3013. http://dx.doi.org/10.1029/2006TC002030.

Allmendinger, R.W., Cardozo, N., Fisher, D.M., **2012**. Structural Geology Algorithms: Vectors and Tensors. Cambridge University Press.

Andrieux, J., Fontbote, J.M., Mattauer, M., **1971**. Sur un modele explicatif de l'arc de Gibraltar. Earth Planet. Sci. Lett. 12 (2), 191-198.

Argus, D.F., Gordon, R.G., **1991**. No-net-rotation model of current plate velocities incorporating plate motion model NUVEL-1. Geophys. Res. Lett. 18 (11), 2039-2042.

Argus, D.F., Gordon, R.G., Demets, C., **2011**. Geologically current motion of 56 plates relative to the no-net-rotation reference frame. Geochem. Geophys. Geosyst. 12 (11). http://dx.doi.org/10.1029/2011GC003751.

Argus, D.F., Gordon, R.G., Heflin, M.B., Ma, C., Eanes, R.J., Willis, P., Peltier, W.R., Owen, S.E., **2010**. The angular velocities of the plates and the velocity of Earth's centre from space geodesy. Geophys. J. Int. 180 (3), 913-960. http://dx.doi.org/DOI: 10.1111/j.1365-246X.2009.04463.x.

Asensio, A., Khazaradze, G., Echeverria, A., **2014**. Modelo cinemático de bloques de la región Ibero-Magrebí a partir de datos geodésicos, in: Álvarez Gómez, J.A., Martín González, F. (Eds.), Segunda Reunión Ibérica sobre Fallas Activas y Paleosismología (IberFault), Lorca, Murcia, Spain, pp. 221-224

Asensio, E., **2014**. Estudios de la deformación cortical de la península ibérica mediante observaciones GPS. PhD thesis, Universitat de Barcelona, Barcelona, p. 208

Bath, M., **1981**. Earthquake magnitude-recent research and current trends. Earth-Science Reviews 17 (4), 315-398. http://dx.doi.org/10.1016/0012-8252(81)90014-3.

Bell, J.W., Amelung, F., King, G.C.P., **1997**. Preliminary late quaternary slip history of the Carboneras fault, southeastern Spain. J. Geodyn. 24 (1-4), 51-66.

Benito, B., Capote, R., Murphy, P., Gaspar-Escribano, J.M., Martinez-Diaz, J.J., Tsige, M., Stich, D., Garcia-Mayordomo, J., Garcia Rodriguez, M.J., Jimenez, M.E., Insua-Arevalo, J.M., Alvarez-Gomez, J.A., Canora, C., **2007**. An overview of the damaging and low magnitude M (sub w) 4.8 La Paca earthquake on 29 January 2005; context, seismotectonics, and seismic risk implications for Southeast Spain. Bull. Seismol. Soc. Am. 97 (3), 671-690. http://dx.doi.org/10.1785/0120050150.

Berrocoso, M., Páez, R., Sánchez-Alzola, A., Pérez-Peña, A., Ramírez, M.E., Jimenez, Y., Hermosilla, A., Redondo, M., **2006**. The RAP Net: A Geodetic Positioning Network for Andalusia (South Spain), Symposium of the IAG Subcommission for Europe (EUREF), Riga, Latvia, 14 - 17 June 2006, p. poster

Beyreuther, M., Barsch, R., Krischer, L., Megies, T., Behr, Y., Wassermann, J., **2010**. ObsPy: A Python Toolbox for Seismology. Seismol. Res. Lett. 81 (3), 530-533. http://dx.doi.org/10.1785/gssrl.81.3.530.

Bezada, M.J., Humphreys, E.D., Toomey, D.R., Harnafi, M., Dávila, J.M., Gallart, J., **2013**. Evidence for slab rollback in westernmost Mediterranean from improved upper mantle imaging. Earth Planet. Sci. Lett. 368, 51-60. http://dx.doi.org/10.1016/j.epsl.2013.02.024.

Blanco, M.J., Spakman, W., **1993**. The P-wave velocity structure of the mantle below the Iberian Peninsula: evidence for subducted lithosphere below southern Spain. Tectonophysics 221, 13-34.

Blewitt, G., **1997**. Basics of the GPS Technique: Observation Equations, in: Johnson, B. (Ed.), Geodetic Applications of GPS. Nordic Geodetic Commission, Sweden, pp. 10-54.

Blewitt, G., **2009**. GPS and Space-Based Geodetic Methods, in: Herring, T. (Ed.), Treatise on Geophysics. Elsevier, Amsterdam, pp. 351-390.

Blewitt, G., Lavallée, D., **2002**. Effect of annual signals on geodetic velocity. J. Geophys. Res. 107 (7), 9-1. http://dx.doi.org/10.1029/2001JB000570

Boccaletti, M., Papani, G., Gelati, R., Rodríguez-Fernández, J., López Garrido, A.C., Sanz de Galdeano, C., **1987**. Neogene-Quaternary sedimentary-tectonic evolution of the Betic Cordillera. Acta naturalia de l'Ateneo parmense 23 (4), 179-200.

Boehm, J., Niell, A., Tregoning, P., Schuh, H., **2006**. Global Mapping Function (GMF): A new empirical mapping function based on numerical weather model data. Geophys. Res. Lett. 33 (7), L07304. http://dx.doi.org/10.1029/2005gl025546.

Bonnin, M., Nolet, G., Villaseñor, A., Gallart, J., Thomas, C., **2014**. Multiple-frequency tomography of the upper mantle beneath the African/Iberian collision zone. Geophys. J. Int. 198 (3), 1458-1473. http://dx.doi.org/10.1093/gji/ggu214.

Booth-Rea, G., Azañón, J.M., Azor, A., García-Dueñas, V., **2004**. Influence of strike-slip fault segmentation on drainage evolution and topography. A case study: The Palomares Fault Zone (southeastern Betics, Spain). J. Struct. Geol. 26 (9), 1615-1632.

Bos, M.S., Fernandes, R.M.S., Williams, S.D.P., Bastos, L., **2013**. Fast error analysis of continuous GNSS observations with missing data. J. Geodesy 87 (4), 351-360. http://dx.doi.org/10.1007/s00190-012-0605-0.

Bousquet, J.C., **1979**. Quaternary strike-slip faults in southeastern Spain. Tectonophysics 52, 277-286.

Bousquet, J.C., Montenant, C., **1974**. La néotectonique dans les Cordillères Bétiques orientales, 2ème Reunion des Sciences de la Terre, Nancy, France

Bruyninx, C., **2004**. The EUREF Permanent Network: a multi-disciplinary network serving surveyors as well as scientists. GeoInformatics 7, 32-35.

Buforn, E., Benito, B., Sanz de Galdeano, C., del Fresno, C., Muñoz, D., Rodriguez, I., **2005**. Study of the Damaging Earthquakes of 1911, 1999, and 2002 in the Murcia, Southeastern Spain, Region: Seismotectonic and Seismic-Risk Implications. Bull. Seismol. Soc. Am. 95 (2), 549-567. http://dx.doi.org/10.1785/0120040041.

Buforn, E., Bezzeghoud, M., Udías, A., Pro, C., **2004**. Seismic Sources on the Iberia-African Plate Boundary and their Tectonic Implications. Pure Appl. Geophys. 161 (3), 623 - 646. http://dx.doi.org/10.1007/s00024-003-2466-1.

Buforn, E., Pro, C., Cesca, S., Udias, A., del Fresno, C., **2011**. The 2010 Granada, Spain, Deep Earthquake. Bull. Seismol. Soc. Am. 101 (5), 2418-2430. http://dx.doi.org/10.1785/0120110022.

Buforn, E., Sanz de Galdeano, C., **2001**. Focal mechanism of Mula (Murcia, Spain) earthquake of February 2, 1999. J. Seismol. 5 (2), 277-280. http://dx.doi.org/10.1023/a:1011472400818.

Buforn, E., Sanz de Galdeano, C., Udías, A., **1995**. Seismotectonics of the Ibero-Maghrebian region. Tectonophysics 248 (3-4), 247-261.

Bus, Z., Grenerczy, G., Tóth, L., Mónus, P., **2009**. Active crustal deformation in two seismogenic zones of the Pannonian region - GPS versus seismological observations. Tectonophysics 474 (1-2), 343-352.

Calvert, A., Sandvol, E., Seber, D., Barazangi, M., Roecker, S., Mourabit, T., Vidal, F., Alguacil, G., Jabour, N., **2000**. Geodynamic evolution of the lithosphere and upper mantle beneath the Alboran region of the western Mediterranean: Constraints from travel time tomography. J. Geophys. Res. 105 (B5), 10871-10898 http://dx.doi.org/10810.11029/12000JB900024.

Calvo, M., Vegas, R., Osete, M.L., **1997**. Palaeomagnetic results from Upper Miocene and Pliocene rocks from the Internal Zone of the eastern Betic Cordilleras (southern Spain). Tectonophysics 277 (4), 271-283. http://dx.doi.org/10.1016/S0040-1951(97)00033-4.

Cano Villaverde, M.A., Sánchez Sobrino, J.A., Valdés Pérez de Vargas, M., Gonzalo López, P., **2011**. La red de estaciones permanentes GNSS del Instituto Geográfico Nacional (ERGNSS). Topografía y cartografía 28 (161), 22-28.

Cardozo, N., Allmendinger, R.W., **2009**. SSPX: A program to compute strain from displacement/velocity data. Computers and Geoscinces 35 (6), 1343-1357. http://dx.doi.org/10.1016/j.cageo.2008.05.008.

Castellote, M., Fleta, J., Goula, X., Surinach, E., Talaya, J., Termens, A., **1997**. Red GPS para el control de las fallas activas del SE de la Peninsula Iberica (Proyecto CuaTeNeo),

Crespo-Blanc, A., Frizon de Lamotte, D., **2006**. Structural evolution of the external zones derived from the Flysch trough and the South Iberian and Maghrebian paleomargins around the Gibraltar arc: a comparative study. Bull. Soc. Geol. Fr. 177 (5), 267-282.

D'Estevou, P.O., Montenat, C., **1985**. (Structural evolution of the Eastern Betic Zone (Spain) from the Tortonian to the Holocene Periods). Evolution structurale de la zone betique orientale (Espagne) du Tortonien a l'Holocene. 300 (8), 363-368.

De Larouzière, F.D., Bolze, J., Bordet, P., Hernandez, J., Montenat, C., Ott d'Estevou, P., **1988**. The Betic segment of the lithospheric Trans-Alboran shear zone during the Late Miocene. Tectonophysics 152, 41-52.

De Michele, M., Briole, P., Raucoules, D., Lemoine, A., Rigo, A., **2013**. Revisiting the shallow Mw 5.1 Lorca earthquake (southeastern Spain) using C-band InSAR and elastic dislocation modelling. Remote Sensing Letters 4 (9), 863-872. http://dx.doi.org/10.1080/2150704x.2013.808777.

De Vicente, G., Cloetingh, S., Muñoz-Martín, A., Olaiz, A., Stich, D., Vegas, R., Galindo-Zaldívar, J., Fernández-Lozano, J., **2008**. Inversion of moment tensor focal mechanisms for active stresses around the microcontinent Iberia: Tectonic implications. Tectonics 27 (TC1009). http://dx.doi.org/10.1029/2006TC002093.

DeMets, C., Gordon, R.G., Argus, D.F., **2010**. Geologically current plate motions. Geophys. J. Int. 181 (1), 1-80. http://dx.doi.org/10.1111/j.1365-246X.2009.04491.x.

DeMets, C., Gordon, R.G., Argus, D.F., Stein, S., **1994**. Effect of recent revisions to the geomagnetic reversal time scale on estimates of current plate motions. Geophys. Res. Lett. 21 (20), 2191-2194. http://dx.doi.org/10.1029/94gl02118.

Dewey, J.F., Helman, M.L., Turco, E., Hutton, D.H.W., Knott, S.D., **1989**. Kinematics of the western Mediterranean, in: Coward, M.P., Dietrich, D., Park, R.G. (Eds.), Alpine Tectonics. Geological Society, pp. 265-283.

Diaz, J., Gallart, J., Villaseñor, A., Mancilla, F., Pazos, A., Cordoba, D., Pulgar, J.A., Ibarra, P., Harnafi, M., **2010**. Mantle dynamics beneath the Gibraltar Arc (western Mediterranean) from shear-wave splitting measurements on a dense seismic array. Geophys. Res. Lett. 37 (18).

Dong, D., Herring, T.A., King, R.W., **1998**. Estimating regional deformation from a combination of space and terrestrial geodetic data. J. Geodesy 72 (4), 200-214 http://dx.doi.org/210.1007/s001900050161.

Dow, J., Neilan, R., Rizos, C., **2008**. The International GNSS Service in a changing landscape of Global Navigation Satellite Systems. J. Geodesy 83 (3), 191-198. http://dx.doi.org/10.1007/s00190-008-0300-3.

Drewes, H., **1998**. Combination of VLBI, SLR and GPS determined station velocities for actual plate kinematic and crustal deformation models, Geodesy on the Move. Springer, pp. 377-382.

Drewes, H., **2009**. The Actual Plate Kinematic and Crustal Deformation Model APKIM2005 as Basis for a Non-Rotating ITRF, Geodetic Reference Frames. Springer Berlin Heidelberg, pp. 95-99.

Drewes, H., Angermann, D., **2001**. The actual plate kinematic and crustal deformation model 2000 (APKIM 2000) as a geodetic reference system. Proc. IAG Scientific Assembly.

Duggen, S., Hoernle, K., van den Bogaard, P., Harris, C., **2004**. Magmatic evolution of the Alboran region: the role of subduction in forming the western Mediterranean and causing the Messinian Salinity Crisis. Earth Planet. Sci. Lett. 218 (1-2), 91-108.

Dziewonski, A.M., Chou, T.A., Woodhouse, J.H., **1981**. Determination of earthquake source parameters from waveform data for studies of global and regional seismicity. J. Geophys. Res. 86 (B4), 2825-2852.

Echeverria, A., Khazaradze, G., Asensio, A., Gárate, J., Dávila, J.M., Suriñach, E., **2013**. Crustal deformation in eastern Betics from CuaTeNeo GPS network. Tectonophysics 608, 600-612. http://dx.doi.org/10.1016/j.tecto.2013.08.020.

Echeverria, A., Khazaradze, G., Asensio, A., Masana, E., **Submitted**. Geodetic evidence for continuing tectonic activity of the Carboneras fault (SE Spain). Tectonophysics. http://dx.doi.org/10.1016/j.tecto.2013.08.020.

Echeverria, A., Khazaradze, G., Gárate, J., Asensio, A., Surinach, E., **2012**. Deformación cortical de las Béticas Orientales mediante GPS y su relación con el terremoto de Lorca. Fisica de la Tierra 24, 113-127. http://dx.doi.org/10.5209/rev_FITE2012.v24.40134.

El Moudnib, L., Villaseñor, A., Harnafi, M., Gallart, J., Pazos, A., Serrano, I., Córdoba, D., Pulgar, J.A., Ibarra, P., Himmi, M.M., Chourak, M., **2015**. Crustal structure of the Betic-Rif system, western Mediterranean, from local earthquake tomography. Tectonophysics 643, 94-105. http://dx.doi.org/10.1016/j.tecto.2014.12.015.

Faccenna, C., Becker, T.W., Auer, L., Billi, A., Boschi, L., Brun, J.P., Capitanio, F.A., Funiciello, F., Horvàth, F., Jolivet, L., Piromallo, C., Royden, L., Rossetti, F., Serpelloni, E., **2014**. Mantle dynamics in the Mediterranean. Rev. Geophys. 52 (3), 2013RG000444. http://dx.doi.org/10.1002/2013rg000444.

Faccenna, C., Piromallo, C., Crespo-Blanc, A., Jolivet, L., Rossetti, F., **2004**. Lateral slab deformation and the origin of the western Mediterranean arcs. Tectonics 23 (1), TC1012.

Fadil, A., Vernant, P., McClusky, S., Reilinger, R., Gomez, F., Sari, D.B., Mourabit, T., Feigl, K., Barazangi, M., **2006**. Active tectonics of the western Mediterranean: Geodetic evidence for rollback of a delaminated subcontinental lithospheric slab beneath the Rif Mountains, Morocco. Geology 34 (7), 529-532. http://dx.doi.org/10.1130/G22291.1

Faulkner, D.R., Lewis, A.C., Rutter, E.H., **2003**. On the internal structure and mechanics of large strike-slip fault zones; field observations of the Carboneras Fault in southeastern Spain. Tectonophysics 367 (3-4), 235-251.

Fernandes, R.M.S., Ambrosius, B.A.C., Noomen, R., Bastos, L., Wortel, M.J.R., Spakman, W., Govers, R., **2003**. The relative motion between Africa and Eurasia as derived from ITRF2000 and GPS data. Geophys. Res. Lett. 30 (16), 1828. http://dx.doi.org/10.1029/2003GL017089.

Fernandes, R.M.S., Miranda, J.M., Meijninger, B.M.L., Bos, M.S., Noomen, R., Bastos, L., Ambrosius, B.A.C., Riva, R.E.M., **2007**. Surface velocity field of the Ibero-Maghrebian segment of the Eurasia-Nubia plate boundary. Geophys. J. Int. 169 (1), 315-324. http://dx.doi.org/10.1111/j.1365-246X.2006.03252.x.

Fernández-Ibáñez, F., Soto, J.I., **2008**. Crustal rheology and seismicity in the Gibraltar Arc (western Mediterranean). Tectonics 27 (2). http://dx.doi.org/10.1029/2007TC002192.

Ferrater, M., Ortuño, M., Masana, E., Perea, H., Baize, S., Pallàs, R., García-Meléndez, E., Echeverria, A., Martínez Diaz, J.J., Rockwell, T., **2015**. First lateral slip-rates along the left-lateral strike-slip Alhama de Murcia fault obtained with 3D trenching (SE Iberian Peninsula), 6th International INQUA Meeting on Paleoseismology, Active Tectonics and Archaeoseismology, Fucino Basin, Italy

Fisher, N.I., **1995**. Statistical analysis of circular data. Cambridge University Press.

Frizon de Lamotte, D., Jarrige, J.J., Vidal, J.C., **1980**. Le magmatisme béticorifain est-il lié à une zone d'accidents décrochants "Trans-Alboran"?, Huitième Réunion Annuelle des Sciences de la Terre, Abstracts. Societé Geologique de France, Marseille

Frontera, T., Concha, A., Blanco, P., Echeverria, A., Goula, X., Arbiol, R., Khazaradze, G., Pérez, F., Suriñach, E., **2012**. DInSAR coseismic deformation of the May 2011 Mw 5.1 Lorca earthquake, (Southern Spain). Solid Earth 3, 111-119. http://dx.doi.org/10.5194/se-3-111-2012.

Galindo-Zaldivar, J., Gil, A.J., Borque, M.J., González-Lodeiro, F., Jabaloy, A., Marin-Lechado, C., Ruano, P., Sanz de Galdeano, C., **2003**. Active faulting in the internal zones of the central Betic Cordilleras (SE, Spain) J. Geodyn. 36 (1-2), 239-250.

Galindo-Zaldívar, J., González-Lodeiro, F., Jabaloy, A., **1993**. Stress and palaeostress in the Betic-Rif cordilleras (Miocene to present). Tectonophysics 227, 105-126.

Galindo-Zaldívar, J., Jabaloy, A., Serrano, I., Morales, J., González-Lodeiro, F., Torcal, F., **1999**. Recent and present-day stresses in the Granada Basin (Betic Cordilleras): Example of a late Miocene-present-day extensional basin in a convergent plate boundary. Tectonics 18, 686-702.

Garate, J., Martin-Davila, J., Khazaradze, G., Echeverria, A., Asensio, E., Gil, A.J., de Lacy, M.C., Armenteros, J.A., Ruiz, A.M., Gallastegui, J., Alvarez-Lobato, F., Ayala, C., Rodríguez-Caderot, G., Galindo-Zaldívar, J., Rimi, A., Harnafi, M., **2015**. Topo-Iberia project: CGPS crustal velocity field in the Iberian Peninsula and Morocco. GPS Solutions 19 (2), 287-295. http://dx.doi.org/10.1007/s10291-014-0387-3.

García-Dueñas, V., Balanya, J.C., Martinez-Martinez, J.M., **1992**. Miocene extensional detachments in the outcropping basement of the northern Alboran Basin (Betics) and their tectonic implications. Geo-Mar. Lett. 12, 88-95.

Garcia-Dueñas, V., Sanz De Galdeano, C., De Miguel, F., Vidal, F., **1984**. Neotectónica y sismicidad en las Cordilleras Béticas: una revisión de resultados. Rev. C. Energía Nuclear 28, 149-150.

García-Mayordomo, J., **2005**. Caracterización y Análisis de la Peligrosidad Sísmica en el Sureste de España. PhD thesis, Universidad Complutense de Madrid, p. 373

García-Mayordomo, J., Insua-Arévalo, J.M., Martínez-Díaz, J.J., Jiménez-Díaz, A., Martín-Banda, R., Martín-Alfageme, S., Álvarez-Gómez, J.A., Rodríguez-Peces, M., Pérez-López, R., Rodríguez-Pascua, M.A., Masana, E., Perea, H., Martín-González, F., Giner-Robles, J., Nemser, E.S., Cabral, J., **2012**. The Quaternary active faults database of Iberia (QAFI v.2.0). J. Iberian Geol. 38 (1), 285-302.

García-Mayordomo, J., Jiménez-Díaz, A., **2010a**. Las Moreras - Escarpe de Mazarrón: Sierra de las Moreras - Puerto de Mazarrón (ES612), In: Quaternary Active Faults Database of Iberia v.2.0 - December 2011 (García-Mayordomo et al., eds.), IGME, Madrid.

García-Mayordomo, J., Jiménez-Díaz, A., **2010b**. Palomares: Carboneras-Sierra de Almenara (ES609), In: Quaternary Active Faults Database of Iberia v.2.0 - December 2011 (García-Mayordomo et al., eds.), IGME, Madrid.

García-Mayordomo, J., Martínez-Díaz, J.J., **2006**. Caracterización sísmica del anticlinorio del Bajo Segura (Alicante): Fallas del Bajo Segura, Torrevieja y San Miguel de Salinas. Geogaceta (40), 19-22.

Giaconia, F., Booth-Rea, G., Martínez-Martínez, J.M., Azañón, J.M., Pérez-Peña, V., Pérez-Romero, J., Villegas, I., **2012**. Geomorphic evidence of active tectonics in the Sierra Alhamilla (eastern Betics, SE Spain). Geomorphology 145-146, 90-106. http://dx.doi.org/10.1016/j.geomorph.2011.12.043.

Giaconia, F., Booth-Rea, G., Martínez-Martínez, J.M., Azañón, J.M., Pérez-Romero, J., Villegas, I., **2013**. Mountain front migration and drainage captures related to fault segment linkage and growth: The Polopos transpressive fault zone (southeastern Betics, SE Spain). J. Struct. Geol. 46 (0), 76-91. http://dx.doi.org/10.1016/j.jsg.2012.10.005.

Giaconia, F., Booth-Rea, G., Martínez-Martínez, J.M., Azañón, J.M., Storti, F., Artoni, A., **2014**. Heterogeneous extension and the role of transfer faults in the development of the southeastern Betic basins (SE Spain). Tectonics, 33. http://dx.doi.org/10.1002/2014tc003681.

Gil, A.J., Rodriguez, C.G., Lacy, M.C., Ruiz, A.M., Sanz, d.G.C., Alfaro, P., **2002**. Establishment of a non-permanent GPS network to monitor the recent NE-SW deformation in the Granada Basin (Betic Cordillera, southern Spain). Studia Geophysica et Geodetica 46 (3), 395-410 (doi:310.1023/A:1019530716324).

González, P.J., Tiampo, K.F., Palano, M., Cannavo, F., Fernandez, J., **2012**. The 2011 Lorca earthquake slip distribution controlled by groundwater crustal unloading. Nature Geosci 5 (11), 821-825. http://dx.doi.org/10.1038/ngeo1610.

Gràcia, E., Bartolomé, R., Lo Iacono, C., Moreno, X., Stich, D., Martínez-Diaz, J.J., Bozzano, G., Martínez-Loriente, S., Perea, H., Diez, S., **2012**. Acoustic and seismic imaging of the Adra Fault (NE Alboran Sea): in search of the source of the 1910 Adra earthquake. Nat. Hazards Earth Syst. Sci. 12, 3255-3267. http://dx.doi.org/10.5194/nhess-12-3255-2012.

Gràcia, E., Pallas, R., Soto Juan, I., Comas, M., Moreno, X., Masana, E., Santanach, P., Diez, S., Garcia, M., Danobeitia, J., Bartolome, R., Farran, M., Gomez, M., Alpiste, M.J.R., Lastras, G., Wilmott, V., Perea, H., Blondel, P., Gomez, O., Bullock, L., Jacobs, C., Rouse, I., White, D., Whittle, S., Terrinha, P., Gafeira, J., Roque, C., Hits Scientific Party, I., **2006**. Active faulting offshore SE Spain (Alboran Sea); implications for earthquake hazard assessment in the southern Iberian margin. Earth Planet. Sci. Lett. 241 (3-4), 734-749. http://dx.doi.org/10.1016/j.epsl.2005.11.009.

Gripp, A.E., Gordon, R.G., **1990**. Current plate velocities relative to the hotspots incorporating the Nuvel-1 global plate motion model. Geophys. Res. Lett. 17, 1109-1112.

Gripp, A.E., Gordon, R.G., **2002**. Young tracks of hotspots and current plate velocities. Geophys. J. Int. 150 (2), 321-361. http://dx.doi.org/10.1046/j.1365-246X.2002.01627.x.

Gutscher, M.-A., **2012**. Subduction beneath Gibraltar? Recent studies provide answers. Eos, Transactions American Geophysical Union 93 (13), 133-134. http://dx.doi.org/10.1029/2012eo130001.

Gutscher, M.A., Dominguez, S., Westbrook, G.K., Le Roy, P., Rosas, F., Duarte, J.C., Terrinha, P., Miranda, J.M., Graindorge, D., Gailler, A., Sallares, V., Bartolome, R., **2012**. The Gibraltar subduction: A decade of new geophysical data. Tectonophysics 574-575, 72-91. http://dx.doi.org/10.1016/j.tecto.2012.08.038.

Gutscher, M.A., Malod, J., Rehault, J.P., Contrucci, I., Klingelhoefer, F., Mendes, V.L., Spakman, W., **2002**. Evidence for active subduction beneath Gibraltar. Geology (Boulder) 30 (12), 1071-1074.

Hall, S.H., **1983**. Post Alpine tectonic evolution of SE Spain and the structure of fault gouges. PhD Thesis, Imperial College London (University of London)

Hanks, T.C., Kanamori, H., **1979**. A moment magnitude scale. J. Geophys. Res. 84 (B5), 2348-2350.

Henares, J., López Casado, C., Sanz de Galdeano, C., Delgado, J., Peláez, J.A., **2003**. Stress fields in the Iberian-Maghrebi region. J. Seismol. 7 (1), 65-78. http://dx.doi.org/10.1023/A:1021294015027.

Herraiz, M., De Vicente, G., Lindo-Ñaupari, R., Giner, J., Simón, J.L., González-Casado, J.M., Vadillo, O., Rodriguez-Pascua, M.A., Cicuéndez, J.I., Casas, A., Cabañas, L., Rincón, P., Cortés, A.L., Ramírez, M., Lucini, M., **2000**. The recent (upper miocene ot quaternary) and present tectonic stress distributions in the Iberian Peninsula. Tectonics 19 (4), 762-786.

Herring, T., **2003**. MATLAB Tools for viewing GPS velocities and time series. GPS Solutions 7 (3), 194 - 199. http://dx.doi.org/10.1007/s10291-003-0068-0.

Herring, T.A., King, R.W., McClusky, S.C., **2010a**. GLOBK Reference Manual. Department of Earth, Atmospheric, and Planetary Sciences. Massachusetts Institute of Technology, p. 95

Herring, T.A., King, R.W., McClusky, S.C., **2010b**. Introduction to GAMIT/GLOBK. Department of Earth, Atmospheric, and Planetary Sciences. Massachusetts Institute of Technology, p. 48

Hofmann-Wellenhof, B., Lichtenegger, H., Collins, J., **2001**. Global positioning system : theory and practice. Springer, Viena.

Houseman, G.A., McKenzie, D.P., Molnar, P., **1981**. Convective instability of a thickened boundary layer and its relevance for the thermal evolution of continental convergent belts. J. Geophys. Res. 86 (B7), 6115-6132. http://dx.doi.org/10.1029/JB086iB07p06115

IGN, **2011**. INFORME DEL SISMO DE LORCA DEL 11 DE MAYO DE 2011. Instituto Geográfico Nacional de España (http://www.ign.es/ign/resources/sismologia/www/lorca/Lorcainfo2011.pdf), Madrid, p. 138

IGN, **2013**. Actualización de mapas de peligrosidad sísmica de España 2012. CNIG, Madrid, España.

Insua-Arévalo, J.M., García-Mayordomo, J., Salazar, A., Rodríguez-Escudero, E., Martínez-Díaz, J.J., Ávarez-Gómez, J.A., Canora, C., Martín-Banda, R., Pérez-López, R., Rodríguez-Pascua, M.A., **2012**. Actividad holocena de la Falla de Carrascoy, Murcia. Resultados preliminares de un análisis paleosísmico. Geo-Temas 13, 1511-1514.

Jackson, J., McKenzie, D., **1988**. The relationship between plate motions and seismic moment tensors, and the rates of active deformation in the Mediterranean and Middle East. Geophys. J. Roy. Astron. Soc. 93 (1), 45-73.

Jeffrey, C., **2010**. An introduction to GNSS. NovAtel, Inc., Calgary, Canada.

Jenny, S., Goes, S., Giardini, D., Kahle, H.-G., **2004**. Earthquake recurrence parameters from seismic and geodetic strain rates in the eastern Mediterranean. Geophys. J. Int. 157 (3), 1331-1347.

Jolivet, L., Augier, R., Faccenna, C., Negro, F., Rimmele, G., Agard, P., Robin, C., Rossetti, F., Crespo-Blanc, A., **2008**. Subduction, convergence and the mode of backarc extension in the

Mediterranean region. Bull. Soc. Geol. Fr. 179 (6), 525-550. http://dx.doi.org/10.2113/gssgfbull.179.6.525.

Jost, M.L., Herrmann, R.B., **1989**. A student's guide to and review of moment tensors. Seismol. Res. Lett. 60 (2), 37-57.

Keller, E.A., Pinter, N., **1996**. Active tectonics: earthquakes, uplift, and landscape. Prentice Hall.

Keller, J.V.A., Hall, S.H., Dart, C.J., McClay, K.R., **1995**. The geometry and evolution of a transpressional strike-slip system; the Carboneras Fault, SE Spain. J. Geol. Soc. London 152 (Part 2), 339-351.

Khazaradze, G., Moreno, X., Asensio, E., Masana, E., **2010**. Geodetic evidence for a present-day activity of the Carboneras fault in the Eastern Betics, in: Insua Arévalo, J.M., Martín González, F. (Eds.), Primera Reunión Ibérica sobre Fallas Activas y Paleosismología (IberFault). Contribución de la Geología al Análisis de la Peligrosidad Sísmica, Sigüenza, Spain, pp. 93-96.

Kostrov, V.V., **1974**. Seismic moment and energy of earthquakes, and seismic flow of rock. Izv. Acad. Sci. USSR Phys. Solid Earth 1 (English Transl.), 13-21.

Kotzev, V., Nakov, R., Georgiev, T., Burchfiel, B.C., King, R.W., **2006**. Crustal motion and strain accumulation in western Bulgaria. Tectonophysics 413 (3-4), 127-145. http://dx.doi.org/10.1016/j.tecto.2005.10.040.

Koulali, A., Ouazar, D., Tahayt, A., King, R.W., Vernant, P., Reilinger, R.E., McClusky, S., Mourabit, T., Davila, J.M., Amraoui, N., **2011**. New GPS constraints on active deformation along the Africa-Iberia plate boundary. Earth Planet. Sci. Lett. 308 (1-2), 211-217. http://dx.doi.org/10.1016/j.epsl.2011.05.048.

Kreemer, C., Holt, W.E., Goes, S., Govers, R., **2000**. Active deformation in eastern Indonesia and the Philippines from GPS and seismicity data. J. Geophys. Res. 105 (1), 663-680.

Kreemer, C., Holt, W.E., Haines, A.J., **2003**. An integrated global model of present-day plate motions and plate boundary deformation. Geophys. J. Int. 154 (1), 8-34. http://dx.doi.org/10.1046/j.1365-246X.2003.01917.x.

Krieger, L., Heimann, S., **2012**. MoPaD - Moment Tensor Plotting and Decomposition: A Tool for Graphical and Numerical Analysis of Seismic Moment Tensors. Seismol. Res. Lett. 83 (3), 589-595. http://dx.doi.org/10.1785/gssrl.83.3.589.

Langbein, J., Johnson, H., **1997**. Correlated errors in geodetic time series; implications for time-dependent deformation. J. Geophys. Res. 102 (1), 591-604.

Leblanc, D., Olivier, P., **1984**. Role of strike-slip faults in the Betic-Rifian orogeny. Tectonophysics 101 (3-4), 345-355.

Levander, A., Bezada, M.J., Niu, F., Humphreys, E.D., Palomeras, I., Thurner, S.M., Masy, J., Schmitz, M., Gallart, J., Carbonell, R., Miller, M.S., **2014**. Subduction-driven recycling of continental margin lithosphere. Nature 515 (7526), 253-256. http://dx.doi.org/10.1038/nature13878.

Lonergan, L., White, N., **1997**. Origin of the Betic-Rif mountain belt. Tectonics 16 (3), 504-522.

López-Comino, J.-Á., Mancilla, F., Morales, J., Stich, D., **2012**. Rupture directivity of the 2011, Mw 5.2 Lorca earthquake (Spain). Geophys. Res. Lett. 39 (3), L03301. http://dx.doi.org/10.1029/2011gl050498.

Lopez Casado, C., Sanz de Galdeano, C., Delgado, J., Peinado, M.A., **1995**. The b parameter in the Betic Cordillera, Rif and nearby sectors; relations with the tectonics of the region. Tectonophysics 248 (3-4), 277-292. http://dx.doi.org/10.1016/0040-1951(94)00278-H.

Lyard, F., Lefevre, F., Letellier, T., Francis, O., **2006**. Modelling the global ocean tides: Modern insights from FES2004. Ocean Dyn. 56 (5-6), 394-415.

Mancilla, L.F.d., Stich, D., Berrocoso, M., Martín, R., Morales, J., Fernandez-Ros, A., Páez, R., Pérez-Peña, A., **2013**. Delamination in the Betic Range: Deep structure, seismicity, and GPS motion. Geology 41 (3), 307-310. http://dx.doi.org/10.1130/g33733.1.

Mao, A., Harrison, C.G., Dixon, T.H., **1999**. Noise in GPS coordinate estimates. J. Geophys. Res. 104, 2797-2816. http://dx.doi.org/10.1029/1998JB900033.

Marín-Lechado, C., Galindo-Zaldívar, J., Rodríguez-Fernández, L.R., Serrano, I., Pedrera, A., **2005**. Active faults, seismicity and stresses in an internal boundary of a tectonic arc (Campo de Dalías and Níjar, southeastern Betic Cordilleras, Spain). Tectonophysics 396 (1-2), 81-96. http://dx.doi.org/10.1016/j.tecto.2004.11.001.

Marone, C., Richardson, E., **2012**. Learning to read fault-slip behavior from fault-zone structure. Geology 38 (8), 767-768. http://dx.doi.org/10.1130/focus082010.1.

Martín-Banda, R., García-Mayordomo, J., Insua-Arévalo, J.M., Salazar-Rincón, A.E., Rodrígez-Escudero, E., Álvarez-Gómez, J.A., Martínez-Díaz, J.J., Medialdea, a., Herrero, M.J., **2014**. Seismogenic potential of the SW segment of the Carrascoy Fault, Betic Ranges (SE Spain), in: Álvarez gómez, J.A., Martín González, F. (Eds.), Segunda Reunión Ibérica sobre Fallas Activas y Paleosismología (IberFault), Lorca, Murcia, Spain, pp. 31-34

Martin-Rojas, I., Alfaro, P., Estévez, A., **2014**. Evolución tectónica del borde norte de la cuenca del Bajo Segura. Implicaciones en la evolución de la falla de Crevillente (sector Abanilla-Alicante). Cuaternario y Geomorfología 28 (3-4), 85-94.

Martínez-Díaz, J.J., **1998**. Neotectónica y tectónica activa del sector Centro-occidental de la región de Murcia y sur de Almería (Cordillera Bética- España). Universidad Complutense de Madrid, Spain, p. 446

Martínez-Díaz, J.J., **2002**. Stress field variation related to fault interaction in a reverse oblique-slip fault: the Alhama de Murcia fault, Betic Cordillera, Spain. Tectonophysics 356 (4), 291-305. http://dx.doi.org/10.1016/S0040-1951(02)00400-6.

Martínez-Díaz, J.J., Bejar-Pizarro, M., Álvarez-Gómez, J.A., Mancilla, F., Stich, D., Herrera, G., Morales, J., **2012a**. Tectonic and seismic implications of an intersegment rupture. The damaging May 11th 2011 Mw 5.2 Lorca, Spain, earthquake. Tectonophysics 546-547 (0), 28-37. http://dx.doi.org/10.1016/j.tecto.2012.04.010.

Martínez-Díaz, J.J., García-Mayordomo, J., Jiménez-Díaz, A., **2010**. Alhama de Murcia: Lorca-Totana (ES627), Totana-Alhama (ES628), Alhama-Alcantarilla (ES629), In: Quaternary Active Faults Database of Iberia v.2.0 - December 2011 (García-Mayordomo et al., eds.), IGME, Madrid.

Martínez-Díaz, J.J., Hernández-Enrile, J.L., **2004**. Neotectonics and morphotectonics of the southern Almería region (Betic Cordillera-Spain) kinematic implications. Int. J. Earth Sci. 93 (2), 189-206. http://dx.doi.org/10.1007/s00531-003-0379-y.

Martínez-Díaz, J.J., Hernandez Enrile, J.L., **1992**. Tectonica reciente y rasgos sismotectonicos en el sector Lorca-Totana de la falla de Alhama de Murcia. Estudios Geológicos 48 (3-4), 153-162.

Martinez-Diaz, J.J., Masana, E., Hernandez-Enrile, J.L., Santanach, P., **2001**. Evidence for coseismic events of recurrent prehistoric deformation along the Alhama de Murcia fault, Southeastern Spain. Acta Geologica Hispanica 36 (3-4), 315-327.

Martínez-Díaz, J.J., Masana, E., Hernández-Enrile, J.L., Santanach, P., **2003**. Effects of repeated paleoeartquakes on the Alhama de Murcia fault (Betic Cordillera, Spain) on the Quaternary evolution of an alluvial fan system. Ann. Geophys. 46 (5), 775-792.

Martínez-Díaz, J.J., Masana, E., Ortuño, M., **2012b**. Active tectonics of the Alhama de murcia fault, Betic Cordillera, Spain. J. Iberian Geol. 38 (1), 269-286. http://dx.doi.org/10.5209/rev_JIGE.2012.v38.n1.39218.

Martínez-Martínez, J.M., Azañón, J.M., **1997**. Mode of extensional tectonics in the southeast Betics (SE Spain): Implications for the tectonic evolution of the peri-Alboran orogenic system. Tectonics 16, 205-225.

Martínez-Martínez, J.M., Booth-Rea, G., Azañón, J.M., Torcal, F., **2006**. Active transfer fault zone linking a segmented extensional system (Betics, southern Spain): Insight into heterogeneous extension driven by edge delamination. Tectonophysics 422 (1-4), 159-173.

Martínez del Olmo, W., Klimowitz, J., Hernández, E., **2006**. The miocene extensive system of the Alhama de Murcia fault. El despegue extensional mioceno de la zona de falla de Alhama de Murcia 117 (3), 363-377.

Martínez Solares, J.M., Mezcua, J., **2002**. Catálogo Sísmico de la Península Ibérica (880 a.c. - 1900). Monografía de Instituto Geográfico Nacional de España 18, 253.

Masana, E., Martínez-Díaz, J.J., Hernández-Enrile, J.L., Santanach, P., **2004**. The Alhama de Murcia fault (SE Spain), a seismogenic fault in a diffuse plate boundary: Seismotectonic implications for the Ibero-Magrebian region. J. Geophys. Res. 109 (B01301). http://dx.doi.org/10.1029/2002JB002359.

Masana, E., Pallàs, R., Perea, H., Ortuño, M., Martínez-Díaz, J.J., García-Meléndez, E., Santanach, P., **2005**. Large Holocene morphogenic earthquakes along the Albox fault, Betic Cordillera, Spain. J. Geodyn. 40 (2-3), 119-133. http://dx.doi.org/10.1016/j.jog.2005.07.002,.

Masson, F., Chéry, J., Hatzfeld, D., Martinod, J., Vernant, P., Tavakoli, F., Ghafory-Ashtiani, M., **2005**. Seismic versus aseismic deformation in Iran inferred from earthquakes and geodetic data. Geophys. J. Int. 160 (1), 217-226.

Mattei, M., Cifelli, F., Rojas, I.M., Crespo Blanc, A., Comas, M., Faccenna, C., Porreca, M., **2006**. Neogene tectonic evolution of the Gibraltar Arc: New paleomagnetic constrains from the Betic chain. Earth Planet. Sci. Lett. 250 (3-4), 522-540. http://dx.doi.org/10.1016/j.epsl.2006.08.012.

McCaffrey, R., **2009**. Time-dependent inversion of three-component continuous GPS for steady and transient sources in northern Cascadia. Geophys. Res. Lett. 36 (7). http://dx.doi.org/10.1029/2008gl036784.

McCarthy, D.D., **1996**. IERS conventions (1996), IERS Technical Note 21, International Earth Rotation Service

McCarthy, D.D., Petit, G., **2004**. IERS conventions (2003), IERS Technical Note 32, Verlag des Budesamts fur Kartographie und Geodasie, Frankfurt, 2004

McClusky, S., Balassanian, S., Barka, A., Demir, C., Ergintav, S., Georgiev, I., Gurkan, O., Hamburger, M., Hurst, K., Kahle, H., Kastens, K., Kekelidze, G., King, R., Kotzev, V., Lenk, O., Mahmoud, S., Mishin, A., Nadariya, M., Ouzounis, A., Paradissis, D., Peter, Y., Prilepin, M., Reilinger, R., Sanli, I., Seeger, H., Tealeb, A., Toksoz, M.N., Veis, G., **2000**. Global Positioning System constraints on plate kinematics and dynamics in the eastern Mediterranean and Caucasus. Journal of Geophysical Research 105 (B3), 5695-5719. http://dx.doi.org/10.1029/1999JB900351.

McClusky, S., Reilinger, R., Mahmoud, S., Ben Sari, D., Tealeb, A., **2003**. GPS constraints on Africa (Nubia) and Arabia plate motions. Geophys. J. Int. 155 (1), 126-138. http://dx.doi.org/10.1046/j.1365-246X.2003.02023.x.

Means, W.D., **1976**. Stress and strain: basic concepts of continuum mechanics for geologists. Springer-Verlag, New York.

Meghraoui, M., Morel, J.L., Andrieux, J., Dahmani, M., **1996**. Tectonique plio-quaternaire de la chaîne tello-rifaine et de la mer d'Alboran. Une zone complexe de convergence continent-continent. Bull. Soc. geol. France 167, 141-157.

Meijninger, B.M.L., Vissers, R.L.M., **2006**. Miocene extensional basin development in the Betic Cordillera, SE Spain revealed through analysis of the Alhama de Murcia and Crevillente faults. Basin Res. 18 (4), 547-571.

Mezcua, J., Rueda, J., **1997**. Seismological evidence for a delamination process in the lithosphere under the Alboran Sea. Geophys. J. Int. 129 (1), F1-F8.

Miller, M.S., Allam, A.A., Becker, T.W., Di Leo, J.F., Wookey, J., **2013**. Constraints on the tectonic evolution of the westernmost Mediterranean and northwestern Africa from shear wave splitting analysis. Earth Planet. Sci. Lett. 375, 234-243. http://dx.doi.org/10.1016/j.epsl.2013.05.036.

Molnar, P., **1979**. Earthquake recurrence intervals and plate tectonics. Bull. Seismol. Soc. Am. 69 (1), 115-133.

Montenat, C., D'Estevou, P.O., La Chappelle, G., **1990**. Le Bassin de Nijar-Carboneras et le Couloir du Bas-Andarax, Documents et Travaux. Intitute de Geologique Albert de Lapparent 12, 129-164.

Montenat, C., Ott D'estevou, P., Masse, P., **1987**. Tectonic- sedimentary characters of the Betic Neogene basins evolving in a crustal transcurrent shear zone (SE Spain). Bulletin - Centres de Recherches Exploration-Production Elf- Aquitaine 11 (1), 1-22.

Morel, J.L., **1989**. Etats de contrainte et cinématique de la chaîne rifaine (Maroc) du Tortonien à l'actuel. Geodin. Acta 3, 283-294.

Moreno, X., **2011**. Neotectonic and Paleoseismic Onshore-Offshore integrated study of the Carboneras Fault (Eastern Betics, SE Iberia). PhD thesis, Universitat de Barcelona, Barcelona, p. 365

Moreno, X., Gràcia, E., Masana, E., **2010a**. Carboneras: Southern (ME015), In: Quaternary Active Faults Database of Iberia v.2.0 - December 2011 (García-Mayordomo et al., eds.), IGME, Madrid.

Moreno, X., Masana, E., Gràcia, E., **2010b**. Carboneras: Northern (ES630), In: Quaternary Active Faults Database of Iberia v.2.0 - December 2011 (García-Mayordomo et al., eds.), IGME, Madrid.

Moreno, X., Masana, E., Gràcia, E., Bartolomé, R., Piqué-Serra, O., **2008**. Estudio paleosismológico de la Falla de Carboneras: Evidencias tierra-mar de actividad tectónica reciente. GeoTemas 10, 1035-1038.

Niemeijer, A., Vissers, R.L.M., **2014**. Earthquake rupture propagation inferred from the spatial distribution of fault rock frictional properties. Earth Planet. Sci. Lett. 396, 154-164. http://dx.doi.org/10.1016/j.epsl.2014.04.010.

Nocquet, J.M., Calais, E., **2004**. Geodetic measurements of crustal deformation in the Western Mediterranean and Europe. Pure Appl. Geophys. 161 (3), 661-681. http://dx.doi.org/10.1007/s00024-003-2468-z.

Okada, Y., **1985**. Surface deformation due to shear and tensile faults in a half-space. Bull. Seismol. Soc. Am. 75, 1135-1154.

Okada, Y., **1992**. Internal deformation due to shear and tensile faults in a half-space. Bull. Seismol. Soc. Am. 82 (2), 1018-1040.

Ortuño, M., Masana, E., García-Meléndez, E., Martínez-Díaz, J.J., Štěpančíková, P., Cunha, P.P., Sohbati, R., Canora, C., Buylaert, J.P., Murray, A.S., **2012**. An exceptionally long paleoseismic record of a slow-moving fault: The Alhama de Murcia fault (Eastern Betic shear zone, Spain). Geol. Soc. Am. Bull. 124 (9-10), 1474-1494. http://dx.doi.org/10.1130/B30558.1

Palano, M., González, P.J., Fernández, J., **2013**. Strain and stress fields along the Gibraltar Orogenic Arc: Constraints on active geodynamics. Gondwana Res. 23 (3), 1071-1088. http://dx.doi.org/10.1016/j.gr.2012.05.021.

Palano, M., Guarrera, E., Mattia, M., **2012**. GPS ground deformation patterns at Mount St. Helens (Washington, USA) from 2004 to 2010. Terra Nova, no-no. http://dx.doi.org/10.1111/j.1365-3121.2011.01049.x.

Palomeras, I., Thurner, S., Levander, A., Liu, K., Villasenor, A., Carbonell, R., Harnafi, M., **2014**. Finite-frequency Rayleigh wave tomography of the western Mediterranean: Mapping its lithospheric structure. Geochem. Geophys. Geosyst. 15 (1), 140-160. http://dx.doi.org/10.1002/2013gc004861.

Pancha, A., Anderson, J.G., Kreemer, C., **2006**. Comparison of Seismic and Geodetic Scalar Moment Rates across the Basin and Range Province. Bull. Seismol. Soc. Am. 96 (1), 11-32. http://dx.doi.org/10.1785/0120040166.

Papazachos, C.B., Kiratzi, A.A., **1992**. A formulation for reliable estimation of active crustal deformation and its application to central Greece. Geophys. J. Int. 111 (3), 424-432.

Pedrera, A., Galindo-Zaldívar, J., Ruiz-Bustos, A., Rodríguez-Fernádez, J., Ruiz-Constá, A., **2009**. The role of small-scale fold and fault development in seismogenic zones: Example of the western Huércal-Overa Basin (eastern Betic Cordillera, Spain). J. Quat. Sci. 24 (6), 581-592.

Pedrera, A., Galindo-Zaldívar, J., Sanz de Galdeano, C., López-Garrido, Á.C., **2007**. Fold and fault interactions during the development of an elongated narrow basin: The Almanzora Neogene-Quaternary Corridor (SE Betic Cordillera, Spain). Tectonics 26 (6), TC6002. http://dx.doi.org/10.1029/2007tc002138.

Pedrera, A., Mancilla, F.D.L., Ruiz-Constán, A., Galindo-Zaldívar, J., Morales, J., Arzate, J., Marín-Lechado, C., Ruano, P., Buontempo, L., Anahnah, F., Stich, D., **2010**. Crustal-scale transcurrent fault development in a weak-layered crust from an integrated geophysical research: Carboneras Fault Zone, eastern Betic Cordillera, Spain. Geochem. Geophys. Geosyst. 11 (12).

Pedrera, A., Marín-Lechado, C., Galindo-Zaldívar, J., Rodríguez-Fernández, L.R., Ruiz-Constán, A., **2006**. Fault and fold interaction during the development of the Neogene-Quaternary Almería-Níar basin (SE Betic Cordilleras), Geol. Soc. Spec. Pub., pp. 217-230

Pérez-Peña, A., Martín-Dávila, J., Gárate, J., Berrocoso, M., Buforn, E., **2010**. Velocity field and tectonic strain in Southern Spain and surrounding areas derived from GPS episodic measurements. J. Geodyn. 49 (3-4), 232-240. http://dx.doi.org/10.1016/j.jog.2010.01.015.

Pérez-Valera, L.A., Sánchez-Gómez, M., Azor, A., Pérez-Valera, F., **2014**. Quaternary activity of the structures associated with the Socovos fault system (Eastern Betics), in: Álvarez Gómez, J.A., Martín González, F. (Eds.), Segunda Reunión Ibérica sobre Fallas Activas y Paleosismología (IberFault), Lorca, Murcia, Spain, pp. 35-38

Pérouse, E., Vernant, P., Chéry, J., Reilinger, R., McClusky, S., **2010**. Active surface deformation and sub-lithospheric processes in the western Mediterranean constrained by numerical models. Geology 38 (9), 823-826.

Platt, J.P., Vissers, R.L.M., **1989**. Extensional collapse of thickened continental lithosphere: a working hypothesis for the Alboran Sea and Gibraltar arc. Geology 17 (6), 540.

Quirós Donate, R., Barandillo Fernández, A., **1996**. Proyecto regente Una nueva red geodésica Nacional. Física de la Tierra Nº 8, 23-38.

Reicherter, K., Hübscher, C., **2007**. Evidence for a seafloor rupture of the Carboneras Fault Zone (southern Spain): Relation to the 1522 Almería earthquake? J. Seismol. 11 (1), 15-26. http://dx.doi.org/10.1007/s10950-006-9024-0.

Reicherter, K.R., Reiss, S., **2001**. The carboneras fault zone (Southeastern Spain) revisited with ground penetrating radar - Quaternary structural styles from high-resolution images. Geologie en Mijnbouw/Netherlands Journal of Geosciences 80 (3-4), 129-138.

Reid, H.F., **1910**. The Mechanics of the Earthquake, The California Earthquake of April 18, 1906 (Vol. 2), Report of the State Investigation Commission, Carnegie Institution of Washington, Washington, p. 205

Reilinger, R., McClusky, S., Vernant, P., Lawrence, S., Ergintav, S., Cakmak, R., Ozener, H., Kadirov, F., Guliev, I., Stepanyan, R., Nadariya, M., Hahubia, G., Mahmoud, S., Sakr, K., ArRajehi, A., Paradissis, D., Al-Aydrus, A., Prilepin, M., Guseva, T., Evren, E., Dmitrotsa, A., Filikov, S.V., Gomez, F., Al-Ghazzi, R., Karam, G., **2006**. GPS constraints on continental deformation in the Africa-Arabia-Eurasia continental collision zone and implications for the dynamics of plate interactions. J. Geophys. Res. 111 (B5), 26. http://dx.doi.org/10.1029/2005JB004051.

Rodríguez-Escudero, E., Martínez-Díaz, J.J., Álvarez-Gómez, J., Insua-Arévalo, J.M., Capote del Villar, R., **2013**. Tectonic setting of the recent damaging seismic series in the Southeastern Betic Cordillera, Spain. Bull. Earthquake Eng. 12, 1-24. http://dx.doi.org/10.1007/s10518-013-9551-3.

Rodriguez-Escudero, E., Martínez-Díaz, J.J., Tsige, M., **2012**. Pseudoductile deformations under fragile regime along a slow active fault: the Alhama de Murcia fault. Seismotectonic implications. GeoTemas 13, 1531-1534.

Rodríguez-Escudero, E., Martínez-Díaz, J.J., Tsige, M., **2012**. Deformaciones dúctiles en régimen frágil en una falla activa lenta: La falla de Alhama de Murcia. Implicaciones sismotectónicas. Geo-Temas 13, 4.

Rodriguez-Escudero, E., Martínez-Díaz, J.J., Tsige, M., Giner-Robles, J.L., Cuevas-Rodríguez, J., **2014**. Pulverized quartz in phyllosilicate-rich fault gouge from the Alhama de Murcia Fault: A coseismic effect?, in: Álvarez Gómez, J.A., Martín González, F. (Eds.), Segunda Reunión Ibérica sobre Fallas Activas y Paleosismología (IberFault), Lorca, Murcia, Spain, pp. 177-180

Rodríguez-Estrella, T., Navarro, F., Ros, M., Carrión, J., Atenza, J., **2011**. Holocene morphogenesis along a tectonically unstable coastline in the Western Mediterranean (SE Spain). Quat. Int. http://dx.doi.org/10.1016/j.quaint.2011.07.016.

Rodríguez-Pascua, M.A., De Vicente, G., **2001**. Present stress field in the Eastern Betic Chain. Estado de esfuerzos actual en la Cordillera Bética Oriental 112 (4), 79-95.

Rontogianni, S., **2010**. Comparison of geodetic and seismic strain rates in Greece by using a uniform processing approach to campaign GPS measurements over the interval 1994-2000. J. Geodyn. 50 (5), 381-399. http://dx.doi.org/10.1016/j.jog.2010.04.008.

Rosenbaum, G., Lister, G.S., Duboz, C., **2002**. Relative motions of Africa, Iberia and Europe during Alpine orogeny. Tectonophysics 359 (1-2), 117-129. http://dx.doi.org/10.1016/S0040-1951(02)00442-0.

Royden, L.H., **1993**. Evolution of retreating subduction boundaries formed during continental collision. Tectonics 12 (3), 629-638.

Ruiz-Constán, A., Galindo-Zaldívar, J., Pedrera, A., Célérier, B., Marín-Lechado, C., **2011**. Stress distribution at the transition from subduction to continental collision (northwestern and central Betic Cordillera). Geochem. Geophys. Geosyst. 12 (12), Q12002. http://dx.doi.org/10.1029/2011gc003824.

Rutter, E.H., Faulkner, D.R., Burgess, R., **2012**. Structure and geological history of the Carboneras Fault Zone, SE Spain: Part of a stretching transform fault system. J. Struct. Geol. 45, 68-86. http://dx.doi.org/10.1016/j.jsg.2012.08.009.

Sánchez-Alzola, A., Borque, M.J., Martín-Rojas, I., García-Tortosa, F.J., Alfaro, P., Estévez, A., Molina, S., Rodríguez-Caderot, G., Lacy, C.d., García-Armenteros, J.A., Avilés, M., Herrera-Olmo, A., Rosa, S., Gil, A.J., **2014**. Tasas de deformación GPS en la cuenca del Bajo Segura (Cordillera Bética oriental). Geogaceta 56, 3-6.

Sánchez-Gómez, M., Martínez-Sánchez, C., García-García, F., Peláez, J.A., Pérez-Valera, F., Martínez-Andreu, M., Pérez-Valera, L.A., **2011**. Evidence for a 4700-2100 BC palaeoearthquake recorded in a fluvial-archaeological sequence of the Segura River, SE Spain. Quat. Int. 242 (1), 106-114. http://dx.doi.org/10.1016/j.quaint.2011.03.025.

Sanz de Galdeano, C., **1983**. Los accidentes y fracturas principales de las Cordilleras Béticas. Estudios geológicos 39 (3), 157-165.

Sanz de Galdeano, C., **1990**. Geologic evolution of the Betic Cordilleras in the western Mediterranean, Miocene to the present. Tectonophysics 172 (1-2), 107-119.

Sanz de Galdeano, C., **1996**. Tertiary tectonic framework of the Iberian Peninsula, in: Friend, P.F., Dabrio, C.J. (Eds.), Tertiary Basins of Spain, the stratigraphic record of crustal kinematics. Cambridge University Press, pp. 9-14.

Sanz de Galdeano, C., **2008**. The Cadiz-Alicante Fault: an important discontinuity in the Betic Cordillera. Revista de la Sociedad Geológica de España 21 (1-2), 49-58.

Sanz de Galdeano, C., Alfaro, P., **2004**. Tectonic significance of the present relief of the Betic Cordillera. Geomorphology 63 (3-4), 175-190.

Sanz de Galdeano, C., López-Garrido, A.C., **2000**. Las fallas tortonienses a cuaternarias entre Granada y la costa: el límite occidental del Nevado-Filábride y de las unidades alpujárrides inferiores. (13), 519-528.

Sanz de Galdeano, C., Shanov, S., Galindo-Zalívar, J., Radulov, A., Nikolov, G., **2010**. A new tectonic discontinuity in the Betic Cordillera deduced from active tectonics and seismicity in the Tabernas Basin. J. Geodyn. 50 (2), 57-66. http://dx.doi.org/10.1016/j.jog.2010.02.005.

Savage, J.C., **1980**. Dislocations in seismology, Dislocations in Solids. F.R.N. Nabarro (ed.), North-Holland, New York, pp. 251-339.

Savage, J.C., Burford, R.O., **1970**. Accumulation of tectonic strain in California. Bull. Seismol. Soc. Am. 60 (6), 1877-1896.

Schwarz, K.P., Cannon, M., Wong, R.V.C., **1987**. The Use of GPS in Exploration Geophysics - A Comparison of Kinematic Models, IUGG Meeting, Vancouver, p. 20

Seber, D., Barazangi, M., Ibenbrahim, A., Demnati, A., **1996**. Geophysical evidence for lithospheric delamination beneath the Alboran Sea and Rif-Betic mountains. Nature 379, 785-790.

Sella, G.F., Dixon, T.H., Mao, A., **2002**. REVEL: A model for Recent plate velocities from space geodesy. J. Geophys. Res. 107 (B4), 2081. http://dx.doi.org/10.1029/2000JB000033.

Serpelloni, E., Vannucci, G., Pondrelli, S., Argnani, A., Casula, G., Anzidei, M., Baldi, P., Gasperini, P., **2007**. Kinematics of the western Africa-Eurasia plate boundary from focal mechanisms and GPS data. Geophys. J. Int. 169 (3), 1180-1200. http://dx.doi.org/10.1111/j.1365-246X.2007.03367.x.

Shen, Z.K., King, R.W., Agnew, D.C., Wang, M., Herring, T.A., Dong, D., Fang, P., **2011**. A unified analysis of crustal motion in Southern California, 1970-2004: The SCEC crustal motion map. J. Geophys. Res. 116 (B11), B11402. http://dx.doi.org/10.1029/2011jb008549.

Silva, P.G., **1994**. Evolución geodinámica de la Depresión del Guadalentín desde el Mioceno Superior hasta la actualidad: Neotectónica y Geomorfología. PhD thesis, Universidad Complutense de Madrid, Madrid, Spain, p. 642

Silva, P.G., Goy, J.L., Somoza, L., Zazo, C., Bardaji, T., **1993**. Landscape response to strike-slip faulting linked to collisional settings; Quaternary tectonics and basin formation in the eastern Betics, southeastern Spain. Tectonophysics 224 (4), 289-303. http://dx.doi.org/10.1016/0040-1951(93)90034-H.

Silva, P.G., Goy, J.L., Zazo, C., Lario, J., Bardaji, T., **1997**. Paleoseismic indications along 'Aseismic' fault segments in the Guadelentin depression (SE Spain). J. Geodyn. 24 (1-4), 105-115.

Soro, M., Giménez, J., Fleta, J., **1997**. Descripció dels emplaçaments per a observacions GPS del marge sudoriental de la Peninsula Ibèrica (prov. Almería i Murcia). Projecte CuaTeNeo. ICC, Barcelona, Spain

Soto, J.I., Fernández-Ibáñez, F., Fernández, M., García-Casco, A., **2008**. Thermal structure of the crust in the Gibraltar Arc: Influence on active tectonics in the western Mediterranean. Geochem. Geophys. Geosyst. 9 (10), 27.

Steblov, G.M., Kogan, M.G., King, R.W., Scholz, C.H., Bürgmann, R., Frolov, D.I., **2003**. Imprint of the North American plate in Siberia revealed by GPS. Geophys. Res. Lett. 30 (18). http://dx.doi.org/10.1029/2003GL017805.

Stich, D., Ammon, C.J., Morales, J., **2003**. Moment tensor solutions for small and moderate earthquakes in the Ibero-Maghreb region. J. Geophys. Res. 108 (B3), 1972-2012. http://dx.doi.org/10.1029/2002JB002057.

Stich, D., Martín, J.B., Morales, J., **2007**. Deformación sísmica y asísmica en la zona Béticas-Rif-Alborán. Revista de la Sociedad Geológica de España 20 (3-4), 311-319.

Stich, D., Martín, R., Morales, J., **2010**. Moment tensor inversion for Iberia-Maghreb earthquakes 2005-2008. Tectonophysics 483, 390-398. http://dx.doi.org/10.1016/j.tecto.2009.11.006.

Stich, D., Serpelloni, E., Mancilla, F., Morales, J., **2006**. Kinematics of the Iberia-Maghreb plate contact from seismic moment tensors and GPS observations. Tectonophysics 426 (3-4), 295-317. http://dx.doi.org/10.1016/j.tecto.2006.08.004.

Sue, C., Delacou, B., Champagnac, J.-D., Allanic, C., Burkhard, M., **2007**. Aseismic deformation in the Alps: GPS vs. seismic strain quantification. Terra Nova 19 (3), 182-188. http://dx.doi.org/doi:10.1111/j.1365-3121.2007.00732.x.

Tahayt, A., Mourabit, T., Rigo, A., Feigl, K.L., Fadil, A., McClusky, S., Reilinger, R., Serroukh, M., Ouazzani-Touhami, A., Sari, D.B., Vernant, P., **2008**. Mouvements actuels des blocs tectoniques dans l'arc Bético-Rifain à partir des mesures GPS entre 1999 et 2005. Comptes Rendus Geosciences 340 (6), 400-413.

Thatcher, W., **1990**. Present-day crustal movements and the mechanics of cyclic deformation. The San Andreas Fault system, California, Geological Survey Professional Paper 1515, 189-205.

Torres-Roldán, R.L., Poli, G., Peccerillo, A., **1986**. An Early Miocene arc-tholeiitic magmatic event from the Alboran Sea - Evidence for precollisional subduction and back-arc crustal extension in the westernmost Mediterranean. Geol. Rundsch. 75, 219-234.

Tregoning, P., van Dam, T., **2005**. Atmospheric pressure loading corrections applied to GPS data at the observation level. Geophys. Res. Lett. 32 (22), L22310. http://dx.doi.org/10.1029/2005gl024104.

Turcotte, D.T., Schubert, G., **1982**. Geodynamics, Applications of Continuum Physics to Geological Problems. John Wiley & Sons, New York, N.Y., USA.

Valera, J.L., Negredo, A.M., Villaseñor, A., **2008**. Asymmetric delamination and convective removal numerical modeling: Comparison with evolutionary models for the Alboran Sea region. Pure Appl. Geophys. 165 (8), 1683-1706. http://dx.doi.org/10.1007/s00024-008-0395-8.

Van Balen, R.T., Forzoni, A., Van Dam, J.A., **2013**. Active faulting and folding along the Jumilla Fault Zone, northeastern Betics, Spain. Geomorphology. http://dx.doi.org/10.1016/j.geomorph.2013.12.001.

Van der Pluijm, B.A., Marshak, S., **1997**. Earth structure: an introduction to structural geology and tectonics. WCB/McGraw-Hill; 1st ed.

Vergés, J., Fernàndez, M., **2012**. Tethys-Atlantic interaction along the Iberia-Africa plate boundary: The Betic-Rif orogenic system. Tectonophysics 579, 144-172. http://dx.doi.org/10.1016/j.tecto.2012.08.032.

Vernant, P., **2015**. What can we learn from 20 years of interseismic GPS measurements across strike-slip faults? Tectonophysics In Press. http://dx.doi.org/10.1016/j.tecto.2015.01.013.

Vernant, P., Fadil, A., Mourabit, T., Ouazar, D., Koulali, A., Davila, J.M., Garate, J., McClusky, S., Reilinger, R., **2010**. Geodetic constraints on active tectonics of the Western Mediterranean: Implications for the kinematics and dynamics of the Nubia-Eurasia plate boundary zone. J. Geodyn. 49 (3-4), 123-129. http://dx.doi.org/016/j.jog.2009.10.007.

Vissers, R.L.M., Meijninger, B.M.L., **2011**. The 11 May 2011 earthquake at Lorca (SE Spain) viewed in a structural-tectonic context. Solid Earth 2 (2), 199-204. http://dx.doi.org/10.5194/se-2-199-2011.

Wallace, R.E., **1986**. Active tectonics: Impact on society. Studies in geophysics, National Academy Press, Washington, D.C.

Wang, R., Martín, F.L., Roth, F., **2003**. Computation of deformation induced by earthquakes in a multi-layered elastic crust-"FORTRAN programs DGRN/EDCMP. Computers & Geosciences 29 (2), 195-207. http://dx.doi.org/10.1016/S0098-3004(02)00111-5.

Ward, S.N., **1998**. On the consistency of earthquake moment rates, geological fault data, and space geodetic strain: the United States. Geophys. J. Int. 134 (1), 172-186.

Watson, C., Tregoning, P., Coleman, R., **2006**. Impact of solid Earth tide models on GPS coordinate and tropospheric time series. Geophys. Res. Lett. 33 (8), L08306. http://dx.doi.org/10.1029/2005gl025538.

Weijermars, R., **1987**. The Palomares brittle-ductile Shear Zone of southern Spain. J. Struct. Geol. 9, 139-157.

Weijermars, R., Roep, T.B., Van den Eeckhout, B., Postma, G., Kleverlaan, K., **1985**. Uplift history of a Betic fold nappe inferred from Neogene-Quaternary sedimentation and tectonics (in the Sierrra Alhamilla and Almeria, Sorbas and Tabernas Basins of the Betic Cordilleras, SE Spain). Geol. Mijnbouw 64, 397-411.

Wiemer, S., **2001**. A software package to analyze seismicity: ZMAP. Seismol. Res. Lett. 72 (3), 373-382.

Williams, S., **2008**. CATS: GPS coordinate time series analysis software. GPS Solutions 12 (2), 147-153.

Williams, S.D.P., Bock, Y., Fang, P., Jamason, P., Nikolaidis, R.M., Prawirodirdjo, L., Miller, M., Johnson, D.J., **2004**. Error analysis of continuous GPS position time series. J. Geophys. Res. 109 (B3). http://dx.doi.org/10.1029/2003jb002741.

Wyss, M., **1973**. Towards a physical understanding of the earthquake frequency distribution. Geophys. J. Roy. Astron. Soc. 31 (4), 341-359.

Zeck, H.P., **1996**. Betic-Rif Orogeny; subduction of Mesozoic Tethys lithosphere under eastward drifting Iberia, slab detachment shortly before 22 Ma, and subsequent uplift and extensional tectonics. Tectonophysics 254, 1-16.

Appendix A

Eastern Betics geological map with SGPS and CGPS stations.

Geological map: IGME - Mapa geológico de la Península Ibérica, Baleares y Canarias a escala 1/1.000.000; http://mapas.igme.es/Servicios/default.aspx#IGME_Geologico_1M

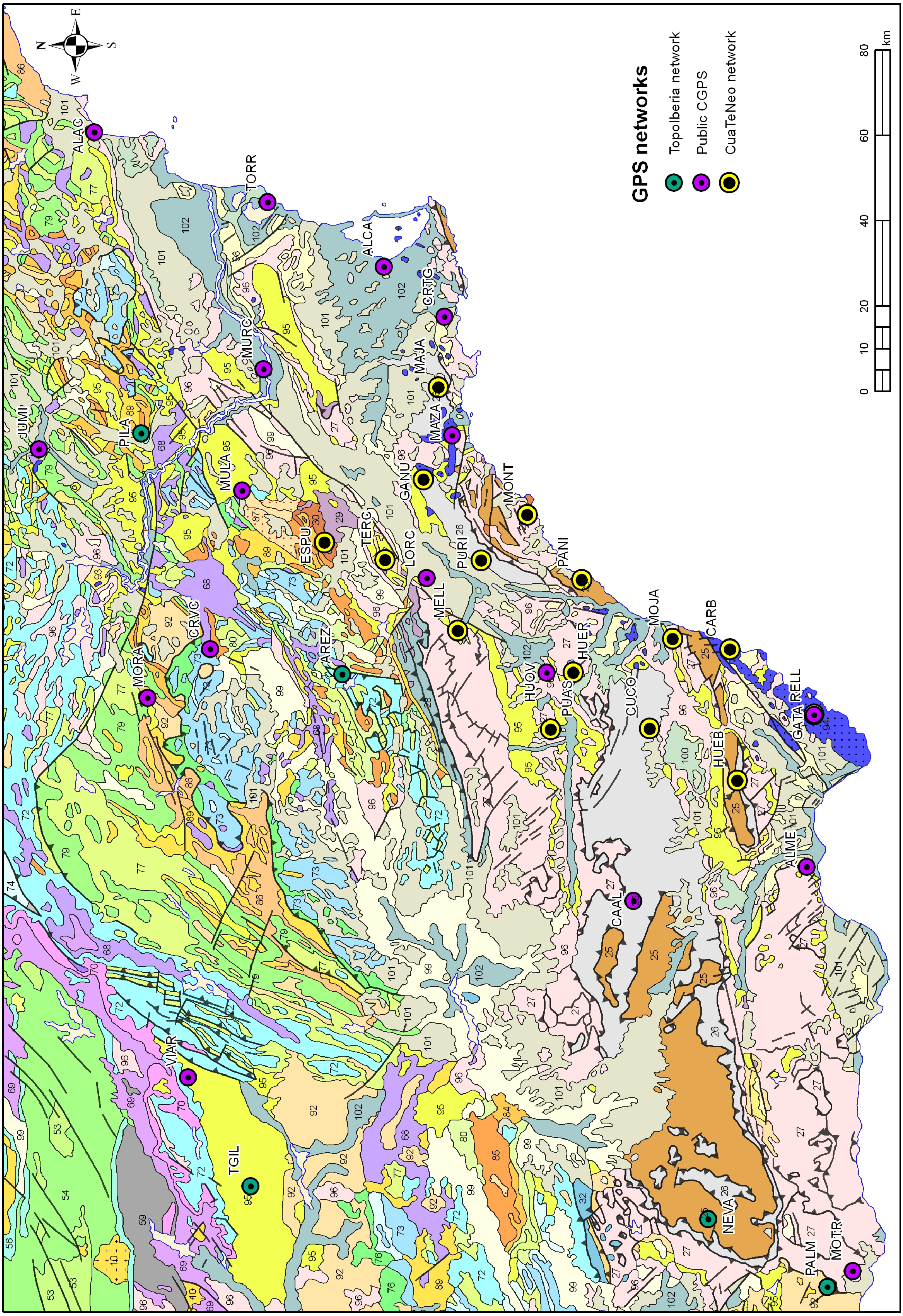
GPS networks
TopoIberia network
Public CGPS
CuaTeNeo network
0 10 20 40 60 80 km
N
E
S
W
ALAC
TORR
ALCA
CRTG
MAJA
MAZA
MURC
JUMI
PILA
MULA
GANU
MONT
ESPU
TERC
LORC
PURI
PANI
MELL
CRVG
MORA
AREZ
MOJA
CARB
HUOV
HUER
PUAS
CUCO
GATA
RELL
HUEB
ALME
CAAL
VIAR
TGIL
NEVA
PALM
MOTR

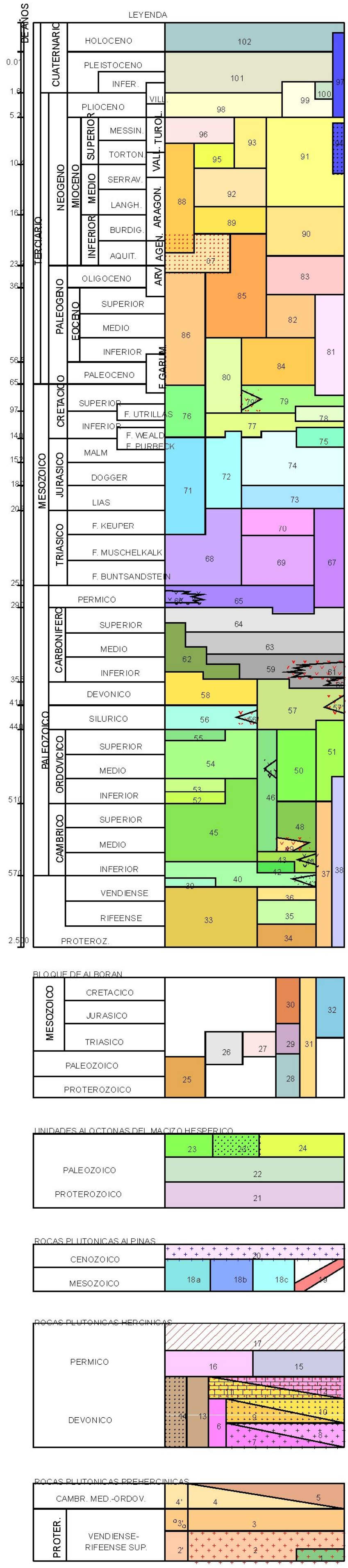

102 Gravas, arenas, arcillas y limos. Aluvial, playas, fechas litorales

101 Conglomerados, gravas, arenas, areniscas, arenas, limos y arcillas. Terrazas fluviales y marinas

100 Conglomerados, areniscas y arcillas

99 Conglomerados, areniscas, arcillas, calizas y/o yesos

98 Calcarenitas, arenas y limos amarillos

97 Basaltos alcalinos

96 Conglomerados, arenas, arrecifes, limos amarillos, yesos y sales haloideas. Conglomerados, arenas y calizas lacustres

95 Conglomerados, calcarenitas, calizas arrecifales, areniscas y margas con niveles turbiditicos

94 Rocas volcanicas calcoalcalinas (andesitas, dacitas, riolitas, shoshonitas, lamproitas)

93 Conglomerados, areniscas, arcillas, calizas y yesos

92 Conglomerados, calizas y margas. Margas con olistostromas de origen diverso

91 Conglomerados, areniscas, arenas arcosicas, arcillas, calizas y yesos

90 Calizas arrecifales, calcarenitas y conglomerados. Arcillas con olistolitos

89 Calizas, biocalcarenitas y margas. Margas y margoclizas blancas con radiolarios (moronitas o albarizas)

88 Areniscas siliceas turbiditicas. Calizas y margas arenosas

87 Conglomerados, areniscas y arcillas. Calizas y/o yesos

86 Conglomerados, areniscas, arenas, arcillas, margas y yesos

85 Turbiditas calcareas, calizas y margas. Pudingas, areniscas y margas arenosas. Areniscas y calizas lacustres

84 Turbiditas calcareas, calizas, margas, conglomerados, areniscas y arcillas. Calizas lacustres

83 Turbiditas calcareas. Calizas, calizas arenosas, areniscas y margas arenosas

82 Areniscas siliceas y arcillas

80 Dolomias, calizas y margas. Margocalizas, calizas arenosas, areniscas y arcillas

79 Margas y arcillas con niveles turbiditicos. Margocalizas y calizas margosas (Capas rojas)

78 Gravas, arenas, areniscas y arcillas. Carbon

77 Margas y margocalizas. Margas arcillosas turbiditicas. Calizas arenosas, areniscas, arenas y margas.

76 turbiditas siliceas, Margas con turbiditas y margocalizas. Calizas bioclasticas, calcarenitas, arenas, margas, dolomias y calizas

75 Conglomerados, areniscas, arenas y margas

74 calizas, margas, calizas nodulosas y radiolaritas. Rocas volcanicas

73 Dolomias, calizas y calizas nodulosas

72 Dolomias, calizas, calizasooliticas y nodulosas

71 Dolomias, margas y calizas nodulosas

70 arcillas versicolores y yesos

69 Conglomerados, areniscas, arcillas, dolomias, calizas y margas

68 Areniscas, conglomerados, dolomias, calizas, arcillas y yesos

65 Lutitas, areniscas, conglomerados y vulcanitas o calizas

63 Pizarras, areniscas, conglomerados, carbon y calizas

61 Vulcanitas y rocas vulcanoclasticas

59 Pizarras y grauwacas; conglomerados y calizas

58 Areniscas, pizarras, calizas, cuarcitas y rocas vulcanoclasticas

57 Pizarras, esquistos, areniscas, calizas, ampelitas y liditas

56 Ampelitas, cuarcitas, liditas y rocas vulcanoclasticas

54 Pizarras, areniscas, cuarcitas y calizas o rocas vulcanoclasticas

53 Ortocuarcitas, areniscas y pizarras

52 Conglomerados, areniscas, cuarcitas y pizarras

43 Calizas y dolomias

42 Areniscas, pizarras y calizas

41 Vulcanitas acidas y rocas vulcanoclasticas

40 Pizarras, grauwacas o arcosas, conglomerados y calizas

39 Pizarras, areniscas, conglomerados y calizas

38 Cuarcitas, gneises, esquistos, pizarras y grauwacas

37 Genises, migmatitas, cuarcitas y marmoles

36 Vulcanitas y/o rocas vulcanoclasticas y metasedimentos

35 Esquistos o pizarras, grauwacas y liditas

34 Gneises y anfibolitas

33 Pizarras, grauwacas, conglomerados o porfiroides

32 Dolomias, calizas, margas, areniscas y arcillas (M. Dorsal)

31 Filitas, areniscas, calizas, dolomias, margas

30 Dolomias, calizas, margocalizas, y margas arenosas

29 Dolomias, areniscas, conglomerados, arcillas, y margas

28 Filitas, pelitas, areniscas, grauwacas, calizas y conglomerados

27 Genises, migmatitas, micasquistos, esquistos, filitas, marmoles, calizas y dolomias (M. Alpujarride)

26 Anfibolitas, serpentinitas, micaesquistos, y marmoles (M. del Mulhacen)

25 Micaesquistos grafitosos con granates (M. del Veleta)

18 Metagranitos

17 Granitoides de tendencia alcalina postcinematicos

16 Granitoides s.l. indiferenciado

15 Rocas basicas y ultrabasicas

10 Granitoides biotiticos

2 Granitoides calcoalcalinos

Appendix B

Residual position time-series of the CuaTeNeo GPS stations with 1σ uncertainties.

CARB

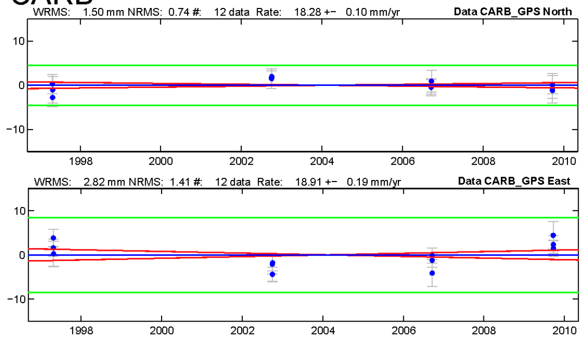

GANU

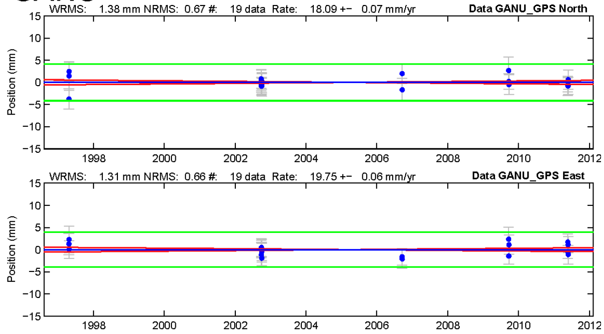

CART

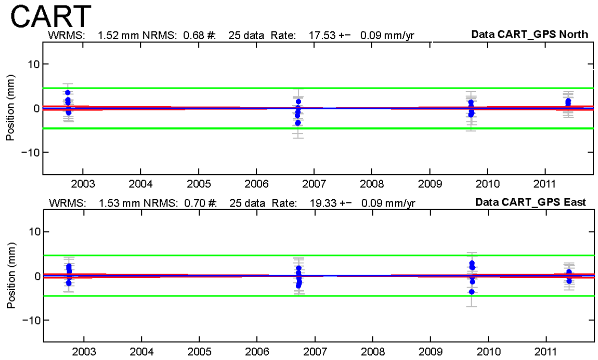

HUEB

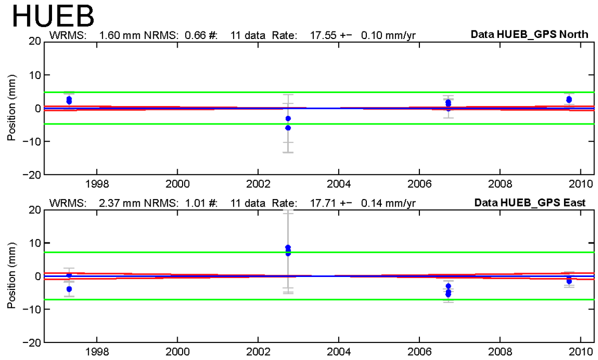

CUCO

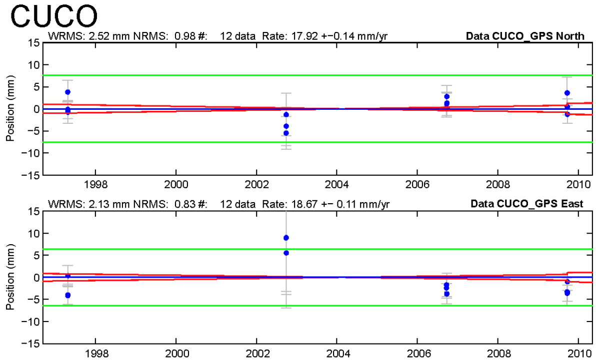

HUER

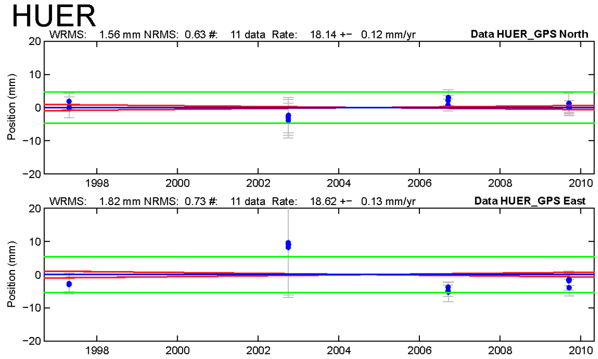

ESPU

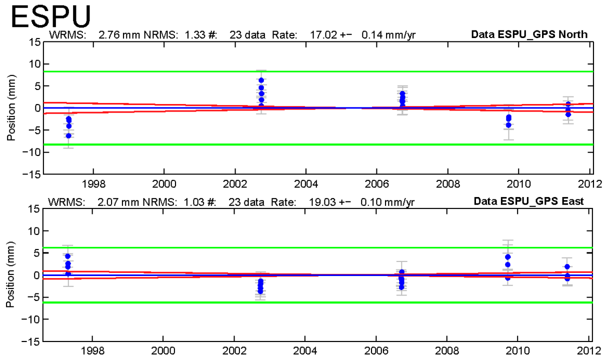

MAJA

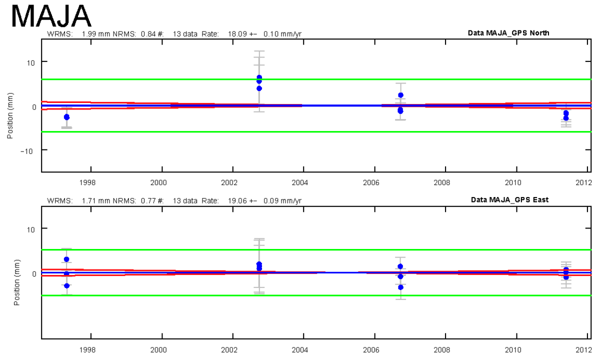

MELL

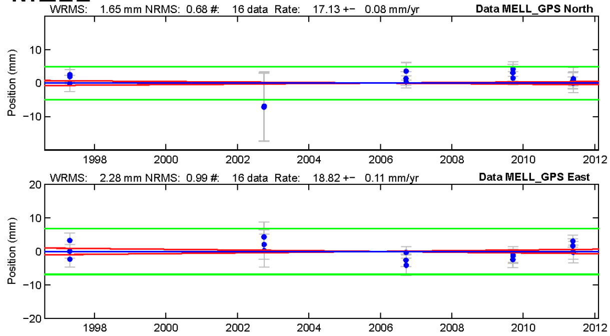

PUAS

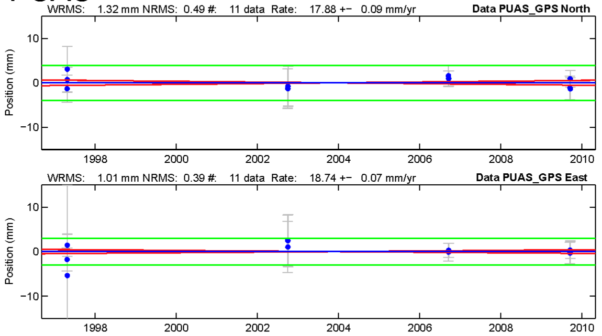

MOJA

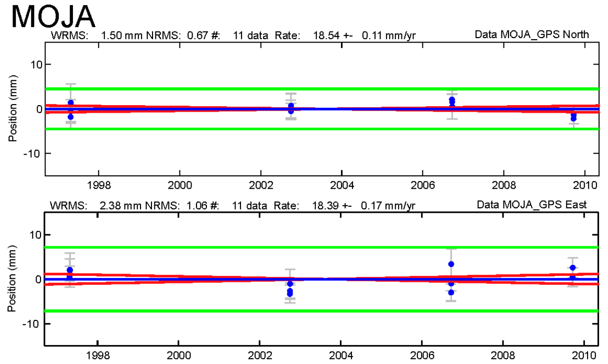

PURI

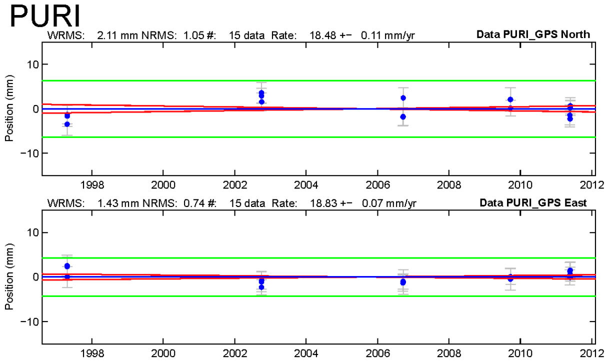

MONT

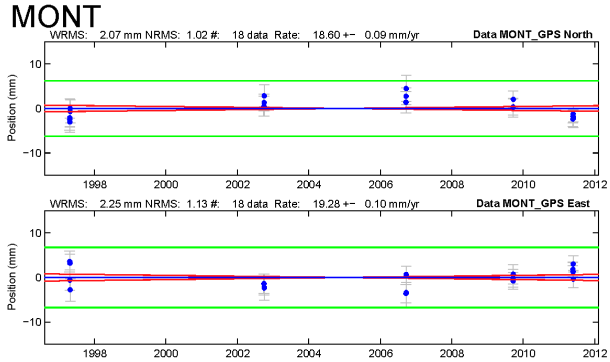

RELL

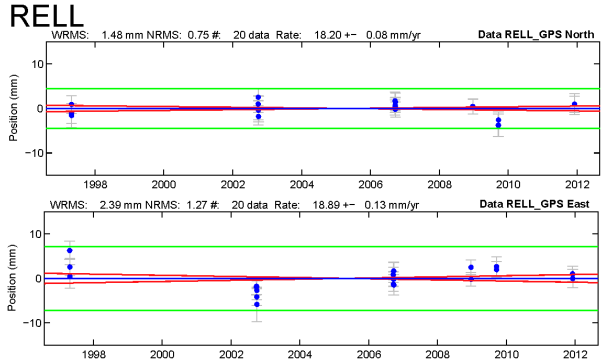

PANI

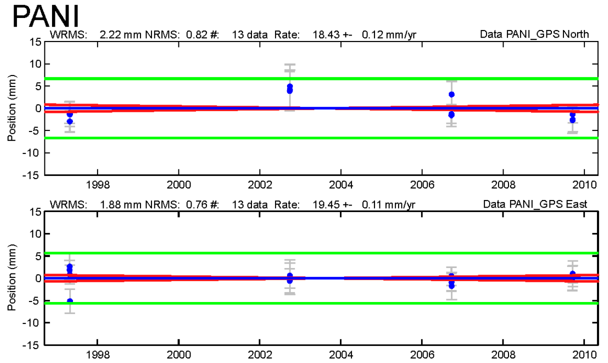

TERC

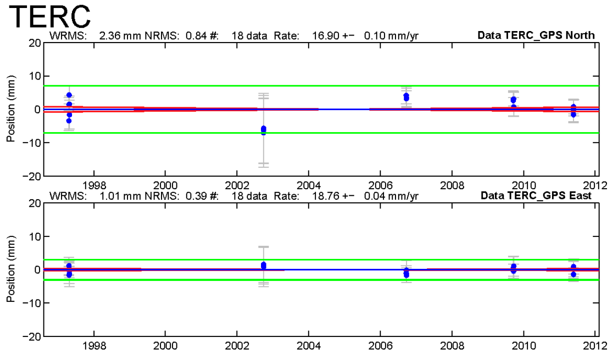

Appendix C

Published and submitted papers:

- Echeverria, A., Khazaradze, G., Gárate, J., Asensio, A., Surinach, E., **2012**. Deformación cortical de las Béticas Orientales mediante GPS y su relación con el terremoto de Lorca. Fisica de la Tierra 24, 113-127.

- Frontera, T., Concha, A., Blanco, P., Echeverria, A., Goula, X., Arbiol, R., Khazaradze, G., Pérez, F., Suriñach, E., **2012**. DInSAR coseismic deformation of the May 2011 Mw 5.1 Lorca earthquake, (Southern Spain). Solid Earth 3, 111-119.

- Echeverria, A., Khazaradze, G., Asensio, A., Gárate, J., Dávila, J.M., Suriñach, E., **2013**. Crustal deformation in eastern Betics from CuaTeNeo GPS network. Tectonophysics 608, 600-612.

- Echeverria, A., Khazaradze, G., Asensio, A., Masana, E., **Submitted**. Geodetic evidence for continuing tectonic activity of the Carboneras fault (SE Spain). Tectonophysics.

Deformación cortical de las Béticas Orientales observada mediante GPS y su relación con el terremoto de Lorca

ANNA ECHEVERRÍA[1], GIORGI KHAZARADZE[1], EVA ASENSIO[1], JORGE GÁRATE[2] & EMMA SURIÑACH[1]

[1] Grupo RISKNAT, Dept. de Geodinàmica i Geofísica, Universitat de Barcelona, C/Martí i Franquès s/n, 08028, Barcelona, España
[2] Real Instituto y Observatorio de la Armada, C/ Cecilio Pujazón s/n, 1110 San Fernando, España
anna.echeverria@ub.edu

Recibido: 02/05/2012
Aceptado: 24/09/2012

Resumen
El 11 de Mayo del 2011 tuvo lugar una serie sísmica en la localidad murciana de Lorca. El terremoto principal de M_w5.2 se atribuye a la Falla de Alhama de Murcia, una de las fallas más activas del SE de la Península Ibérica. Mediante el análisis de las cinco campañas GPS de la red CuaTeNeo realizadas entre 1997 y 2011 se ha caracterizado el campo inter-sísmico de velocidades de la zona. Las velocidades de las estaciones más cercanas a la Falla Alhama de Murcia detectan el carácter inverso y de desgarre de esta falla. Las estaciones situadas entre la costa Mediterránea y la falla presentan las máximas velocidades de la zona (entre 1.4 y 1.8 mm/a) con una orientación NNO, oblicuas a la traza de esta. La cinemática de la falla deducida a través de las tasas deformación obtenidas a partir de los vectores GPS de la red CuaTeNeo coincide con el mecanismo focal obtenido para el terremoto. El análisis en detalle de la estación GPS continua en Lorca permite la detección de un salto co-sísmico de ~6 mm hacia el Norte.
Palabras clave: deformación cortical, GPS, Béticas, terremoto de Lorca.

GPS crustal deformation of the Eastern Betics and its relationship with the Lorca earthquake

Abstract
On May 11th of 2011, a seismic series occurred near the city of Lorca (Murcia). The main earthquake of magnitude M_w 5.2 has been attributed to the Alhama de Murcia Fault, one of the most active faults in the SE Iberian Peninsula. We analyzed data from 5 GPS campaigns of the CuaTeNeo network conducted between 1997 and 2011. The velocities of the stations closest to the Alhama de Murcia Fault show the reverse and strike-slip direction of motion. Stations located on the southeastern side of the fault have the maximum velocities in the area (between 1.4 and 1.8 mm/yr), oriented towards NNW direction, obliquely to the trace of the fault. The kinematics of the fault and the strain rate directions obtained from the CuaTeNeo network GPS measurements matches the calculated focal mechanism of Lorca earthquake. Detailed analysis of the time-series from the continuous GPS station at the Lorca city allows the detection of co-seismic offset of ~6 mm to the North.
Keywords: crustal deformation, GPS, Betics, Lorca earthquake.

ISSN: 0214-4557
http://dx.doi.org/10.5209/rev_FITE2012.v24.40134

Referencia normalizada
Echeverría, E., Khazaradze, G., Asensio, E., Gárate, J., Suriñach, E. (2012). Deformación cortical de las Béticas Orientales observada mediante GPS y su relación con el terremoto de Lorca. *Física de la Tierra*, Vol. 24, 113-127.

Introducción

La zona sísmicamente más activa de la Península Ibérica corresponde al margen suroriental, abarcando la zona de Valencia, Murcia y Andalucía (Buforn et al., 1995). La deformación cortical en este área está controlada principalmente por la convergencia entre las placas de Nubia y Eurasia. Gran parte de esta sismicidad se atribuye a las fallas con componente de desgarre de la Zona de Cizalla de las Béticas Orientales (ZCBO o EBSZ en inglés). La ZCBO, de orientación NE-SO, está formada principalmente por las siguientes fallas: Falla Bajo Segura, Falla Carrascoy, Falla Alhama de Murcia (FAM), Falla Palomares y la Falla Carboneras. La sismicidad instrumental en la ZCBO se caracteriza por terremotos superficiales de magnitud baja a moderada, no superiores a M_w6 (e.g. Buforn et al., 2004; Buforn et al., 1995; Stich et al., 2003).

El último terremoto destacable de la zona ocurrió el 11 de Mayo del 2011 en la ciudad de Lorca (e.g. Martínez-Díaz *et al.*, 2012). Este terremoto de M_w5.2 causó notables daños materiales así como nueve víctimas. El terremoto principal tuvo casi dos horas antes un precursor de magnitud M_w 4.5 y fue seguido por diversas réplicas de menor magnitud. La sismicidad histórica de la localidad de Lorca muestra registros de terremotos destacables, como el de 1579 o el de 1674, de intensidades EMS VII y VIII, respectivamente (Martínez Solares and Mezcua, 2002). En el registro instrumental, otras series sísmicas parecidas a la de Lorca ocurrieron en un radio de 50 km: en 1999 en Mula (M_w 5.1), en 2002 en Bullas (M_w 4.6) y en 2005 en La Paca (M_w 4.7).

El terremoto de Lorca se atribuye a la FAM, la traza de la cual pasa por Lorca. (e.g IGME, 2011; Vissers and Meijninger, 2011). Martínez-Díaz (2012) propone como fuente del terremoto el área entre los segmentos de Goñar-Lorca y Lorca-Totana, formada por una compleja estructura. Los mecanismos focales publicados (e.g. López-Comino et al., 2012) muestran una componente de desgarre sinestral e inversa, donde la traza de uno de los planos nodales coincide con la orientación general de la falla (Figura 1). La relocalización de los sismos principales y las réplicas, recientemente publicadas por López-Comino (2012), se sitúan al norte y alineadas paralelamente a la traza superficial de la FAM (Figura 1). No obstante, en el reconocimiento de campo, no se detectaron rupturas superficiales (IGME, 2011).

1. Datos GPS

Para este trabajo se han utilizado dos tipos de registro de datos GPS que se diferencian según el modo de observación: continua o intermitente (campañas).

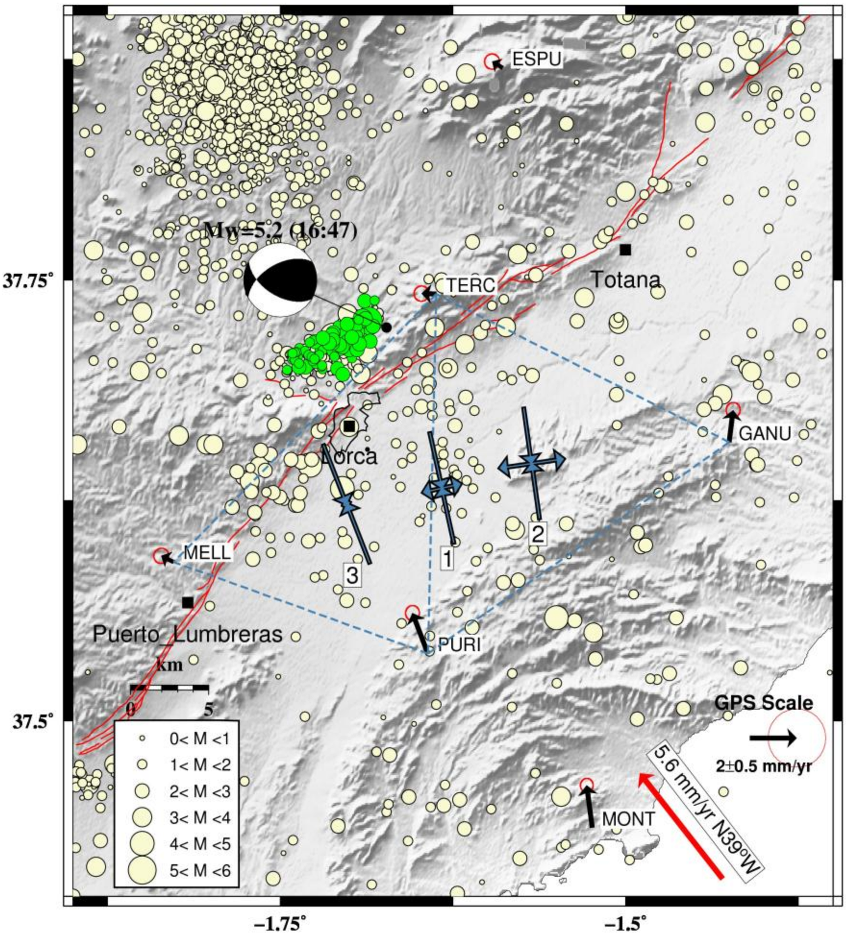

Fig. 1: Localización del mecanismo focal del terremoto principal (M_w5.2) de Lorca de 11/05/2011 junto con las réplicas (color verde) según López-Comino (2012). La sismicidad instrumental del catálogo del IGN (*www.ign.es*) está representada con círculos amarillos. Las velocidades horizontales de las estaciones GPS de la red CuaTeNeo están respecto a Eurasia. Las tasas de deformación estimadas a partir de las velocidades de las estaciones TERC, MELL, PURI y GANU están indicadas con las flechas azules (ver Tabla 1). El vector rojo indica la convergencia entre las placas Eurasiática y Nubia según el modelo MORVEL (DeMets et al., 2010). La traza de la Falla de Alhama de Murcia ha sido obtenida de Martínez-Díaz, (1998) y García-Mayordomo (2010).

1.1 Datos GPS continuos

En la ciudad de Lorca existen dos estaciones de referencia GPS con registro continuo (CGPS), una perteneciente a la red Meristemum, de la Dirección General de Patrimonio Natural y Biodiversidad (*http://gps.medioambiente.carm.es/),* y la otra a la red REGAM, del Servicio de Cartografía de la Consejería de Obras Públicas (*www.iderm.es/geodesia/index.htm*), ambas de la Región de Murcia. Las dos estaciones disponen un acceso libre y gratuito a los datos. Debido a que las dos estaciones se denominan LORC, a partir de ahora la estación de la red Meristemum se nombrará como LRCA.

Fig. 2: Estaciones GPS en las inmediaciones de Lorca. A) Estación permanente LORC de la red REGAM (www.cartomur.com/geodesia/lorca.htm). B) Estación TERC de la red CuaTeNeo situada en la Sierra de Tercia. C) Estación continua LRCA de la red Meristemum (imágenes cedidas por la Dirección General de Medio Ambiente de la Región de Murcia).

La estación GNSS de referencia **LORC** (red REGAM) está instalada sobre el tejado de un edificio del Parque de Bomberos (Figura 2A). La antena se encuentra enroscada a un mástil de acero, cuya base es un cubo de hormigón de 0,5 m de lado, solidario con la estructura. Los daños estructurales a causa del terremoto fueron apreciables, afectando en consecuencia a la antena (com. pers. de Ramón Pablo García de la Comunidad Autónoma de la Región de Murcia). Durante la ocurrencia del terremoto la estación no estaba operativa, de modo que no hay datos registrados en esa época.

La estación de referencia permanente **LRCA** (red Meristemum) está situada en el tejado de una casa de una planta (Figura 2C). La estación fue instalada en 2006 pero hasta el 2008 no se han utilizado los datos registrados ya que se cambió su ubicación. Esta estación registró datos durante el evento.

1.2. Datos GPS de campañas

La red GPS CuaTeNeo (Cuantificación de la Tectónica y Neotectónica en la parte oriental de la Península Ibérica) fue establecida en 1996 con el fin de cuantificar las deformaciones tectónicas actuales del SE de las Béticas, especialmente en las fallas de Alhama de Murcia, Palomares y Carboneras (Soro et al., 1997). La red está formada por 15 vértices. Once están construidos en una base de hormigón de 0.5x0.5x1m fijada en el substrato (ver la Figura 2B) y 4 vértices materializados en un clavo de acero incrustado directamente en la roca. La red abarca un área de ~6000 km^2 entre Murcia y Almería, con una distancia media entre los vértices de 25 km. La red se estableció gracias al proyecto PB93-0743-C02, realizado por la Universitat de Barcelona (UB) y el Institut Cartogràfic de Catalunya (ICC). Posteriormente, el Real Observatorio de la Armada Española (ROA) se unió al equipo para realizar observaciones de la red.

La red ha sido observada en su totalidad en 4 ocasiones: 1997, 2002, 2006 y 2009 (*Khazaradze et al.*, 2008). Durante cada campaña, la estación es observada durante al menos 3 días (máximo 6 días), en sesiones de un mínimo de ocho horas. En las ocasiones en que se ha podido dejar el equipo por la noche, se ha registrado de manera continua. En las primeras dos campañas (1997 y 2002) los instrumentos utilizados fueron receptores Trimble 4000SSE y antenas Trimble 22020.00_gp. En las posteriores campañas, se utilizaron receptores Topcon GB1000 con antenas PG-A1_6_gp.

Dos semanas después del terremoto de Lorca del 2011, se llevó a cabo una campaña de medición extraordinaria. El motivo principal de esta campaña era poder detectar posibles deformaciones co-sísmicas en las estaciones de la red CuaTeNeo. En esta ocasión se midieron los 7 vértices más cercanos al epicentro: ESPU, TERC, MELL, MONT, PURI, GANU y MAJA. El tiempo de registro medio para cada estación fue de 4 días de manera continuada, a excepción de ESPU que fueron 3 y MELL 5.

2. Campo de velocidades

Los datos de las campañas han sido procesados mediante el software de alta precisión GAMIT/GLOBK (Herring *et al.* 2010; *www-gpsg.mit.edu/~simon/gtgk/*), desarrollado por el Massachusetts Institute of Technology. Se han empleado los tres pasos propuestos por McClusky (2000). Los resultados obtenidos son las velocidades horizontales con un límite de confianza del 95% (las elipses de error), respecto a Eurasia (Figura 1). Estas velocidades representan una fase inter-sísmica de deformación promedio entre los 15 años de registro (1997-2011).

La principal característica del campo de velocidades GPS es la uniformidad del movimiento de las tres estaciones situadas en el lado SE de la FAM (MONT, PURI y GANU) hacia el NNO, aproximadamente en dirección de la convergencia entre Eurasia y Nubia. En cambio, las estaciones situadas en el bloque occidental de la falla (TERC, ESPU y MELL) muestran una velocidad de magnitud inferior, sobre los 0.5-0.6±0.3 mm/a y con un pequeño componente oeste respecto a Eurasia. Es obvio que la Falla de Alhama de Murcia sirve como divisora entre dos regímenes tectónicos diferentes y acumula la mayoría de la deformación observada a través de las medidas de GPS. El movimiento relativo entre las estaciones a los dos lados de la FAM indica una compresión oblicua, donde predomina el movimiento de compresión.

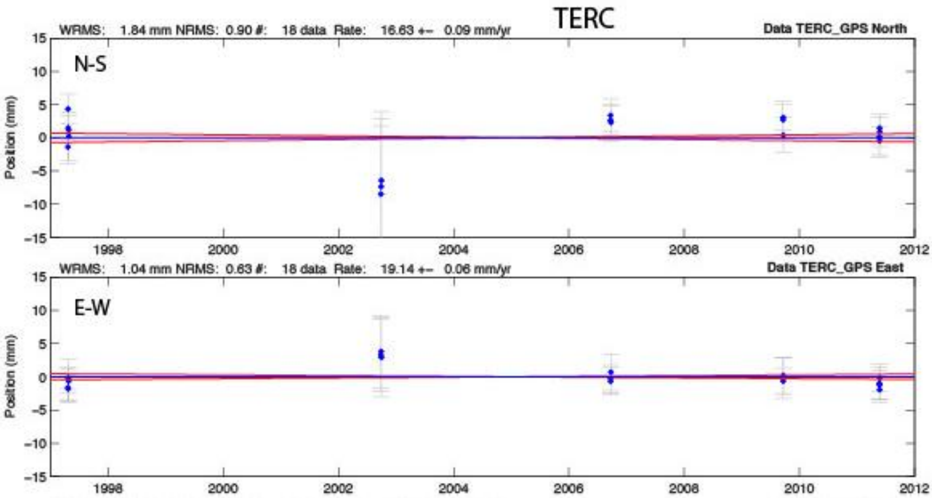

Fig. 3: Serie temporal residual de la estación TERC de la red CuaTeNeo en las dos componentes horizontales (N-S y E-O) en el sistema de referencia ITRF2008. Cada agrupación de puntos pertenece a los datos de una campaña de medición. Las rectas de regresión (líneas rojas) representan las incertidumbres asociadas al pendiente (e.g. velocidad). A la campaña del 2002 se le ha dado menos peso (ver las barras de error más grandes) ya que presenta alguna anomalía.

Respecto de la campaña de 2011, la cual se realizó después del terremoto de Lorca, existía la posibilidad que las medidas de esta campaña tuvieran efectos co-sísmicos relacionados con el terremoto. No obstante, el análisis en detalle de las series temporales de todas las estaciones medidas en la campaña de 2011 no muestra ningún salto debido al terremoto de Lorca. En la Figura 3 se muestra la serie temporal de la estación TERC de la red CuaTeNeo, la más cercana al epicentro, donde no se puede apreciar ningún salto co-sísmico entre las dos últimas campañas realizadas antes y después del terremoto de Lorca. La ausencia de deformación co-sísmica en las estaciones de CuaTeNeo no es sorprendente, debido a la relativamente pequeña magnitud del terremoto (M_w5.2) y a la ausencia de rotura superficial en la zona del epicentro (IGME, 2012). La modelización numérica presentada en el apartado 3.3, también corrobora esta afirmación.

3. Discusión de los resultados

3.1 Velocidades GPS inter-sísmicas

El campo de velocidades inter-sísmico obtenido a partir de las mediciones de la red CuaTeNeo muestra una cinemática en el área que coincide con la cinemática de la FAM (e.g. Martínez-Díaz, 2002) y con el tipo de mecanismo focal del terremoto del Lorca (López-Comino et al., 2012). Hemos escogido la estación más representativa de este tipo de movimiento, PURI, para un simple ejercicio. La velocidad horizontal obtenida en esta estación es de 1.7±0.3 mm/a respecto Eurasia. La descomposición de esta velocidad en la componente paralela y perpendicular a la FAM muestra 0.55 y 1.6 mm/a, respectivamente. Se ha considerado una dirección de 235º para la FAM, coincidente con la traza a su paso por Lorca (Figura 1) y con la dirección obtenida por los modelos de inversión de Martínez-Díaz et al. (2012) (235º) y López-Comino (2012) (240º), así como uno de los planos nodales de los mecanismos focales publicados (e.g. 230º en la solución del IGN (2011)). La velocidad perpendicular a la falla es tres veces superior a la de la componente paralela. Este tipo de relación 3:1 es parecida al mecanismo focal del terremoto de Lorca, donde predomina la componente compresiva ante la de salto en dirección.

En el mapa de velocidades (Figura 1), también se puede observar que todas las estaciones GPS localizadas al SE de la FAM, presentan unas velocidades entre 1.2±0.3 mm/a (GANU) y 1.7±0.3 mm/a (PURI y MONT) con una orientación hacia el N-NNO. Estas orientaciones están un poco más desviadas hacia el norte que la orientación de la convergencia entre las placas Eurasiática y de Nubia (Figura 1). La convergencia en la zona según el modelo MORVEL (DeMets et al., 2010) es de 5.6±0.3 mm/a, con una orientación hacia el NNO de N321.3±1.8º. Estos valores muestran que el 20-30% de la convergencia entre las dos placas se está produciendo en el margen suroriental de las Cordilleras Béticas.

El análisis en detalle de las series temporales de las dos únicas estaciones CGPS existentes en la zona, LRCA y LORC, anteriores al terremoto de Lorca, indica un comportamiento altamente anómalo. La estación LRCA mostraba un hundimiento con una tasa de 95.0±1.0 mm/a (Figura 4a) y un movimiento horizontal hacia el N230°E con la velocidad de 26.0±0.5 mm/a respecto Eurasia. La estación LORC, también revela un movimiento anómalo, aunque en menor grado: 6.7±0.7 mm/a hacia N121°E y con una subsidencia significativamente menor: -6.5±0.1 mm/a (Figura 4b).

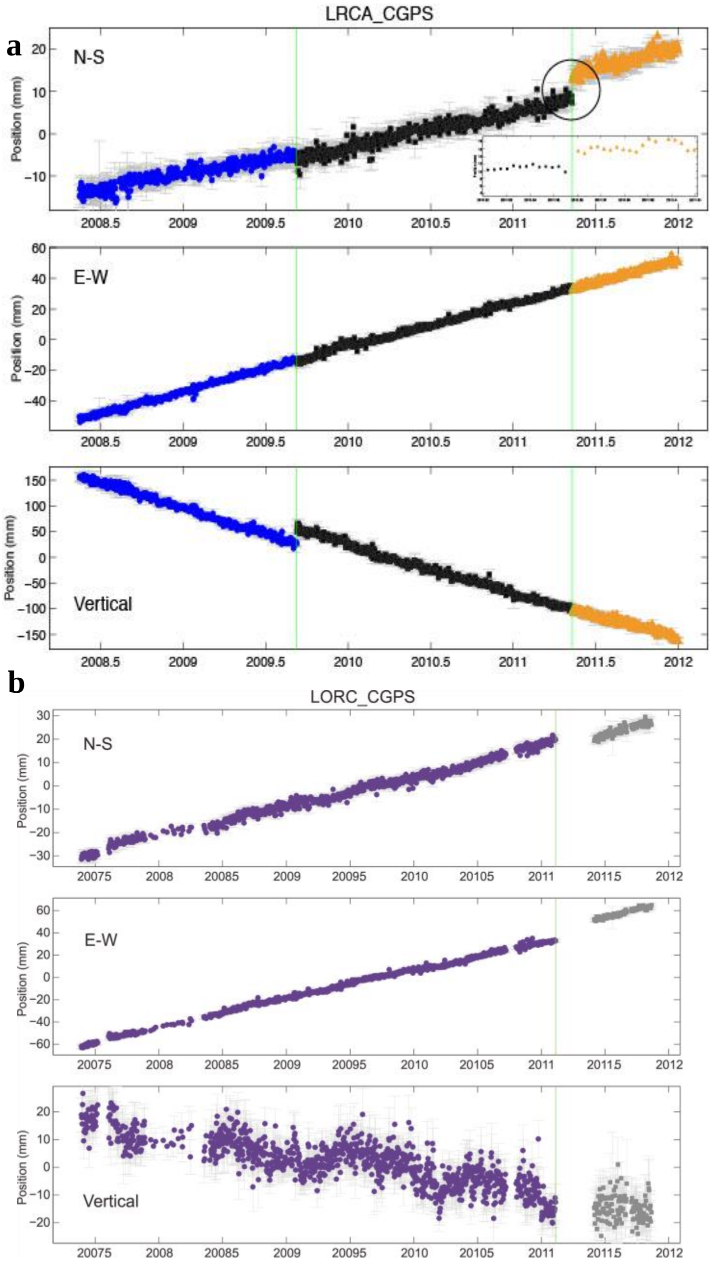

Fig. 4: Series temporales de la estación CGPS LRCA (a) y LORC (b) en el sistema de referencia de ITRF2008. a) La primera línea vertical verde (09/09/2009) corresponde a un cambio en la antena y la segunda al terremoto de Lorca del 11/05/2011. En la componente

N-S, donde se detecta el salto co-sísmico, se ha incluido una ampliación de la serie temporal. a) El periodo de ausencia de datos coincide con el terremoto de Lorca de 2011.

En principio se pensó que estos movimientos anómalos correspondían a una inestabilidad del terreno, del edificio o del monumento geodésico donde se localizaban las estaciones, pero el hecho que las dos estaciones indican un movimiento anómalo hace pensar en una causa más general. Los estudios recientes de la deformación cortical mediante la utilización de datos InSAR han proporcionado una posible explicación de los movimientos anómalos en las estaciones CGPS alrededor de Lorca: es probable que estén afectadas por la subsidencia relacionada con la extracción de agua del acuífero en el valle del Guadalentín (Frontera et al., 2012; González and Fernández, 2011), un fenómeno de escala más regional.

3.2 Tasas de deformación

Para analizar con más detalle la relación entre el campo de las velocidades GPS inter-sísmicas y el terremoto de Lorca, hemos elegido las cuatro estaciones más cercanas al epicentro, TERC, MELL, PURI y GANU, y hemos formado tres sub-áreas (1 rectángulo y 2 triángulos). Para estas áreas hemos calculado las tasas de deformación (Figura 1 y Tabla 1) mediante el programa strnet (K. Wang, com. pers.) basado principalmente en la metodología presentada por Malvern (1969). Se puede observar que en la sección de Lorca-Totana de la FAM, las tasas de deformación cortical indican un predominio de la compresión uniaxial en dirección NNO oblicua a la traza de la falla. Dicha orientación, como ya hemos mencionado antes, implica una compresión perpendicular a la FAM con una componente menor de desgarre sinestro. Este tipo de régimen tectónico está en acuerdo con la cinemática obtenida mediante el mecanismo focal del terremoto (López-Comino et al., 2012) y el análisis de datos neo-tectónicos (Martínez-Díaz et al., 2012).

Tabla 1: Ejes principales de deformación (máximo $\dot{\varepsilon}_1$ y mínimo $\dot{\varepsilon}_2$) estimados a partir de las velocidades GPS de las estaciones TERC, MELL, PURI y GANU (Figura 1). El signo negativo significa compresión.

Subárea	**$\dot{\varepsilon}_1$ (nstrain) (extensión)**	**$\dot{\varepsilon}_1$ acimut (N°E)**	**$\dot{\varepsilon}_2$ (nstrain) (compresión)**	**$\dot{\varepsilon}_2$ acimut (N°E)**
1	+26.9 ± 4.9	77 ± 3	-78.3 ± 8.3	167 ± 3
2	+45.5 ± 7.8	82 ± 3	-77.3 ± 8.3	172 ± 3
3	+5.0 ± 8.9	69 ± 4	-88.0 ± 9.3	159 ± 4

El eje de la tasa de deformación mínima ($\dot{\varepsilon}_2$) obtenido a partir de las velocidades GPS (~N167ºE) es parecido al eje de presión P-axes (entre N167°E y N190°E), calculado mediante la inversión del tensor momento del terremoto de Lorca por

López-Comino (2012). Lo mismo sucede con el eje de deformación máxima ($\dot{\varepsilon}_1$) (~N77ºE) y el eje de la tensión T-axes obtenido por López-Comino (2012) (N90ºE). La coincidencia entre las medidas sísmicas y de GPS no siempre se observa, ya que corresponden a parámetros físicos diferentes: el primero refleja la orientación de esfuerzos principales que causan el terremoto y el segundo la dirección de la deformación de la corteza (e.g.Wang, 2000). Además, los dos parámetros pueden exhibir variaciones espacio-temporales considerables, debido a perturbaciones locales controladas por estructuras preexistentes (e.g.Martínez-Díaz et al., 2012).

Los valores de la tasas de deformación dadas en la Tabla 1 indican claramente la actividad tectónica continua de la región y de la FAM en particular. Por ejemplo, en los Pirineos, las tasas de deformación calculadas a partir de mediciones de GPS indican la extensión de un orden de magnitud inferior: 2.5±0.5 nstrain/yr (Asensio et al., 2012).

3.3 Desplazamientos co-sísmicos y su modelización

Referente a las deformaciones co-sísmicas, las estaciones de la red CuaTeNeo no han registrado ningún tipo de deformación relacionado con el terremoto de Lorca. En este tipo de estaciones, dado que no registran de manera continuada, es más difícil detectar un salto de pequeña magnitud. En cambio, los registros continuos de las estaciones CGPS son más idóneas para estudiar deformaciones co- y post-sísmicas. La única estación CGPS que estaba funcionado durante el terremoto en la zona de Lorca era la estación LRCA.

Con el objetivo de cuantificar el posible desplazamiento co-sísmico debido al terremoto de Lorca hemos realizado un análisis en detalle de la serie temporal de LRCA. Específicamente, se ha variado: i) el rango de serie temporal (e.g. quitar los datos anteriores al cambio de antena), ii) la modelización de la señal anual y/o la señal semi-anual iii) eliminación de observaciones aparentemente anómalas. Como resultado s obtenido unos desplazamientos co-sísmicos robustos y que concuerdan con todas las pruebas realizadas. El salto detectado en la componente N-S es de 6±0.6 mm hacia el norte (Figura 4a y Tabla 3). En la componente E-W el salto es menos apreciable (-0.7±0.5 mm). Mientras, en la componente vertical se observa un salto debido al cambio de antena en el 2009 pero no se puede detectar un salto co-sísmico significativo (Figura 4a) debido al elevado ruido. Las causas son: corto registro después del terremoto, la presencia de una señal anual fuerte en la componente vertical, y el error inherente del GPS en la vertical.

La otra estación CGPS en la zona (LORC) no estaba en funcionamiento durante el mes del terremoto (Figura 4b), pero el análisis de los datos después de la segunda parte de 2011, nos ayudan a calcular el salto que ha sufrido la estación entre Febrero y Junio de 2011, parcialmente relacionado con el terremoto de Lorca: Norte: -0.8±0.7 mm; Este: 9.9±1.1 mm. La aparente contradicción entre los desplazamientos co-sísmicos destacados en LRCA y LORC se explican por los daños estructurales importantes al edificio de LORC que afectan, en consecuencia, a la antena. Por esta razón, los datos de la estación LORC y quizás parcialmente, la estación LRCA, deben ser tratados teniendo en cuenta que los movimientos pueden ser de carácter no tectónico. Los movimientos co-sísmicos horizontales de LRCA y LORC obtenidos están indicados con vectores de color verde en la Figura 1.

Para la interpretación de las deformaciones co-sísmicas, hemos empleado dos modelos numéricos. El primero, presentado por Frontera (2012), emplea un modelo con varias capas de Wang et al., (2003) y utiliza parámetros de la falla y su ruptura basados en la primera localización del terremoto principal y las réplicas del IGN. Para la estación LRCA el modelo daba el valor 8.6 mm de movimiento co-sísmico hacia el norte, comparando con ~6 mm observados con medidas geodésicas (Figura 1 y Tabla 3).

Para proporcionar unas predicciones de desplazamientos co-sísmicos más actualizadas, hemos adaptado un nuevo modelo para las deformaciones superficiales asociadas con el terremoto de Lorca utilizando el modelo de dislocación elástica de (Okada, 1985). Dado que sólo disponíamos de una medición fiable del desplazamiento co-sísmico, no ha sido posible realizar una inversión formal del desplazamiento sísmico de la falla ni ajustar los parámetros de la falla con el fin de mejorar la coincidencia entre los vectores modelados a los observados. Por lo tanto, simplemente se han utilizado los parámetros utilizados por Martínez-Díaz (2012), obtenidos mediante la inversión de datos InSAR. En la Tabla 2 se muestran los parámetros utilizados en la modelización, donde el desplazamiento co-sísmico de la falla en la dirección de movimiento (39º) es de 12.5 cm. En la estación LRCA la concordancia entre el movimiento horizontal detectado y el del modelo es sorprendentemente bueno (Tabla 3).

Utilizando las predicciones del modelo de la deformación co-sísmica también se puede explicar la ausencia de deformación co-sísmica en las estaciones de CuaTeNeo, y en particular en la estación TERC (Figuras 3 y 5)

Tabla 2: Parámetros para el modelo de dislocación elástica de *uniform slip* (12.5 cm) adaptados de Martinez-Diaz et al. (2012). Htop y Hbot son las profundidades de la falla y L es la longitud de la falla medida en la dirección del strike. Long y Lat indican las coordenadas del centro de la falla proyectada a la superficie (ver Figura 5).

Strike (°)	Dip (°)	Rake (°)	Long (°)	Lat (°)	Htop (km)	Hbot (km)	L (km)
235	55	39	-1.680	37.689	1.5	5.0	4.0

Tabla 3: Comparación de los resultados de la modelización numérica con las observaciones en la estación CGPS LRCA.

Desplazamiento	**Datos (mm) ± 1σ (LRCA CGPS)**	**Modelo (mm) (uniform slip)**
S-N	6 ± 0.6	6.4
W-E	-0.7 ± 0.5	-0.2

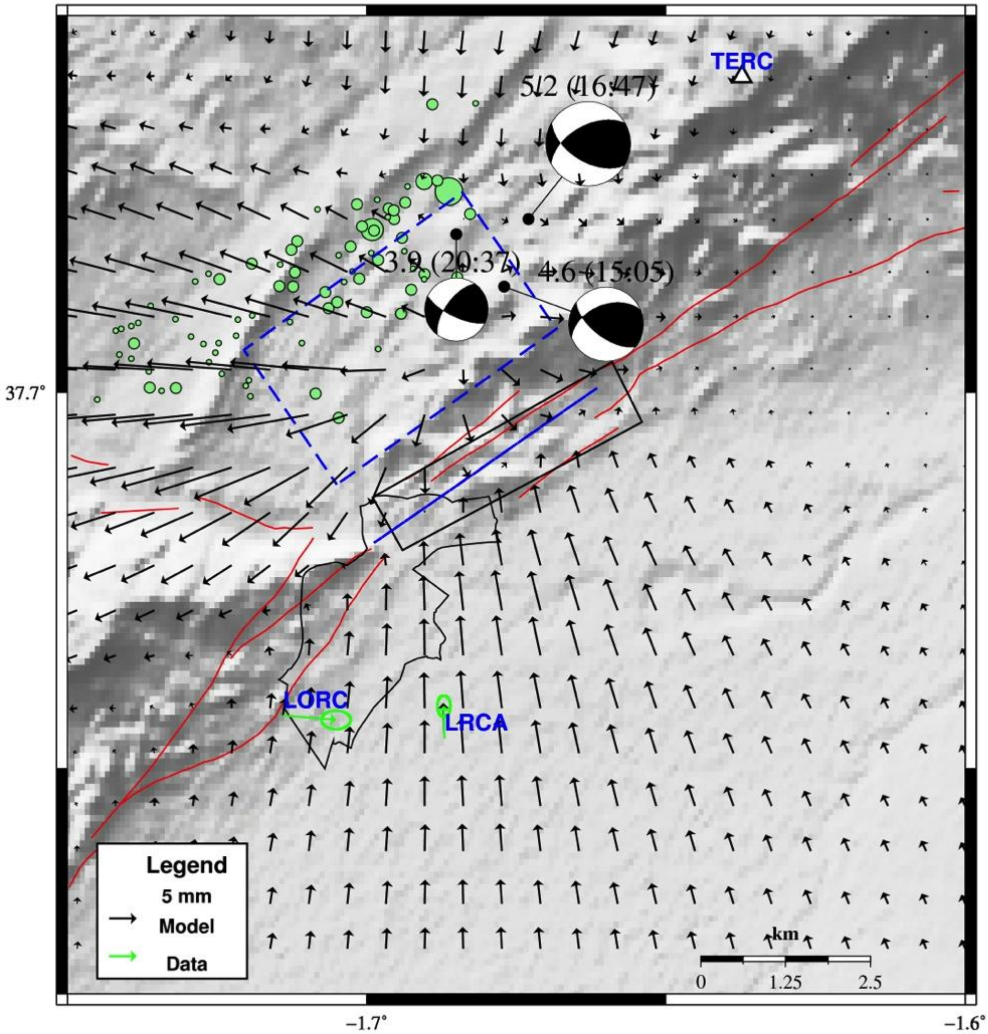

Fig. 5: Modelo de los desplazamientos co-sísmicos horizontales. La falla usada en el modelo está representada mediante un rectángulo en línea discontinua y su proyección en la superficie como una línea continua azul. Los tres mecanismos focales corresponden a los tres terremotos más importantes de la serie sísmica (el principal, Mw 5.2, un precursor de Mw 4.6 y una réplica de Mw 3.9), tomados de López-Comino et al., (2012). Los vectores representan los desplazamientos co-sísmicos observados en las estaciones CGPS LORC y LRCA. Se puede observar la ausencia de deformación para la estación TERC de la red CuaTeNeo.

4. Conclusiones

Mediante el análisis de cinco campañas GPS de la red CuaTeNeo, realizadas entre 1997 y 2011, se ha observado la cinemática inversa y sinestral del sector de Lorca-Totana de la Falla de Alhama de Murcia, la cual coincide con la cinemática obtenida mediante el mecanismo focal del terremoto de Lorca (López-Comino et al., 2012) y el análisis de datos neo-tectónicos (Martínez-Díaz, 2002).

Las estaciones del bloque sur-oriental de la falla muestran unas velocidades con orientación NNO, aproximadamente paralela a la convergencia entre las placas Eurasiática y Nubia. Esta convergencia es la principal causante de la deformación en la zona, absorbiéndose una tercera parte en el margen sur-oriental de las Béticas. Las estaciones situadas en el bloque noroccidental de la falla, presentan unas velocidades de magnitud muy inferior y orientadas hacia el oeste.

Las estaciones GPS de la red CuaTeNeo no han registrado ningún tipo de deformación co-sísmica relacionada con el terremoto de Lorca. El análisis detallado de la estación continua LRCA, muestra un salto de 6±0.6 mm hacia el norte. El modelo de dislocación elástica, construido utilizando los parámetros de la falla y del terremoto proporcionados en recientes publicaciones de López-Comino (2012) y de Martínez-Díaz (2012) predicen un movimiento co-sísmico en la misma localidad muy similar al observado.

Agradecimientos

Este trabajo ha sido subvencionado por los proyectos CuaTeNeo (CGL2004-21666-E) y CONSOLIDER Topo-Iberia (CSD2006-00041). A.E. es beneficiaria de una beca pre-doctoral APIF de la Universidad de Barcelona, y E.A. de una beca FPU del Ministerio de Educación de España. La campaña del 2011 fue subvencionada por la Facultat de Geologia de la Universitat de Barcelona y por el Laboratori d'Estudis Geofísics Eduard Fontserè del Institut d'Estudis Catalans. También nos gustaría agradecer la información y los datos aportados a la Dirección General de Patrimonio Natural y Biodiversidad y a la Consejería de Obras Publicas de la Región de Murcia. Agradecemos a todas las personas que han colaborado y realizado las campañas de campo.

Referencias bibliográficas

ASENSIO, E., KHAZARADZE, G., ECHEVERRIA, A., KING, R.W. & VILAJOSANA, I., (2012). GPS studies of active deformation in the Pyrenees. *Geoph. J. Int*., 190, 913-921.

BUFORN, E., BEZZEGHOUD, M., UDÍAS, A. & PRO, C., (2004). Seismic Sources on the Iberia-African Plate Boundary and their Tectonic Implications. *Pure Appl. Geophys*. 161, 623 - 646, doi: 610.1007/s00024-00003-02466-00021.

BUFORN, E., SANZ DE GALDEANO, C. & UDÍAS, A. (1995), Seismotectonics of the Ibero-Maghrebian region. *Tectonophysics* 248, 247-261.

DEMETS, C., GORDON, R.G. & ARGUS, D.F. (2010). Geologically current plate motions. *Geoph. J. Int*. 181, 1-80.

FRONTERA, T., CONCHA, A., BLANCO, P., ECHEVERRIA, A., GOULA, X., ARBIOL, R., KHAZARADZE, G., PÉREZ, F. & SURIÑACH, E. (2012). DInSAR coseismic deformation of the May 2011 Mw 5.1 Lorca earthquake, (Southern Spain). *Solid Earth* 3, 111-119.

GARCÍA-MAYORDOMO, J., INSÚA-ARÉVALO, J.M., MARTÍNEZ-DÍAZ, J.J., JIMÉNEZ-DÍAZ, A., ALVÁREZ-GOMEZ, J.A., PÉREZ-LÓPEZ, R., RODRÍGUEZ-PASCUA, M.A., MARTÍN-GONZÁLEZ, F., GINER-ROBLES, J., MASANA, E., NEMSER, E. & CABRAL, J. (2010). Quaternary Active Faults DataBase of Iberia v 01. Technical editor: S. Martín Alfageme, Instituto Geológico y Minero de España, Madrid.

GONZÁLEZ, P.J. & FERNÁNDEZ, J. (2011). Drought-driven transient aquifer compaction imaged using multitemporal satellite radar interferometry. *Geology* 39, 551-554.

IGME (2011): INFORME GEOLÓGICO PRELIMINAR DEL TERREMOTO DE LORCA DEL 11 DE MAYO DEL AÑO 2011, 5.1 Mw. Instituto Geológico y Minero de España *(www.igme.es)*, Madrid, p. 47.

IGN (2011): INFORME DEL SISMO DE LORCA DEL 11 DE MAYO DE 2011. Instituto Geográfico Nacional de España *(http://www.ign.es/ign/resources/sismologia/www/lorca/Lorcainfo2011.pdf)*, Madrid, p. 138.

LÓPEZ-COMINO, J.-Á., MANCILLA, F.D.L., MORALES, J. & STICH, D. (2012), Rupture directivity of the 2011, Mw 5.2 Lorca earthquake (Spain). *Geophys. Res. Lett*. 39, L03301.

MALVERN, L.E. (1969): Introduction to the mechanics of a continuous medium. *Prentice-Hall*, Englewood Cliffs, N.J.

MARTÍNEZ-DÍAZ, J.J. (2002). Stress field variation related to fault interaction in a reverse oblique-slip fault: the Alhama de Murcia fault, Betic Cordillera, Spain. *Tectonophysics* 356, 291-305.

MARTÍNEZ-DÍAZ, J.J., BEJAR-PIZARRO, M., ÁLVAREZ-GÓMEZ, J.A., MANCILLA, F.D.L., STICH, D., HERRERA, G. & MORALES, J. (2012). Tectonic and seismic implications of an intersegment rupture. The damaging May 11th 2011 Mw 5.2 Lorca, Spain, earthquake. *Tectonophysics* 546-547, 28-37.

MARTÍNEZ SOLARES, J.M. & MEZCUA, J. (2002). Catálogo Sísmico de la Península Ibérica (880 a.c. - 1900). *Monografía de Instituto Geográfico Nacional de España* 18, 253.

MCCLUSKY, S., BALASSANIAN, S., BARKA, A., DEMIR, C., ERGINTAV, S., GEORGIEV, I., GURKAN, O., HAMBURGER, M., HURST, K., KAHLE, H., KASTENS, K., KEKELIDZE, G., KING, R., KOTZEV, V., LENK, O., MAHMOUD, S., MISHIN, A., NADARIYA, M., OUZOUNIS, A., PARADISSIS, D., PETER, Y., PRILEPIN, M., REILINGER, R., SANLI, I., SEEGER, H., TEALEB, A., TOKSOZ, M.N. & VEIS, G. (2000). Global Positioning System constraints on plate kinematics and dynamics in the eastern Mediterranean and Caucasus. *J. Geophys. Res.* 105, 5695-5719.

OKADA, Y. (1985). Surface deformation due to shear and tensile faults in a half-space. *Bull. Seismol. Soc. Am.* 75, 1135-1154.

SORO, M., GIMÉNEZ, J. & FLETA, J. (1997). Descripció dels emplaçaments per a observacions GPS del marge sudoriental de la Peninsula Ibèrica (prov. Almería i Murcia). Projecte CuaTeNeo. ICC, Barcelona, Spain.

STICH, D., AMMON C. J. & MORALES, J. (2003). Moment tensor solutions for small and moderate earthquakes in the Ibero-Maghreb region. *J. Geophys. Res.* 108, B3, 2148.

VISSERS, R.L.M. & MEIJNINGER, B.M.L. (2011). The 11 May 2011 earthquake at Lorca (SE Spain) viewed in a structural-tectonic context. *Solid Earth* 2, 199-204.

WANG, K. (2000). Stress-strain `paradox', plate coupling, and forearc seismicity at the Cascadia and Nankai subduction zones. *Tectonophysics* vol. 319, 321-338.

Solid Earth, 3, 111–119, 2012
www.solid-earth.net/3/111/2012/
doi:10.5194/se-3-111-2012

Solid Earth

DInSAR Coseismic Deformation of the May 2011 M_w 5.1 Lorca Earthquake (southeastern Spain)

T. Frontera[1], **A. Concha**[2], **P. Blanco**[3], **A. Echeverria**[4], **X. Goula**[1], **R. Arbiol**[3], **G. Khazaradze**[4], **F. Pérez**[3], **and E. Suriñach**[4]

[1]Institut Geològic de Catalunya, Seismology Dept., Balmes 209–211, Barcelona 08006, Spain
[2]Institut Geològic de Catalunya, Geological Engineering and Hazards Dept., Balmes 209–211, Barcelona 08006, Spain
[3]Institut Cartogràfic de Catalunya, Remote Sensing Dept., Parc de Montjuïc s/n, Barcelona 08038, Spain
[4]Risknat Group, Universitat de Barcelona (UB), Departament de Geodinàmica i Geofísica, Facultat de Geologia, Martí i Franquès s/n, 08028 Barcelona, Spain

Correspondence to: T. Frontera (tfrontera@igc.cat)

Received: 14 October 2011 – Published in Solid Earth Discuss.: 9 November 2011
Revised: 27 February 2012 – Accepted: 4 March 2012 – Published: 2 April 2012

Abstract. The coseismic superficial deformation at the region of Lorca (Murcia, southeastern Spain) due to the M_w 5.1 earthquake on 11 May 2011 was characterized by a multidisciplinary team, integrating information from DInSAR, GPS and numerical modelling techniques.

Despite the moderate magnitude of the event, quantitative information was obtained from the interferometric study of a pair of TerraSAR-X images. The DinSAR results defined the trace of the fault plane and evidenced uplift of the hanging wall block in agreement with the estimated deformation obtained through an elastic rupture dislocation numerical model. Meanwhile for the footwall block, interferometric results showed that tectonic deformation is masked by an important subsidence related to groundwater extraction previously identified at the area of study.

Horizontal crustal deformation rates and velocity vectors, obtained from GPS stations existent at the area, were also coherent with the tectonic setting of the southern margin of the Iberian Peninsula and with the focal mechanism calculated for the Lorca event. The analysis of a continuous GPS site in Lorca showed good agreement with the horizontal N–S direction component relative to the numerical model and tectonics of the region.

This is the first time at this seismic active area that a multitechnique analysis has been performed immediately after the occurrence of a seismic event, comparing the existing deformation data with a theoretical numerical model based on estimated seismic rupture dislocation.

1 Introduction

On 11 May 2011, two shallow moderate magnitude earthquakes occurred at less than 5 km northeast of the city of Lorca (Murcia, southeastern Spain). The first event (Mw 4.5) took place at 15:05 (UTC), and had a maximum intensity of VI in the European Macroseismic Scale (EMS). The second and main event (Mw 5.1) occurred at 16:47 (UTC), with an epicentre of coordinates 37.69° N, 1.67° W and a depth of 2 km (IGN, 2011), Fig. 1. The main event, which was assigned a maximum intensity of VII (IGN, 2011), did not cause surface rupture, but caused nine human deaths and extensive damages to dwelling buildings, schools and monuments (Irizarry et al., 2011).

Around the area of study there have occurred damaging earthquakes both in the historical and the instrumental periods. The city of Lorca had suffered two damaging earthquakes in 1579 and 1674, with intensities estimated to be VII (EMS) and VIII (EMS), respectively (Martínez-Solares and Mezcua, 2002). In 1829, an earthquake with a maximum intensity of X (EMS) and an estimated magnitude Ms 6.9 (Muñoz and Udías, 1991; Buforn et al., 2006) occurred near the town of Torrevieja (Alicante Province).

On 6 June 1977, an earthquake of magnitude m_{bLg} 4.2 (Mezcua et al., 1984) was registered at 10 km SW from the city of Lorca and it had a maximum intensity of VI (EMS). In the region of Murcia, another damaging earthquake occurred near the town of Mula, 45 km to the NE of Lorca, on 2 February 1999. Its magnitude was M_w 5.1 (Buforn et al.,

Published by Copernicus Publications on behalf of the European Geosciences Union.

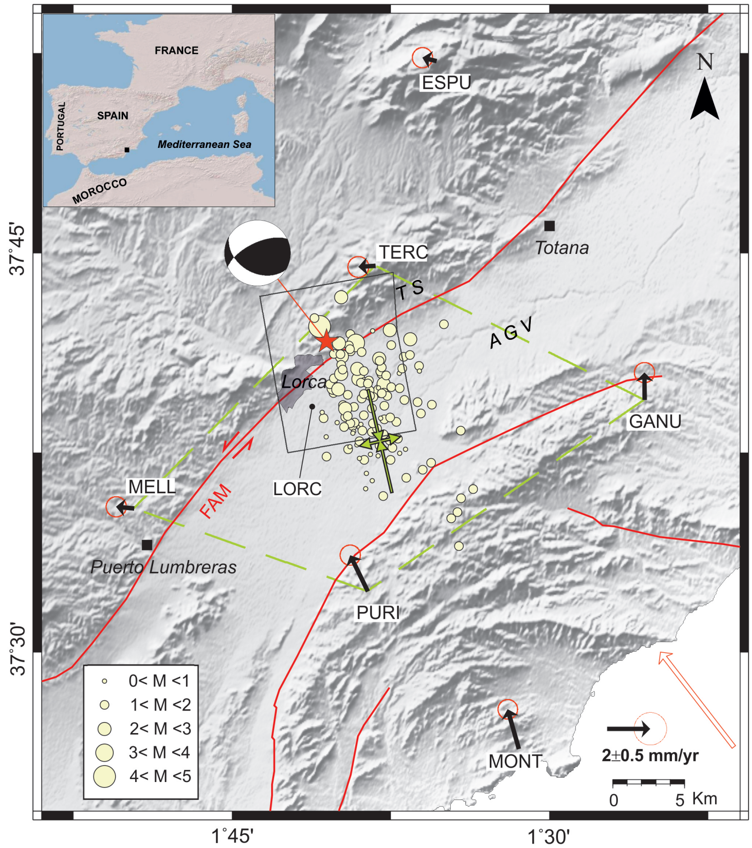

Fig. 1. Study area in SE of Spain, showing the main fault traces in red lines; the GPS stations with their associated horizontal displacement vectors; the epicentral location of the main seismic event (red star) and aftershocks (yellow spots) (IGN, 2011); focal mechanism of the main earthquake (Delouis, 2011); the plate convergence between Eurasia-Nubia plates based on the MORVEL model (DeMets et al., 2010) is shown as a red vector on the lower right corner; the principal strain rates are calculated for the four stations connected by the green dashed lines (see Table 1 for numerical values). The black contour delimits the area for Figs. 3 and 4. AGV: Alto Guadalentín Valley; FAM: Alhama de Murcia Fault; TS: Sierra de la Tercia.

2005), and according to IGN (1999), the maximum intensity reached a value of VI (EMS). On 6 August 2002, an earthquake occurred 40 km west of Mula near the town of Bullas. It had a magnitude of M_w 4.6 and a maximum intensity of V (EMS) (Buforn et al., 2005). In the same town on 29 January 2005, there was another earthquake near Bullas (Buforn et al., 2006) with a magnitude of M_w 4.7; the IGN (2005) assigned a maximum intensity of VII (EMS). This last earthquake was more damaging than the one in 2002, probably due to the weakening effect produced by the 2002 previous shock on some structures. Though those events had mainly moderate magnitudes ($M_w \leq 5.5$), they produced damage to structures and noticeable alarm in the population (Gaspar-Escribano et al., 2008). Nevertheless, it should be pointed out that the Lorca event on 11 May 2011 is the first one during the instrumental period that has caused human deaths in the region.

The earthquakes on 11 May 2011 took place in the eastern part of the Betic Cordillera, along the Alhama de Murcia fault (FAM) (Bousquet, 1979). It is a high seismogenic potential strike-slip reverse fault, with a strike between N45° E and N65° E, and a movement of about 4–5 mm yr^{-1} since Neogene times (Masana et al., 2004; Vissiers and Meijninger, 2011). It is located close to the convergent plate limit between the Eurasian and African plates. The convergence direction of this fault has remained constant since late Miocene to present day (Martínez-Díaz, 2002).

According to Delouis (2011), the Lorca main event focal mechanism (Mw 5.1) showed a reverse sinistral motion, compatible with geological and GPS observations. One of the calculated fault planes coincides with the same orientation of the FAM (Fig. 1).

In accordance with IGN (2011), the number of aftershock events decreased quickly through time to less than five events per day in five days. Curiously, these events were not located along the inferred FAM fault plane, dipping towards NNW, but rather they were spread in seemingly non-linear fashion towards the SE from the main shock into the Alto Guadalentín Valley (AGV), Fig. 1. This supposed mislocation might have been due to the generation of aftershocks in a zone with high concentration of the static Mohr-Coulomb stresses out of the FAM plane.

Table 1. Strain rate estimates (maximum and minimum principal axis, $\dot{\varepsilon}_1$ and $\dot{\varepsilon}_2$ respectively) based on the GPS velocities of the TERC, MELL, PURI and GANU stations. Negative sign means compression.

$\dot{\varepsilon}_1$ (μstrain)	$\dot{\varepsilon}_1$ azimuth (°)	$\dot{\varepsilon}_2$ (μstrain)	$\dot{\varepsilon}_2$azimuth (°)
0.31 ± 0.28	77.0 ± 7.6	-0.80 ± 0.10	167.0 ± 7.6

2 GPS data

The GPS data considered in this study consist of the analysis of one continuous GPS (CGPS) station located in Lorca (LORC) and six campaign data belonging to the CuaTeNeo (Cuantificación de la Tectónica actual y Neotectónica) geodetic network, which was established in 1996 to quantify the current rates of crustal deformation in the eastern part of the Betic Cordillera (Colomina et al., 1999). It consists of 15 geodetic markers covering an area approximately 6000 km^2 in Murcia and Almeria. The presented data are based on the analysis of four campaigns performed in 1997, 2002, 2006 (Khazaradze et al., 2008) and 2009. During each campaign every site was observed for three consecutive days (in some cases up to five days) in sessions of at least 8 hours. Some of the sites were observed throughout the campaign in a continuous mode, since it was possible to leave the instruments unattended.

Horizontal velocities of the six CuaTeNeo sites falling within the study area are shown in Fig. 1. These velocities represent an inter-seismic phase of deformation averaged over the 12 years of observations. The stations on the SE side of the FAM (PURI and GANU) show oblique compression with left-lateral direction of motion, 1.9 ± 0.5 mm yr^{-1}, relative to the stations on the NW (MELL and TERC) in accordance to geological observations and calculated focal mechanism of the Lorca earthquake (Fig. 1). The decomposition of the station PURI vector into fault parallel and perpendicular components, give velocity estimates of 0.29 mm yr^{-1} and 1.87 mm yr^{-1}, respectively. This decomposition was performed by projecting the GPS calculated vector of PURI to the trace of the FAM fault, deduced from the focal mechanism and used in the numerical model (N65° E). In consequence, the relative weight of compression vs. extension is significantly higher than expected from the focal mechanism. On the contrary, when we used an alternative N45° E orientation for the FAM fault, more in accordance to the geology (see Fig. 1), the fault parallel and perpendicular velocities of PURI became 0.92 mm yr^{-1} and 1.66 mm yr^{-1}, respectively. These values are in better agreement with approximately 30 % strike slip and 70 % compression component of the Lorca earthquake focal mechanism (Delouis, 2011).

We also calculated strain rates for the four stations surrounding the earthquake epicentre (TERC, MELL, PURI and GANU) using the SSPX software (Cardozo and Allmendinger, 2009). The obtained results (Fig. 1 and Table 1) are also in good agreement with the calculated focal mechanism of the main event. Specifically, the orientations of $\dot{\varepsilon}_1$ (∼N77° E) and $\dot{\varepsilon}_2$ (∼N167° E), deduced from the GPS velocities, agree well with the orientations of the T-axis (N111° E) and P-axis (N178° W) (Delouis, 2011). Although this agreement is not always guaranteed or necessary, since the two measurements represent two different physical parameters, strain and stress, which are not always coincident (see Wang (2000) for further details). The NNW orientation of the GPS velocities of the three stations located closer to the coast (MONT, PURI and GANU) indicates that the main driving force behind their motion is related to the convergence between the Nubia and Eurasia plates (see the convergence vector in Fig. 1). This, convergence according to the MORVEL model (DeMets et al., 2010), equals to 5.6 ± 0.3 mm yr^{-1} and is oriented N322.1° E $\pm$ 1.8°. These values show that roughly one-third of the overall convergence between the two tectonic plates is taking place on the southern margin of the Iberian Peninsula, at the Betic Cordillera.

These values also agree with other published GPS results in a wider region of SE Spain (e.g. Koulali et al., 2011; Pérez-Peña et al., 2010), which provide velocities ranging between 0 to 2 mm yr^{-1} oriented in the NNW direction. However, a detailed comparison with our results presented in this paper is not possible, since these studies do not include observations that fall within the geographic area considered here.

Two weeks after the occurrence of the Lorca earthquake, the UB group organized a special post-event campaign of the CuaTeNeo sites located near the epicentre of the earthquake. The preliminary results indicated no signs of detectable co-seismic deformation. Nevertheless, our analysis of a continuous GPS site LORC, belonging to the Meristemum public network (Garrido et al., 2011) and located in the city of Lorca (Figure 1), showed a horizontal co-seismic jump of 5 to 6 mm (5.5 ± 0.2 mm) towards the north and statistically marginal subsidence in the vertical direction of -2.0 ± 0.9 mm (Fig. 2, Table 2). It must be pointed out that before the occurrence of the Lorca earthquake, our analysis of the LORC data from 2008 had already indicated a highly anomalous behaviour at this site, which was most likely due to the instability of the terrain surrounding the building where it is located (Echeverria et al., 2011). Specifically, we had estimated that the LORC CGPS station was subsiding with a rate of

Table 2. Comparison of coseismic displacement components between the LORC CGPS station and numerical model. Negative vertical displacement means subsidence.

	LORC GPS	Numerical model
S–N direction	5.5 ± 0.2 mm	8.6 mm
W–E direction	0.0 ± 0.2 mm	1.0 mm
Up direction	-2.0 ± 0.9 mm	-2.5 mm

$98.5 \pm 1.9\,\mathrm{mm\,yr^{-1}}$ (Table 3) and moving horizontally with a rate of $12.7 \pm 1.2\,\mathrm{mm\,yr^{-1}}$ in the SE direction with respect to stable Eurasia.

3 DInSAR analysis

The use of Synthetic Aperture Radar Differential Interferometry (DInSAR) technique for quantifying coseismic deformations has been previously used at the Africa-Eurasian plate boundary at the western Mediterranean area, e.g. in Morocco (Belabbes et al., 2009; Akoglu et al., 2006); and in the Iberian Peninsula, also at the same seismogenic area in the Betic Cordillera (González et al., 2009). Nevertheless, this is the first time in this area that a processing has been performed immediately after the occurrence of a seismic event and it has been compared to theoretical numerical modelled vertical elastic deformation based on estimated seismic rupture dislocation.

A DInSAR processing (Hanssen, 2001; Mora et al., 2007) of one pre- and one post-event stripmap TerraSAR-X image (25 July 2008 and 14 May 2011) was performed for the Lorca event. In order to reduce temporal decorrelation and avoid non-seismic deformation phenomena, a shorter temporal baseline would be desirable. Unfortunately, that was the only pre-event image available in the TerraSAR-X archive for the study zone. Topography was cancelled employing an interpolated SRTM DTM. Atmospheric effects were considered non-significant, as the detected fringe spatial gradient does not correspond to the typical atmospheric pattern (Hanssen, 2001).

Figure 3a shows the filtered deformation fringes of the differential phase in radians. Each color cycle is equivalent to a deformation of 1.55 centimetres along the line of sight (LOS) of the radar ($\sim 35°$ of incidence angle). The well marked fringe pattern is aligned along the trace of the FAM, showing a defined deformation gradient perpendicular to its trace. Further to the S and SE of the epicentral area, the quality of the signal (measured by the coherence parameter) is lower outside the urban areas, mostly associated to agricultural fields in the AGV, showing a concentric low coherence fringe pattern.

A vertical displacement map was generated by unwrapping the phase of the differential interferogram (Costantini, 1998). A high coherence pixel with a zero deformation value according to the numerical model (see next section) was employed to fix the solution. A median filter was applied to the deformation map to reduce the impact of the low coherence pixels (Fig. 3b).

The northern (hanging wall) block of the fault has a maximum upward movement of about 3 cm that agrees with the reported focal mechanism, while the southern (footwall) block of the fault shows a maximum downward movement of 18 cm (Fig. 3b). There is a remarkable difference of order of magnitude between the displacements in each one of the blocks. The limit of these movement tendencies coincides clearly with the FAM trace (Fig. 3a), reflecting also the local change in the strike of the fault from N35° E to N60° E and the geological contrasts between the sediments of AGV and the Tertiary rocks of Sierra de la Tercia (TS).

The maximum downward movement of 18 cm in the southern block would represent a constant rate of movement of about $64.2\,\mathrm{mm\,yr^{-1}}$. This motion is most likely caused by non-tectonic deformation (Table 3; González et al., 2011) and similar to the terrain instability reported earlier for the LORC CGPS station. It must be pointed out that the accuracy of the calculated deformation may be lower in the southern block than in the northern block. This is justified by the large deformation gradient (compared to the DInSAR signal's wavelength) in this area. As not all the pixels have enough quality to participate in the unwrapping, some fringes may be skipped and the overall deformation may be underestimated. Assuming this, we consider compatible both DInSAR's $64.2\,\mathrm{mm\,yr^{-1}}$ constant rate and the inter-seismic subsidence rate of $98.5\,\mathrm{mm\,yr^{-1}}$ detected at the LORC CGPS station (Table 3 and Fig. 2).

4 Numerical model of coseismic vertical deformation

The surface deformation numerical model produced by the M_w 5.1 earthquake was generated using the method of Wang et al. (2003), which considers an elastic deformation field. In a first step, the Green's functions are computed for a number of source depths and distances given a layered half-space velocity crustal model. For the Lorca area, the chosen crustal model was taken from Dañobeitia et al. (1998) which consists of 7 layers between 0 and 35 km in depth.

A second step sets the source rectangular rupture surface by defining six fault parameters: slip, length, width, strike, dip and rake of the dislocation. For the present analysis, the first three parameters were set at 15 cm, 4 km and 2 km respectively, attending the mean values for a M_w 5.1 given by Wells and Coppersmith (1994) and in agreement with the seismic moment (4.9×10^{23} dyn $\times$ cm) calculated by Delouis (2011). The moment tensor inversion, calculated by the same author, was used to determine the orientation and slip

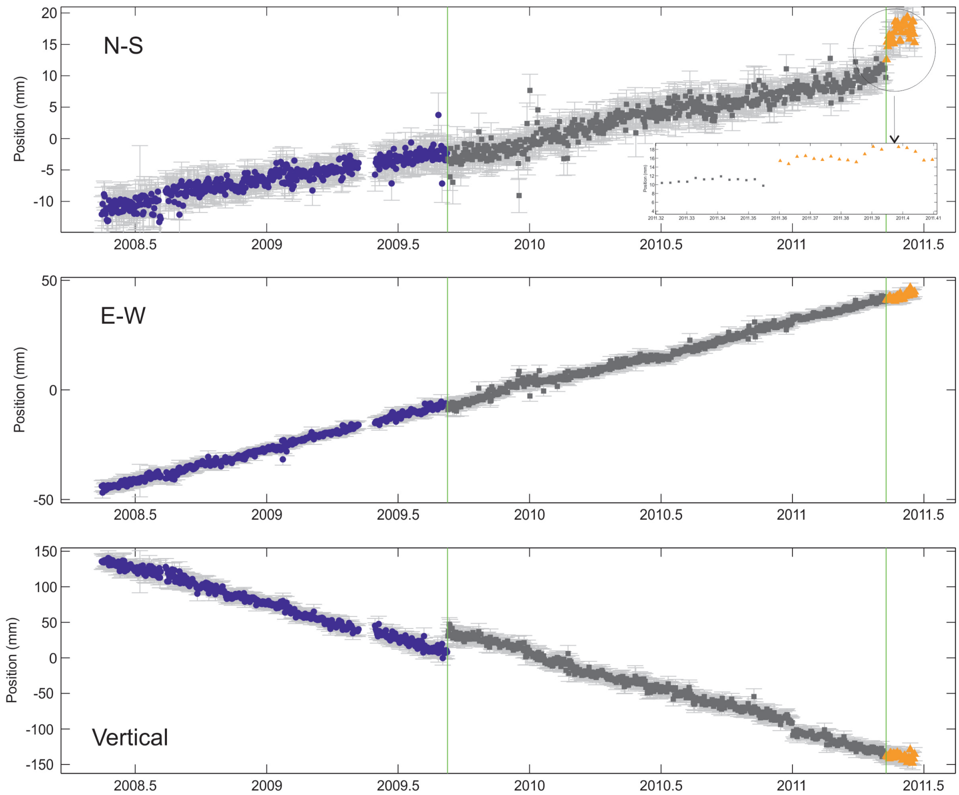

Fig. 2. Time-series of LORC continuous GPS station belonging to the Meristemum network (http://gps.medioambiente.carm.es/). The analysis was performed by the UB group using the GAMIT-GLOBK software from MIT. Reference frame is ITRF08. Vertical green lines depict dates of hardware changes and/or earthquake occurrence. The 1st jump in 2009 is due to an antenna change and the 2nd jump is due to a Lorca earthquake of 11 May 2011. The N–S component, where the co-seismic offset of 5 to 6 mm can be seen, includes a zoom of the time-series.

Table 3. Comparison of the numerical model vertical displacement results with reported values of maximum displacements and calculated rates from different GPS and DInSAR studies, at both FAM blocks. Negative sign means subsidence.

Technique	Northern block maximum vertical displacement (mm)	Southern block maximum vertical displacement (mm)	Southern block vertical displacement rate (mm yr^{-1})
GPS LORC (2008–2011) (Echeverria et al., 2011)	–	–	−98.5*
DInSAR (2008–2011) (this study)	+30	−180	−64.2
DInSAR (1992–2007) (González and Fernández, 2011)	–	–	−100*
Numerical model Lorca Event (this study)	+40	−10	–

* Measurements made before the Lorca earthquake on 11 May 2011.

of the fault, i.e. 245° for the strike, 65° for the dip and 58° for the rake. According to the hypocenter depth of 2 km, and a fault width of 2 km, we assumed that the top of the rupture stops at a depth of 1 km (Fig. 3b).

Considering the geometry described above, the model predicts a maximum vertical deformation of 1 cm subsidence 2 km SE from the epicentre and around 4 cm uplift near the epicentre (Fig. 3b). As shown in Table 3, even if there is a good agreement between DInSAR and numerical model results in the northern block, there is a noticeable discrepancy in the southern one.

It should be pointed out that slip, length and width of the rupture area have been chosen considering the average values proposed by Wells and Coppersmith (1994); the estimation

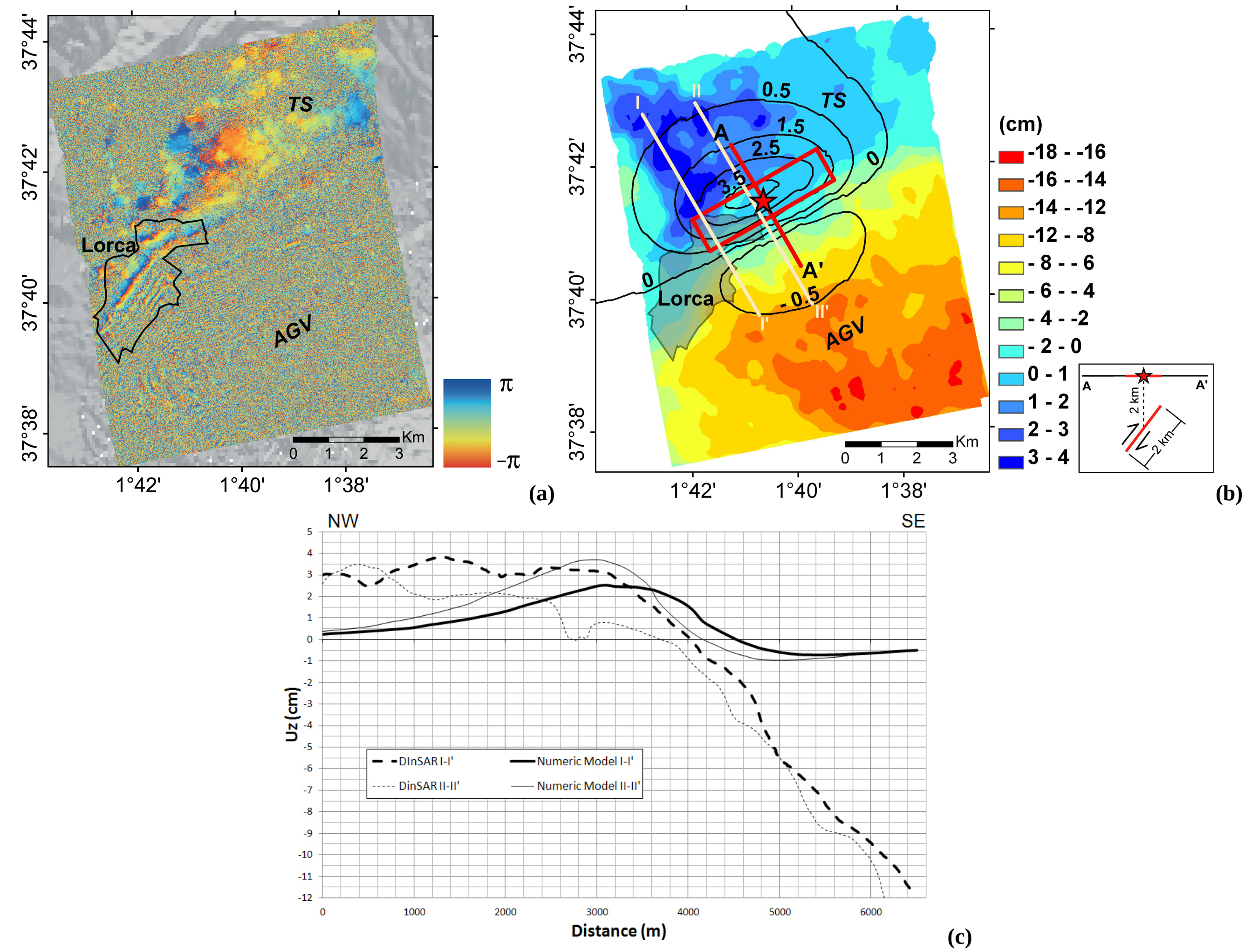

Fig. 3. (a) Filtered deformation fringes of the differential interferometric phase in radians. Each color cycle is equivalent to deformation along LOS of about 1.55 cm. The limit of the Lorca urban area is shown for reference; **(b)** Vertical displacement map. The colour scale shows the displacement measured by DInSAR. The black curves show the isovalues obtained by the numerical model in cm. The red rectangle and cross-section line A–A′ show the dimensions and location of the rupture plane considered in the numerical model. White lines, I–I′ and II–II′, are the traces of vertical displacement profiles shown on Fig. 3c. The limit of the Lorca urban area is shown for reference; **(c)** Vertical displacement profiles comparing measured DInSAR vs. numerical model results.

of those parameters assumes a standard value for the shear modulus (μ= 30 GPa) that might not fit in this case study given the zone peculiarities, such as the existence of pre-fractured rocks and the shallowness of the focal depth.

A lower value for the shear modulus might be considered and a parametric analysis was performed to compute a new vertical surface displacement by considering a lower value of μ with the subsequent different compatible rupture and slip dimensions at diverse hypocentral depths. Finally, we compared the results with those obtained from numerical model and DInSAR results.

Considering the current velocity models used for observational seismology (Delouis et al., 2009) we took a S-wave velocity v_s of 1.9 km s^{-1} and a density ρ of 2 g cm^{-3} to obtain a lower limit for the shear modulus value $\mu = \rho\, v_s^2$ = 7.22 GPa, which is approximately 6 times lower than the μ considered in the first calculations presented above. Therefore, to maintain the same value of seismic moment tensor, Mo, it is necessary to multiply by 6 the factor slip-times rupture surface. The model had been constructed by considering two alternative assumptions on the amount of slip: the first one with an average slip of 15 cm and the second with an average slip of 30 cm. For each case, three different focal depths were chosen. For the case which considers an average slip of 15 cm, a hypocentral depth of about 4 km provides a maximum surface displacement of 4.5 cm.

And for an average slip of 30 cm and a hypocentral depth of 6 km, maximum surface displacement of 4 cm is obtained. Thus, the results from the μ variations show similar vertical displacement configurations at land surface of the northern block. Therefore, even by considering a lower value of μ, which implies different slip values (between 15 and 30 cm) and hypocentral depths (between 2 and 6 km), we obtained in the northern block synthetic displacements in accordance with the first assumption.

Considering again the former results, once they were validated by reviewing other μ values, we present two vertical displacement profiles, perpendicular to the strike of the fault plane used for the numerical model and parallel to the schematic section A–A′ (Fig. 3c). The traces of both profiles are shown in Fig. 3b. Profile I–I′ trace passes through the maximum of DInSAR vertical movement, mainly concentrated to the northwest of the epicentre. Profile II–II′ trace passes through the maximum value of the numerical model, very close to the epicentre. In Fig. 3c, computed and DInSAR vertical displacements (U_z -axe) were compared along the profiles. Positive values are located at the northern block of the fault while the ones in the southern block are negative. Maximum values in the northern block are of the same order of DInSAR and numerical model results, very close to 4.0 cm, though differences are reflected in their distribution: along profile I–I′, DInSAR measured movements are constant decreasing rapidly close to the fault trace; while along profile II–II′, DInSAR shows more irregularities, decreasing constantly towards the fault trace.

At the southern block differences are more accentuated. The DInSAR movement increases constantly almost at the same rates in both profiles until reaching more than 10.0 cm, while the model results tendency is for a maximum of 0.5 cm and going back zero as it gets away from the fault trace. Clearly in this block there is the superimposition of other vertical movement source added to the earthquake deformation. Unfortunately, separation in the DInSAR “signal” of coseismic deformation component from other terrain instabilities is not possible. Moreover, as the numerical model magnitude is of the order of the DInSAR uncertainty, it is not possible to differentiate coseismic deformation from other type of subsidence.

Due to its acquisition geometry, the sensitivity of the DInSAR signal to horizontal displacements is significantly lower than to vertical displacements. In fact it is almost blind to the N–S component. Therefore, even if it is possible to project LOS deformation in its horizontal component due to its high degree of uncertainty, we have not performed any comparison between DInSAR and the modelled horizontal movement components. Therefore, only GPS data has been compared to the horizontal model component.

The horizontal deformation predicted by the numerical model (Fig. 4 and Table 2) agrees well with the co-seismic jump observed at the LORC CGPS station from the analysis of the N–S, E–W and vertical GPS time-series. The examination of the modelled horizontal motion makes easier to appreciate why we were not able to detect any co-seismic motion even at the closest CuaTeNeo station TERC after performing a post-earthquake campaign.

5 Discussion and conclusions

Using the numerical model as reference for the coseismic displacement, we found a good agreement between the DInSAR measurements (3 cm) and the model estimated values (4 cm) on the northern hanging wall block of the fault. This match, as well as the distribution of the vertical movement gradient along the FAM trace, allows to state that the numerical model is a good approximation of the coseismic deformation (Fig. 3b). The largest difference is the areal extent of the deformation and concentration of displacements on the north-western sector of the study area. This difference might be due to changes of geology and definition of local tectonic blocks (Martínez-Díaz, 2002) in the area, and to a possible heterogeneous rupture process not considered in our uniform dislocation model.

On the other hand, there are differences for the southern block with both DInSAR and CGPS (LORC station) results (Table 3). González and Fernández (2011) report important subsidence rates (Table 3) at the AGV sedimentary basin, of about 100 mm yr^{-1}, due to intensive groundwater extraction, which could be responsible of the large differences obtained by numerical and field techniques (DInSAR and GPS). Considering possible DInSAR movement magnitude underestimation in this area due to low coherence pixels, both DInSAR and LORC measurements show reasonable correspondence.

This intensive groundwater extraction might generate changes of the stress field that could contribute to the generation of the aftershocks (IGN, 2011) out of the FAM trace, but further away within AGV (Fig. 1). While model predicted coseismic vertical deformation is less than few centimetres, as mentioned earlier, subsidence related deformation is of the order of tens of centimetres. Unfortunately, as the model magnitude is of the order of the DInSAR, uncertainty it is not possible to differentiate coseismic deformation from the groundwater extraction related subsidence. The coseismic jump of the LORC station is of the same order as that obtained by the numerical model, and only remarkable in the north direction.

In synthesis, by combining remote sensing measurements (DInSAR), in-situ field measurements (CGPS station LORC) and numerical models of fault rupture, we were able to characterize the coseismic deformation for the 11 May 2011, Mw 5.1 earthquake. This is the first time that results from interferometry technique are obtained and confirmed by a multi-technique and multi-disciplinary study for an earthquake in Spain.

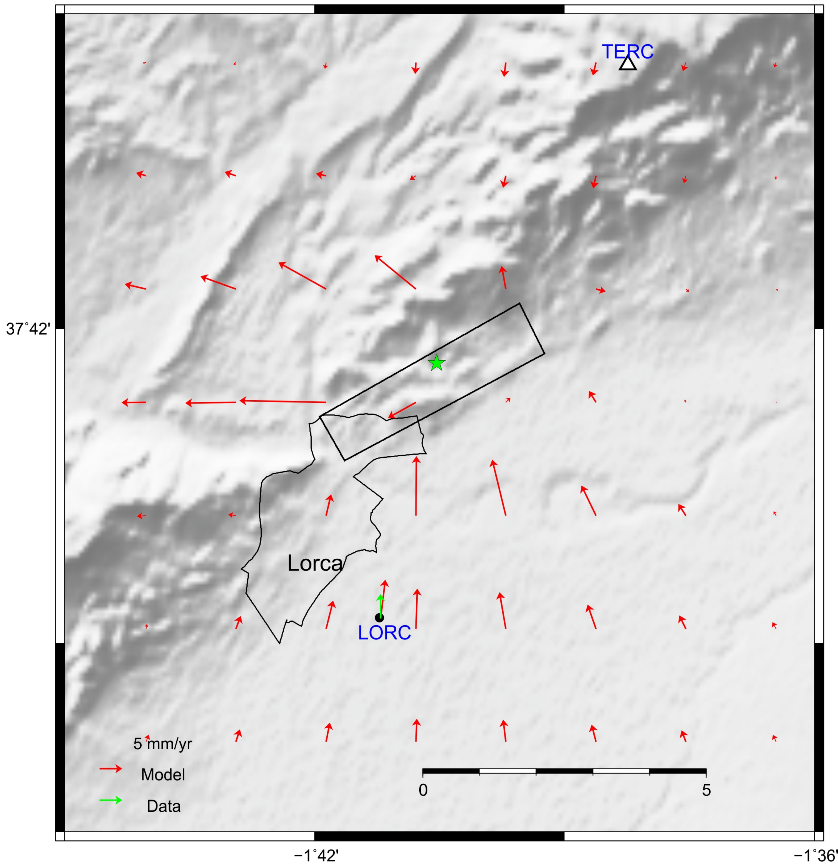

Fig. 4. Horizontal coseismic displacement field. A projection of the modelled fault is shown as a rectangle. Green star depicts an epicentre of the 11 May 2011 Mw 5.1 Lorca earthquake. LORC CGPS station includes measured (green) and modelled (red) displacement vectors. TERC CuaTeNeo station location is shown to illustrate a low level of expected co-seismic deformation at this site.

Acknowledgements. The authors would like to thank INFOTERRA for providing the TerraSAR-X images and the Instituto Geológico Minero Español (IGME) for providing helpful information at the area; the Spanish Ministerio de Ciencia e Innovación project CuaTeNeo (CGL2004-21666-E); the Consejería de Agricultura y Agua of Región de Murcia, for the Meristemm GPS Network data; the University of Barcelona (UB) APIF pre-doctoral grant to A.E; Financial support by the UB Faculty of Geology and the Laboratori d'Estudis Geofísics Eduard Fontserè of Institut d'Estudis Catalans. We thank the numerous volunteers, who have participated in the field campaigns. We are also very grateful to the two anonymous reviewers and to R. L. M. Vissers and C. Gaina whose comments and revisions greatly improved the content of the final version of this paper.

Edited by: C. Gaina

References

Akoglu, A. M., Cakir, Z., Meghraoui, M., Belabbes, S., El Alami, S. O., Ergintav, S., and Akyuz, H. S.: The 1994-2004 Al Hoceima (Morocco) earthquake sequence: Conjugate fault ruptures deduced from InSAR, Earth Planet. Sci. Lett., 252, 467–480, 2006.

Belabbes, S., Wicks, C., Cakir, Z., and Meghraoui, M.: Rupture parameters of the 2003 Zemmouri (Mw 6.8), Algeria, earthquake from joint inversion of interferometric synthetic aperture radar, coastal uplift, and GPS, J. Geophys. Res., 11, B03406, doi:10.1029/2008JB005912, 2009.

Bousquet, J. C.: Quaternary strike-slip faults in southeastern Spain, Tectonophysics, 52, 277–286, 1979.

Buforn, E., Benito, B., Sanzde Galdeano, C., del Fresno, C., Muñoz, D., and Rodríguez, I.: Study of the damaging earthquakes of 1911, 1999, and 2002 in the Murcia, Southeastern Spain region: seismotectonic and seismic-risk implications, Bull. Seism. Soc. Am., 95, 549–567, 2005.

Buforn, E., Cesca, S., Goded, T., del Fresno, C., and Muñoz, D.: The Bullas (Murcia, SE Spain) earthquake, 29 January 2005, J. Seismol., 10, 65–72, 2006.

Cardozo, N. and Allmendinger, R. W.: SSPX: A program to compute strain from displacement/velocity data, Comput. Geosci., 35, 1343–1357, 2009.

Colomina, I., Fleta, J., Giménez, J., Goula, X., Masana, E., Ortiz, M. A., Santanach, P., Soro, M., Suriñach, E., Talaya, J., and Térmens, A.: The CuaTeNeo GPS network to quantify horizontal movements in the Southeastern of the IberianPeninsula, edited by: Garcia, J. M. and Romacho, M. D., International Symposium Assesment and reduction of natural risk, I Ass. Hispano Portuguesa, Almeria. IGN, SIM1_01.do, 1999.

Costantini, M.: A novel phase unwrapping method based on network programming, IEEE Trans. Geosci. Remote Sens., 36, 813–821, 1998.

Dañobeitia, J. J, Sallarès, V., and Gallart, J.: Local earthquakes seismic tomography in the Betic Cordillera (southern Spain), Earth and Planet. Sci. Lett., 160, 225–239, 1998.

Delouis, B.: http://www.emsc-csem.org/Files/event/221132/result_Lorca_EQ.jpg, 2011.

Delouis, B., Charlety, J., and Vallée, M.: A Method for Rapid Determination of Moment Magnitude M_W for Moderate Earthquakes from the Near-Field Spectra of Strong-Motion Records (MWSYNTH), Bull. Seismol. Soc. Am., 99, 1827–1840, doi:10.1785/0120080234, 2009.

DeMets, C., Gordon, R. G., and Argus, D. F.: Geologically current plate motions, Geophys. J. Int., 181, 1–80, 2010.

Echeverria, A., Khazaradze, G., Gárate, J., Asensio, A., Masana, E., and Suriñach, E.: Present-day GPS crustal deformation rates in the Eastern Betics (SE Spain), Geophys. Res. Abstr., 13 (EGU2011-8005), 1, 2011.

Garrido, M. S., Giménez, E., de Lacy, M. C., and Gil, A. J.: Surveying at the limits of local RTK 25 networks: Test results from the perspective of high accuracy users, Int. J. Appl. Earth Obs., 13, 256–264, 2011.

Gaspar-Escribano, J. M., Benito, B., and García-Mayordomo, J.: Hazard-consistent response spectra in the Region of Murcia (Southeast Spain): comparison to earthquake-resistant provisions, Bull Earthquake Eng., 6, 179–196, doi:10.1007/s10518-007-9051-4, 2008.

González P. J. and Fernández, J.: Drougth-driven transient aquifer compaction imaged using multitemporal satellinte radar interferometry, Geology, 39, 551–554, 2011.

González, P. J., Fernández, J., and Luzón, F.: Interferometría radar aplicada a terremotos de magnitud moderada en las Cordilleras Béticas, SO España (in Spanish), Revista de cartografía, sistemas de información geográfica y teledetección, 133, 18–23, 2009.

Hanssen, R.: Radar Interferometry, Kluwer Academic Publishers, 2001.

IGN: Serie sísmica de Mula (Murcia). Segundo Informe General, Subdirección General de Geodesia y Geofísica,Instituto Geográfico Nacional, Madrid, 35 pp., 1999 (in Spanish).

IGN, El terremoto del SW de Bullas (Murcia) del 29 de enero de 2005, Subdirección General de Geodesia y Geofísica, Instituto Geográfico Nacional, Madrid, 2005 (in Spanish).

IGN: Serie terremoto NE Lorca, 11 mayo 2011, http://www.ign.es/ign/resources/sismologia/Lorca.pdf, 2011.

Irizarry, J., Frontera, T., Goula, X., and Barbat, A. H.: Learning from Earthquakes Lorca, Spain, Earthquakes of May 11, 2011, EERI Newsletter, June 2011, 45, 3, 2011.

Khazaradze, G., Gárate, J., Suriñach, E., Dávila, J. M., and Asensio, E.: Crustal deformation in south-eastern Betics from CuaTeNeo GPS network, GeoTemas, 10, 10123–10127, 2008.

Koulali, A., Ouazar, D., Tahayt, A., King, R. W., Vernant, P., Reilinger, R. E., McClusky, S., Mourabit, T., Davila, J. M., and Amraoui, N.: New GPS constraints on active deformation along the Africa-Iberia plate boundar, Earth Planet. Sc. Lett., 308, 211–217, 2011.

Martínez-Díaz, J. J.: Stress field variety related to fault interaction in a reverse oblique-slip fault: the Alhama de Murcia Fault, Betic Cordillera, Spain, Tectonophysics, 356, 291–305, 2002.

Martínez-Solares, J. M. and Mezcua, J.: Catálogo sísmico de la Península Ibérica (880 a.C.-1900), Monografía núm. 18, Subdirección General de Geodesia y Geofísica, Instituto Geográfico Nacional, Madrid, 2002 (in Spanish).

Masana, E., Martínez-Díaz, J. J., Hernández-Enrile, J. L., and Santanach, P.: The Alhama de Murcia fault (SE Spain), a seismogenic fault in a diffuse plate boundary: Seismotectonic implications for the Ibero-Magrebian region, J. Geophys. Res., 109, B01301, doi:10.1029/2002JB002359, 2004.

Mezcua, J., Herraiz, M., and Buforn, E.: Study of the June 6, 1977 Lorca (Spain) earthquake and its aftershock sequence, Bull. Seism. Soc. Am., 74, 167–179, 1984.

Mora, O., Arbiol, R., and Palà, V.: ICC's Project for DInSAR Terrain Subsidence Monitoring of the Catalonian Territory, Proceedings of IGARSS 2007, 4953–4956, 2007.

Muñoz, D. and Udías, A.: Three large historical earthquakes in southeastern Spain. In: Seismicity, Seismotectonics and Seismic Risk of the Ibero Maghrebian Region, Instituto Geográfico Nacional, Madrid, 175–182, 1991.

Pérez-Peña, A., Martín-Davila, J., Gárate, J., Berrocoso, M., and Buforn, E.: Velocity field and tectonic strain in Southern Spain and surrounding areas derived from GPS episodic measurements, J. Geodynam., 49, 232–240, 2010.

Vissers, R. L. M. and Meijninger, B. M. L.: The 11 May 2011 earthquake at Lorca (SE Spain) viewed in a structural-tectonic context, Solid Earth, 2, 199–204, doi:10.5194/se-2-199-2011, 2011.

Wang, K.: Stress-strain "paradox", plate coupling, and forearc seismicity at the Cascadia and Nankai subduction zones, Tectonophysics, 319, 321–338, 2000.

Wang, R., Lorenzo-Martín, F., and Roth, F.: Computation of deformation induced by earthquakes in a multi-layered elastic crust – FORTRAN programs EDGRN/EDCMP, Computers & Geosciences, 29, 195–207, 2003.

Wells, D. L. and Coppersmith, K. J.: New empirical relationships among magnitude, rupture length, rupture width, rupture area, and surface displacement, Bull, Seismol. Soc. Am. , 84, 974–1002, 1994.

Tectonophysics 608 (2013) 600–612

Contents lists available at ScienceDirect

Tectonophysics

journal homepage: www.elsevier.com/locate/tecto

Crustal deformation in eastern Betics from CuaTeNeo GPS network

Anna Echeverria [a,*], Giorgi Khazaradze [a], Eva Asensio [a], Jorge Gárate [b], José Martín Dávila [b], Emma Suriñach [a]

[a] *Risknat Group, Dpt. de Geodinàmica i Geofísica, Universitat de Barcelona, 08028 Barcelona, Spain*
[b] *Real Instituto y Observatorio de la Armada, 11110 San Fernando, Spain*

ARTICLE INFO

Article history:
Received 24 May 2013
Received in revised form 11 August 2013
Accepted 19 August 2013
Available online 26 August 2013

Keywords:
Betic Cordillera
Crustal deformation
Active faults
Geodynamics
GPS
Lorca earthquake

ABSTRACT

The eastern Betic Cordillera, Spain, is the most seismically active area within the Iberian Peninsula. We present a Global Positioning System (GPS)-derived horizontal crustal deformation obtained from five occupations of the CuaTeNeo GPS network (1997, 2002, 2006, 2009 and 2011) that clearly shows continuing tectonic activity in the SE Betics. The most prominent feature of the GPS velocity field is the NW oriented motion of the majority of the stations at rates ranging from 2 mm/yr near the coast to 0.5 mm/yr inland. This type of deformation indicates that the main driving force responsible for the observed velocities is related to the on-going convergence between Nubia and Eurasia plates. The calculated deformation field shows evidence for localized deformation related to active faults within the area. Most of the deformation is concentrated on the Alhama de Murcia fault, the source of the 2011 Lorca earthquake (M_w 5.2). We estimate a reverse-sinistral geodetic slip rate of 1.5 ± 0.3 mm/yr for this fault. Our crustal deformation field and analyses are important contributions to estimating seismic hazard for the eastern Betics, since it is the first time crustal deformation rates at this scale are presented.

1. Introduction

Global Positioning Systems (GPS) provide a fundamental tool for observing the kinematics of contemporary crustal deformation rates that can be used to identify tectonically active faults or regions. The main objective of this study is to determine deformation rates using episodic GPS observations in the eastern Betic Cordillera, Spain, and to identify currently active faults.

The western limit of the Alpine–Mediterranean system is the Gibraltar Arc, an arcuate shaped fold-and-thrust belt formed as a result of complex tectonic processes that involve convergence between Africa and Eurasia tectonic plates (e.g. Dewey et al., 1989). The Gibraltar Arc is formed by the Betic Cordillera in southern Spain, together with the Rif Mountains in northern Africa and the Alborán Sea basin in between (Fig. 1). Structurally the Betic Cordillera is divided into three major domains: the Internal and External zones and the Flysch Trough units. The CuaTeNeo ("Cuantificación de la Tectónica actual y Neotectónica") GPS network is located within the Internal zone, formed by three overthrusted complexes: Nevado-Filábride, Alpujárride and Maláguide. These complexes are composed mainly of metamorphosed Paleozoic and Mesozoic rocks separated by Neogene intermontane basins. The External Zone consists of Mesozoic to Tertiary rocks not affected by metamorphism and is characterized by thin-skinned tectonics. The Flysch Trough units are formed by siliciclastic deposits sedimented in a deep basin. The most recent phase of the Internal Zone evolution is related to formation of Neogene to Quaternary basins (Alborán back arc basin, Guadalquivir foreland basin and intermountain basins, such as Guadalentín near the town of Lorca) that were filled after the general alpine folding and uplifted rapidly since Pliocene, driven by continuing convergence of the Africa and Eurasia plates (Rosenbaum et al., 2002). The present-day convergence between these two plates is of the order of 4 to 6 mm/yr directed approximately in the NW direction based on geodetic, geophysical and seismologic data (Argus et al., 2011; DeMets et al., 2010; Fernandes et al., 2007; McClusky et al., 2003; Sella et al., 2002; Serpelloni et al., 2007). Depending on the study, this orientation can vary up to 45°. Throughout the text, we have opted to use the NNR-MORVEL56 (Argus et al., 2011) model, constructed from marine geophysical, seismologic and geodetic data instead of the GEODVEL model (Argus et al., 2010) obtained from geodetic observations (GPS, VLBI, SLR and DORIS) due to better agreement with the calculated velocity vectors. We attribute this discrepancy to the reference frame realization for our regional scale study, where we used the Western Eurasia frame as opposed to the entire Eurasian plate, as used in GEODVEL.

2. Seismotectonic setting

2.1. Active faults

The NE–SW trending Trans-Alboran Shear Zone (TASZ) is a main structural feature in Gibraltar Arc (De Larouzière et al., 1988; Frizon de Lamotte et al., 1980) (Fig. 1). The Eastern Betic Shear Zone (EBSZ)

* Corresponding author. Tel.: +34 934035914.
E-mail address: anna.echeverria@ub.edu (A. Echeverria).

0040-1951/$ – see front matter © 2013 Elsevier B.V. All rights reserved.
http://dx.doi.org/10.1016/j.tecto.2013.08.020

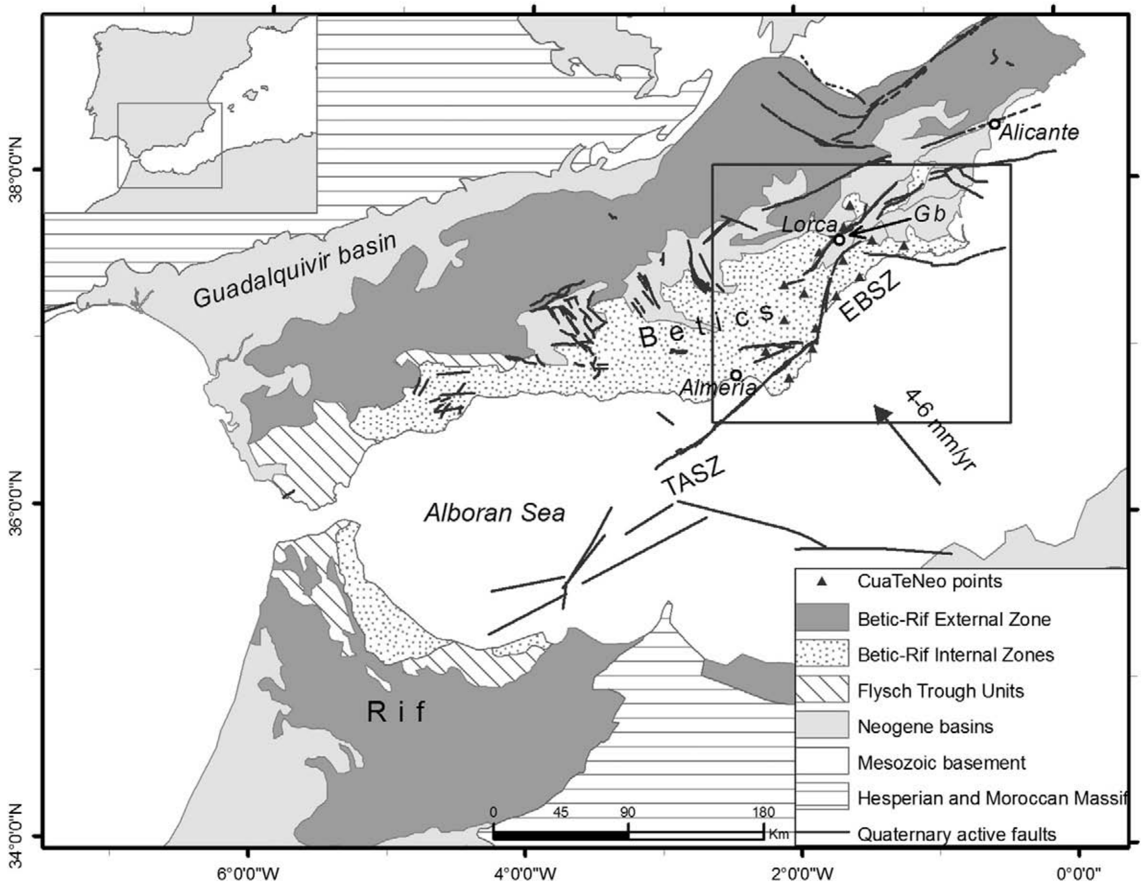

Fig. 1. Geo-tectonic map of the Gibraltar Arc. Black thick lines indicate Quaternary active faults from QAFI database (García-Mayordomo et al., 2012). Arrow shows convergence vector between Eurasia and Nubia plates. Study area marked with a rectangle and triangles indicate the CuaTeNeo GPS network sites. Abbreviations: EBSZ — Eastern Betic Shear Zone; TASZ — Trans-Alboran Shear Zone; Gb — Guadalentin basin.

forms the NE continuation of the TASZ (Bousquet, 1979; De Larouzière et al., 1988; Silva et al., 1993; Weijermars, 1987) and consists of several left-lateral strike-slip faults, spanning over 250 km from Alicante to Almeria: the Bajo-Segura, Carrascoy, Alhama de Murcia, Albox, Palomares and Carboneras faults (Fig. 2). The EBSZ faults accommodated a large part of Neogene and Quaternary shortening (Bousquet, 1979; Sanz de Galdeano, 1990). According to stress field variations (from NW–SE to N–S), these structures are reverse or sinistral strike-slip faults (De Larouzière et al., 1988). Paleoseismic and geologic studies suggest several paleo-earthquakes (e.g. Masana et al., 2004). Although, no direct GPS observations have been published for the EBSZ, Vernant et al. (2010) do determine 0.9–1.2 mm/yr of left-lateral and 0.2–0.8 mm/yr of fault normal slip rates for the EBSZ from block modeling. Below we provide a brief overview of the most important faults of the EBSZ (Figs. 1 and 2).

The Bajo-Segura fault (BSF) is a ~60 km long blind reverse fault with an ENE–WSW orientation characterized by net vertical slip of 0.2 mm/yr (García-Mayordomo, 2005). The Carrascoy fault (CaF) is ~30 km long and is the western continuation of the BSF (e.g. Silva et al., 1993). The CaF has a sinistral and reverse sense of movement, with an estimated horizontal rate of 0.5 mm/yr based on channel offset studies (García-Mayordomo, 2005; Silva, 1994). The Alhama de Murcia fault (AMF) is the longest onshore fault in the EBSZ and is divided into segments based on seismicity, tectonics and geomorphology. This fault is considered one of the most active faults in the Eastern Betics and was studied extensively during the last two decades. The AMF is a reverse and left-lateral strike-slip fault with horizontal slip rates determined by paleoseismology ranging between 0.06 and 0.53 mm/yr (Martínez-Díaz et al., 2012b; Masana et al., 2004; Ortuño et al., 2012). The Albox fault (AF) is a WSW–ENE reverse fault located south to AMF. Most of the N–S shortening during recent times was accommodated by the AF (Masana et al., 2005). The southern Palomares fault (PF) runs NNE–SSW and changes its orientation to NE–SW in the northern part, oriented approximately parallel to the southern termination of the AMF (Fig. 2). The PF kinematic evolution included changing in its behavior from mainly left-lateral strike-slip before the Messinian to normal type extension afterwards (García-Mayordomo, 2005). The southernmost fault of the EBSZ is the Carboneras fault (CF), a left-lateral transpressive structure that extends ~50 km onshore and runs south offshore under the Alborán Sea for ~100 km (Gràcia et al., 2006). The CF has a clear morphologic expression revealing its relatively young activity. Paleoseismologic studies reveal a minimum offset of 1.3 mm/yr for the NE part of the CF (Moreno, 2011).

Other important faults that fall within the study area, but are not part of the EBSZ, include the Crevillente fault (CrF), Moreras fault (MF) and the Alpujarras fault zone (AFZ). The ENE–WSW CrF is formed by dextral reverse parallel faults and constitutes an important crustal discontinuity (Sanz de Galdeano, 2008). The Moreras fault is a WNW–ESE trending right-lateral and normal fault (Rodríguez-Estrella et al., 2011). The AFZ is composed of several faults with an E–W orientation that acted as right lateral strike-slip faults in the Lower Miocene, but which are dominantly reverse since Upper Miocene (Sanz de Galdeano, 1996). The AFZ has been interpreted as a transfer faults ensemble (Sanz de Galdeano, 1996; Sanz de Galdeano et al., 2010). The dextral-reverse Polopos fault is one of the AFZ constituent faults (Fig. 2) with recent activity (up to late Pleistocene) (Giaconia et al.,

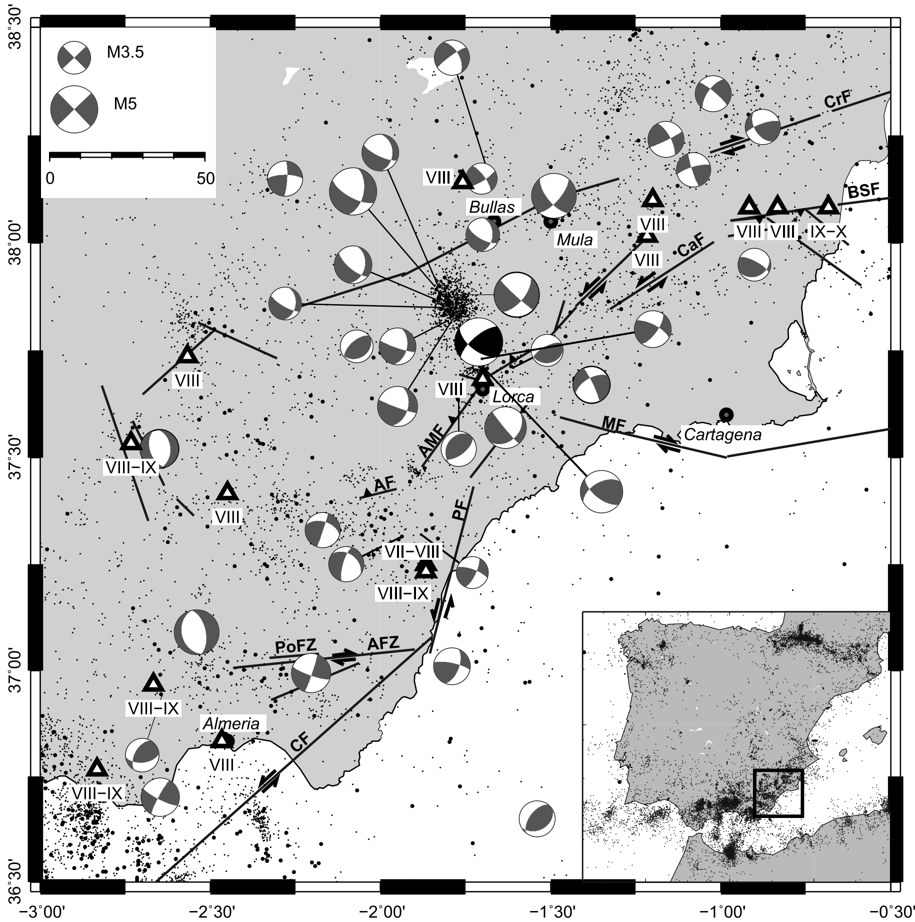

Fig. 2. Seismotectonic map of the eastern Betics. Instrumental seismicity from IGN catalog (1973–2011) (http://www.ign.es) with depths ranging 0–50 km. Thicker black points indicate earthquakes with M > 3. Historical seismicity (white triangles) is from the IGN catalog and is labeled by MSK intensity. Gray focal mechanisms are from Stich et al. (2003, 2006, 2010) (1984–2008) and IGN catalog (2009–2011) (http://www.ign.es). The black focal mechanism corresponds to the main May 11th, 2011 Lorca event (López-Comino et al., 2012). The inset shows seismicity for the entire Iberian Peninsula. Abbreviations are: CrF — Crevillente fault; BSF — Bajo-Segura fault; CaF — Carrascoy fault; AMF — Alhama de Murcia fault; AF — Albox fault; PF — Palomares fault; CF — Carboneras fault; MF — Moreras fault: AFZ — Alpujarras fault zone; PoFZ — Polopos fault zone.

2012). Other families of minor faults were also active during the Quaternary within the study area. Some of these structures are NW–SE trending normal faults related to active extension in the upper crust near Almería (Giaconia et al., 2013; Marín-Lechado et al., 2005; Martínez-Díaz and Hernández-Enrile, 2004; Sanz de Galdeano et al., 2010).

2.2. Instrumental and historical seismicity

The most seismically active region in the Iberian Peninsula includes the Alborán Sea and the Betic Cordillera, including the study area. Most earthquakes are concentrated along the Pyrenees, Betic–Rif chain and northern Algeria (inset, Fig. 2), but no obvious linear distribution along the plate boundaries can be observed. This may be due to the wide zone of deformation, the diffuse plate boundary between the Africa and Eurasia plates (e.g. Stich et al., 2003). The study area is characterized by low to moderate seismicity ($M < 5.5$) with hypocenters located in the crust (0–40 km) (e.g. Buforn et al., 1995; Buforn et al., 2004; Stich et al., 2003).

A cluster of seismicity is located between the Crevillente (CrF) and the Alhama de Murcia (AMF) faults (~37°45′N, −1°45′E, Fig. 2) that corresponds to four notable seismic series since 1999: the 1999 Mula series (Mw 5.1) (Buforn and Sanz de Galdeano, 2001), related to the Crevillente fault (e.g. Buforn et al., 2005), the 2002 Bullas series (Mw 5.0) (Buforn et al., 2005), the 2005 Bullas–La Paca series (Mw 4.8) (Benito et al., 2007) and the 2011 Lorca series (Mw 5.2) (e.g. López-Comino et al., 2012) attributed to the Alhama de Murcia fault (Martínez-Díaz et al., 2012a). The remainder of the study area is characterized by a diffuse seismicity not obviously associated with a fault.

We compiled 35 focal mechanisms (Fig. 2) from Stich et al. (2003, 2010, 2006), who estimated moment tensors for regional earthquakes of $M_w > 3.2$ from 1984 to 2008, and the Instituto Geográfico Nacional (IGN) (http://www.ign.es) for focal mechanism acquired between 2009 and 2011 with $M_w > 3.5$. The majority of focal mechanisms indicate strike-slip motion with minor normal or thrust slip. No obvious groups or clusters of similar mechanisms are clearly identified. Nevertheless, in the NE–SW striking bend roughly following the EBSZ, left-lateral strike-slip events are common. However, in the middle of the bend between the AMF and PF, two focal mechanisms with purely thrust type motion are present.

On May 11th, 2011 a $M_w = 5.2$ earthquake took place near the city of Lorca (Fig. 2) (e.g. López-Comino et al., 2012) that resulted in nine casualties and considerable damage to numerous buildings and had a major impact on media and society in Spain. This earthquake was preceded by another significant magnitude 4.5 event and was followed by numerous aftershocks of magnitudes lower than 3.9. The 2011 Lorca earthquake series has been attributed to the AMF, specifically to the intersegment zone between Goñar–Lorca and Lorca–Totana segments (Martínez-Díaz et al., 2012a; Vissers and Meijninger, 2011), and SW propagating rupture along the fault (López-Comino et al., 2012). The focal mechanism of the main event shows oblique reverse faulting (IGN, 2011; López-Comino et al., 2012), compatible with the kinematics determined by geologic studies for the AMF (e.g. Martínez-Díaz et al., 2012b; Masana et al., 2004).

In terms of the historical seismicity of the area (Martínez Solares and Mezcua, 2002), this part of the Betics has experienced since the 15th century at least 10 MSK intensity > X earthquakes. Most of them are linked to the EBSZ faults, such as AMF or PF. The most important events include the Torrevieja (1829, I = IX–X), Almería (1522, I = IX), Dalías (1804, I = VIII–IX), Baza (1531, I = VIII–IX), Vera (1406, I = VII–VIII and 1518, I = VIII–XI), and Lorca (1674, I = VIII) earthquakes (Lopez Casado et al., 1995) (Fig. 2). Interestingly, no earthquakes with MSK intensity > VIII have been recorded within the study area since modern instruments have been installed.

Several studies have estimated the stress field in the area, based on the inversion of earthquake focal mechanisms. From a regional point of view, the Betic Cordillera and Alborán Sea are under a horizontal compression in NW–SE to N–S direction with some localized horizontal tension in E–W to WSW–ENE direction (e.g. Buforn et al., 1995; Buforn et al., 2004; Henares et al., 2003; Herraiz et al., 2000; Stich et al., 2006). The coexistence of tension and compression is perhaps due to local changes in the positions of σ_1 and σ_2 (horizontal and vertical stresses, respectively) (De Vicente et al., 2008; Sanz de Galdeano et al., 2010). Rodríguez-Pascua and De Vicente (2001) determine two simultaneous orientations of maximum horizontal stress from the inversion of 28 focal mechanisms for the Eastern Betics: the NW–SE, defined by reverse faults and coincident with the plate convergence, and the NE–SW, defined by normal faults.

2.3. Previous geodetic studies

Currently, very few GPS-derived studies of the eastern Betics are published. Nonetheless, several more regional studies partially included the area (e.g. Fernandes et al., 2003; Fernandes et al., 2007; McClusky et al., 2003; Nocquet and Calais, 2004; Palano et al., 2013; Serpelloni et al., 2007; Stich et al., 2006; Tahayt et al., 2008; Vernant et al., 2010). These works concentrate on studying a wider region of Betic–Rif plate boundary and may be relevant to this study. In most of these studies, the GPS velocities within our study area were statistically insignificant at 95% confidence level.

In summary, the main results and observations of previous geodetic works include: 1) A general NW–SE oriented trend of motion in the Rif and western Betics (e.g. Palano et al., 2013) parallel to the Nubia/Eurasia convergence with rates of 1 to 4 mm/yr. 2) An anomalous westerly motion of up to ~4 mm/yr in the central part of the Rif (Fadil et al., 2006; Koulali et al., 2011; Vernant et al., 2010). 3) Dominantly W–SW motion along the southern margin of the Betics, from Almeria to Cádiz, on the order of 1 to 3 mm/yr (Koulali et al., 2011; Palano et al., 2013), which was linked by Stich et al. (2006) to an on-going SW–NE extension. 4) More to the east, close to the city of Cartagena, Pérez-Peña et al. (2010) found dominantly northward motion of up to ~2 mm/yr.

Variations in velocity orientation in the Betics and north Africa have been explained in the context of Eurasia–Nubia plate boundary geometry with two recent kinematic block models: Vernant et al. (2010) characterize a 1–2 mm/yr W–NW motion on the Betic Cordillera and define two additional blocks in the boundary zone: the Alborán–Rif block and the Betic block. Alternatively, Koulali et al. (2011) prefer a plate boundary geometry that combines the SW Betics, Alborán Sea and central Rif in a one block.

3. GPS data

3.1. CuaTeNeo GPS network

The CuaTeNeo geodetic network was built in 1996 to quantify current crustal deformation rates in the eastern Betic mountains (Figs. 1 and 5). The project was initiated by the University of Barcelona (UB) and the Institut Cartogràfic de Catalunya (ICC) (Castellote et al., 1997), and later joined by the Royal Naval Observatory (ROA). The network consists of 15 GPS monuments, from which 11 were built using concrete monuments with steel rebar perforating the bedrock up to 1 meter depth (to ensure good coupling) with embedded 5/8″ threads (to ensure correct centering of GPS antennas during observational campaigns) (see Fig. 3a). The remaining 4 monuments, due to difficult access, consist of simple 5/8″ threads cemented into bedrock and referred to as nail type monuments (see Fig. 3b).

Results are based on five campaigns conducted in 1997, 2002, 2006, 2009 and 2011. In general, intermittent campaigns should be conducted in the same months to minimize seasonal effects. The campaigns were conducted in the months of September and October, except for the 1997 and 2011 campaigns. The 1997 campaign was conducted in April. The 2011 campaign was organized in spring instead of the autumn, since it was specifically aimed to measure possible co-seismic deformation caused by the May 11, 2011 Lorca earthquake. For this reason, in the 2011 campaign only the seven nearest points to the earthquake were observed: ESPU, TERC, MELL, MONT, PURI, GANU and MAJA (Fig. 1 and Fig. 5). All sites occupied during each campaign were

Fig. 3. Photos of the two types of monuments of CuaTeNeo network. a) Concrete monument with the adapter and antenna. b) Nail type monument.

observed for three or more consecutive days in at least 8 hour long sessions. The first two campaigns (1997 and 2002) used Trimble 4000SSE receivers with Trimble 22020.00 GP antennas. Topcon GB1000 receivers with PG-A1_6 w/GP antennas were used since 2006. We employed special antenna adapters (Fig. 3a) to ensure correct antenna orientation to North and to avoid errors in antenna height.

3.2. GPS data and analysis

We processed data from 44 GPS stations. Among these, 16 stations were survey-mode GPS stations (SGPS): the 15 points of the CuaTeNeo network and one station placed in Cartagena (CART), belonging to the San Fernando Naval Observatory (ROA). Station CART is a continuously recording site installed in 1998. Since the data availability was intermittent, we treated it as a SGPS station, analyzing data from the same days as the 2002, 2006, 2009 and 2011 CuaTeNeo surveys. In addition, we analyzed 28 continuously recording GPS (CGPS) stations, the majority belonging to EUREF (Bruyninx, 2004) and/or International GNSS Service (IGS) (Dow et al., 2008) networks and are distributed throughout Iberia, Eurasia and Africa (Table 1 and Supplementary material). CGPS sites were selected using a criterion of having at least 10 years of data availability to ensure similar time span as of the CuaTeNeo data. To ensure robust velocity estimation and consequently, a better reference frame for the SGPS sites, we analyzed these CGPS stations for an entire time-span of the campaign data from 1997 to the end of 2011. To accelerate the processing procedure, especially at the post-processing step of the data analysis, CGPS data were processed for every 10 days instead of daily observations.

GPS data were processed using GAMIT/GLOBK 10.4 (Herring et al., 2010) software developed at Massachusetts Institute of Technology (MIT) (http://gpsg.mit.edu/simon/gtgk). This package uses double differences of phase and code data to compute a network solution. To obtain GPS station velocities we followed a three-step approach based on McClusky et al. (2000). First, daily GPS phase observations were processed using GAMIT by applying loose a priori constraints (in order to estimate station coordinates), the zenith delay of the atmosphere at each station and orbital and Earth orientation parameters. Second, consistent station coordinates were obtained from the loosely constrained solutions using GLOBK. The daily time series of each site were inspected and obvious outliers removed. Offsets due to earthquakes, antenna or hardware changes were corrected. In the final step all data were combined into a single solution, estimating positions, velocities and uncertainties for each station in a given reference frame. This final step is divided into two following Kotzev et al. (2006) and Steblov et al. (2003). First, the GPS solution is realized in the ITRF2008 global reference frame (Altamimi et al., 2011) by minimizing the differences using Helmert transformation between our estimated horizontal velocities for the reference stations and their corresponding velocities in ITRF2008. Second, assuming that stations belong to a non-deforming block, we transform the ITRF2008 solution into a western Europe reference frame by estimating rotation vectors. A group of CGPS stations used to define this reference frame was selected after considering various sets of stations forming part of the western Eurasia plate. A selection criteria were: horizontal residual velocity less than 0.5 mm/yr and errors less than 0.3 mm/yr. As a result, we derived a set of 6 sites (identified with stars in Table 1 and Fig. S1) that define our reference frame with a weighted root mean square of 0.17 mm/yr (Fig. 4). The Euler pole of rotation was calculated at Longitude 97.75 ± 0.52°W and Latitude 54.94 ± 0.75°N with a rotation rate of 0.2603 ± 0.001°/Myr. The Supplementary material includes a figure with the location and the velocities of the 6 sites used in the reference frame definition.

A rigorous estimation of uncertainties for the GPS velocities is especially important due to the low deformation rates (<2 mm/yr). Assuming only pure white noise (random) and ignoring correlated ('red') noise in GPS time-series lead to underestimation of the calculated velocity uncertainties (e.g. Mao et al., 1999). For our 28 CGPS sites, random

Table 1
Horizontal GPS velocities in western Europe reference frame with 1σ uncertainties and correlations (ρ) between the east (V_e) and north (V_n) components of velocity. V_{Hor} and Az are the horizontal velocity magnitudes and azimuths. Stars (*) indicate CGPS stations used to define the western Europe reference frame (see also the velocity plot in the Supplementary material). Station codes in italics refer to CuaTeNeo stations with a nail type monument (Fig. 3b). Sites presented in Fig. 5 are in bold.

CODE	Long. (°E)	Lat. (°N)	Ve (mm/yr)	1σ	Vn (mm/yr)	1σ	ρ	V_{Hor} (mm/yr)	1σ	Az (°N)
ALAC	359.519	38.339	−0.4	0.2	0.3	0.1	0.009	0.50	0.14	312
CART	358.988	37.587	−0.8	0.3	0.9	0.3	0.015	1.20	0.25	321
MAJA	358.819	37.623	−0.6	0.2	1.3	0.2	0.002	1.40	0.20	335
GANU	358.575	37.658	0.0	0.2	1.3	0.2	0.001	1.27	0.20	1
MONT	358.476	37.439	−0.4	0.2	1.7	0.2	−0.002	1.78	0.19	347
ESPU	358.411	37.870	−0.7	0.2	0.3	0.2	−0.001	0.71	0.20	294
TERC	358.363	37.742	−0.8	0.2	0.0	0.2	0.001	0.82	0.20	269
PURI	358.357	37.538	−0.8	0.2	1.7	0.2	0.000	1.86	0.19	334
PANI	358.302	37.325	−0.4	0.3	0.8	0.3	0.005	0.92	0.26	336
MELL	358.173	37.590	−0.7	0.2	0.2	0.2	0.004	0.73	0.20	287
MOJA	358.144	37.134	−1.3	0.3	1.6	0.3	0.015	2.06	0.27	321
CARB	358.115	37.012	−0.8	0.2	1.4	0.2	0.003	1.57	0.22	329
HUER	358.058	37.346	−0.9	0.3	1.2	0.3	0.008	1.49	0.28	324
RELL	357.941	36.836	−1.0	0.2	1.3	0.2	0.003	1.66	0.19	323
PUAS	357.908	37.395	−1.2	0.2	0.7	0.3	0.018	1.39	0.24	301
CUCO	357.907	37.184	−0.8	0.2	1.0	0.2	0.005	1.33	0.23	321
HUEB	357.769	36.999	−1.8	0.3	0.6	0.3	0.008	1.93	0.25	288
ALME	357.541	36.853	−1.7	0.1	−0.2	0.1	0.003	1.69	0.11	263
YEBE	356.911	40.525	−0.4	0.1	−0.1	0.1	0.002	0.40	0.11	260
VILL	356.048	40.444	0.0	0.2	0.2	0.2	−0.017	0.24	0.22	9
IFRN	354.892	33.540	−3.5	0.2	1.1	0.1	0.015	3.68	0.15	287
TETN	354.637	35.562	−4.4	0.1	0.2	0.1	0.009	4.44	0.12	272
SFER	353.794	36.464	−2.6	0.6	0.6	0.2	0.017	2.67	0.53	284
RABT	353.146	33.998	−3.6	0.1	1.4	0.1	0.003	3.86	0.11	292
LAGO	351.332	37.099	−1.6	0.1	0.9	0.1	0.002	1.83	0.11	300
CASC	350.581	38.693	−0.6	0.3	0.1	0.3	0.000	0.56	0.34	278
MAS1	344.367	27.764	−3.5	0.3	1.4	0.4	−0.023	3.73	0.27	293
PDEL	334.337	37.748	−3.5	0.1	0.3	0.1	0.036	3.47	0.14	275
METS	24.395	60.217	0.2	0.1	−1.5	0.1	0.054	1.54	0.10	171
MATE	16.704	40.649	0.1	0.2	4.3	0.2	−0.016	4.28	0.17	2
GRAZ	15.493	47.067	0.2	0.2	0.5	0.2	−0.003	0.58	0.22	21
POTS	13.066	52.379	−0.4	0.1	−0.5	0.1	0.020	0.60	0.10	222
WTZR*	12.879	49.144	−0.1	0.1	−0.1	0.1	−0.003	0.15	0.10	238
ONSA	11.926	57.395	−0.7	0.1	−1.0	0.1	0.023	1.21	0.11	213
MEDI	11.647	44.520	1.2	0.1	2.1	0.1	0.010	2.45	0.12	30
CAGL	8.973	39.136	−0.4	0.1	0.4	0.1	0.004	0.59	0.12	312
TORI*	7.661	45.063	−0.1	0.1	−0.1	0.1	0.007	0.08	0.11	220
GRAS*	6.921	43.755	−0.3	0.2	0.2	0.2	0.001	0.32	0.20	300
KOSG*	5.810	52.178	0.0	0.1	0.1	0.2	0.021	0.13	0.15	9
MARS	5.354	43.279	−0.4	0.5	0.0	0.2	0.001	0.43	0.54	275
BRUS*	4.359	50.798	0.1	0.2	0.0	0.2	0.004	0.11	0.16	90
TLSE*	1.481	43.561	0.2	0.1	0.0	0.1	0.002	0.21	0.11	87
EBRE	0.492	40.821	−0.1	0.1	−0.3	0.1	−0.006	0.27	0.11	193
HERS	0.336	50.867	−0.3	0.1	0.2	0.1	0.000	0.35	0.12	313

noise may be reduced to a negligible level and the character of the correlated noise can be evaluated (e.g. Bos et al., 2013; Williams et al., 2004). Correlated noise can be estimated from time series using spectral analysis but cannot be easily implemented in a GLOBK velocity solution, which is performed with a Kalman filter that accepts only first-order Gauss–Markov processes. Instead, we use the realistic sigma (RS) method developed by Herring (2003) and described later by Reilinger et al. (2006) for the CGPS sites. The RS method assumes a first-order Gauss–Markov process to take into account the fact that in the presence of correlated noise, χ^2/dof of the time series as a function of averaging time does not remain constant (as with white noise) but increases asymptotically. By estimating amplitude and the time constant of the exponential function, and afterwards evaluating the function for infinite averaging time, we determine the random-walk value that will produce a realistic uncertainty for the velocity estimate (see Shen et al., 2011 for details). We applied the RS algorithm to our continuous station time series after removing the best-fit annual signal, and then included the estimated random walk for each component of each station in our velocity solution. No attempt to apply the RS algorithm was made on the campaign sites (SGPS) where random (white) noise is dominant.

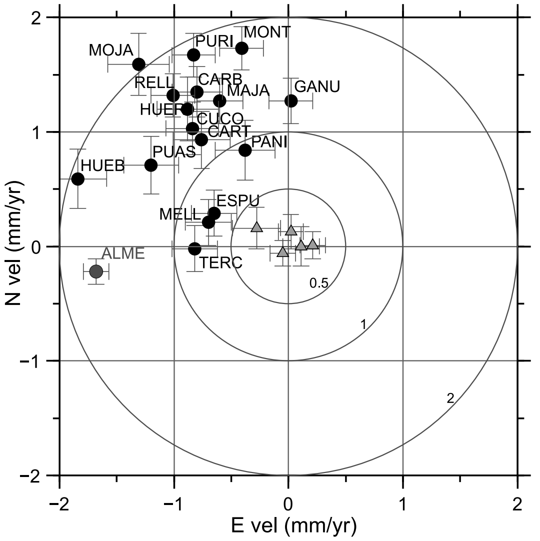

Fig. 4. East and north component velocities in western Europe reference frame. CuaTeNeo sites and ALME are black circles. CGPS sites used to define the reference frame (sites with asterisk in Table 1) are gray triangles. Error bars represent 1σ uncertainties.

Instead, we added 0.4 mm/√yr and 0.6 mm/√yr (for the nail type monuments) of random walk noise for SGPS stations to account for possible random walk due to monument instability (see Langbein and Johnson, 1997 for details). Additionally, several SGPS observations for the 2002 campaign are downweighted (see Supplementary material for the time-series). Human error likely accounts for these outliers since the same team and equipment measured these problematic stations.

4. Results

4.1. GPS velocities

Our present-day velocity vectors are shown in Fig. 5 and Table 1. To derive these results, we used an assumption of constant velocities between the five surveys (1997–2011 campaigns). Although this assumption is used commonly when treating the survey style GPS data, one should still be careful when dealing with possible disturbances due to nearby earthquakes or local site instabilities. The velocity field includes the 16 survey style GPS stations (15 CuaTeNeo and CART) and the CGPS station ALME, located in Almeria and belonging to the ERGNSS network of the IGN (www.ign.es). This is the only CGPS station within the study area that had observations comparable to the duration of the CuaTeneo data.

Eastern Betics GPS-derived velocities in a western Europe reference frame are shown in Figs. 4 and 5. The most prominent features are the dominant direction of motion roughly parallel to Nubia/Eurasia convergence and the reduction of motion inland. Stations in the middle of the network have 1–2 mm/yr velocities oriented 329 ± 15° (i.e. NW–NNW), which aligns well with the convergence direction between Nubia and Eurasia plates (323° ± 1.8) and is predicted by NNR-MORVEL56 (Fig. 5) (Argus et al., 2011). Within this group some stations exhibit small anomalous behavior, such as GANU (northward motion) and PANI (slower motion than the other coastal stations). On the extremities of the network, however, a more coherent motion of stations is noticed. Three GPS sites located west of AMF (ESPU, TERC and MELL) show the lowest velocities (<1 mm/yr) with a more westerly orientation (Fig. 5). The same sense of motion is present for two stations in the southern part (ALME and HUEB), but with twice as much velocity. Variations in the velocity field may be due to the presence of different tectonic behaviors, which will be discussed (see Section 5.1).

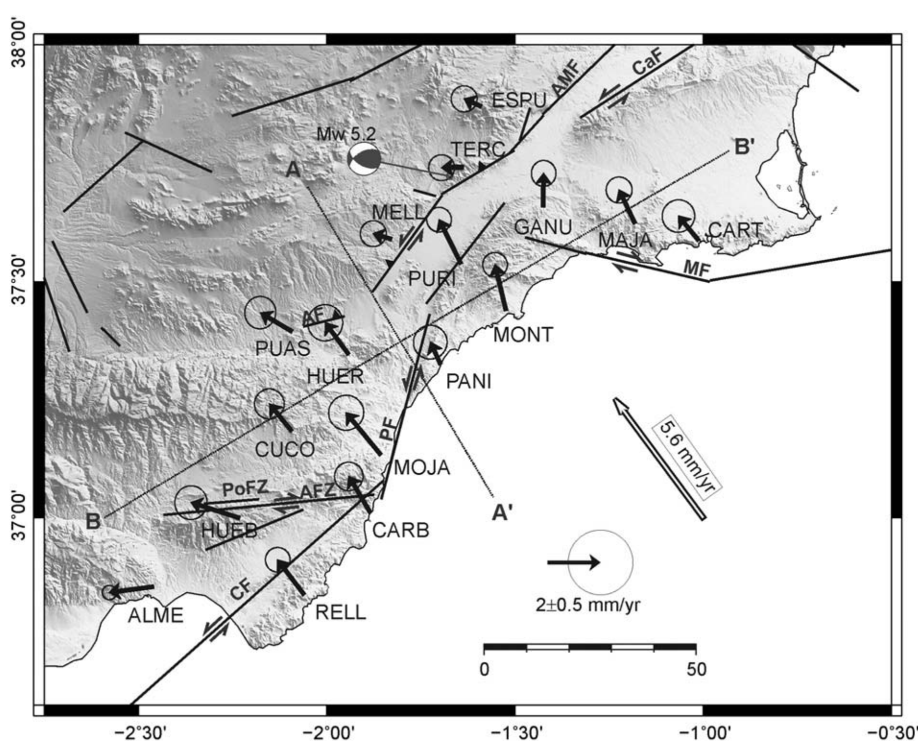

Fig. 5. CuaTeNeo GPS velocities in western Europe reference frame with 95% confidence error ellipses. Plate convergence velocity from NNR-MORVEL56 model (Argus et al., 2011) and a focal mechanism of the 2011 Lorca earthquake (López-Comino et al., 2012) are shown. Transects A–A′ and B–B′ are velocity profiles shown in Fig. 6. See Fig. 2 for fault abbreviations.

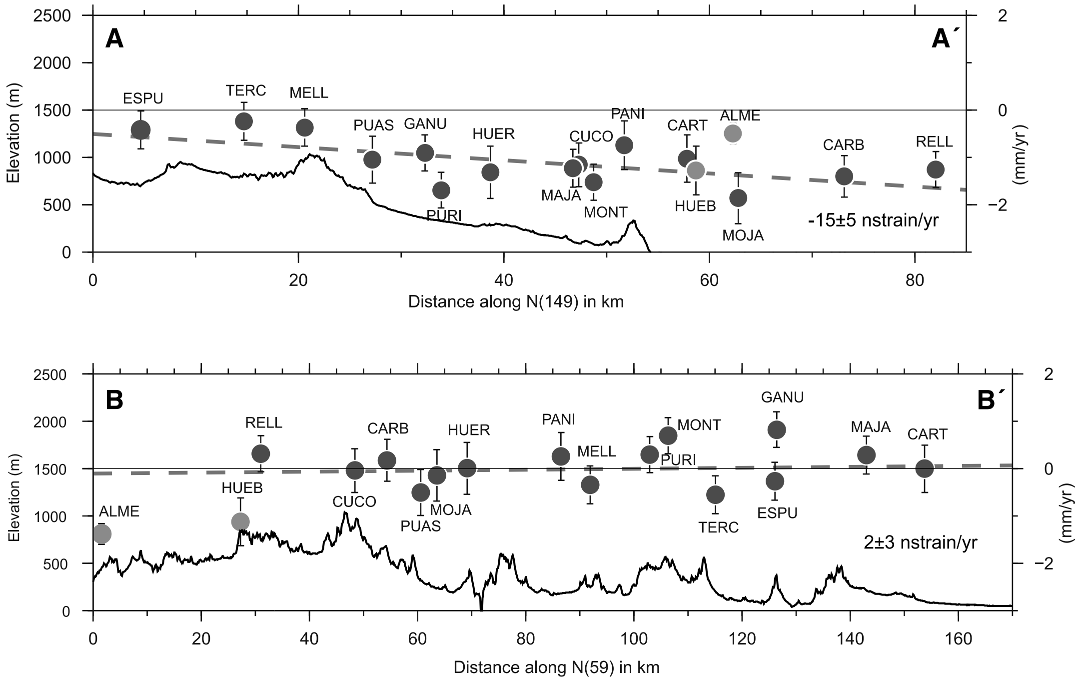

Fig. 6. Projected parallel (A–A′) and perpendicular (B–B′) velocities to plate motion direction (Fig. 5) with 1σ uncertainties (vertical error bars). The irregular line on the bottom shows the topography along the corresponding profile, with a vertical exaggeration of 1:9 and 1:17 for A–A′ and B–B′, respectively. Top) Profile A–A′ along the direction of plate motion and predominant velocity (N149°). Bottom) Profile B–B′ along the coast, N59°, perpendicular to the A–A′ profile. ALME and HUEB, plotted in light gray, have been excluded in slope estimate.

Horizontal velocities are plotted parallel and perpendicular to the dominant velocity direction (N329°), which roughly coincides with plate convergence direction (Fig. 6). Profile A–A′ shows -0.015 ± 0.005 (mm/yr)/km of shortening, equivalent to 15 ± 5 nstrain/yr (Fig. 6) that indicates that the coastal stations are moving faster than inland stations. The highest variation in velocities is observed near AMF. We will concentrate on this region in more detail in Section 5.3. The strain rate along the coastal profile B–B′ is statistically insignificant at 1σ level: 2 ± 3 nstrain/yr, indicating no differential motion for the time period observed (Fig. 6). In the calculation of the linear trends for the above profiles, we have excluded stations ALME and HUEB, since they clearly exhibit a different sense of motion, most probably due to escape tectonics as explained below in Section 5.1 (Fig. 6B).

4.2. Strain rate calculation

Strain rate parameters were calculated using the estimated velocities for the 15 CuaTeNeo stations plus CART and ALME using the SSPX software package (Cardozo and Allmendinger, 2009). We used the grid-nearest neighbor approach that computes strain rate at the center of each square. The following optimal parameters were chosen for the strain calculation: a grid spacing of 10 km and the 6 nearest stations located within a distance of 50 km. These parameters ensure small local variations and avoid smoothed regional patterns, since the strain field is not homogeneous throughout the area. The horizontal principal strain rate axes ($\dot{\varepsilon}_{max}$ and $\dot{\varepsilon}_{min}$) and dilatation are shown in Fig. 7a. Fig. 7b shows maximum shear strain rates ($\dot{\varepsilon}_{sh-max}$) and their directions. Only

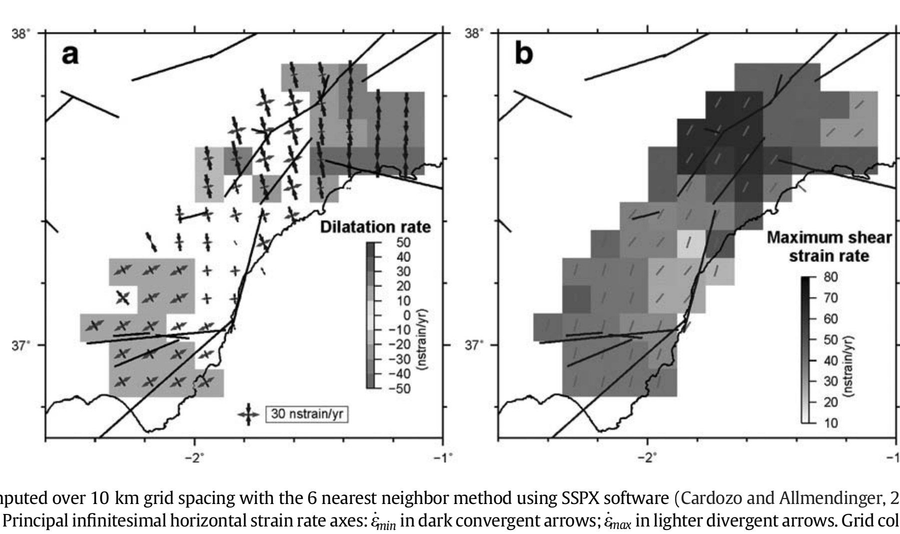

Fig. 7. GPS strain-rate field computed over 10 km grid spacing with the 6 nearest neighbor method using SSPX software (Cardozo and Allmendinger, 2009). Only statistically significant values at 1σ level are shown. a) Principal infinitesimal horizontal strain rate axes: $\dot{\varepsilon}_{min}$ in dark convergent arrows; $\dot{\varepsilon}_{max}$ in lighter divergent arrows. Grid coloring indicates 2D dilatation rates where red is extension and green is compression. b) Maximum shear strain rates ($\dot{\varepsilon}_{sh-max}$) represented by gray shaded square grids. Left-lateral plane orientations are shown.

significant values at 1σ level are presented. A convention of positive strain rates indicating extension is used.

The absolute values of the calculated strain rates show that the $\dot{\varepsilon}_{min}$ is usually greater than $\dot{\varepsilon}_{max}$. The maximum shortening rate equals to $\dot{\varepsilon}_{min} = 49 \pm 5$ nstrain/yr while the maximum extension rate ($\dot{\varepsilon}_{max}$) is 29 ± 8 nstrain/yr at 1σ level (Fig. 7a). The orientation of shortening and extension axes is mostly NNW–SSE and ENE–WSW, respectively, as expected from Nubia/Eurasia plate convergence. The highest shortening rates are located in the northern sector (around AMF–PF and Cartagena) and decrease significantly in the southern, where extension becomes dominant (Fig. 7a). The maximum shear strain rate ($\dot{\varepsilon}_{sh-max}$) is a measure of a maximum change in the angle between two line segments that were orthogonal in the undeformed state (Turcotte and Schubert, 1982). Maximum values of $\dot{\varepsilon}_{sh-max}$ are obtained around the AMF zone (65 ± 9 nstrain/yr at 1σ level) (Fig. 7b). Furthermore, the orientation of the left-lateral shear planes of $\dot{\varepsilon}_{sh-max}$ in this region (~210°N) is in good agreement with the strike of the AMF (~225°N).

Summing the shortening and extension rates and assuming a constant volume can compute the 2D dilatation rate. A negative value of dilatation indicates an excess of shortening in the horizontal plane and requires vertical thickening to maintain a constant volume. On the contrary, when the dilatation is positive, we get an excess of extension and vertical thinning is required to maintain a constant volume (Allmendinger et al., 2007). The calculated 2D dilatation rates show only two areas where statistically significant rates at 1σ level are present (Fig. 7a). On the one hand, the area in the NE part shows negative dilatation rates, which remain significant at 2σ level. In the SW part, the dilatation rates are positive but less robust since they are statistically insignificant at 2σ level. In terms of calculated rates, the maximum thickening in the NE area is -44 ± 12 nstrain/yr, and the maximum thinning in SW is 16 ± 15 nstrain/yr.

A clear dominance of the counterclockwise rotation (CCW) is observed in most of the study area (see Supplementary material). The highest rotation rates are seen near the AMF–PF left-lateral faults in the north and CF in the south-west. The CCW rotation rates range between 1.25 ± 0.04°/Myr to 0.07 ± 0.05°/Myr at 1σ level, assuming a constant rate through time.

5. Discussion

Our velocity field and strain rate calculations (described above) provide clear evidence of on-going crustal deformation in the SE Betics, implying continuing activity on regional faults. In the previous section we described the main characteristics of our GPS velocity field and strain rate calculation on a grid as well as along two profiles. Here we discuss the significance of these results and present our interpretation in terms of the regional tectonics and geology.

5.1. Velocity field

The dominant, roughly parallel direction of motion to convergence of Nubia and Eurasia plates (Fig. 5) provides the main driving force responsible for the ongoing crustal deformation in the region and is observed as the most prominent features in our velocity field. As expected, the observed velocities reach their highest values along the coast, with a maximum rate at MOJA of ~2 mm/yr. This value represents approximately 1/3 of the overall convergence rate (5.6 mm/yr) between the two plates calculated from NNR-MORVEL56 (Argus et al., 2011). The remainder of this convergence occurs within the wide deformation zone that includes the Alborán Sea and the Rif mountains. It is not clear whether this deformation is distributed uniformly with the analyzed data. However, judging by elevated rates of seismicity (Fig. 2) and geodetic studies in the Rif (e.g. Tahayt et al., 2008), we consider the bulk of the missing 3 to 4 mm/yr of deformation is most likely concentrated in northern Africa.

Directly comparing our velocity field with other published velocities is difficult because no work has been published with detailed results of GPS crustal deformation within the study area. Also, although there have been some publications with a more regional emphasis that included some continuous GPS velocities within the study area (Koulali et al., 2011; Palano et al., 2013; Pérez-Peña et al., 2010), as a rule, these velocities where characterized by large uncertainties, often exceeding the presented velocity values. Hence, a statistically meaningful comparison of these results is not useful. Nevertheless, in general terms, our results are consistent with previous studies, where the velocities within the EBSZ range between 1 and 3 mm/yr with respect to Eurasia.

This paper does not address vertical deformation rates since the analyzed campaign style GPS velocities do not provide sufficient resolution to detect possible deformations of a few mm/yr. It is noteworthy to mention that previous InSAR and GPS studies of the Guadalentín sedimentary basin where the city of Lorca is located (Figs. 1 and 2) have experienced subsidence of up to 1 m in the last ten years (at a rate of ~100 mm/yr) related to groundwater extraction (Echeverria et al., 2012; Frontera et al., 2012; González and Fernández, 2011; González et al., 2012). This rate of subsidence is two orders of magnitude higher than the expected tectonic signal and is more than sufficient to be detected by the campaign observations. Nevertheless, the CuaTeNeo GPS stations have not shown any appreciable subsidence at any of its stations. This is not surprising, since all of the network monuments were installed in bedrock and the observed subsidence takes place within the sedimentary basin.

Comparing the orientation of the 17 velocity vectors and the plate convergence azimuth (NNR-MORVEL56 model at 1°W, 37°N), three main groups of stations with approximately homogenous sense of motion can be identified (Fig. 5): *i*) the group of 12 stations that move parallel to the Nubia/Eurasia convergence direction, with the rates ranging from 1 to 2 mm/yr. In this group there are several stations that exhibit small anomalous behavior. PUAS, for example, is moving in a more westward direction than the dominant motion of the group, especially compared to the nearest station HUER. This motion could be caused by the proximity to the Albox fault (AF) or the horse-tail termination of the AMF. Station PANI at the coast, moves considerably slower than the neighboring coastal stations (<1 mm/yr). This behavior can be real, although we suspect that the instability of the monument and/or observational errors are the cause. This marker is a nail type monument, located in highly fractured rock that can easily suffer local anomalous motion. Finally, stations GANU and MONT move more northward, deviating from the dominant convergence direction. This motion could be related to Palomares fault (PF) or other minor faults in the area. *ii*) The group formed by ESPU, TERC and MELL located on the west side of the AMF is characterized with the smallest velocities and suggests that they belong to stable Iberia. The observed minor westerly component of motion at these three stations may be due to the motion of the AMF or other faults to the north (e.g. Crevillente). *iii*) ALME and HUEB, located in the SW corner of the network, exhibit a dominant westerly motion. Similar direction of motion has also been detected for stations located farther to the west, that fall outside the study area (Palano et al., 2013; Vernant et al., 2010). We think that this distinct behavior indicates that these stations belong to a different crustal block that escapes westwards along the boundaries formed by the Carboneras and Alpujarras faults and is driven by Nubia and Eurasia plate convergence (e.g. Martínez-Díaz and Hernández-Enrile, 2004; Rutter et al., 2012; Vegas, 1992). This escape tectonic feature could be linked with the extensional tectonics of the Almeria region, favoring the presence of NW–SE normal faults (Giaconia et al., 2013; Marín-Lechado et al., 2005). Moreover, previous geodetic leveling studies (Giménez et al., 2000) measured a subsidence of 1.5 mm/yr that they associate with the NW–SE normal faults and to the E–W reverse faults present in this region. Therefore, the westerly motion detected by GPS and this subsidence is compatible with NW–SE trending normal faults.

5.2. Strain field

The orientation and magnitude of the principal strain rate axes obtained by the inversion of the GPS data (Fig. 7) are in agreement with more regional studies (Palano et al., 2013) that calculate the strain tensor for the Gibraltar Arc area. Principal strain rates and dilatations (Fig. 7a) indicate two distinct zones of significant deformation but opposite behavior. The NE sector, with $|\dot{\varepsilon}_{min}| > |\dot{\varepsilon}_{max}|$ and negative 2-D dilatation, is coherent with a convergent regime. Maximum shear strain values are also observed in this region (Fig. 7b), indicating the presence of a transpressive regime, expressed by reverse and left-lateral faults (e.g. AMF). The SW sector around Almería, presents the opposite situation, with a $|\dot{\varepsilon}_{max}| > |\dot{\varepsilon}_{min}|$ and, to a lesser extent, positive 2-D dilatation, consistent with active normal faulting. On a larger scale, this behavior is also consistent with the geodynamic scenarios proposed for the Betic evolution in this area, which includes a SW motion due to a roll-back subduction (e.g. Gutscher et al., 2012) and/or delamination process (e.g. Calvert et al., 2000; Mancilla et al., 2013). Between these two zones (Fig. 7), we observe a sector with significantly less internal deformation (i.e. dilatation), although individual points move with significant velocities. This zone can be interpreted as a rigid block that translates to the N–NW, where the majority of strain is accommodated on the AMF.

The $\dot{\varepsilon}_{min}$ axes in the northern area rotate from NNW–SSE in the AMF zone to N–S in the Cartagena area where extension axes are insignificant, indicating uni-axial N–S convergence. This type of convergence would suggest reverse fault kinematics for the Moreras fault (MF) (Fig. 5) located in this region, contradicting the description provided by the QAFI geological database (García-Mayordomo et al., 2012) where the MF is characterized by a normal/dextral motion. More regional studies of the earthquake focal mechanisms, however, suggest a N–S compression for this region (Henares et al., 2003). It should be mentioned that our strain rates calculation for the region is based over an irregular distribution of GPS stations. In the NE part of the network where the stations are arranged linearly forms an E–W trend and no data are available to the south (Alborán Sea) or to the north. Hence, further investigation of the Moreras fault is necessary.

The CCW rotation calculated from the GPS velocities (see Supplementary material) is in agreement with the general trends of paleomagnetic rotation rates computed in the Eastern Betics Internal Zone (e.g. Calvo et al., 1997; Mattei et al., 2006). This CCW motion has been attributed to the presence of left-lateral faults (e.g. Calvo et al., 1997). Indeed, the maximum rotation rate calculated from our GPS field coincides with the area of the AMF and PF in the north and CF in the south-west.

5.3. Alhama de Murcia fault

We focus our work on the AMF–PF region since our strain rate field, local geology, tectonics and seismicity (e.g. Lorca earthquake) suggest that the bulk of the observed crustal deformation is concentrated here (Fig. 7). We chose the 6 nearest stations to AMF–PF system: 3 stations on the NW side of the fault (ESPU, TERC and MELL) and 3 stations on the SE side (GANU, PURI and MONT). We chose an AMF normal profile (C–C′) with a strike of 315° (Fig. 8). Our goal is to quantitatively

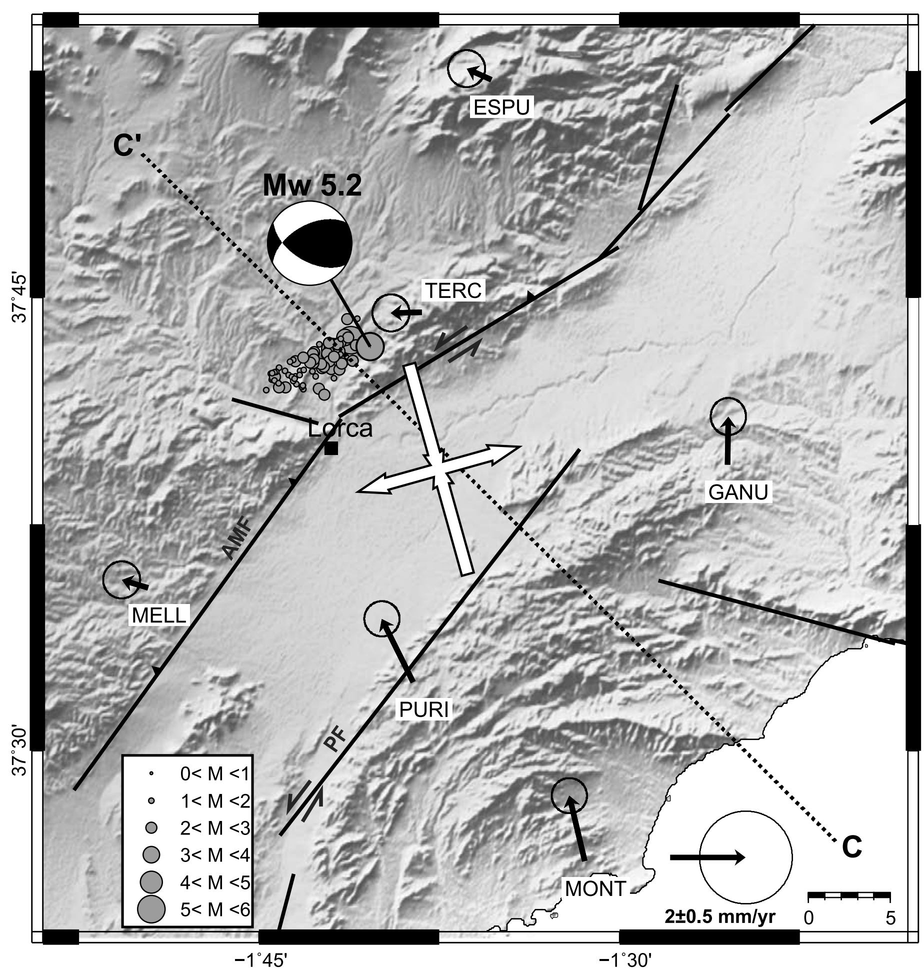

Fig. 8. Detailed zoom of the AMF–PF zone. The focal mechanism of the main 2011 Lorca earthquake and its aftershock distribution are shown. Calculated strain rates determined at the center of the 6 stations are shown as a white cross with: $\dot{\varepsilon}_{max} = 26 \pm 22$ nstrain/yr and $\dot{\varepsilon}_{min} = -39 \pm 3$ nstrain/yr. See Fig. 9 for the projected velocities along the profiles (C–C′).

measure differential motion between the two groups of stations. We estimated a slope by linear regression for each group separately, instead of performing linear fit for all six stations. This way we calculated offsets between the two groups (Fig. 9), which we interpret as geodetically estimated slip rate for the AMF (and PF). It is important to keep in mind that this analysis does not include the NE segment of the AMF.

We detect statistically significant (at 1σ level) differential motion between the two groups in both profiles as a velocity offset (ΔV_c and ΔV_{ss}). The calculated slopes for each group of stations are essentially flat, indicating that each group of stations is on a rigid block, without any significant strain rate accumulation. The profile parallel velocity component (i.e. AMF perpendicular) indicates a compression rate of $\Delta V_c = 0.8 \pm 0.4$ mm/yr in N315° direction between the SE and NW blocks (Fig. 9a). The offset calculated for the profile perpendicular velocity component ("strike-slip") is $\Delta V_{ss} = 1.3 \pm 0.2$ mm/yr in N225° direction (Fig. 9b). The ratio of these two offsets indicates the dominance of the left-lateral strike-slip kinematics with an approximate ratio of 60% vs. 40%.

These offsets are calculated for a swath of ~12 km width that encompasses the two important faults: AMF and PF. Currently, the relative partitioning of deformation between these two faults cannot be determined, since no measurements are available within the area separating the two faults. Nevertheless, we believe that the bulk of the measured offset comes from the AMF, which presents considerably higher seismicity (instrumental and historical) than the PF and has more geologic evidence of quaternary activity (Martínez-Díaz et al., 2012b).

We calculated the horizontal offset from ΔV_c and ΔV_{ss} from the GPS velocity profiles to compare with geologic slip rates. The total horizontal slip rate is 1.5 ± 0.3 mm/yr with an azimuth of N12°E with respect to the north-western block. The slip rate for the AMF segments based on paleoseismological studies suggests lower values of slip rates that range between 0.06 and 0.53 mm/yr (Martínez-Díaz et al., 2012b; Masana et al., 2004; Ortuño et al., 2012). The underestimation of the paleoseismological slip rates is expected, since these values do not correspond to the entire fault, but rather to a specific segment of the fault. On the other hand, the GPS slip rates represent an upper bound of the overall slip rate (e.g. Reilinger et al., 2006), since it has been assumed that all the measured deformations occur on the AMF and no slip on secondary faults and/or internal strain accumulation has been considered. Taking the above arguments into account, the estimated geodetic slip rate can be considered to be in agreement with paleoseismological slip rate estimates.

The SW segment of the AMF may be aseismic (e.g. Rodríguez-Escudero et al., 2012) while other sections are obviously seismic since they produce significant earthquakes, such as the 1964 and 2011 Lorca earthquakes (Fig. 2). Several studies, based on comparison of the seismic moment release with geodetic deformation, have suggested a dominance of aseismic deformation in the Betics, Alborán Sea and north of Morocco (Pérez-Peña et al., 2010; Stich et al., 2007). In order to distinguish whether the measured geodetic deformation is indicative of aseismic or locked type behavior of the AMF, we used a 2D elastic dislocation model following Okada's (1992) formulation. As can be seen from Fig. 9, our modeling results cannot differentiate between the shallow locked fault and the aseismic (i.e. stepwise) motion across the fault. However, the preference for a shallower locked fault is clear, since the 12 km deep fault produces significantly worse fit with the data. This observation is also in agreement with a shallow hypocenter (4.6 km) of the 2011 Lorca earthquake (López-Comino et al., 2012). In conclusion, based on this simple modeling effort, we can say that our results preclude the distinction of the aseismic or seismic nature of deformation across the SW part of the AMF and/or PF. It would be essential to establish new geodetic points in the region separating the two faults.

5.4. Lorca earthquake of 11/05/2011

On May 11th, 2011 a Mw = 5.2 earthquake occurred near the city of Lorca (Figs. 2 and 8) that was attributed to slip on the south-central section of the AMF (e.g. Martínez-Díaz et al., 2012a). Our detailed analysis of the CuaTeNeo data has not identified any co-seismic deformation related to the earthquake, including at a closest station TERC located just

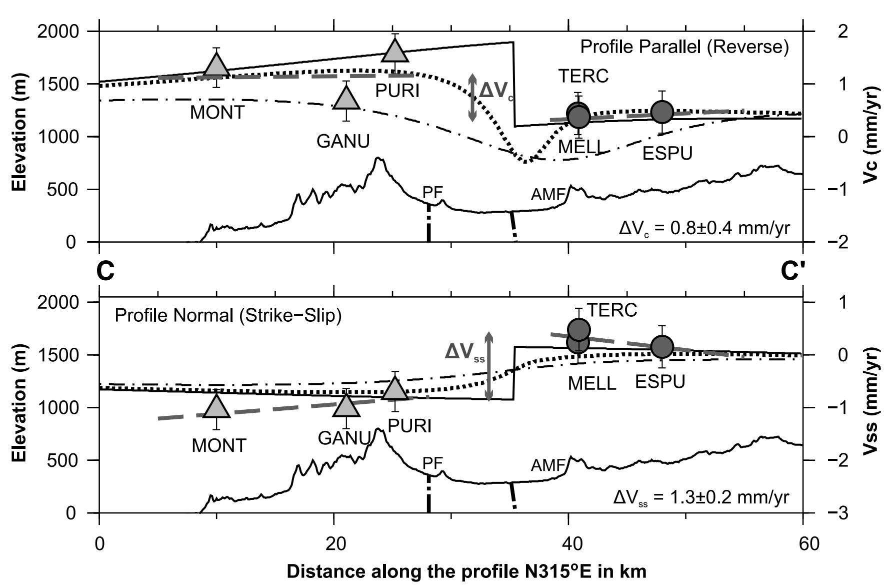

Fig. 9. C–C′ profile (azimuth N315°E) parallel and normal velocities with 1 sigma uncertainties (vertical bars). Location of the profile is shown in Fig. 8. Dashed straight gray lines show linear regression fit for the individual group of stations, used to estimate the offsets. Three other curves represent the prediction of the 2D elastic dislocation model according to Okada's (1992) formulation: 1) continuous straight line represents an aseismic motion; 2) thick-dotted line corresponds to a fault locked to 3 km depth; and 3) dashed-dotted line is a model prediction for the fault locked to 12 km depth. In all 3 models we used the far field displacement corresponding to the MORVEL model velocities projected along the AMF (simple trace with azimuth N225°E). Topography is represented with an irregular line with a vertical exaggeration of 1:9. Stations on the NW side of the AMF are plotted as triangles and as circles on the SE side. The intersections with the AMF and PF are shown as short vertical lines on the bottom. Top: Profile parallel (AMF normal) velocities. ΔV_c is the compressive differential motion (velocity offset) between the two blocks. Bottom: Profile normal (AMF parallel) velocities. ΔV_{ss} is the strike-slip differential motion between the two blocks.

4 km NE from the epicenter of the earthquake (Fig. 8). The absence of co-seismic signal in the CuaTeNeo data is expected, since the elastic dislocation model for the event predicts no co-seismic displacement for any of its stations (Echeverria et al., 2012; Frontera et al., 2012). However, a continuous station placed in Lorca, did detect a co-seismic jump of ~4–6 mm to the north as predicted by the modeling (Echeverria et al., 2012; Frontera et al., 2012).

Since the co-seismic signal of the Lorca earthquake was not detected by the CuaTeNeo network, the GPS velocities presented in this study represent the inter-seismic phase of earthquake deformation cycle. The oblique (reverse-sinistral) slip rate of 1.5 $\pm$ 0.3 mm/yr calculated for the AMF (Fig. 9) is consistent with the behavior of the fault suggested by geologic observations (Martínez-Díaz et al., 2012b; Masana et al., 2004; Ortuño et al., 2012) and also is in agreement with the 2011 Lorca earthquake focal mechanism (Fig. 8). The P and T axes orientations for the focal mechanism of the main earthquake (López-Comino et al., 2012) are N167–190E and N270°E, respectively. GPS principal strain axes orientations calculated at the center of AMF–PF region using 6 stations (Fig. 8) are $\dot{\varepsilon}_{min}$ = N164°E° $\pm$ 7°E and $\dot{\varepsilon}_{max}$ = N254° $\pm$ 7°E (at 1σ level), in good agreement with the above P–T axes orientations.

6. Conclusions

We present rates of crustal deformation for the eastern Betics. This work is an important contribution for the seismic hazard estimation of eastern Betics because it is the first time crustal deformation rates at this scale and details are presented. A GPS-derived horizontal velocity field representing the present-day crustal deformation rates in the eastern Betics based on the analysis of 16 survey style GPS stations of the CuaTeNeo network measured over a 15 yr period from 1997 to 2011 is presented. The velocity field and subsequent strain rate analyses clearly illustrate that the SE part of the Betics is currently tectonically active near the Alhama de Murcia fault. The most prominent feature of our velocity field is the NW oriented dominant motion of the majority of the stations at rates ranging from 2 $\pm$ 0.2 mm/yr at the coast to 0.7 $\pm$ 0.2 mm/yr inland. This deformation indicates that the main driving force behind the observed velocities is related to the on-going convergence between the Nubia and the Eurasia plates.

GPS velocities and the derived strain rate field suggest a dominant NW–SE oriented compression, with a local SW–NE extension in the south-western part of the network. On a more detailed scale, we find two distinct zones with significant deformation but opposite behavior: The NE sector is consistent with a convergent regime, where $|\dot{\varepsilon}_{min}| > |\dot{\varepsilon}_{max}|$ and 2-D dilatation is negative. Also in this zone shear strain rate values are maximum, indicating a presence of a transpressive regime, expressed by reverse and left-lateral faults, such as the Alhama de Murcia fault. In the SW sector near Almeria the dominance of $\dot{\varepsilon}_{max}$ could indicate a presence of a thinning or extensional kinematics, possibly related to the block escape tectonics.

Most of the observed deformation is concentrated within the Alhama de Murcia–Palomares fault region. The geodetic oblique slip rate (reverse-sinistral) of 1.5 $\pm$ 0.3 mm/yr calculated for the AMF and PF fault system is in good agreement with geologic observations as well as the focal mechanism of the 2011 Lorca earthquake. Based on the predictions of the 2-D elastic dislocation model for the AMF, we could say that the geodetic measurements indicate that locked portion of the fault is shallow (less than 5 km depth). However, due to the absence of GPS data between the AMF and PF, our results preclude the distinction between the aseismic and/or shallow locked fault behavior at the SW part of the AMF. It is also impossible to determine the relative partitioning of deformation between the AMF and PF faults. In the future, it would be necessary to establish new geodetic points in the region separating the two faults.

Supplementary data to this article can be found online at http://dx.doi.org/10.1016/j.tecto.2013.08.020.

Acknowledgments

We thank all the individuals and institutions who contributed to the installation and observations of the CuaTeNeo network as well as the property owners who kindly gave their permission for the construction of the monuments. This work was supported by the Spanish Ministry of Science and Innovation projects: Topo-Iberia (CSD2006-00041), EVENT (CGL2006-12861-C02-01) and CuaTeNeo (CGL2004-21666-E). We thank an APIF pre-doctoral grant of the University of Barcelona for A.E. and an FPU pre-doctoral grant (AP-2008-01482) of the Spanish Ministry of Education for E.A. Financial support by the UB Faculty of Geology and the Laboratori d'Estudis Geofísics Eduard Fontseré of Institut d'Estudis Catalans for the 2011 campaign is appreciated. We also acknowledge the institutions responsible for the operation of the continuous GPS stations: IGN, ROA, EUREF and IGS. We thank Gina Schmalzle for her careful review of the manuscript. The constructive comments of Philippe Vernant and anonymous reviewer contributed to the improvement of this work. Most graphics are from Generic Mapping Tools GMT software (Wessel and Smith, 1991).

References

Allmendinger, R.W., Reilinger, R., Loveless, J., 2007. Strain and rotation rate from GPS in Tibet, Anatolia, and the Altiplano. Tectonics 26 (3). http://dx.doi.org/10.1029/2006TC002030 (TC3013).

Altamimi, Z., Collilieux, X., Métivier, L., 2011. ITRF2008: an improved solution of the international terrestrial reference frame. J. Geod. 457–473. http://dx.doi.org/10.1007/s00190-011-0444-4.

Argus, D.F., Gordon, R.G., Heflin, M.B., Ma, C., Eanes, R.J., Willis, P., Peltier, W.R., Owen, S.E., 2010. The angular velocities of the plates and the velocity of Earth's centre from space geodesy. Geoph. J. Int. 180 (3), 913–960. http://dx.doi.org/10.1111/j.1365-246X.2009.04463.x.

Argus, D.F., Gordon, R.G., Demets, C., 2011. Geologically current motion of 56 plates relative to the no-net-rotation reference frame. Geochem. Geophys. Geosyst. 12 (11). http://dx.doi.org/10.1029/2011GC003751.

Benito, B., Capote, R., Murphy, P., Gaspar-Escribano, J.M., Martinez-Diaz, J.J., Tsige, M., Stich, D., Garcia-Mayordomo, J., Garcia Rodriguez, M.J., Jimenez, M.E., Insua-Arevalo, J.M., Alvarez-Gomez, J.A., Canora, C., 2007. An overview of the damaging and low magnitude M (sub w) 4.8 La Paca earthquake on 29 January 2005; context, seismotectonics, and seismic risk implications for Southeast Spain. Bull. Seismol. Soc. Am. 97 (3), 671–690. http://dx.doi.org/10.1785/0120050150.

Bos, M.S., Fernandes, R.M.S., Williams, S.D.P., Bastos, L., 2013. Fast error analysis of continuous GNSS observations with missing data. J. Geod. 87 (4), 351–360. http://dx.doi.org/10.1007/s00190-012-0605-0.

Bousquet, J.C., 1979. Quaternary strike-slip faults in southeastern Spain. Tectonophysics 52, 277–286.

Bruyninx, C., 2004. The EUREF Permanent Network: a multi-disciplinary network serving surveyors as well as scientists. GeoInformatics 7, 32–35.

Buforn, E., Sanz de Galdeano, C., 2001. Focal mechanism of Mula (Murcia, Spain) earthquake of February 2, 1999. J. Seismol. 5 (2), 277–280. http://dx.doi.org/10.1023/a:1011472400818.

Buforn, E., Sanz de Galdeano, C., Udías, A., 1995. Seismotectonics of the Ibero-Maghrebian region. Tectonophysics 248 (3–4), 247–261.

Buforn, E., Bezzeghoud, M., Udías, A., Pro, C., 2004. Seismic sources on the Iberia–African Plate Boundary and their Tectonic Implications. Pure Appl. Geophys. 161 (3). http://dx.doi.org/10.1007/s00024-003-2466-1.

Buforn, E., Benito, B., Sanz de Galdeano, C., del Fresno, C., Muñoz, D., Rodriguez, I., 2005. Study of the damaging earthquakes of 1911, 1999, and 2002 in the Murcia, Southeastern Spain, Region: seismotectonic and seismic-risk implications. Bull. Seismol. Soc. Am. 95 (2), 549–567. http://dx.doi.org/10.1785/0120040041.

Calvert, A., Sandvol, E., Seber, D., Barazangi, M., Roecker, S., Mourabit, T., Vidal, F., Alguacil, G., Jabour, N., 2000. Geodynamic evolution of the lithosphere and upper mantle beneath the Alboran region of the western Mediterranean: constraints from travel time tomography. Journal of Geophysical Research 105 (B5), 10871–10898 (10810.11029/12000JB900024).

Calvo, M., Vegas, R., Osete, M.L., 1997. Palaeomagnetic results from Upper Miocene and Pliocene rocks from the Internal Zone of the eastern Betic Cordilleras (southern Spain). Tectonophysics 277 (4), 271–283. http://dx.doi.org/10.1016/S0040-1951(97)00033-4.

Cardozo, N., Allmendinger, R.W., 2009. SSPX: a program to compute strain from displacement/velocity data. Comput. Geosci. 35 (6), 1343–1357. http://dx.doi.org/10.1016/j.cageo.2008.05.008.

Castellote, M., Fleta, J., Goula, X., Surinach, E., Talaya, J., Termens, A., 1997. Red GPS para el control de las fallas activas del SE de la Peninsula Iberica (Proyecto CuaTeNeo).

De Larouzière, F.D., Bolze, J., Bordet, P., Hernandez, J., Montenat, C., Ott d'Estevou, P., 1988. The Betic segment of the lithospheric Trans-Alboran shear zone during the Late Miocene. Tectonophysics 152, 41–52.

De Vicente, G., Cloetingh, S., Muñoz-Martín, A., Olaiz, A., Stich, D., Vegas, R., Galindo-Zaldívar, J., Fernández-Lozano, J., 2008. Inversion of moment tensor focal mechanisms for active stresses around the microcontinent Iberia: tectonic implications. Tectonics 27. http://dx.doi.org/10.1029/2006TC002093 (TC1009).

DeMets, C., Gordon, R.G., Argus, D.F., 2010. Geologically current plate motions. Geoph. J. Int. 181 (1), 1–80. http://dx.doi.org/10.1111/j.1365-246X.2009.04491.x.

Dewey, J.F., Helman, M.L., Turco, E., Hutton, D.H.W., Knott, S.D., 1989. Kinematics of the western Mediterranean. In: Coward, M.P., Dietrich, D., Park, R.G. (Eds.), Alpine Tectonics. Geological Society, pp. 265–283.

Dow, J., Neilan, R., Rizos, C., 2008. The International GNSS Service in a changing landscape of Global Navigation Satellite Systems. J. Geod. 83 (3), 191–198. http://dx.doi.org/10.1007/s00190-008-0300-3.

Echeverria, A., Khazaradze, G., Gárate, J., Asensio, A., Surinach, E., 2012. Deformación cortical de las Béticas Orientales mediante GPS y su relación con el terremoto de Lorca. Fisica de la Tierra 24, 113–127. http://dx.doi.org/10.5209/rev_FITE2012.v24.40134.

Fadil, A., Vernant, P., McClusky, S., Reilinger, R., Gomez, F., Sari, D.B., Mourabit, T., Feigl, K., Barazangi, M., 2006. Active tectonics of the western Mediterranean: Geodetic evidence for rollback of a delaminated subcontinental lithospheric slab beneath the Rif Mountains, Morocco. Geology 34 (7), 529–532. http://dx.doi.org/10.1130/G22291.1.

Fernandes, R.M.S., Ambrosius, B.A.C., Noomen, R., Bastos, L., Wortel, M.J.R., Spakman, W., Govers, R., 2003. The relative motion between Africa and Eurasia as derived from ITRF2000 and GPS data. Geophys. Res. Lett. 30 (16), 1828. http://dx.doi.org/10.1029/2003GL017089.

Fernandes, R.M.S., Miranda, J.M., Meijninger, B.M.L., Bos, M.S., Noomen, R., Bastos, L., Ambrosius, B.A.C., Riva, R.E.M., 2007. Surface velocity field of the Ibero-Maghrebian segment of the Eurasia–Nubia plate boundary. Geoph. J. Int. 169 (1), 315–324. http://dx.doi.org/10.1111/j.1365-246X.2006.03252.x.

Frizon de Lamotte, D., Jarrige, J.J., Vidal, J.C., 1980. Le magmatisme béticorifain est-il lié à une zone d'accidents décrochants "Trans-Alboran"?, Huitième Réunion Annuelle des Sciences de la Terre. Abstracts. Societé Geologique de France, Marseille.

Frontera, T., Concha, A., Blanco, P., Echeverria, A., Goula, X., Arbiol, R., Khazaradze, G., Pérez, F., Suriñach, E., 2012. DInSAR coseismic deformation of the May 2011 Mw 5.1 Lorca earthquake (Southern Spain). Solid Earth 3, 111–119. http://dx.doi.org/10.5194/se-3-111-2012.

García-Mayordomo, J., 2005. Caracterización y Análisis de la Peligrosidad Sísmica en el Sureste de España. (PhD thesis) Universidad Complutense de Madrid 373.

García-Mayordomo, J., Insua-Arévalo, J.M., Martínez-Díaz, J.J., Jiménez-Díaz, A., Martín-Banda, R., Martín-Alfageme, S., Álvarez-Gómez, J.A., Rodríguez-Peces, M., Pérez-López, R., Rodríguez-Pascua, M.A., Masana, E., Perea, H., Martín-González, F., Giner-Robles, J., Nemser, E.S., Cabral, J., 2012. The Quaternary active faults database of Iberia (QAFI v. 2.0). J. Iber. Geol. 38 (1), 285–302.

Giaconia, F., Booth-Rea, G., Martínez-Martínez, J.M., Azañón, J.M., Pérez-Peña, V., Pérez-Romero, J., Villegas, I., 2012. Geomorphic evidence of active tectonics in the Sierra Alhamilla (eastern Betics, SE Spain). Geomorphology 145–146. http://dx.doi.org/10.1016/j.geomorph.2011.12.043 (90–106).

Giaconia, F., Booth-Rea, G., Martínez-Martínez, J.M., Azañón, J.M., Pérez-Romero, J., Villegas, I., 2013. Mountain front migration and drainage captures related to fault segment linkage and growth: the Polopos transpressive fault zone (southeastern Betics, SE Spain). J. Struct. Geol. 46 (0), 76–91. http://dx.doi.org/10.1016/j.jsg.2012.10.005.

Giménez, J., Suriñach, E., Goula, X., 2000. Quantification of vertical movements in the eastern Betics (Spain) by comparing levelling data. Tectonophysics 317, 237–258. http://dx.doi.org/10.1016/S0040-1951(99)00318-2.

González, P.J., Fernández, J., 2011. Drought-driven transient aquifer compaction imaged using multitemporal satellite radar interferometry. Geology 39 (6), 551–554. http://dx.doi.org/10.1130/G31900.1.

González, P.J., Tiampo, K.F., Palano, M., Cannavo, F., Fernandez, J., 2012. The 2011 Lorca earthquake slip distribution controlled by groundwater crustal unloading. Nat. Geosci. 5 (11), 821–825. http://dx.doi.org/10.1038/ngeo1610.

Gràcia, E., Pallas, R., Soto Juan, I., Comas, M., Moreno, X., Masana, E., Santanach, P., Diez, S., Garcia, M., Danobeitia, J., Bartolome, R., Farran, M., Gomez, M., Alpiste, M.J.R., Lastras, G., Wilmott, V., Perea, H., Blondel, P., Gomez, O., Bullock, L., Jacobs, C., Rouse, I., White, D., Whittle, S., Terrinha, P., Gafeira, J., Roque, C., Hits Scientific Party, I., 2006. Active faulting offshore SE Spain (Alboran Sea); implications for earthquake hazard assessment in the southern Iberian margin. Earth Planet. Sci. Lett. 241 (3–4), 734–749. http://dx.doi.org/10.1016/j.epsl.2005.11.009.

Gutscher, M.A., Dominguez, S., Westbrook, G.K., Le Roy, P., Rosas, F., Duarte, J.C., Terrinha, P., Miranda, J.M., Graindorge, D., Gailler, A., Sallares, V., Bartolome, R., 2012. The Gibraltar subduction: a decade of new geophysical data. Tectonophysics 574–575. http://dx.doi.org/10.1016/j.tecto.2012.08.038 (72–91).

Henares, J., López Casado, C., Sanz de Galdeano, C., Delgado, J., Peláez, J.A., 2003. Stress fields in the Iberian-Maghrebi region. J. Seismol. 7 (1), 65–78. http://dx.doi.org/10.1023/A:1021294015027.

Herraiz, M., De Vicente, G., Lindo-Ñaupari, R., Giner, J., Simón, J.L., González-Casado, J.M., Vadillo, O., Rodriguez-Pascua, M.A., Cicuéndez, J.I., Casas, A., Cabañas, L., Rincón, P., Cortés, A.L., Ramírez, M., Lucini, M., 2000. The recent (upper Miocene to Quaternary) and present tectonic stress distributions in the Iberian Peninsula. Tectonics 19 (4), 762–786.

Herring, T., 2003. MATLAB tools for viewing GPS velocities and time series. GPS Solutions 7 (3), 194–199. http://dx.doi.org/10.1007/s10291-003-0068-0.

Herring, T.A., King, R.W., McClusky, S.C., 2010. Introduction to GAMIT/GLOBK. Department of Earth, Atmospheric, and Planetary Sciences. Massachusetts Institute of Technology 48.

IGN, 2011. INFORME DEL SISMO DE LORCA DEL 11 DE MAYO DE 2011. Instituto Geográfico Nacional de España. http://www.ign.es/ign/resources/sismologia/www/lorca/Lorcainfo2011.pdf (Madrid p. 138).

Kotzev, V., Nakov, R., Georgiev, T., Burchfiel, B.C., King, R.W., 2006. Crustal motion and strain accumulation in western Bulgaria. Tectonophysics 413 (3–4), 127–145. http://dx.doi.org/10.1016/j.tecto.2005.10.040.

Koulali, A., Ouazar, D., Tahayt, A., King, R.W., Vernant, P., Reilinger, R.E., McClusky, S., Mourabit, T., Davila, J.M., Amraoui, N., 2011. New GPS constraints on active deformation along the Africa–Iberia plate boundary. Earth Planet. Sci. Lett. 308 (1–2), 211–217. http://dx.doi.org/10.1016/j.epsl.2011.05.048.

Langbein, J., Johnson, H., 1997. Correlated errors in geodetic time series; implications for time-dependent deformation. J. Geophys. Res. 102 (1), 591–604.

Lopez Casado, C., de Galdeano, Sanz, Delgado, J., Peinado, M.A., 1995. The b parameter in the Betic Cordillera, Rif and nearby sectors; relations with the tectonics of the region. Tectonophysics 248 (3–4), 277–292. http://dx.doi.org/10.1016/0040-1951(94)00278-H.

López-Comino, J.-Á., Mancilla, F., Morales, J., Stich, D., 2012. Rupture directivity of the 2011, Mw 5.2 Lorca earthquake (Spain). Geophys. Res. Lett. 39 (3), L03301. http://dx.doi.org/10.1029/2011gl050498.

Mancilla, L.F.d, Stich, D., Berrocoso, M., Martín, R., Morales, J., Fernandez-Ros, A., Páez, R., Pérez-Peña, A., 2013. Delamination in the Betic Range: deep structure, seismicity, and GPS motion. Geology 41 (3), 307–310. http://dx.doi.org/10.1130/g33733.1.

Mao, A., Harrison, C.G., Dixon, T.H., 1999. Noise in GPS coordinate estimates. J. Geophys. Res. 104, 2797–2816. http://dx.doi.org/10.1029/1998JB900033.

Marín-Lechado, C., Galindo-Zaldívar, J., Rodríguez-Fernández, L.R., Serrano, I., Pedrera, A., 2005. Active faults, seismicity and stresses in an internal boundary of a tectonic arc (Campo de Dalías and Níjar, southeastern Betic Cordilleras, Spain). Tectonophysics 396 (1–2), 81–96. http://dx.doi.org/10.1016/j.tecto.2004.11.001.

Martínez Solares, J.M., Mezcua, J., 2002. Catálogo Sísmico de la Península Ibérica (880 a.c.–1900). Monografía de Instituto Geográfico Nacional de España 18, 253.

Martínez-Díaz, J.J., Hernández-Enrile, J.L., 2004. Neotectonics and morphotectonics of the southern Almería region (Betic Cordillera-Spain) kinematic implications. Int. J. Earth Sci. 93 (2), 189–206. http://dx.doi.org/10.1007/s00531-003-0379-y.

Martínez-Díaz, J.J., Bejar-Pizarro, M., Álvarez-Gómez, J.A., Mancilla, F., Stich, D., Herrera, G., Morales, J., 2012a. Tectonic and seismic implications of an intersegment rupture. The damaging May 11th 2011 Mw 5.2 Lorca, Spain, earthquake. Tectonophysics (0), 546–547. http://dx.doi.org/10.1016/j.tecto.2012.04.010 (28–37).

Martínez-Díaz, J.J., Masana, E., Ortuño, M., 2012b. Active tectonics of the Alhama de murcia fault, Betic Cordillera, Spain. J. Iber. Geol. 38 (1), 269–286. http://dx.doi.org/10.5209/rev_JIGE.2012.v38.n1.39218.

Masana, E., Martínez-Díaz, J.J., Hernández-Enrile, J.L., Santanach, P., 2004. The Alhama de Murcia fault (SE Spain), a seismogenic fault in a diffuse plate boundary: seismotectonic implications for the Ibero-Magrebian region. J. Geophys. Res. 109, B01301. http://dx.doi.org/10.1029/2002JB002359.

Masana, E., Pallàs, R., Perea, H., Ortuño, M., Martínez-Díaz, J.J., García-Meléndez, E., Santanach, P., 2005. Large Holocene morphogenic earthquakes along the Albox fault, Betic Cordillera, Spain. J. Geodyn. 40 (2–3), 119–133. http://dx.doi.org/10.1016/j.jog.2005.07.002.

Mattei, M., Cifelli, F., Rojas, I.M., Crespo Blanc, A., Comas, M., Faccenna, C., Porreca, M., 2006. Neogene tectonic evolution of the Gibraltar Arc: new paleomagnetic constrains from the Betic chain. Earth Planet. Sci. Lett. 250 (3–4), 522–540. http://dx.doi.org/10.1016/j.epsl.2006.08.012.

McClusky, S., Balassanian, S., Barka, A., Demir, C., Ergintav, S., Georgiev, I., Gurkan, O., Hamburger, M., Hurst, K., Kahle, H., Kastens, K., Kekelidze, G., King, R., Kotzev, V., Lenk, O., Mahmoud, S., Mishin, A., Nadariya, M., Ouzounis, A., Paradissis, D., Peter, Y., Prilepin, M., Reilinger, R., Sanli, I., Seeger, H., Tealeb, A., Toksoz, M.N., Veis, G., 2000. Global Positioning System constraints on plate kinematics and dynamics in the eastern Mediterranean and Caucasus. J. Geophys. Res. 105 (B3), 5695–5719. http://dx.doi.org/10.1029/1999JB900351.

McClusky, S., Reilinger, R., Mahmoud, S., Ben Sari, D., Tealeb, A., 2003. GPS constraints on Africa (Nubia) and Arabia plate motions. Geoph. J. Int. 155 (1), 126–138. http://dx.doi.org/10.1046/j.1365-246X.2003.02023.x.

Moreno, X., 2011. Neotectonic and Paleoseismic Onshore–Offshore Integrated Study of the Carboneras Fault (Eastern Betics, SE Iberia). (PhD thesis) Universitat de Barcelona, Barcelona 365.

Nocquet, J.M., Calais, E., 2004. Geodetic measurements of crustal deformation in the Western Mediterranean and Europe. Pure Appl. Geophys. 161 (3), 661–681. http://dx.doi.org/10.1007/s00024-003-2468-z.

Okada, Y., 1992. Internal deformation due to shear and tensile faults in a half-space. Bull. Seismol. Soc. Am. 82 (2), 1018–1040.

Ortuño, M., Masana, E., García-Meléndez, E., Martínez-Díaz, J.J., Štěpančíková, P., Cunha, P.P., Sohbati, R., Canora, C., Buylaert, J.P., Murray, A.S., 2012. An exceptionally long paleoseismic record of a slow-moving fault: the Alhama de Murcia fault (Eastern Betic shear zone, Spain). Geol. Soc. Am. Bull. 124 (9–10), 1474–1494. http://dx.doi.org/10.1130/B30558.1.

Palano, M., González, P.J., Fernández, J., 2013. Strain and stress fields along the Gibraltar Orogenic Arc: constraints on active geodynamics. Gondwana Res. 23 (3), 1071–1088. http://dx.doi.org/10.1016/j.gr.2012.05.021.

Pérez-Peña, A., Martín-Dávila, J., Gárate, J., Berrocoso, M., Buforn, E., 2010. Velocity field and tectonic strain in Southern Spain and surrounding areas derived from GPS episodic measurements. J. Geodyn. 49 (3–4), 232–240. http://dx.doi.org/10.1016/j.jog.2010.01.015.

Reilinger, R., McClusky, S., Vernant, P., Lawrence, S., Ergintav, S., Cakmak, R., Ozener, H., Kadirov, F., Guliev, I., Stepanyan, R., Nadariya, M., Hahubia, G., Mahmoud, S., Sakr, K., ArRajehi, A., Paradissis, D., Al-Aydrus, A., Prilepin, M., Guseva, T., Evren, E., Dmitrotsa, A., Filikov, S.V., Gomez, F., Al-Ghazzi, R., Karam, G., 2006. GPS constraints on continental deformation in the Africa–Arabia–Eurasia continental collision zone and implications for the dynamics of plate interactions. J. Geophys. Res. 111 (B5), 26. http://dx.doi.org/10.1029/2005JB004051.

Rodríguez-Escudero, E., Martínez-Díaz, J.J., Tsige, M., 2012. Deformaciones dúctiles en régimen frágil en una falla activa lenta: La falla de Alhama de Murcia. Implicaciones sismotectónicas. Geo-Temas 13, 4.

Rodríguez-Estrella, T., Navarro, F., Ros, M., Carrión, J., Atenza, J., 2011. Holocene morphogenesis along a tectonically unstable coastline in the Western Mediterranean (SE Spain). Quat. Int. http://dx.doi.org/10.1016/j.quaint.2011.07.016.
Rodríguez-Pascua, M.A., De Vicente, G., 2001. Present stress field in the Eastern Betic Chain. Estado de esfuerzos actual en la Cordillera Bética Oriental 112 (4), 79–95.
Rosenbaum, G., Lister, G.S., Duboz, C., 2002. Relative motions of Africa, Iberia and Europe during Alpine orogeny. Tectonophysics 359 (1–2), 117–129. http://dx.doi.org/10.1016/S0040-1951(02)00442-0.
Rutter, E.H., Faulkner, D.R., Burgess, R., 2012. Structure and geological history of the Carboneras Fault Zone, SE Spain: part of a stretching transform fault system. J. Struct. Geol. 45, 68–86. http://dx.doi.org/10.1016/j.jsg.2012.08.009.
Sanz de Galdeano, C., 1990. Geologic evolution of the Betic Cordilleras in the western Mediterranean, Miocene to the present. Tectonophysics 172 (1–2), 107–119.
Sanz de Galdeano, C.M., 1996. Tertiary tectonic framework of the Iberian Peninsula. In: Friend, P.F., Dabrio, C.J. (Eds.), Tertiary Basins of Spain, the Stratigraphic Record of Crustal Kinematics. Cambridge University Press, pp. 9–14.
Sanz de Galdeano, C., 2008. The Cadiz–Alicante Fault: an important discontinuity in the Betic Cordillera. Revista de la Sociedad Geológica de España 21 (1–2), 49–58.
Sanz de Galdeano, C., Shanov, S., Galindo-Zalívar, J., Radulov, A., Nikolov, G., 2010. A new tectonic discontinuity in the Betic Cordillera deduced from active tectonics and seismicity in the Tabernas Basin. J. Geodyn. 50 (2), 57–66. http://dx.doi.org/10.1016/j.jog.2010.02.005.
Sella, G.F., Dixon, T.H., Mao, A., 2002. REVEL: a model for recent plate velocities from space geodesy. J. Geophys. Res. 107 (B4), 2081. http://dx.doi.org/10.1029/2000JB000033.
Serpelloni, E., Vannucci, G., Pondrelli, S., Argnani, A., Casula, G., Anzidei, M., Baldi, P., Gasperini, P., 2007. Kinematics of the western Africa–Eurasia plate boundary from focal mechanisms and GPS data. Geoph. J. Int. 169 (3), 1180–1200. http://dx.doi.org/10.1111/j.1365-246X.2007.03367.x.
Shen, Z.K., King, R.W., Agnew, D.C., Wang, M., Herring, T.A., Dong, D., Fang, P., 2011. A unified analysis of crustal motion in Southern California, 1970–2004: the SCEC crustal motion map. J. Geophys. Res. 116 (B11), B11402. http://dx.doi.org/10.1029/2011jb008549.
Silva, P.G., 1994. Evolución geodinámica de la Depresión del Guadalentín desde el Mioceno Superior hasta la actualidad: Neotectónica y Geomorfología. Universidad Complutense de Madrid, Madrid, Spain 642 (PhD thesis).
Silva, P.G., Goy, J.L., Somoza, L., Zazo, C., Bardaji, T., 1993. Landscape response to strike-slip faulting linked to collisional settings; quaternary tectonics and basin formation in the eastern Betics, southeastern Spain. Tectonophysics 224 (4), 289–303. http://dx.doi.org/10.1016/0040-1951(93)90034-H.
Steblov, G.M., Kogan, M.G., King, R.W., Scholz, C.H., Bürgmann, R., Frolov, D.I., 2003. Imprint of the North American plate in Siberia revealed by GPS. Geophys. Res. Lett. 30 (18). http://dx.doi.org/10.1029/2003GL017805.
Stich, D., Ammon, C.J., Morales, J., 2003. Moment tensor solutions for small and moderate earthquakes in the Ibero-Maghreb region. J. Geophys. Res. 108 (B3). http://dx.doi.org/10.1029/2002JB002057.
Stich, D., Serpelloni, E., Mancilla, F., Morales, J., 2006. Kinematics of the Iberia-Maghreb plate contact from seismic moment tensors and GPS observations. Tectonophysics 426 (3–4), 295–317. http://dx.doi.org/10.1016/j.tecto.2006.08.004.
Stich, D., Martín, J.B., Morales, J., 2007. Deformación sísmica y asísmica en la zona Béticas–Rif–Alborán. Revista de la Sociedad Geológica de España 20 (3–4), 311–319.
Stich, D., Martín, R., Morales, J., 2010. Moment tensor inversion for Iberia-Maghreb earthquakes 2005–2008. Tectonophysics 483, 390–398. http://dx.doi.org/10.1016/j.tecto.2009.11.006.
Tahayt, A., Mourabit, T., Rigo, A., Feigl, K.L., Fadil, A., McClusky, S., Reilinger, R., Serroukh, M., Ouazzani-Touhami, A., Sari, D.B., Vernant, P., 2008. Mouvements actuels des blocs tectoniques dans l'arc Bético-Rifain à partir des mesures GPS entre 1999 et 2005. Comptes Rendus Geosci. 340 (6), 400–413.
Turcotte, D.T., Schubert, G., 1982. Geodynamics, Applications of Continuum Physics to Geological Problems. John Wiley & Sons, New York, N.Y., USA.
Vegas, R., 1992. Sobre el tipo de deformación distribuida en el contacto Africa y la Península Ibérica. Física de la Tierra 4, 41–56.
Vernant, P., Fadil, A., Mourabit, T., Ouazar, D., Koulali, A., Davila, J.M., Garate, J., McClusky, S., Reilinger, R., 2010. Geodetic constraints on active tectonics of the Western Mediterranean: implications for the kinematics and dynamics of the Nubia–Eurasia plate boundary zone. J. Geodynamics 49 (3–4), 123–129 (http://dx.doi.org/016/j.jog.2009.10.007).
Vissers, R.L.M., Meijninger, B.M.L., 2011. The 11 May 2011 earthquake at Lorca (SE Spain) viewed in a structural–tectonic context. Solid Earth 2 (2), 199–204. http://dx.doi.org/10.5194/se-2-199-2011.
Weijermars, R., 1987. The Palomares brittle–ductile Shear Zone of southern Spain. J. Struct. Geol. 9, 139–157.
Wessel, P., Smith, W.H.F., 1991. Free software helps map and display data. Eos Trans. AGU 72 (41), 441. http://dx.doi.org/10.1029/90EO00319.
Williams, S.D.P., Bock, Y., Fang, P., Jamason, P., Nikolaidis, R.M., Prawirodirdjo, L., Miller, M., Johnson, D.J., 2004. Error analysis of continuous GPS position time series. J. Geophys. Res. 109 (B3). http://dx.doi.org/10.1029/2003jb002741.

Geodetic evidence for continuing tectonic activity of the Carboneras fault (SE Spain)

Anna Echeverria[1], Giorgi Khazaradze[1], Eva Asensio[1], Eulalia Masana[1]

[1]RISKNAT Group, Departament de Geodinàmica i Geofísica, Facultat de Geologia, Universitat de Barcelona (UB), Martí i Franquès s/n, 08028 Barcelona, Spain

Keywords: Betic-Rif Arc; Eastern Betic Shear Zone; Carboneras Fault; Crustal deformation; Active faults; Geodynamics; GPS; Seismicity

ABSTRACT

The Carboneras fault zone (CFZ) is a prominent onshore-offshore strike-slip fault that forms part of the Eastern Betic Shear Zone (EBSZ). In this work, for the first time, we were able to confirm the continuing tectonic activity of the CFZ and quantify its geodetic slip-rates using continuous and campaign GPS observations conducted during the last decade. We find that the left-lateral motion dominates the kinematics of the CFZ, with a strike-slip rate of 1.3±0.2 mm/yr along N48º direction. The shortening component is significantly lower and poorly constrained. The recent onshore and offshore paleoseismic and geomorphologic results across the CFZ have suggested a minimum Quaternary strike-slip rates between 1.1 and 1.3 mm/yr. Considering the similarity of paleoseismic and geodetic slip rates measured at different points along the fault, the northern segment of the CFZ must have been slipping approximately at a constant rate during the Quaternary. We have also found that the Palomares fault (PF) in the NW, is either inactive or is slipping very slowly (< 0.5 mm/yr). Regarding the eastern part of the Alpujarras fault zone corridor (AFZ), our GPS measurements corroborate that this zone is active and accumulates a right-lateral motion to compensate for the observed left-lateral motion of the CFZ. This opposite type strike-slip motion across the AFZ and CFZ is a result of a push-type force due to Nubia and Eurasia plate convergence that results in the westward escape of the block bounded by these faults. However, in order to explain the observed gradually increasing westerly motion and counter-clockwise rotation of the GPS stations located west of longitude 2.5°W, in the proposed conceptual kinematic model, we propose an existence of additional pull-type forces, which are caused by a complex deep sub-lithospheric processes.

Geodetic evidence for continuing tectonic activity of the Carboneras fault (SE Spain)

Anna Echeverria[1], Giorgi Khazaradze[1], Eva Asensio[1], Eulalia Masana[1]

[1]RISKNAT Group, Departament de Geodinàmica i Geofísica, Facultat de Geologia, Universitat de Barcelona (UB), Martí i Franquès s/n, 08028 Barcelona, Spain

Keywords: Betic-Rif Arc; Eastern Betic Shear Zone; Carboneras Fault; Crustal deformation; Active faults; Geodynamics; GPS; Seismicity

Highlights

- We confirm a continuing tectonic activity of the Carboneras fault in SE Betics.
- The fault slips at a rate of 1.3±0.2 mm/yr with a left-lateral strike-slip kinematics.
- Geological and Geodetic slip-rates of the fault are in agreement.
- The Palomares fault is either inactive or is slipping with rate less than 0.5 mm/yr.
- The observed deformations are caused by the combination of the push and pull type forces.

Geodetic evidence for continuing tectonic activity of the Carboneras fault (SE Spain)

Anna Echeverria[1], Giorgi Khazaradze[1], Eva Asensio[1], Eulalia Masana[1]

[1]RISKNAT Group, Departament de Geodinàmica i Geofísica, Facultat de Geologia, Universitat de Barcelona (UB), Martí i Franquès s/n, 08028 Barcelona, Spain

Corresponding author:

Giorgi Khazaradze

Tel: +34934035913

(gkhazar@ub.edu)

Short title: Continuing activity of the Carboneras fault

Keywords: Betic-Rif Arc; Eastern Betic Shear Zone; Carboneras Fault; Crustal deformation; Active faults; Geodynamics; GPS; Seismicity

1. Introduction

GPS geodesy is a useful and efficient tool for identifying tectonically active faults or regions and for quantifying their deformation in terms of the slip and strain rates. Several studies based on permanent and non-permanent GPS networks (e.g. Alfaro et al., 2006; Echeverria et al., 2013; Garate et al., 2014; Gil et al., 2002) and high-precision levelling profiles have been carried out in SE Spain (e.g. Galindo-Zaldívar et al., 2013; Giménez et al., 2000; Marín-Lechado et al., 2005) revealing an on-going tectonic activity of this part of the Iberian Peninsula. However, in many cases the presented results were inconclusive, since in the presence of slow deformation (<2 mm/yr), a long period of observation is required to obtain statistically significant results.

In this paper, we focus on the Carboneras fault zone (CFZ) in SE Spain, which belongs to the NE-SW trending Eastern Betic Shear Zone (EBSZ) (Figure 1a). The EBSZ has been subject to a NNW-SSE oriented shortening with an associated ENE-WSW tension since Miocene (Alfaro et al., 2008; Galindo-Zaldívar et al., 1999). The compression has resulted in the activation of the EBSZ (Bousquet, 1979) and in folding, while the extension is expressed through a number of shorter NW-SE and WNW-ESE normal faults (see for example, AdF and BF faults in Figure 1b), especially in the central Betics (Galindo-Zaldivar et al., 2003) and to the west of the EBSZ, reaching Guadix-Baza basin (Alfaro et al., 2008). In the Iberian Peninsula, the EBSZ absorbs part of the convergence between the Eurasian and Nubian plates (Masana et al., 2004), which is of the order of 4 to 6 mm/yr in the NW direction (e.g. Argus et al., 2011; McClusky et al., 2003; Moreno, 2011; Serpelloni et al., 2007) (Figure 1b).

The CFZ is characterized by the highest geologic fault slip rates (according to the QAFI database, García-Mayordomo et al. (2012)) constrained to date in the Iberian

Peninsula. The estimated geologic slip rates at the CFZ range between 0.05-2 mm/yr depending on the utilized method and the covered time-period (Bell et al., 1997; Hall, 1983; Montenat et al., 1990; Moreno, 2011). The most recent paleoseismologic studies constrained the net-slip rate to 1.1-1.3 mm/yr for the Quaternary period (Moreno, 2011). The instrumental and historical seismicity related to the CFZ is scarce apart from the 1522 Almeria (MSK I=VIII-IX) earthquake that was probably generated by Carboneras offshore fault (Reicherter and Hübscher, 2007; Moreno, 2011). Recent paleoseismological studies (Moreno, 2011) provided evidence for the seismogenic nature of the CFZ by finding the record of the occurrence of surface rupturing earthquakes during late Pleistocene and Holocene.

The main objective of this paper is to present the contemporary crustal deformation velocity field of the Carboneras fault zone, with the aim of obtaining slip rates and comparing them to the mid-and-long-term geologic slip rates. The installation of the GATA GPS station has enabled us to obtain continuous observations from both sides of the fault and consequently, to quantify its slip rate. Apart from our preliminary results (Khazaradze et al., 2010) at the initial stage of the GATA operation, no quantitative estimates of the present-day geodetic slip rates of the CFZ have been previously published.

2. Active faults and seismicity

The south-eastern Betic Cordillera has gone through historical damaging earthquakes and shallow instrumental seismicity (Figure 2) with low to moderate magnitude earthquakes (e.g. Buforn et al., 1995; Stich et al., 2003a) .This seismicity is an evidence for the presence of on-going tectonic activity and active faults. The study area has a variety of faults (Figure 1), where two types of faults dominate: i) major strike-slip shear zones like the Alpujarras (AFZ) (Sanz de Galdeano et al., 1985) and the

Carboneras (CFZ) fault zones (e.g. Bousquet, 1979; Keller et al., 1995) and ii) normal faults of variable scale, oriented NNW-SSE to NW-SE (i.e. the Adra fault (Gràcia et al., 2012) and the Balanegra fault (see BF in Figure 1b) (e.g. Galindo-Zaldivar et al., 2003)). The CFZ is one of the longest continuous structures of the EBSZ, composed from north to south by the Bajo Segura, Carrascoy, Alhama de Murcia, Palomares and Carboneras faults. The 50 km long emerged portion of the CFZ is cut to the north by the Palomares fault (Gràcia et al., 2006) and continues offshore into the Alboran Sea for 100 km (Figure 1) (Moreno, 2011). The CFZ is a major crustal-scale fault and according to some authors can reach down the Moho (e.g. Pedrera et al., 2010). Soto et al. (2008) suggest that the CFZ reaches a domain with partial melting in the deepest crust. On the surface, the fault has a clear morphologic expression, changing its width along the fault trace from a single narrow trace to a 2 km wide fault zone (Moreno et al., 2008). Two first order segments are defined mainly based on changes in the fault trace orientation: the North Carboneras fault (NCF) and the South Carboneras fault (SCF) (Moreno, 2011) (Figure 1b). Another major strike-slip fault has been defined northwest from the CFZ, the Alpujarras fault zone (AFZ), composed by a number of E-W oriented right lateral strike-slip faults, suggested to behave as a transfer fault, active since the Miocene (Martínez-Díaz and Hernández-Enrile, 2004; Sanz de Galdeano et al., 2010). These major strike-slip faults separate domains affected by different structural evolution: the CFZ separates a thinned crust of Neogene volcanics of the Cabo de Gata in the eastern part (Figure 1) from tilted block domains (Neogene sediments and metamorphic basement of Internal Betics) in the western block (e.g. Martínez-Díaz and Hernández-Enrile, 2004; Pedrera et al., 2006; Rutter et al., 2012). In the central part, the AFZ separates the tilted block domain to the south from the Sierra Nevada elongated core-complex to the north (Martínez-Martínez, 2006).

The WNW-ESE to NW-SE Quaternary normal faults are encountered across the central and eastern Betics (Galindo-Zaldivar et al., 2003; Marín-Lechado et al., 2005; Pedrera et al., 2006). In addition to WNW-ESE normal faults, Gràcia et al. (2006) describe N-S oriented offshore normal faults on the northern block of CFZ. Many of these normal faults are found in the area bounded by the dextral AFZ and the sinistral CFZ (Figure 2). For this reason, several authors (e.g Giaconia et al., 2014; Martínez-Díaz and Hernández-Enrile, 2004; Martínez-Martínez et al., 2006; Sanz de Galdeano et al., 2010) have suggested that the CFZ and the AFZ strike-slip faults act in conjuntion with the normal faults. The CFZ and/or the AFZ have been interpreted as deeper transfer faults accommodating heterogeneous extension due to the shallower normal faults (Giaconia et al., 2014; Martínez-Martínez et al., 2006). Martínez-Díaz and Hernández-Enrile (2004) proposed a kinematic model, where a tectonic block bounded by both strike-faults escapes to the west and this way related the observed local extensional structures to the compressive tectonics.

The historical seismicity record of the EBSZ shows the presence of damaging earthquakes with a MSK intensity VIII-IX. Some of the notable examples include destructive earthquakes that affected the city of Almeria: in 1522 (I=VIII-IX), 1658 (I= VIII) and 1804 (I=VIII). The shallow (< 50 km depth) instrumental seismicity, covering a time period from 1926 to 2013, is characterized by low magnitude earthquakes, with no event larger than M_w5.0 (IGN catalogue, www.ign.es) (Figure 2). These earthquakes are usually related to minor faults (e.g. Martínez-Díaz and Hernández-Enrile, 2004) located within the crustal blocks bounded by the major faults, such as AFZ and CFZ (Figure 2). Rodríguez-Escudero et al. (2013) interpret the events with M_w<5 as part of the background seismicity, which can occur at any point within the crustal blocks bounded by the large E-W to NE-SW strike-slip faults. Precisely along these major faults (i.e. CFZ or AFZ) is where earthquakes of Mw>5.5 are expected by these authors. Although the instrumental seismicity that can be attributed to the CFZ is scarce, according to previous paleoseimological studies, the fault is capable of generating large earthquakes of M_w>7 (e.g. Gràcia et al., 2006; Moreno, 2011).

To facilitate the interpretation of the seismo-tectonic activity of the area, a database of earthquake moment tensors based on available literature and public catalogues was compiled (see Figure 2 and Table A1). The master catalogue used was the IAG Regional Moment Tensor catalogue (Stich et al., 2003a; Stich et al., 2010; Stich et al., 2006), since it was specifically created to perform time-domain moment tensor inversion of small to moderate events (m_b>3.5) in the Ibero-Maghreb area. In the cases where only the fault plane solutions were available, we used the MoPaD software (Krieger and Heimann, 2012) to obtain the moment tensor. The final catalogue has 37 focal mechanisms, from 1910 to 2013, with magnitudes ranging from M_w3.3 to 6.1. The 1910 Adra M_w6.1 earthquake (Stich et al., 2003b), the largest event in the catalogue, accounts for most (90%) of the total seismic moment release in the area. A majority of the focal mechanisms indicate normal or strike-slip kinematics (or a combination of both). The orientation of P and T axes, which was obtained with ObsPy software (Beyreuther et al., 2010) is similar for all the events (Figure 2). The average P axis is oriented N338º (NNW-SSE), roughly parallel to the plate convergence (Figure 1), and the T axis has an average orientation of ENE-WSW (N68º), compatible with the NW-SE normal faults.

3. GPS data and analysis

The geodetic study was carried out with continuous GPS stations (CGPS), including the new stations GATA (UB), NEVA and PALM (Topo-Iberia network) and survey mode GPS stations (SGPS) located in the study area from the CuaTeNeo network. The

CuaTeNeo geodetic network was built in 1996 and has been observed 5 times: 1997, 2002, 2006, 2009 and 2011 (Echeverria et al., 2013). The GATA continuous GPS station was installed in December 2008 as part of the *EVENT* Project with the specific objective of quantifying the present-day slip-rates of the CFZ (Khazaradze et al., 2010). The station was installed 2 km SW from the village of Rodalquilar in the Sierra de Cabo de Gata, ~200 m from CuaTeNeo campaign monument RELL. The GATA monumentation consists of the short drill brace type monument designed by UNAVCO (Figure 3), which consists of 4 solid stainless steel rods, anchored at least half a meter into the bedrock (Miocene volcanic rocks). This type of monumentation ensures a good long-term stability of the station. The monument is also equipped with the SCIGN type antenna adapter and a dome. The hardware includes the Leica GRX1200+GNSS receiver and the AT504GG choke-ring antenna, powered by an 80-watt solar panel. Since 2011, the station has experienced hardware problems, related to the malfunction of the solar power system and a GPRS modem (see gaps in the time series in Figure 3).

In total, we processed 4.5 yr data from 75 continuously recording GPS (CGPS) stations located both in eastern Betics and throughout Eurasia and Africa. GPS data were processed using GAMIT/GLOBK software 10.4 (Herring et al., 2010). The data analysis methodology is described in details in Echeverria et al. (2013) and Asensio et al. (2012). The time-span of the analysed data was nearly uniform, from 2008.8 to 2013.3, which equals to 4.5 yr of observations. According to Blewitt and Lavallé (2002) this time-span is sufficient to appropriately model the annual oscillations in the resulting time-series and achieve an optimal resolution of the velocity estimates. The formal errors were obtained firstly removing the annual signal and then applying the Real Sigma (RS) algorithm implemented in the GLOBK module (Herring, 2003). As a result, to obtain the final velocity solution and the error estimate, the estimated random walk through the RS algorithm was included for each component of the individual station (Reilinger et al., 2006; Shen et al., 2011). In order to validate the formal errors we compared the resulting uncertainties with the uncertainties calculated using the CATS software (Williams, 2008), where we estimate velocity uncertainties from the time-series using a model of an annual term, white noise and flicker noise. The mean difference between both models is 0.04 mm/yr for CGPS stations components for which the CATS analysis produced a valid estimate of uncertainty.

The ITRF2008 velocity field was rotated to western Europe reference frame as defined by Echeverria et al. (2013). The rotation was performed using the Velrot program included in GAMIT/GLOBK package (see stations in common used for the rotation in Table A2). The Velrot was also used to combine the SGPS station velocities of Echeverria et al. (2013) with the CGPS velocity field. The resulting average rms of the combination is 0.28 mm/yr, indicating a good adjustment.

4. Results

The present-day horizontal velocity field in the region of the Carboneras fault is shown in Figures 4 and 6 with numerical results provided in Table A2. The estimated velocities range between 1.1 and 3.1 mm/yr. As it would be expected, the stations located closer to the Nubia/Eurasia plate boundary, along the coast, move faster than the stations located farther inland (CUCO, CAAL and NEVA). As mentioned earlier, the overall convergence rate between Nubia/Eurasia plates is of the order of 4 to 6 mm/yr, which means that a significant portion of this overall budget is accommodating within the study area.

The most important feature of the obtained velocity field is a significant change in the orientation of the calculated velocities from east to west (Figure 4). In the western

Europe reference frame, the easternmost stations move at rates of 1.3-2.0 mm/yr in the direction of the Nubia (i.e. Africa)-Eurasia convergence. Stations located to the west, starting from HUEB SGPS station, show a more westerly-south-westerly motion, exhibiting a counter-clockwise rotation. The westernmost PALM and MOTR CGPS stations show the highest velocities (2.8±0.1 and 3.1±0.1 mm/yr, respectively) that are oriented south-west (Figure 4 and Table A2).

To assess the present-day slip-rates related to CFZ we constructed a velocity profile with a strike of 138º, perpendicular to the CFZ trace (Figures 4 and 5). Although there are only a few stations on each side of the fault, the differential motion between each group is evident and can be estimated. The analysis of the profile shows that the stations of the eastern block of CFZ move at 1.6-1.8 mm/yr with an azimuth of 325º (with respect to the western Europe reference frame). The nearest stations to the fault on the western block move at a rate of 1.5-1.9 mm/yr in an average direction of 280º.

To derive the geodetically estimated slip rate we assume that the differential motion between the two groups of stations, located on each side of the CFZ, is related solely to this fault. By projecting the velocities to the profile parallel and perpendicular direction, we obtain the compressive (ΔV_c) and strike-slip (ΔV_{ss}) fault slip-rate components, respectively. Only the strike-slip component shows a significant differential motion across the CFZ (Figure 5). To calculate the slip rate, we assume that each area behaves as a rigid block, without internal strain. This assumption is supported by the fact that the velocities of various stations located on each side of the fault are almost identical. Taking into account the velocity errors, we obtain a minimum and maximum values for ΔV_{ss} of 1.1 to 1.5 mm/yr, which are equivalent to a strike-slip rate of 1.3±0.2 mm/yr. The fault-normal (i.e. profile parallel) compression (ΔV_c) across the CFZ is less statistically insignificant. On the other hand, if we exclude a northerly motion of the station ALMR from the calculations and only consider ALME and HUEB stations, we can obtain a statistically significant compressive slip rate of 0.4±0.2 mm/yr. As a result, taking into account the sparse spatial coverage of the stations and disregarding ALMR (discussion in the next chapter), we can only conclude that the compressive motion (ΔV_c) across the CFZ is considerably less than the strike-slip motion and it should not exceed 0.6 mm/yr.

5. Discussion and implications

In this work, for the first time, we were able to quantify the present-day horizontal crustal deformation rates of the Carboneras fault zone, using continuous and campaign GPS observations conducted during the last decade. The almost identical velocity vectors observed at two closely located stations (GATA (CGPS, 4.5 yr processed) and RELL (SGPS, 15 yr processed)) are an evidence of the high accuracy of the presented results. This good agreement between the two independent observations also reaffirms the usefulness of the campaign-style GPS observations, even when the deformations are slow, like in eastern Betics. By contrast, two other stations located on the opposite side of the CFZ in Almeria: ALME and ALMR exhibit significant differential motion, which is likely due to the instability of the monuments or the buildings (including the surrounding ground) where these stations are emplaced. In addition, since these stations are somewhat farther from the CFZ, the calculated velocities could be affected by other minor faults (e.g. NW-SE normal faults), thus causing the observed variation in the GPS velocities. We assumed, however, that the vectors calculated for these two stations are due to the CFZ since the movement observed at ALMR and ALME is similar to the velocity of the HUEB station, located on the same side of the CFZ but farther to the east (Figures 4 and 6). It should be mentioned that the ALME and ALMR stations, unlike the Topo-Iberia and CuaTeNeo networks and GATA station, were build for the purpose of satisfying surveying needs of the local community, but not for measuring sub-millimetre level tectonic deformations.

The obtained horizontal velocity field for the SE Betics confirms the continuing tectonic activity, at least, of the on-shore section of the northern segment of the Carboneras fault (see NCF in Figure 1b). We find that the left-lateral motion dominates the kinematics of the CFZ, with a strike-slip rate of 1.3±0.2 mm/yr along N48º direction. The shortening component is significantly lower and poorly constrained (ΔV_c=0.4±0.2 mm/yr without ALMR). Thus, the GPS measurements suggest a dominance of the strike-slip motion in the transpressional kinematics of the CFZ, coherent with a positive flower structure in La Serrata (e.g.Moreno, 2011; Reicherter and Reiss, 2001). The GPS derived geodetic fault slip rates presented here can be considered as maximum values, since we assumed that all the observed differential motion is solely due to the CFZ and no possibility of the distributed deformation due to secondary faults was considered. The most recent study, integrating both onshore and offshore paleoseismic and geomorphologic results, using the youngest faulted features, obtain the minimum Quaternary strike-slip rates between 1.1 and 1.3 mm/yr (Moreno, 2011). These results are in good agreement with the geodetic slip rates presented in this work, suggesting that most of the deformation registered by GPS can be attributed solely to the activity of the CFZ. Combining the geologic (minimum values) and geodetic (maximum values) slip rates, we can conclude that the strike-slip rate of the CFZ must be enclosed between the minimum geologic slip rate of 1.1 mm/yr and the maximum geodetic slip rate of 1.5 mm/yr. The slip rates obtained by Moreno (2011) are mainly based on deflected geomorphological and young buried gullies onshore and offshore along the northern segment of the Carboneras fault (NCF) and cover different Quaternary geologic periods. Considering the similarity of paleoseismic and geodetic slip rates measured at different points along the NCF segment, the slip rate of the entire NCF must be approximately constant during the Quaternary.

We calculated the strain rate field (Figure 6) by the inversion of the GPS data using SSPX software (Cardozo and Allmendinger, 2009) for the 6 GPS stations located on both sides of the CFZ. Horizontal principal strain rate axes obtained at the centre of these 6 stations show a predominance of a compressive strain rate: $\dot{\varepsilon}_{min}$= -26.2±8 nstrain/yr oriented N354º. The extensional component is less: $\dot{\varepsilon}_{max}$ of 18.1±7 nstrain/yr with an azimuth of N84º. The orientation of the geodetic compressive and extensive strain rate axes is in agreement with the N338º and N68º orientation of the mean P-T axes that we obtain from the earthquake focal mechanisms (Figure 2). The resulting left-lateral shear plane of the maximum shear strain rate ($\dot{\varepsilon}_{sh-max}$) has an orientation of N39º, sub-parallel to the CFZ trace (N48º). Unfortunately, due to the poor spatial distribution of the GPS stations, we cannot discern with certainty whether the accumulated strain is released aseismically (e.g. as a creep) or the fault is locked and is being loaded for the occurrence of the earthquake. However, taking into account the paleoseismological results that show evidence of repetitive large paleoearthquakes along the CFZ (e.g. Gràcia et al., 2006; Moreno, 2011), a locked fault scenario seems more plausible. In contrast, Faulkner et al. (2003) suggest a mixed mode fault slip behaviour (when fault creep is interspersed with seismic locking) for the CFZ, drawing an analogy with the Parkfield section of the San Andreas fault. The clarification of the issue of seismic or aseismic behaviour of the CFZ is crucial for the seismic hazard calculations and thus, the future studies should include the densification of the measurements along the fault-perpendicular profile.

The north-eastern termination of the CFZ continues into the Palomares fault (PF), a sinistral strike-slip fault oriented N-S (Figures 1 and 6). The velocities of the stations at the south-eastern block of the CFZ (GATA, RELL and CARB) and the western block of PF (CUCO and MOJA) show no appreciable differential motion (Figure 6). This fact suggests that the on-going horizontal tectonic activity of the PF is either undetectable by the current GPS measurements or is simply inexistent. This conclusion is based on the assumption that the eastern part of the CFZ (with stations GATA, RELL and CARB) and the eastern part of the PF, where no GPS stations are present, belong to the same block. The lack of differential motion across the PF is especially clear when examining the relative motion between the CARB and MOJA stations (Figure 6). However, it should be mentioned that some authors do attribute a tectonic activity to the PF, but the suggested slip-rates are of the order of sub-millimetre per year (e.g. Booth-Rea et al., 2004; García-Mayordomo and Jiménez-Díaz, 2010) and are not detectable using the current GPS station spatial and temporal coverage.

In order to ease the interpretation of the CFZ kinematics we fix GATA in Figure 6, instead of using a western Europe fixed reference frame used in Figure 4. The transformed GPS velocities show a clearly opposite sense of kinematics across the Alpujarras and the Carboneras fault zones. The former shows right-lateral motion (CAAL-CUCO stations move to the south while HUEB to the south-west) while the latter shows left-lateral motion (compare GATA-RELL to HUE-ALMR-ALME stations). Martínez-Díaz and Hernández-Enrile (2004) proposed that this type of movement of the AFZ and CFZ induces a westward tectonic escape of the wedge bounded by these two strike-slip faults (Figure 7). The existence of a gradient of deformation in the escaping block favours the formation or reactivation of NNW-SSW normal faults perpendicular to the east-west extensional motion of the block. The observed W-SW gradually increasing motion of the GPS stations located in this escaping block fits well with this model (Figures 4 and 6). However, the picture is more complex. East-to-west increase in the southward motion of the stations located north of the AFZ in GATA fixed reference frame (compare NEVA with CAAL or CUCO in Figure 6) and an apparent counter-clockwise rotation of the stations belonging to the escaping block (compare the stations GATA, HUEB, ALME, PALM and MOTR in Figures 4 and 6) cannot be satisfactorily explained by the convergence of the Nubia plate, resulting in a block escape. Simple *push* cannot cause neither a rotation nor an apparent east to west acceleration in the observed GPS velocities. We hypothesize that in order to satisfactorily explain this complex kinematics of the crustal deformation, it is necessary to introduce an additional *pulling* force. Considering the proximity of the oceanic slab in depth (Figure 1a and Figure 7), which is located further west and possibly attached to the continental crust in central Betics and eastern Rif (e.g. Bonnin et al., 2014), sub-lithospheric processes such as a rollback of the subducting slab, can hypothetically be responsible for such a pull. An observed change in the motion of the GPS velocities, starting from the location of station HUEB (2.5°W, Figures 4 and 6), approximately the same area where a significant east-to-west increase of the lithospheric thickness is deduced from seismic studies (Levander et al., 2014). On a more regional scale, Pérouse et al. (2010), combined GPS data with numerical modelling, and suggested a combined effect of plate convergence, low rigidity of the Alboran Sea region and a S-SW directed traction related to sub-lithospheric processes, as an explanation for the regional geodynamics. In our simplified kinematic model (Figure 7), we propose that the Carboneras fault zone acts as a boundary between the eastern block that moves parallel to the plate convergence and the western block that moves westward due to the block escape and deeper sub-lithospheric processes. For this reason, an area affected by deeper sub-lithospheric processes (shaded region in Figure 7) does not extend south of the CFZ. This assumption can be supported by the description of the CFZ as a major crustal-scale fault that reaches the Moho (e.g. Pedrera et al., 2010).

6. Conclusions

The analysis of the GPS data in the SE Betics, confirm and quantify the on-going tectonic activity of the onshore CFZ as a left-lateral strike slip fault. For the first time, we were able to provide a quantitative measure of the present-day horizontal geodetic slip-rate of the CFZ, suggesting a maximum left-lateral strike slip motion of 1. 3°W ±0.2 mm/yr. The coincidence of the geologic and geodetic strike-slip rates along the CFZ, illustrate that during Quaternary the northern segment of the CFZ has been tectonically active and has been slipping at a rate of 1.1 to 1.5 mm/yr that might have been constant. Further investigations should concentrate in determining the nature of the strain accumulation along the CFZ (e.g. creep vs. locking), since this question is crucial for the improved seismic hazard calculation in the area.

We have also found that the Palomares fault (PF) in the NW of the study area, is currently inactive or is slipping very slowly (< 0.5 mm/yr), at rates that are undetectable by the current GPS station spatial-temporal coverage. Regarding the eastern part of the Alpujarras fault zone corridor (AFZ), our GPS measurements corroborate that this zone is active and accumulates a right-lateral motion to compensate for the observed left-lateral motion of the CFZ. These opposite type strike-slip motion across the AFZ and CFZ is a result of a push-type force due to Nubia and Eurasia plate convergence, that results in the westward escape of the block bounded by these faults. However, in order to explain the observed gradually increasing westerly motion and counter-clockwise rotation of the GPS stations located west of longitude 2.5°W we propose the (?) existence of pull-type forces that are caused by a complex deep sub-lithospheric processes. Although the area directly affected by the presence of the subducting oceanic lithosphere (see Figures 1a and 7) does not reach the study area, we believe that its far-field effect can explain the presented GPS velocities. The implications of the presented results and the simplified model in terms of the regional geodynamics will require further investigations, that should employ the combination of various geophysical and geological data, as well, as numerical modelling.

Acknowledgments

The Topo-Iberia (CSD2006-00041), EVENT (CGL2006-12861-C02-01) and CuaTeNeo (CGL2004-21666-E) projects of the Spanish government funded this research. A. E. was supported by the APIF pre-doctoral grant of the University of Barcelona, and E. A. by the FPU pre-doctoral grant (AP-2008-01482) of the Spanish Ministry of Education. We would also like to acknowledge the institutions responsible for the operation of the continuous GPS stations: IGN, ROA, EUREF, IGS, RAP. Most graphics are from GMT software (Wessel and Smith, 1991). We are thankful to Klaus Reicherter for his helpful comments on the earlier version of this manuscript.

References

Alfaro, P., Delgado, J., de Galdeano, C.S., Galindo-Zaldívar, J., García-Tortosa, F.J., López-Garrido, A.C., López-Casado, C., Marín-Lechado, C., Gil, A., Borque, M.J., 2008. The Baza Fault: a major active extensional fault in the central Betic Cordillera (south Spain). Int. J. Earth Sci. 97(6), 1353-1365. http://dx.doi.org/10.1007/s00531-007-0213-z.

Alfaro, P., Estévez, A., Blázquez, E.B., Borque, M.J., Garrido, M.S., Gil, A.J., Lacy, M.C., Ruiz, A.M., Giménez, J., Molina, S., Rodríguez-Caderot, G., Ruiz-Morales, M., Sanz de Galdeano, C., 2006. Geodetic Control of the Present Tectonic Deformation of the Betic Cordillera (Spain), in: Sansò, F., Gil, A.J. (Eds.), Geodetic Deformation Monitoring: From Geophysical to Engineering Roles. Springer Berlin Heidelberg, pp. 209-216.

Argus, D.F., Gordon, R.G., Demets, C., 2011. Geologically current motion of 56 plates relative to the no-net-rotation reference frame. Geochem. Geophys. Geosyst. 12(11). http://dx.doi.org/10.1029/2011GC003751.

Asensio, E., handadze, G., Echeverria, A., King, R.W., Vilajosana, I., 2012. GPS studies of active deformation in the Pyrenees. Geophys. J. Int. 190(2), 913-921. http://dx.doi.org/10.1111/j.1365-246X.2012.05525.x.

Bell, J.W., Amelung, F., King, G.C.P., 1997. Preliminary late quaternary slip history of the Carboneras fault, southeastern Spain. J. Geodyn. 24(1-4), 51-66.

Beyreuther, M., Barsch, R., Krischer, L., Megies, T., Behr, Y., Wassermann, J., 2010. ObsPy: A Python Toolbox for Seismology. Seismol. Res. Lett. 81(3), 530-533. http://dx.doi.org/10.1785/gssrl.81.3.530.

Blewitt, G., Lavallée, D., 2002. Effect of annual signals on geodetic velocity. J. Geophys. Res. 107(7), 9-1. http://dx.doi.org/10.1029/2001JB000570

Bonnin, M., Nolet, G., Villaseñor, A., Gallart, J., Thomas, C., 2014. Multiple-frequency tomography of the upper mantle beneath the African/Iberian collision zone. Geophys. J. Int. 198(3), 1458-1473. http://dx.doi.org/10.1093/gji/ggu214.

Booth-Rea, G., Azañón, J.M., Azor, A., García-Dueñas, V., 2004. Influence of strike-slip fault segmentation on drainage evolution and topography. A case study: The Palomares Fault Zone (southeastern Betics, Spain). J. Struct. Geol. 26(9), 1615-1632.

Bousquet, J.C., 1979. Quaternary strike-slip faults in southeastern Spain. Tectonophysics 52, 277-286.

Buforn, E., Sanz de Galdeano, C., Udías, A., 1995. Seismotectonics of the Ibero-Maghrebian region. Tectonophysics 248(3-4), 247-261.

Cardozo, N., Allmendinger, R.W., 2009. SSPX: A program to compute strain from displacement/velocity data. Computers and Geoscinces 35(6), 1343-1357. http://dx.doi.org/10.1016/j.cageo.2008.05.008.

Echeverria, A., Khazaradze, G., Asensio, A., Gárate, J., Dávila, J.M., Suriñach, E., 2013. Crustal deformation in eastern Betics from CuaTeNeo GPS network. Tectonophysics 608, 600-612. http://dx.doi.org/10.1016/j.tecto.2013.08.020.

Faulkner, D.R., Lewis, A.C., Rutter, E.H., 2003. On the internal structure and mechanics of large strike-slip fault zones; field observations of the Carboneras Fault in southeastern Spain. Tectonophysics 367(3-4), 235-251.

Galindo-Zaldívar, J., Borque, M.J., Pedrera, A., Marín-Lechado, C., Gil, A.J., López-Garrido, A.C., 2013. Deformation behaviour of the low-rate active Balanegra Fault Zone from high-precision levelling (Betic Cordillera, SE Spain). J. Geodyn. 71, 43-51. http://dx.doi.org/http://dx.doi.org/10.1016/j.jog.2013.07.003.

Galindo-Zaldivar, J., Gil, A.J., Borque, M.J., González-Lodeiro, F., Jabaloy, A., Marin-Lechado, C., Ruano, P., Sanz de Galdeano, C., 2003. Active faulting in the internal zones of the central Betic Cordilleras (SE, Spain) J. Geodyn. 36(1-2), 239-250.

Galindo-Zaldívar, J., Jabaloy, A., Serrano, I., Morales, J., González-Lodeiro, F., Torcal, F., 1999. Recent and present-day stresses in the Granada Basin (Betic Cordilleras): Example of a late Miocene-present-day extensional basin in a convergent plate boundary. Tectonics 18, 686-702.

Garate, J., Martin-Davila, J., Khazaradze, G., Echeverria, A., Asensio, E., Gil, A.J., de Lacy, M.C., Armenteros, J.A., Ruiz, A.M., Gallastegui, J., Alvarez-Lobato, F., Ayala, C., Rodríguez-Caderot, G., Galindo-Zaldívar, J., Rimi, A., Harnafi, M., 2014. Topo-Iberia project: CGPS crustal velocity field in the Iberian Peninsula and Morocco. GPS Solutions, 1-9. http://dx.doi.org/10.1007/s10291-014-0387-3.

García-Mayordomo, J., Insua-Arévalo, J.M., Martínez-Díaz, J.J., Jiménez-Díaz, A., Martín-Banda, R., Martín-Alfageme, S., Álvarez-Gómez, J.A., Rodríguez-Peces, M., Pérez-López, R., Rodríguez-Pascua, M.A., Masana, E., Perea, H., Martín-González, F., Giner-Robles, J., Nemser, E.S., Cabral, J., 2012. The Quaternary active faults database of Iberia (QAFI v.2.0). J. Iberian Geol. 38(1), 285-302.

García-Mayordomo, J., Jiménez-Díaz, A., 2010. Palomares: Carboneras-Sierra de Almenara (ES609), In: Quaternary Active Faults Database of Iberia v.2.0 - December 2011 (García-Mayordomo et al., eds.), IGME, Madrid.

Giaconia, F., Booth-Rea, G., Martínez-Martínez, J.M., Azañón, J.M., Storti, F., Artoni, A., 2014. Heterogeneous extension and the role of transfer faults in the development of the southeastern Betic basins (SE Spain). Tectonics, 33. http://dx.doi.org/10.1002/2014tc003681.

Gil, A.J., Rodriguez, C.G., Lacy, M.C., Ruiz, A.M., Sanz, d.G.C., Alfaro, P., 2002. Establishment of a non-permanent GPS network to monitor the recent NE-SW deformation in the Granada Basin (Betic Cordillera, southern Spain). Studia Geophysica et Geodetica 46(3), 395-410 (doi:310.1023/A:1019530716324).

Giménez, J., Suriñach, E., Goula, X., 2000. Quantification of vertical movements in the eastern Betics (Spain) by comparing levelling data. Tectonophysics 317, 237-258. http://dx.doi.org/10.1016/S0040-1951(99)00318-2.

Gràcia, E., Bartolomé, R., Lo Iacono, C., Moreno, X., Stich, D., Martínez-Diaz, J.J., Bozzano, G., Martínez-Loriente, S., Perea, H., Diez, S., 2012. Acoustic and seismic imaging of the Adra Fault (NE Alboran Sea): in search of the source of the 1910 Adra earthquake. Nat. Hazards Earth Syst. Sci. 12, 3255-3267. http://dx.doi.org/10.5194/nhess-12-3255-2012.

Gràcia, E., Pallas, R., Soto Juan, I., Comas, M., Moreno, X., Masana, E., Santanach, P., Diez, S., Garcia, M., Danobeitia, J., Bartolome, R., Farran, M., Gomez, M., Alpiste, M.J.R., Lastras, G., Wilmott, V., Perea, H., Blondel, P., Gomez, O., Bullock, L., Jacobs, C., Rouse, I., White, D., Whittle, S., Terrinha, P., Gafeira, J., Roque, C., Hits Scientific Party, I., 2006. Active faulting offshore SE Spain (Alboran Sea); implications for earthquake hazard assessment in the southern Iberian margin. Earth Planet. Sci. Lett. 241(3-4), 734-749. http://dx.doi.org/10.1016/j.epsl.2005.11.009.

Hall, S.H., 1983. Post Alpine tectonic evolution of SE Spain and the structure of fault gouges. PhD Thesis, Imperial College London (University of London)

Herring, T., 2003. MATLAB Tools for viewing GPS velocities and time series. GPS Solutions 7(3), 194 - 199. http://dx.doi.org/10.1007/s10291-003-0068-0.

Herring, T.A., King, R.W., McClusky, S.C., 2010. Introduction to GAMIT/GLOBK. Department of Earth, Atmospheric, and Planetary Sciences. Massachusetts Institute of Technology, p. 48

Keller, J.V.A., Hall, S.H., Dart, C.J., McClay, K.R., 1995. The geometry and evolution of a transpressional strike-slip system; the Carboneras Fault, SE Spain. J. Geol. Soc. London 152(Part 2), 339-351.

Khazaradze, G., Moreno, X., Asensio, E., & Masana, E. (2010). Geodetic evidence for a present-day activity of the Carboneras fault in the Eastern Betics. In J. M. Insúa & F. Martín-González (Eds.), Contribución de la Geología al Análisis de la Peligrosidad Sísmica (pp. 93–96). Madrid, Spain: IGME.

Krieger, L., Heimann, S., 2012. MoPaD - Moment Tensor Plotting and Decomposition: A Tool for Graphical and Numerical Analysis of Seismic Moment Tensors. Seismol. Res. Lett. 83(3), 589-595. http://dx.doi.org/10.1785/gssrl.83.3.589.

Levander, A., Bezada, M.J., Niu, F., Humphreys, E.D., Palomeras, I., Thurner, S.M., Masy, J., Schmitz, M., Gallart, J., Carbonell, R., Miller, M.S., 2014. Subduction-driven recycling of continental margin lithosphere. Nature 515(7526), 253-256. http://dx.doi.org/10.1038/nature13878.

Marín-Lechado, C., Galindo-Zaldívar, J., Rodríguez-Fernández, L.R., Serrano, I., Pedrera, A., 2005. Active faults, seismicity and stresses in an internal boundary of a tectonic arc (Campo de Dalías and Níjar, southeastern Betic Cordilleras, Spain). Tectonophysics 396(1-2), 81-96. http://dx.doi.org/10.1016/j.tecto.2004.11.001.

Martínez-Díaz, J.J., Hernández-Enrile, J.L., 2004. Neotectonics and morphotectonics of the southern Almería region (Betic Cordillera-Spain) kinematic implications. Int. J. Earth Sci. 93(2), 189-206. http://dx.doi.org/10.1007/s00531-003-0379-y.

Martínez-Martínez, J.M., Booth-Rea, G., Azañón, J.M., Torcal, F., 2006. Active transfer fault zone linking a segmented extensional system (Betics, southern Spain): Insight into heterogeneous extension driven by edge delamination. Tectonophysics 422(1-4), 159-173.

Masana, E., Martínez-Díaz, J.J., Hernández-Enrile, J.L., Santanach, P., 2004. The Alhama de Murcia fault (SE Spain), a seismogenic fault in a diffuse plate boundary: Seismotectonic implications for the Ibero-Magrebian region. J. Geophys. Res. 109(B01301). http://dx.doi.org/10.1029/2002JB002359.

McClusky, S., Reilinger, R., Mahmoud, S., Ben Sari, D., Tealeb, A., 2003. GPS constraints on Africa (Nubia) and Arabia plate motions. Geophys. J. Int. 155(1), 126-138. http://dx.doi.org/10.1046/j.1365-246X.2003.02023.x.

Montenat, C., D'Estevou, P.O., La Chappelle, G., 1990. Le Bassin de Nijar-Carboneras et le Couloir du Bas-Andarax, Documents et Travaux. Intitute de Geologique Albert de Lapparent 12, 129-164.

Moreno, X., 2011. Neotectonic and Paleoseismic Onshore-Offshore integrated study of the Carboneras Fault (Eastern Betics, SE Iberia). PhD thesis, Universitat de Barcelona, Barcelona, p. 365

Moreno, X., Masana, E., Gràcia, E., Bartolomé, R., Piqué-Serra, O., 2008. Estudio paleosismológico de la Falla de Carboneras: Evidencias tierra-mar de actividad tectónica reciente. GeoTemas 10, 1035-1038.

Pedrera, A., Mancilla, F.D.L., Ruiz-Constán, A., Galindo-Zaldívar, J., Morales, J., Arzate, J., Marín-Lechado, C., Ruano, P., Buontempo, L., Anahnah, F., Stich, D., 2010. Crustal-scale transcurrent fault development in a weak-layered crust from an integrated geophysical research: Carboneras Fault Zone, eastern Betic Cordillera, Spain. Geochem. Geophys. Geosyst. 11(12).

Pedrera, A., Marín-Lechado, C., Galindo-Zaldívar, J., Rodríguez-Fernández, L.R., Ruiz-Constán, A., 2006. Fault and fold interaction during the development of the Neogene-Quaternary Almería-Níar basin (SE Betic Cordilleras), Geol. Soc. Spec. Pub., pp. 217-230

Pérouse, E., Vernant, P., Chéry, J., Reilinger, R., McClusky, S., 2010. Active surface deformation and sub-lithospheric processes in the western Mediterranean constrained by numerical models. Geology 38(9), 823-826.

Reicherter, K., Hübscher, C., 2007. Evidence for a seafloor rupture of the Carboneras Fault Zone (southern Spain): Relation to the 1522 Almería earthquake? J. Seismol. 11(1), 15-26. http://dx.doi.org/10.1007/s10950-006-9024-0.

Reicherter, K.R., Reiss, S., 2001. The carboneras fault zone (Southeastern Spain) revisited with ground penetrating radar - Quaternary structural styles from high-resolution images. Geologie en Mijnbouw/Netherlands Journal of Geosciences 80(3-4), 129-138.

Reilinger, R., McClusky, S., Vernant, P., Lawrence, S., Ergintav, S., Cakmak, R., Ozener, H., Kadirov, F., Guliev, I., Stepanyan, R., Nadariya, M., Hahubia, G., Mahmoud, S., Sakr, K., ArRajehi, A., Paradissis, D., Al-Aydrus, A., Prilepin, M., Guseva, T., Evren, E., Dmitrotsa, A., Filikov, S.V., Gomez, F., Al-Ghazzi, R., Karam, G., 2006. GPS constraints on continental deformation in the Africa-Arabia-Eurasia continental collision zone and implications for the dynamics of plate interactions. J. Geophys. Res. 111(B5), 26. http://dx.doi.org/10.1029/2005JB004051.

Rodríguez-Escudero, E., Martínez-Díaz, J.J., Álvarez-Gómez, J., Insua-Arévalo, J.M., Capote del Villar, R., 2013. Tectonic setting of the recent damaging seismic series in the Southeastern Betic Cordillera, Spain. Bull. Earthquake Eng. 12, 1-24. http://dx.doi.org/10.1007/s10518-013-9551-3.

Rutter, E.H., Faulkner, D.R., Burgess, R., 2012. Structure and geological history of the Carboneras Fault Zone, SE Spain: Part of a stretching transform fault system. J. Struct. Geol. 45, 68-86. http://dx.doi.org/10.1016/j.jsg.2012.08.009.

Sanz de Galdeano, C., Rodriguez Fernandez, J., López Garrido, A.C., 1985. A strike-slip fault corridor within the Alpujarra Mountains (Betic Cordilleras, Spain). Geol. Rundsch. 74, 641-655.

Sanz de Galdeano, C., Shanov, S., Galindo-Zalívar, J., Radulov, A., Nikolov, G., 2010. A new tectonic discontinuity in the Betic Cordillera deduced from active tectonics and seismicity in the Tabernas Basin. J. Geodyn. 50(2), 57-66. http://dx.doi.org/10.1016/j.jog.2010.02.005.

Serpelloni, E., Vannucci, G., Pondrelli, S., Argnani, A., Casula, G., Anzidei, M., Baldi, P., Gasperini, P., 2007. Kinematics of the western Africa-Eurasia plate boundary from focal mechanisms and GPS data. Geophys. J. Int. 169(3), 1180-1200. http://dx.doi.org/10.1111/j.1365-246X.2007.03367.x.

Shen, Z.K., King, R.W., Agnew, D.C., Wang, M., Herring, T.A., Dong, D., Fang, P., 2011. A unified analysis of crustal motion in Southern California, 1970-2004: The SCEC crustal motion map. J. Geophys. Res. 116(B11), B11402. http://dx.doi.org/10.1029/2011jb008549.

Soto, J.I., Fernández-Ibáñez, F., Fernández, M., García-Casco, A., 2008. Thermal structure of the crust in the Gibraltar Arc: Influence on active tectonics in the western Mediterranean. Geochem. Geophys. Geosyst. 9(10), 27.

Stich, D., Ammon, C.J., Morales, J., 2003a. Moment tensor solutions for small and moderate earthquakes in the Ibero-Maghreb region. J. Geophys. Res. 108(B3), 1972-2012. http://dx.doi.org/10.1029/2002JB002057.

Stich, D., Batlló, J., Morales, J., Macià , R., Dineva, S., 2003b. Source parameters of the MW= 6.1 1910 Adra earthquake (southern Spain). Geophys. J. Int. 155(2), 539-546. http://dx.doi.org/10.1046/j.1365-246X.2003.02059.x.

Stich, D., Martín, R., Morales, J., 2010. Moment tensor inversion for Iberia-Maghreb earthquakes 2005-2008. Tectonophysics 483, 390-398. http://dx.doi.org/10.1016/j.tecto.2009.11.006.

Stich, D., Serpelloni, E., Mancilla, F., Morales, J., 2006. Kinematics of the Iberia-Maghreb plate contact from seismic moment tensors and GPS observations. Tectonophysics 426(3-4), 295-317. http://dx.doi.org/10.1016/j.tecto.2006.08.004.

Wessel, P., Smith, W.H.F., 1991. Free software helps map and display data. Eos Trans. AGU 72(41), 441. http://dx.doi.org/10.1029/90EO00319.

Williams, S., 2008. CATS: GPS coordinate time series analysis software. GPS Solutions 12(2), 147-153.

Figure captions

Figure 1. Simplified neotectonic map of the Betic-Rif arc. A) Regional setting. Arcuate shaped shaded region in Figure 1b indicates an approximate location of the high-velocity seismic anomaly at 135 km depth, according to the seismic tomography model (Bonnin et al., 2014). B) Study area. Quaternary active faults are from Gràcia et al. (2012) and QAFI database (García-Mayordomo et al., 2012). A thick arrow indicates a convergence between Nubia and Eurasia plates. Abbreviations: EBSZ: Eastern Betic Shear Zone; AFZ: Alpujarras fault zone; CFZ: Carboneras fault zone; NFCZ and SFCZ: North and South Carboneras fault segments; PF: Palomares fault; BF: Balanegra fault; AF: Adra fault. An included legend is common for the both figures.

Figure 2. Seismotectonic map of the study area showing the seismicity from IGN catalogue (1926-2013) with depths ranging from 0 to 50 km (www.ign.es). Historical seismicity (white triangles) are from IGN catalogue and are labelled by the year of occurrence. P and T axes of the focal mechanisms (Table A1) are shown as grey and white dots, respectively. Stereographic projection of the P and T axes orientations for the displayed focal mechanisms are included in the upper left corner of the figure.

Figure 3. SDBM type monument and time-series of GATA CGPS station, installed in December of 2008. North-south (top) and east-west (bottom) components with 1σ errors are given in global ITRF2008 reference frame.

Figure 4. GPS velocities with 95% confidence error ellipses in western Europe reference frame. Plate convergence velocity from NNR-MORVEL56 model (Argus et al., 2011). CGPS and SGPS stations shown in black and dark grey, respectively. Stations included in A-A' profile (Figure 5) are marked by an asterisk.

Figure 5. A-A' profile perpendicular velocities with 1σ error bars. Location of the profile is shown in Fig. 4. Topography is represented with an irregular line on the bottom. ΔV_{ss} is the fault parallel strike-slip differential motion (velocity offset) between the two blocks. The intersection of the CFZ trace with the profile is shown as short dashed vertical line on the topographic profile.

Figure 6. Map of the GPS horizontal velocities in GATA-fixed reference frame. Calculated strain rates determined at the centre of the 6 stations (marked by an asterisk) are shown as a white cross.

Figure 7. Simplified sketch of a proposed kinematic model. GPS velocities are given with respect to the GATA station. Block escape due to combined movement of CFZ and AFZ is shown in light gray. Striped area, extending to the east up to a longitude 2.5ºW and limited by the CFZ to the southeast, delimits an area possibly affected by deeper sub-lithospheric processes.

Figure 1
Click here to download high resolution image

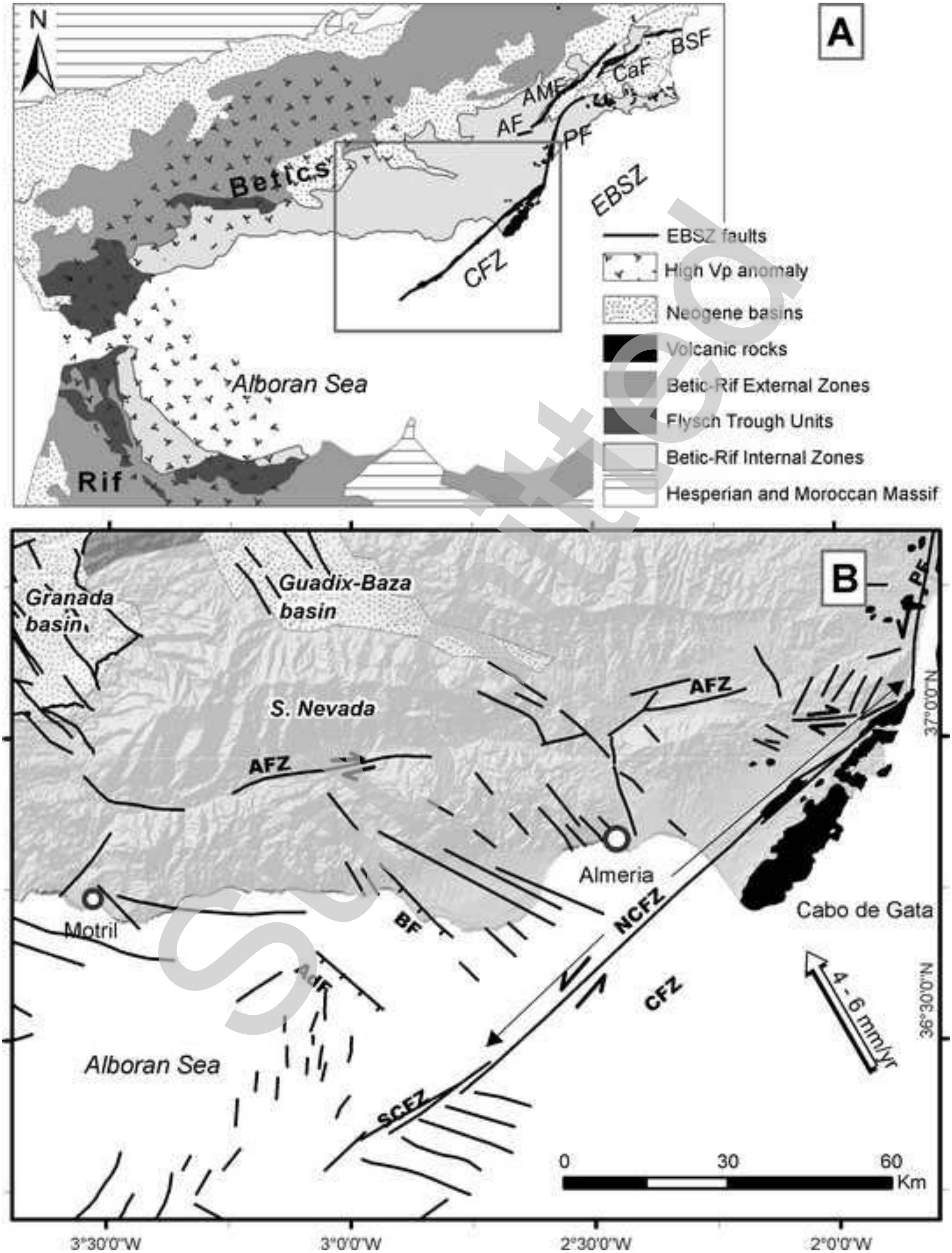

Figure 2
Click here to download high resolution image

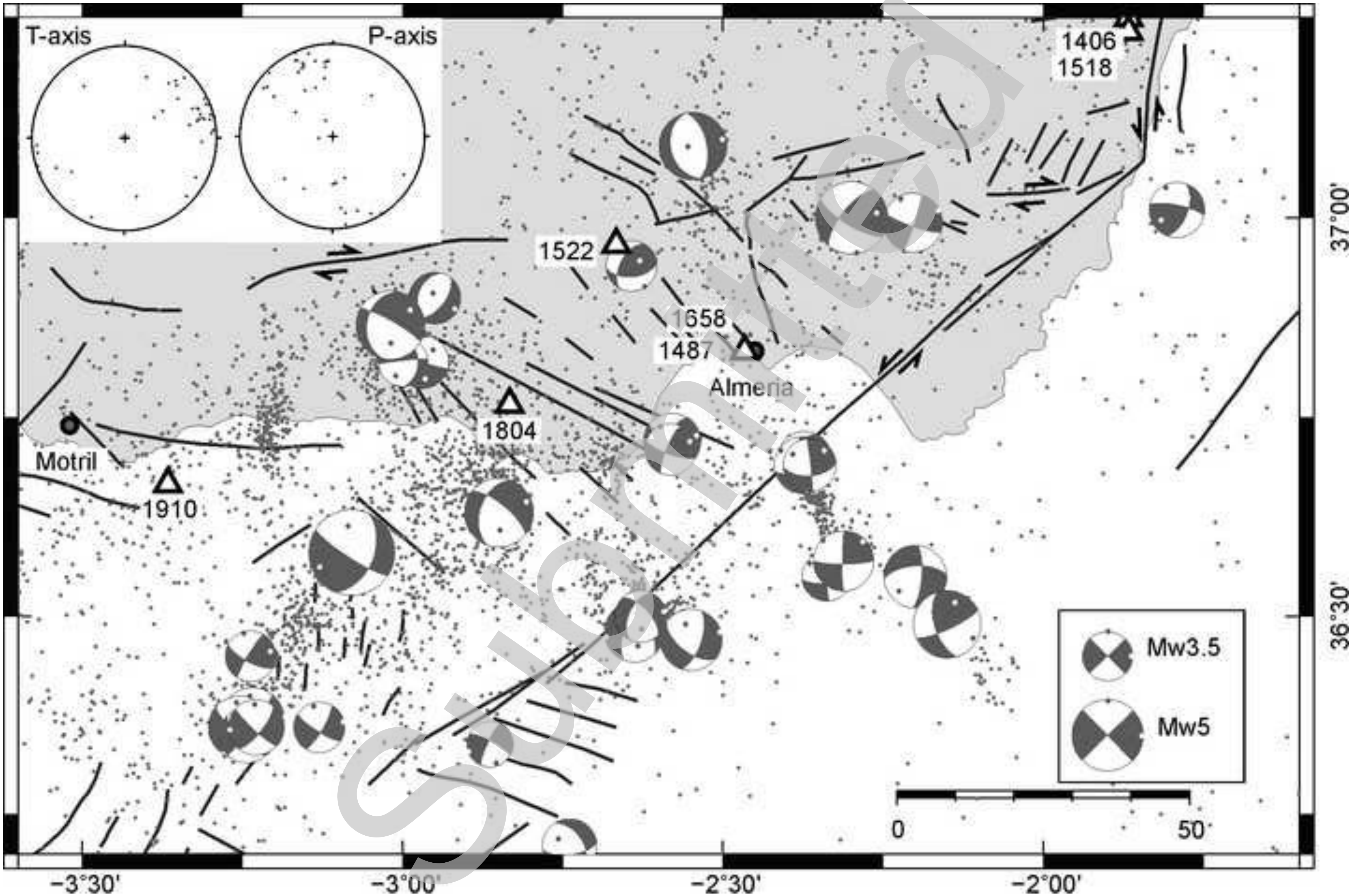

Figure 3
Click here to download high resolution image

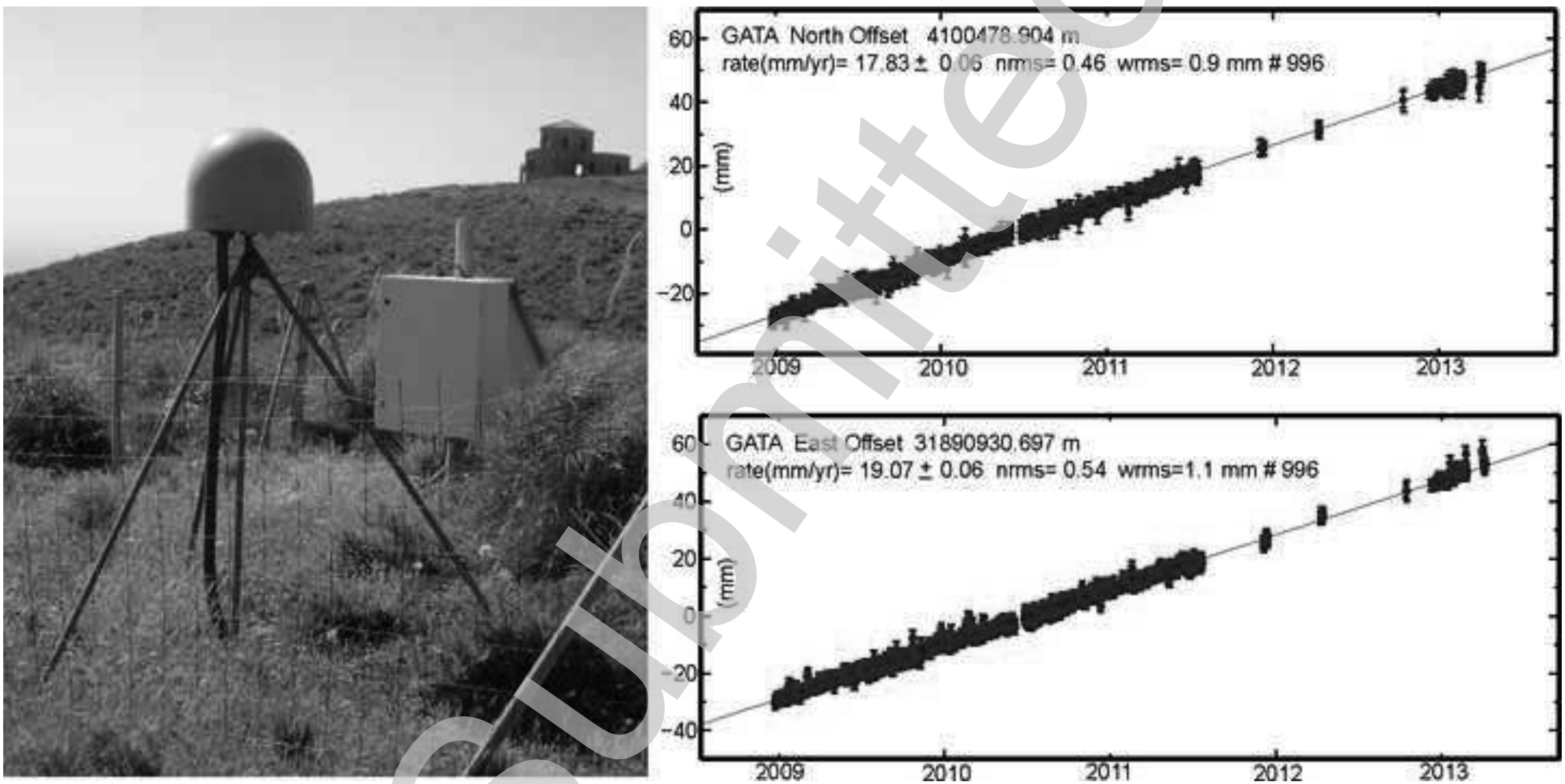

Figure 4
Click here to download high resolution image

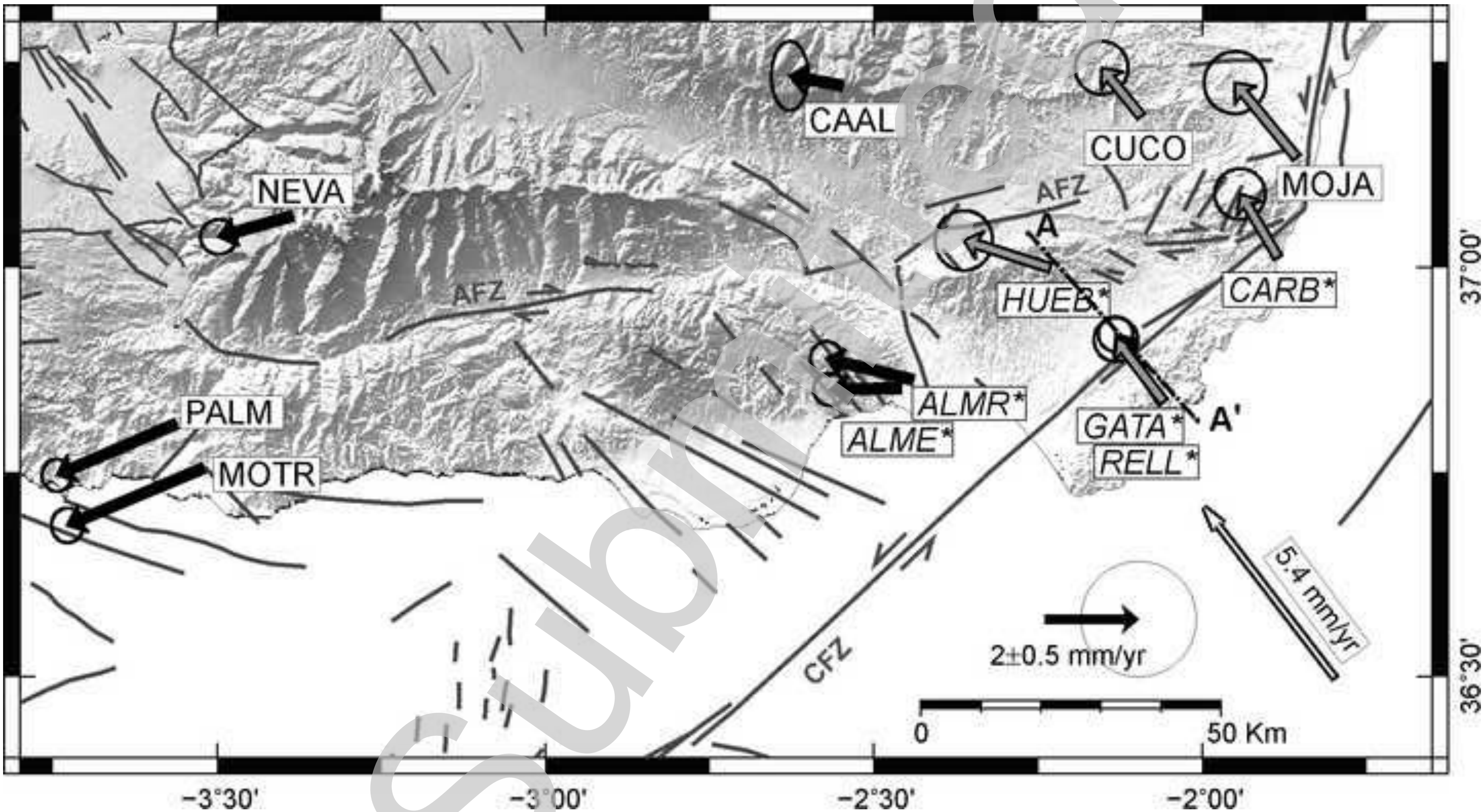

Figure 5
Click here to download high resolution image

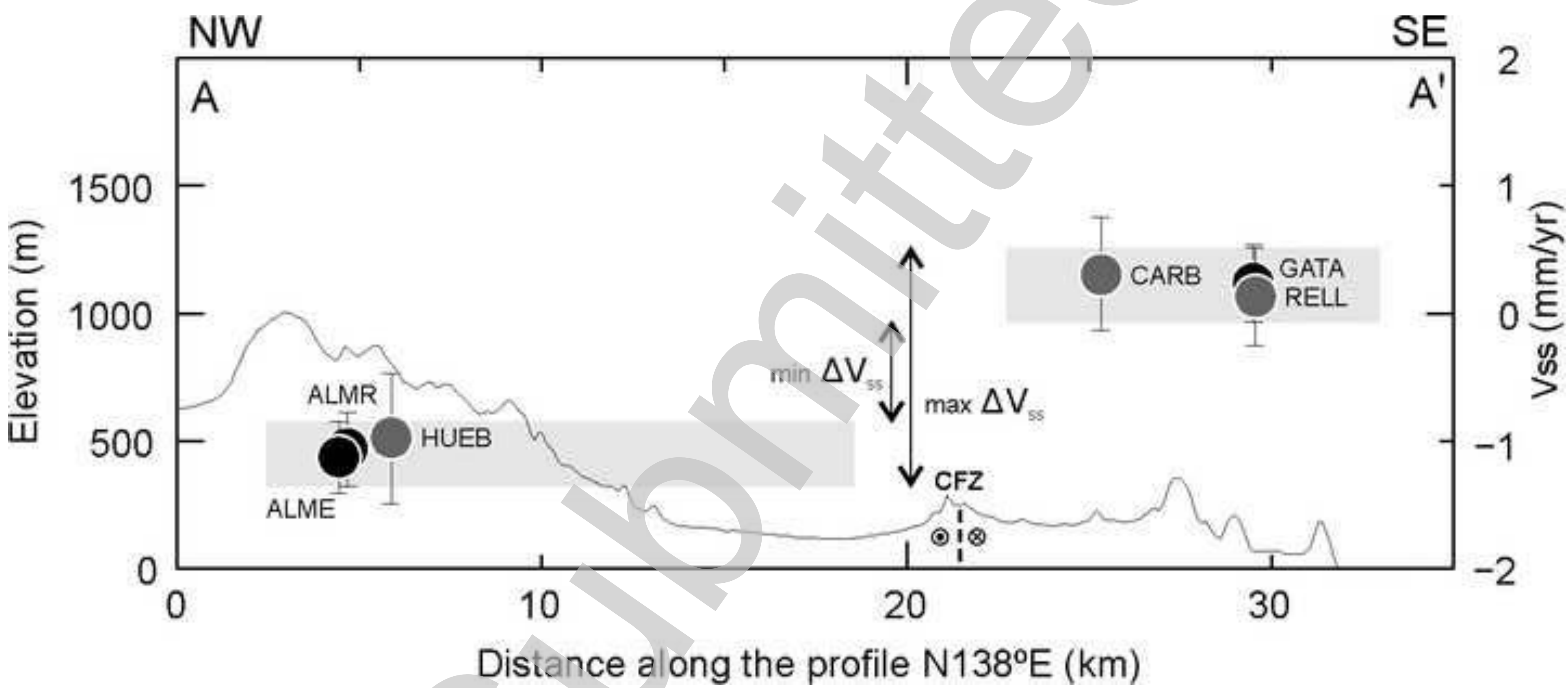

Figure 6
Click here to download high resolution image

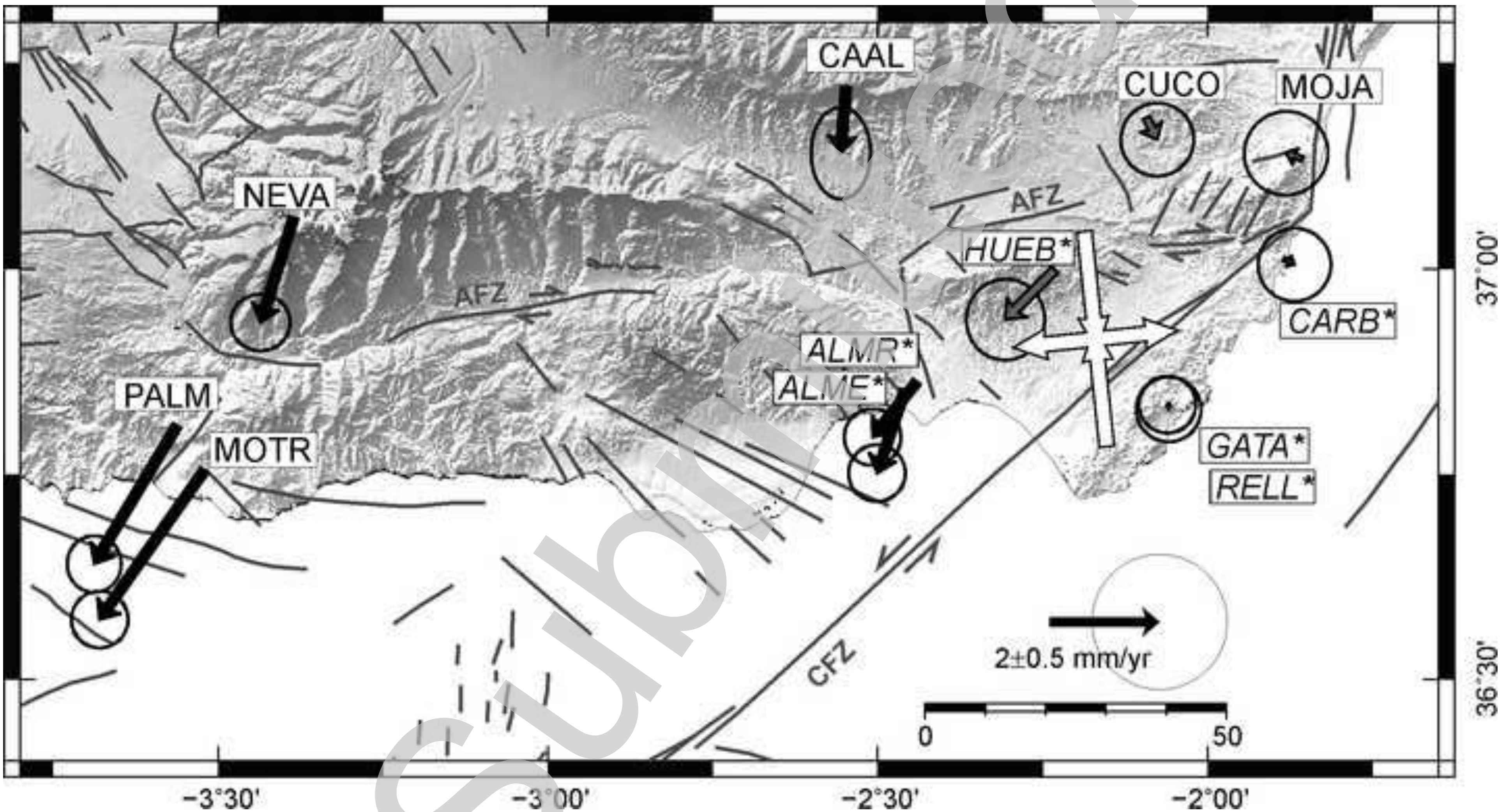

Figure 7
Click here to download high resolution image